

Deformation Mechanisms in Niobium Silicide-Based Composites

by

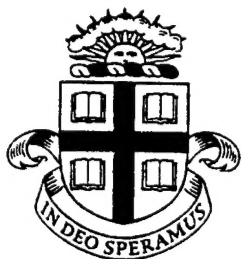
Dr. Bernard P. Bewlay
Dr. Melvin R. Jackson
Prof. Clyde L. Briant

AFOSR FINAL REPORT

This research was sponsored by the Air Force Office of Scientific Research,
Directorate of Aerospace and Materials Science
Under Contract 49620-00-C-0014

The views and conclusions contained in this document are those of the authors and should not be interpreted as necessarily representing the official policies or endorsement, either expressed or implied, of the Air Force Office of Scientific Research or the U.S. Government

February 28, 2001



BROWN UNIVERSITY



GE Corporate Research
& Development

20010404 120

REPORT DOCUMENTATION PAGE

AFRL-SR-BL-TR-01-

0217

Public reporting burden for this collection of information is estimated to average 1 hour per response, including the gathering and maintaining the data needed, and completing and reviewing the collection of information. Send comments regarding this burden estimate or any other aspect of this collection of information, including suggestions for reducing this burden, to Washington Headquarters Services, Directorate for Information Operations and Reports, 1215 Jefferson Davis Highway, Suite 1204, Arlington, VA 22202-4302, and to the Office of Management and Budget, Paperwork Reduction Project (0704-0188) Washington, DC 20503.

1. AGENCY USE ONLY (Leave Blank)		2. REPORT DATE February 28, 2001		3. REPORT TYPE AND DATES COVERED Final Report; March 1, 2000 – February 28, 2001	
4. TITLE AND SUBTITLE Deformation Mechanisms in Niobium Silicide-Based Composites: Report for Period 3-1-2000 to 2-28-2001				3. FUNDING NUMBERS 49620-00-C-0014	
6. AUTHORS Dr. Bernard P. Bewlay, Dr. Melvin R. Jackson, Prof. Clyde L. Briant					
7. PERFORMING ORGANIZATION NAME(S) AND ADDRESS(ES) GE Corporate Research and Development, Schenectady, NY 12301				8. PERFORMING ORGANIZATION REPORT NUMBER 2001SRD001	
9. SPONSORING / MONITORING AGENCY NAME(S) AND ADDRESS(ES) Air Force Office of Scientific Research, Directorate of Aerospace and Materials Science 801 North Randolph Street, Mail Room 732 Arlington, VA 22203-1977				10. SPONSORING / MONITORING AGENCY REPORT NUMBER	
11. SUPPLEMENTARY NOTES					
12a. DISTRIBUTION / AVAILABILITY STATEMENT Approved for public release; distribution is unlimited				<p>AFRL-SR-BL-TR-01-0217</p> <p>NOTICE OF TRANSMITTAL DTIC. THIS TECHNICAL REPORT HAS BEEN REVIEWED AND IS APPROVED FOR PUBLIC RELEASE</p> <p>LAW AFR 190-12 DISTRIBUTION CODE UNCLASSIFIED</p>	
13. ABSTRACT (Maximum 200 words)					
<p>This report describes a 9-month technical effort involving microstructure analysis and modeling of Nb-silicide in-situ composite creep mechanisms. This report will describe both experimental and theoretical modeling of the constitutive creep behavior of Nb-silicide in situ composites. The motivation for this study was to develop an understanding of the creep behavior of a class of materials that possess a long-term high-temperature capability in excess of current nickel-based superalloys. During this program the creep mechanisms that can be enhanced by modification of the microstructure and properties of the metal and silicide phases of the composite have been studied. This investigation has examined the effect of volume fraction of silicide and strength of the metallic phase on the creep performance of the composites. The effect of alloying additions on single-phase and composite creep behavior has also been investigated. This report will describe both experimental and theoretical modeling of the constitutive creep behavior of Nb-silicide in situ composites.</p>					
14. SUBJECT TERMS				15. NUMBER OF PAGES	
				16. PRICE CODE	
17. SECURITY CLASSIFICATION OF REPORT unclassified		18. SECURITY CLASSIFICATION OF THIS PAGE unclassified		19. SECURITY CLASSIFICATION OF ABSTRACT unclassified	
20. LIMITATION OF ABSTRACT UL					

Deformation Mechanisms in Niobium Silicide-Based Composites: Report for Period 3-1-2000 to 2-28-2001

(Contract Number: 49620-00-C-0014)

Research Contributors

Dr. Bernard P. Bewlay, GE-CRD, Staff Metallurgist
Dr. Melvin R. Jackson, GE-CRD, Staff Metallurgist
Prof. Clyde L. Briant, Brown University, Professor

Summary

This report describes a 9-month technical effort involving microstructure analysis and modeling of Nb-silicide in-situ composite creep mechanisms. The motivation for this study was to develop an understanding of the creep behavior of a class of materials that possess long-term high-temperature capability greater than that of current nickel-based superalloys. During this program the creep mechanisms that can be enhanced by modification of the microstructure and properties of the metal and silicide phases of the composite have been evaluated.

This investigation has examined the effect of volume fraction of silicide and strength of the metallic phase on the creep performance of the composites. The effect of alloying additions on single-phase and composite creep behavior has also been investigated. This report will describe first, experimental modeling of composite creep, and second, numerical modeling of the constitutive creep behavior. Finally, there will be a brief description of a study on Nb-silicide eutectoid decomposition.

1.0. Objectives

The objective of the present research was to investigate the fundamental mechanisms that control the high-temperature creep performance of Nb silicide-based in-situ composites. Initial composite creep modeling was developed to provide a framework for a fundamental understanding of the high-temperature behavior of these systems. Fundamental studies of the relationships between high-temperature composite microstructure, individual phase properties and creep processes at high temperature have been performed. The stress sensitivity of the composite creep performance has also been examined.

2.0 Approach

This basic research program has focused on modeling of the creep deformation behavior of Nb silicide-based composites. It has employed modeling tools and sophisticated analytical techniques, such as orientation imaging microscopy. Initial stochastic modeling of the deformation processes that control the overall creep behavior has also been performed. The long-term aim of this approach is to build a set of tools that can be used to design revolutionary materials for high temperature applications.

3.0 Progress and Status of Effort

Composite Creep Analyses

Nb-silicide based in-situ composites are potential candidates for very high temperature structural applications ($>1150^{\circ}\text{C}$), including advanced turbine applications [1-6]. These composites consist of Nb_5Si_3 and Nb_3Si type silicides toughened with a Nb solid solution (abbreviated by (Nb) in the present report). The high-temperature creep performance has been found to be highly dependent of the alloy composition and constituent phases. Alloying elements such as Cr and B have beneficial effects on oxidation resistance, stabilizing Laves phases, and T2 niobium borosilicide phases, respectively. The creep behavior of these phases has not been investigated previously.

The microstructure of the composites from binary hypoeutectic alloys consists of (Nb) dendrites with an interdendritic Nb_3Si -(Nb) eutectic. The Nb_5Si_3 and Nb_3Si have the tI32 and tP32 ordered tetragonal structures with 32 atoms per unit cell. The unit cells also possess large lattice parameters; the large Burgers vectors and complex dislocation cores associated with these structures would suggest that dislocation creep makes only a small contribution to creep deformation in these silicides. When Nb_5Si_3 is alloyed with Ti and Hf, the less complex hP16 structure can also be stabilized [9-11]. Nb_3Si and tetragonal Nb_5Si_3 are beneficial to creep behavior, provided their volume fraction and distribution within the composite are controlled. The crystallography of these silicides will be discussed in more detail subsequently.

The microstructure of a complex composite is shown in Figure 1. This microstructure illustrates the complexity of the mechanical behavior modeling challenge for these composites. The microstructure possesses large-scale faceted Nb_5Si_3 dendrites and (Nb). The Nb_5Si_3 provides the high-temperature structural performance and the (Nb) the low-temperature damage tolerance. The Laves phase provides high-temperature oxidation performance. There are also interdendritic regions of (Nb)- Nb_5Si_3 eutectic; this eutectic is generally considered to be detrimental to the creep performance. In the course of the present study the constitutive properties of the monolithic phases have been investigated.

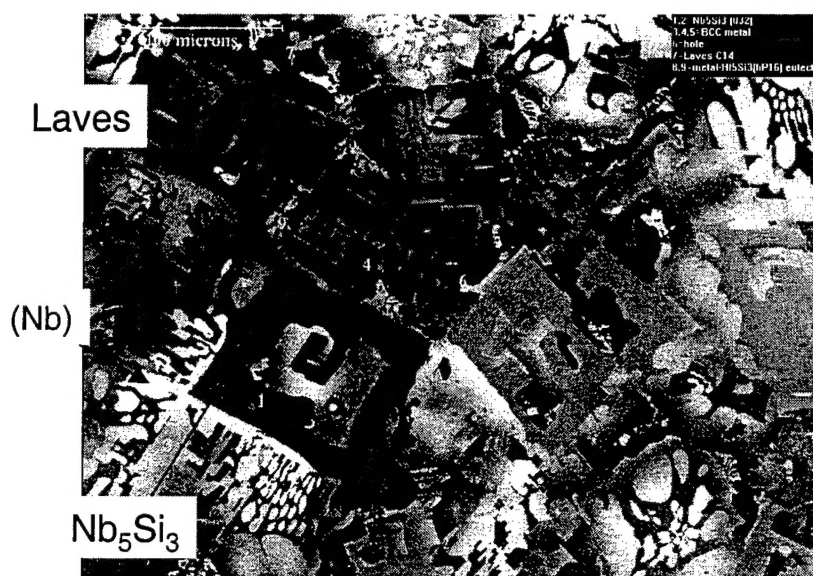


Figure 1. Microstructure of the transverse section of a DS in-situ composite derived from a Nb-21.5Ti-4Hf-18Si-8Cr-2Al alloy.

The present study was performed to determine the creep rates of Nb-silicide based composites, and the monolithic intermetallic phases in complex systems. This study was designed to develop both the constitutive creep laws for these phases and a predictive modeling capability for more complex two-phase and multi-phase systems [12]. The aim of the present section is to describe high-temperature creep behavior of the monolithic intermetallic phases and the resulting Nb-silicide in-situ composites that were produced by directional solidification.

In order to determine the effect of phase volume fraction, Nb-silicide based in-situ composites were directionally solidified from quaternary alloys with compositions of Nb-8Hf-25Ti- X Si, where X was adjusted from 12 to 22%. The directional solidification procedure has been described in more detail previously [1]. Monolithic intermetallic creep samples were prepared using multiple arc melting. Monolithic Nb alloys were also prepared with compositions of Nb-1Si, Nb-46Ti-1Si (denoted as Nb-3 in the present report), and Nb-27Ti-5Hf-2Al-2Cr-0.9Si (denoted as Nb-C), in order to determine the creep performance of the Nb solid solution in the in-situ composites. The samples were examined using scanning electron microscopy and Electron Back-Scatter Diffraction (EBSD) in the SEM.

Table I shows the compositions of the monolithic intermetallic phases that were investigated. The compositions of these phases were selected using electron microprobe analyses (EMPA) of the respective phases in multi-phase composites [9,10]. The monolithic intermetallics that were generated from ternary alloys were given the post-script 3, for example, the Nb₅Si₃ modified with 10% Ti was labeled silicide-3. The monolithic intermetallics that were prepared from quaternary and higher-order alloys were given the post-script C, such as silicide-C.

Compression creep tests were conducted at temperatures of 1100 and 1200°C, and at stress levels of up to 280 MPa in a vacuum of $\sim 5 \times 10^{-5}$ Torr. The cylindrical specimens that were used were 7.6 mm in diameter and up to 30 mm in length. Tensile creep rupture tests were performed in flowing argon with ASTM specification creep frames. Incremental loading and interruption of the creep tests at 24-hour intervals were employed to determine the creep rate at multiple stress levels.

Table I: Compositions (in atom per cent) of the monolithic phases that were investigated. The phases labeled 'silicide' are both based on the Nb_5Si_3 .

PHASE	Nb	Ti	Hf	Si	Cr	Al	B
Laves-C	21.0	11.0	5.5	8.5	53.0	1.0	
Laves-3	30.0			15.0	55.0		
Silicide-C	38.5	16.0	6.0	37.0	1.0	1.0	0.5
Silicide-3	53.0	10.0		37.0			
T2-C	41.5	13.0	3.0	12.5	4.0	0.5	25.5
T2-3	62.5			12.5			25.0
hP16-3	20	44		36.0			
hP16-C	25.5	25.5	13	36.0			
$(\text{Nb})_3\text{Si-C}$	49.0	18.2	7.8	25.0			
$(\text{Nb})\text{-C}$	63.1	27	5	0.9	2	2	
Nb-1Si	99			1			
Nb-46Ti-1Si	53	46		1			

Composite Microstructures

Figure 2 shows the typical microstructure of the composites based on Nb-8Hf-25Ti-XSi alloys with Si concentrations of 20% and less. The microstructure consisted of $(\text{Nb})_3\text{Si}$ tP32 phase (the grey phase) with (Nb) dendrites (the light phase). The dendrites appear to have grown cooperatively to generate an interpenetrating structure. Both the $(\text{Nb})_3\text{Si}$ and the (Nb) possess substantial amounts of Hf and Ti in solid solution [9,10].

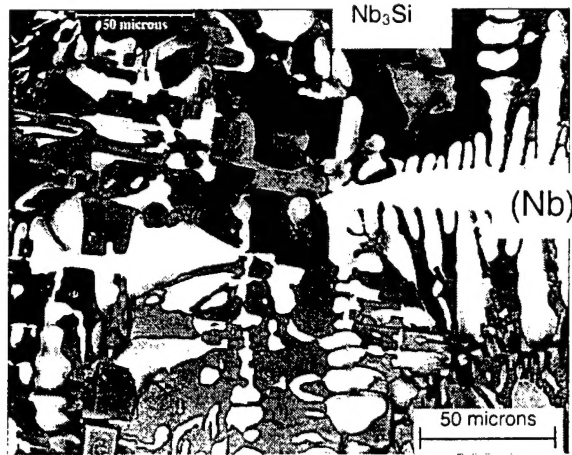


Figure 2. Scanning electron micrograph (BSE image) of the typical microstructure of the transverse section of a DS composite generated from a quaternary Nb-25Ti-8Hf-16Si alloy. The (Nb) is the light phase and the $(\text{Nb})_3\text{Si}$ is the grey faceted phase.

Figure 3 shows the typical microstructure of the composites with Si concentrations greater than 20% and less than 25%Si. In addition to the $(\text{Nb})_3\text{Si}$ and (Nb) phases observed in the composites from lower Si concentrations, the Nb_5Si_3 phase was also observed as the primary solidification phase. The $(\text{Nb})_5\text{Si}_3$ was the large-scale, dark, faceted phase.

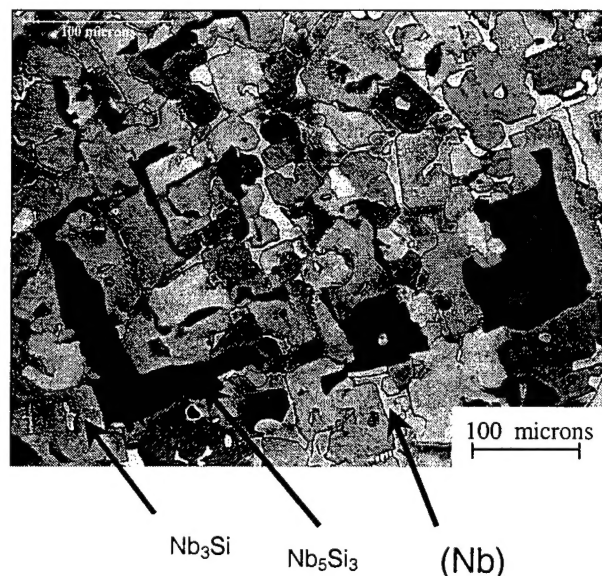


Figure 3. Scanning electron micrograph (BSE image) of the typical microstructure of a transverse section of a DS composite from a quaternary Nb-25Ti-8Hf-22Si alloy. The (Nb) is the light phase, the $(\text{Nb})_3\text{Si}$ is the grey phase, and the $(\text{Nb})_5\text{Si}_3$ the dark phase.

Creep of Composites

Figure 4(a) shows the compression creep rate as a function of Si concentration for the Nb-25Ti-8Hf-XSi composites, where X was adjusted from 12 to 22 atomic percent. Data are shown at 1200°C for stresses of 140 to 280 MPa. Quantitative microscopy indicated that as the Si concentration was increased from 12% to 18%, the volume fraction of $(\text{Nb})_3\text{Si}$ increased from 0.25 to 0.71. There is a broad range of compositions for which the creep rate is less than $3 \times 10^{-8} \text{s}^{-1}$, which is an important design goal for high-temperature applications [4].

There are two important features of these creep data. First, the creep rate possessed a minimum value between 18 and 20 %Si. The compositional width of the creep rate minimum decreased with increasing stress. Second, at higher Si concentrations (>20%) the creep rate increased. Microstructural analysis of samples after creep testing indicated that at low Si concentrations, deformation was controlled by creep of the (Nb) , but at high Si levels, creep deformation was controlled by cracking of the silicide.

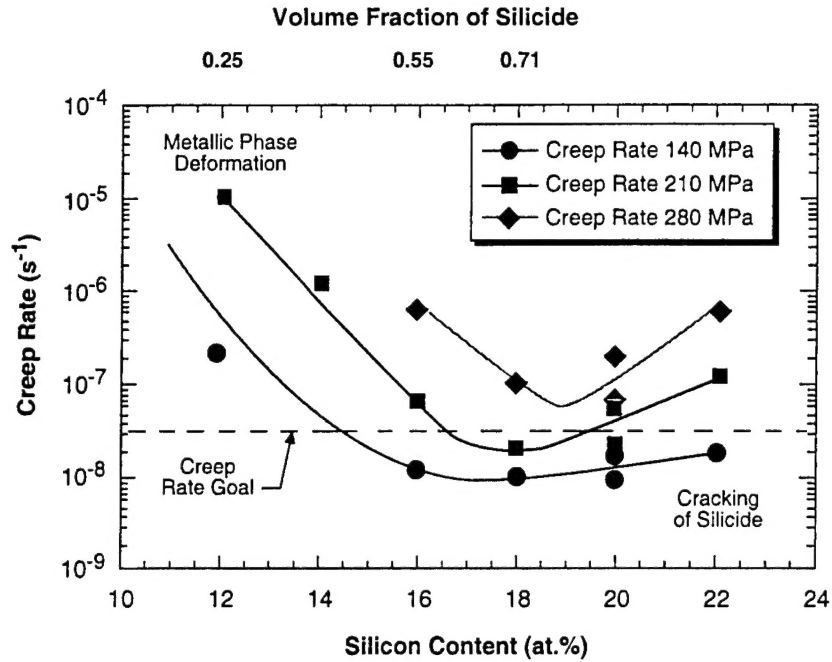


Figure 4(a). Effect of Si concentration (volume fraction of metal and silicide) on the secondary creep rate of Nb-Si based composites for stresses of 70-280 MPa at 1200°C. At low Si concentrations, deformation is controlled by creep of the (Nb) and at high Si concentrations, composite deformation is controlled by cracking of the silicide.

A typical strain-time plot from a tensile creep test is shown in Figure 4(b) for an incremental loading experiment. It shows the primary and secondary creep regimes at the individual stress levels. At stress levels up to 105 MPa the secondary creep regimes were very stable, higher stress levels can lead to the onset of tertiary creep. Primary creep strains and secondary creep rates were obtained at each stress level.

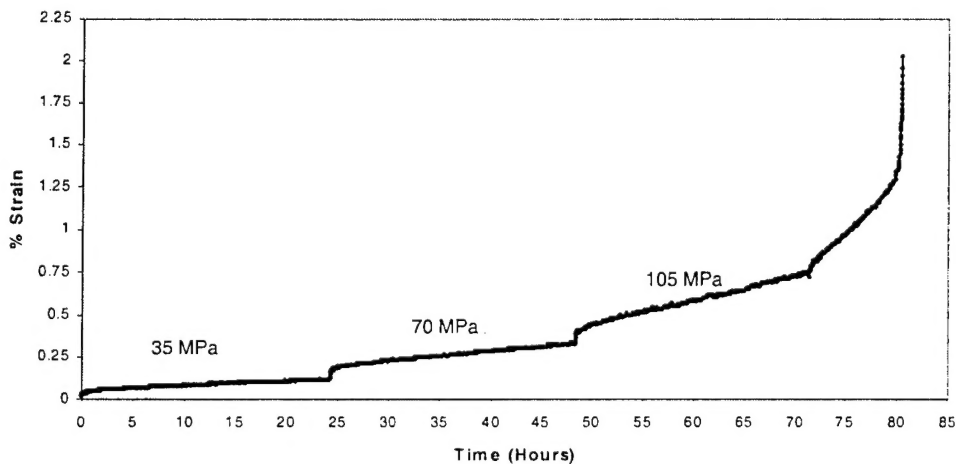


Figure 4(b). Strain-time plot from a tensile creep test for incremental loading.

Figure 4 (c) shows the secondary creep rate as a function of stress at 1200°C for Nb-25Ti-8Hf-XSi composites for Si concentrations from 12 to 22%. The stress exponent was calculated for each composite. The lowest stress exponent was for the Nb-25Ti-8Hf-18Si composite (3.3) and the highest was for the Nb-25Ti-8Hf-12Si (>5). At Si concentrations greater than 18%, the stress exponent also begins to rise from the minimum at the 18%Si composition; for the Nb-25Ti-8Hf-22Si the stress exponent was 5.1. In all composites the stress exponents were closer to those of the (Nb) than to the tI32 silicides. The hypoeutectic composites also only possess (Nb)₃Si rather than the Nb₅Si₃, and this may be contributing to these relatively high stress exponents.

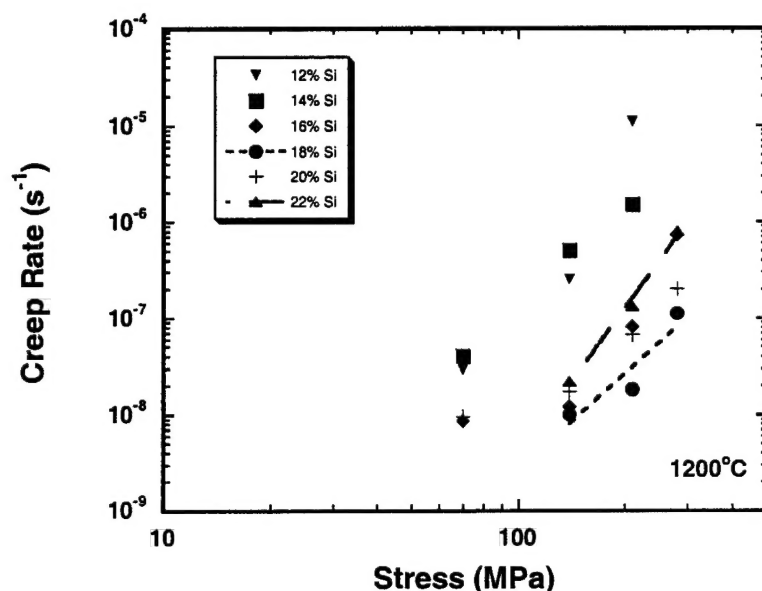


Figure 4(c). Secondary creep rates as a function of stress at 1200°C for Nb-8Hf-25Ti-XSi.

Creep Behavior of the Monolithic Phases at 1100°C and 1200°C

The creep data for the monolithic intermetallics are shown in Figures 5 and 6. Figure 6 also shows data for the binary monolithic Nb₅Si₃, and the Nb₅Si₃-Nb composite prepared from the binary Nb-10Si alloy [11].

The data for the creep tests at 1100°C are shown in Figure 5. The data are not complete for all compositions, as will be discussed below. The data are well behaved for the ternary Nb₅Si₃ silicide-3 and the Nb₃Si-C. There is some scatter in the Nb₅Si₃-C data; the highest creep rate that was measured was 2 × 10⁻⁸ s⁻¹ at 210 MPa, and all other measurements were below this value. At creep rates < 10⁻⁸ s⁻¹ there is generally more scatter in the data because these rates are very close to the measurement limit for the creep system that was employed (~5 × 10⁻⁹ s⁻¹); this limit was governed by the dilatometer resolution, mechanical stability, and electrical noise. The silicide-3 and silicide-C have creep rates that are close to that of the binary Nb₅Si₃, but they are slightly higher. The ternary Nb₅Si₃ with Ti substituted for Nb has a lower creep rate than the Nb₅Si₃-C. The Nb₃Si-C has the highest creep rates. At 1100°C the creep rate of the T2 was ~3 × 10⁻⁸ s⁻¹, but there was little sensitivity of the creep rate to stress.

Due to limited ductility of some of the phases at 1100°C, cracking occurred in some cases during the creep test, and this led to some difficulties/inconsistencies in some creep strain measurements. For some of the alloys, such as Laves-3 and Laves-C, the creep rates were very low ($< 5 \times 10^{-9} \text{ s}^{-1}$) at low stresses (70 MPa), and increasing the stress led to cracking prior to creep. This behavior was observed for the Laves-C at both 1100°C and 1200°C. Thus, there are no data in Figure 5 for the Laves phases and the T2-3 phase. The microstructures of the creep samples were analyzed after the creep test in order to investigate the type of cracking that occurred. Creep data for the binary Nb_5Si_3 at 1200°C, as reported by Subramanian et al. [13], indicate that even at 1200°C the creep rate of the binary Nb_5Si_3 is less than that of any of the other phases at 1100°C.

At 1100°C further analysis of the exponents for the intermetallics is limited by the small data set. Exponents for the silicide-3 and $\text{Nb}_3\text{Si-C}$ were determined, but they had values less than unity. This would suggest that there is some creep threshold, or other complicating factor, that is preventing further interpretation of the data.

At 1200°C the binary Nb_5Si_3 possessed the lowest creep rates and the $\text{Nb}_3\text{Si-C}$ displayed the highest creep rates of the tetragonal phases investigated. The hP16 phases had creep rates similar to the T2-C phase at stresses up to 140 MPa. However, on increasing the stress above 140 MPa the creep rate of the hP16-C increased rapidly to $3 \times 10^{-5} \text{ s}^{-1}$ at 210 MPa, as shown in Figure 6. This behavior suggests a change in creep mechanism with increasing stress. The hP16 phases have the worst performance, and at high stresses these creep rates are beyond the scale of Figure 6.

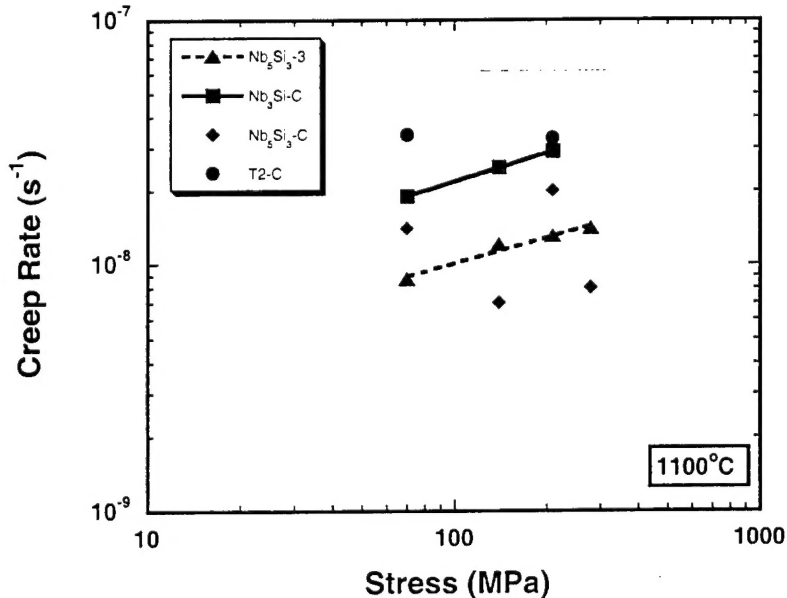


Figure 5. Secondary creep rates at 1100°C for the monolithic silicides that were investigated.

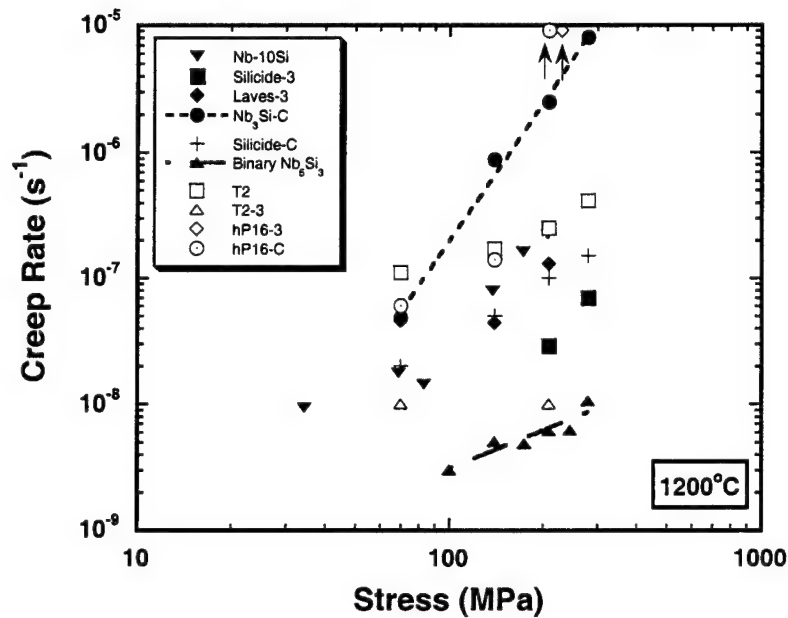


Figure 6. Secondary creep rates at 1200°C for the monolithic silicides, Laves phases, hP16 and T2 phases that were investigated.

The silicide-3 and silicide-C had creep rates that were also higher than those of the binary Nb_5Si_3 . The ternary Nb_5Si_3 with Ti had a lower creep rate than the $\text{Nb}_5\text{Si}_3\text{-C}$. The T2-C creep curve was higher than those of the Nb_5Si_3 type silicides, although it was lower than that of the $\text{Nb}_3\text{Si-C}$. The creep rate of the T2-3 was $\sim 1 \times 10^{-8} \text{ s}^{-1}$, but there was little sensitivity of the creep rate to stress. The T2-3 also had a lower creep rate than the T2-C; the addition of Ti, Hf, Cr and Al led to an increase in the creep rate of the T2. The Laves-3 possessed creep rates similar to those of the silicide-3.

The creep rates of the Nb-1Si, Nb-46Ti-1Si, and Nb-C at 1100°C and 1200°C are shown as a function of stress in Figure 7. These compositions cover the compositions of the Nb-based solid solutions in the composites that have been generated previously from ternary, quaternary, and higher-order alloys. The data at 1200°C indicate that the creep rate of the (Nb) is greater than 10^{-7} s^{-1} even at stresses as low as 70 MPa. The creep rates of these monolithic Nb alloys are similar to those of the composites from the low Si (less than 14%) quaternary alloys shown in Figure 4(a). These results also show that the creep rate of the Nb-Si solid solution is very sensitive to Ti additions.

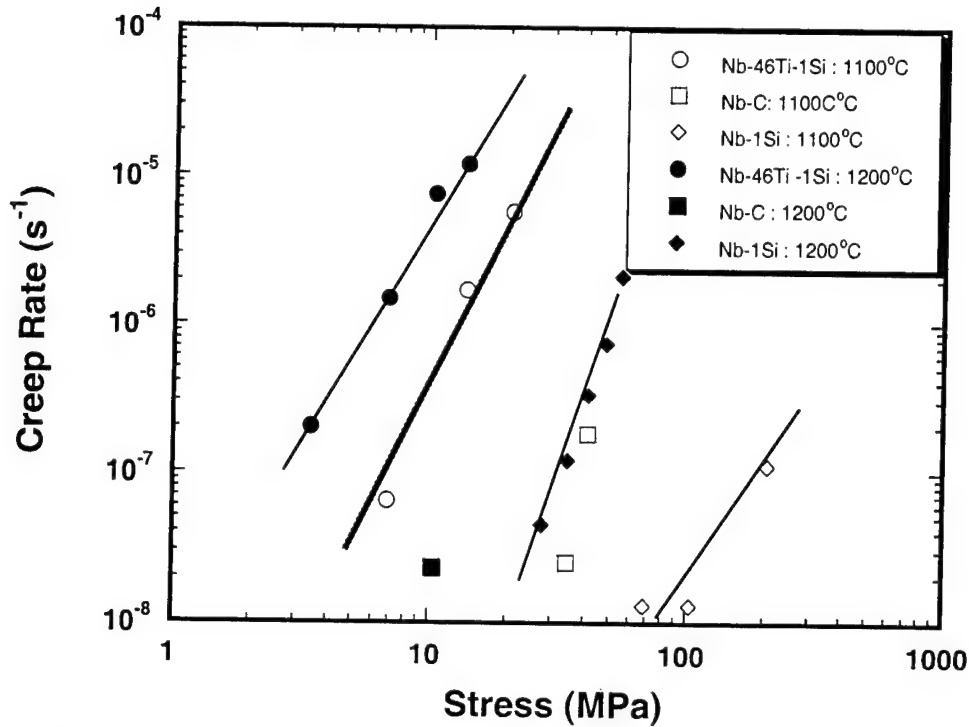


Figure 7. Secondary creep rates as a function of stress at 1100°C and 1200°C for binary Nb-Si, ternary Nb-Ti-Si, and complex Nb-based monolithic solid solutions. Note the stress range is 10 times lower than in Figures 4 and 5. The effect of alloying additions on creep rate is shown.

The stress sensitivity of the creep rate was determined by relating the creep rate ($\dot{\epsilon}$) and stress (σ) using a power law equation of the form, $\dot{\epsilon} = B \sigma^n$; where n is the stress exponent and B is a constant at any specific temperature. The grain size of all the monolithic phases was large and of approximately the same order of magnitude ($\sim 100 \mu\text{m}$). In the present study no attempt was made to incorporate any dependence of the creep rate on grain size.

The stress exponents are shown in Table II. In the case of the Nb_5Si_3 the stress exponent was almost one and the mechanism for creep deformation was reported to be Nabarro-Herring creep, the creep deformation being limited by Nb diffusion [13]. In the cast and heat treated conditions, the dislocation densities in the monolithic intermetallic phases investigated were very low, and Harper-Dorn creep probably did not make a significant contribution to creep. Therefore, the potential creep mechanisms are Nabarro-Herring, grain boundary sliding, or power law creep for the cases where the exponents are close to unity. Examination of the creep exponents in Table II indicates that the creep deformation of the monolithic phases is controlled by a range of mechanisms. For example, the T2-C, Laves-3, and silicide-C constitute the first group that have exponents close to unity, as is the case for binary Nb_5Si_3 . Creep deformation of these phases is probably also controlled by Nabarro-Herring type creep, but the diffusing species that control deformation are still being investigated. The Nb_3Si -C and (Nb) alloys represent a

second group that have higher stress exponents (>3). The monolithic (Nb) alloys have exponents of ~ 3 , and in these systems deformation is probably controlled by dislocation creep. These exponents are similar to those reported previously for Nb-1.25Si [12]. This high stress exponent suggests that creep deformation is controlled by dislocation glide, as is the case for pure metals, despite the fact that the dislocation structures in Nb₃Si-C are complicated.

Table II: Stress, temperature, and power law constants describing secondary creep of the monolithic phases that were investigated.

Phase	Stress Range (MPa)	Temperature (°C)	Constant, B	Exponent n
Nb ₃ Si ₃	100-280	1200	6.16×10^{-11}	1.0
Nb-10Si	70-140	1200	6.57×10^{-12}	1.9
Silicide-C	70-140	1200	3.84×10^{-11}	1.5
Nb ₃ Si-C	70-140	1200	1.07×10^{-14}	3.6
Laves-3	70-140	1200	1.11×10^{-9}	1
T2-C	70-140	1200	2.15×10^{-9}	0.9
(Nb)-3	3-80	1100	1.9×10^{-10}	3.3
(Nb)	3-80	1100	4.7×10^{-14}	2.9
(Nb)-3	3-20	1200	4.5×10^{-9}	3.1
(Nb)	3-30	1200	5.4×10^{-16}	5.5

Composite Creep Modeling

In order to develop an improved understanding of the response of the composite to increasing silicide volume fraction and increasing stress, the creep of the composite was simulated using the equation shown below [12,14,15], where σ_A is the applied stress, n is the stress exponent for the silicide, and m is the stress exponent for the Nb. V_s and V_w are the volume fractions of the silicide and Nb, respectively. B_s and B_w are the pre-exponents in the power law creep expressions for the silicide and Nb, respectively.

$$\sigma_A = V_s \left[\frac{1}{B_s^{1/n}} \right] \dot{\epsilon}^{1/n} + V_w \left[\frac{1}{B_w^{1/m}} \right] \dot{\epsilon}^{1/m} \quad [1]$$

This equation provides a description of secondary/steady-state creep of a continuous composite in terms of the constitutive creep behavior of the individual phases. The composite is assumed to consist of infinitely long fibers and neglects fiber-matrix interactions. It is assumed that the strain is homogenous within the composite, and a volume fraction weighted distribution of the load between the phases. The local strain in the matrix and fibers is equal and identical to the macroscopic strain in the composite. Thus, it is assumed that there is material continuity and there is no cavitation of one

phase in order to compensate for differential strain between the fiber and the matrix phases. These structural assumptions are thus a major approximation of the Nb-silicide based in-situ composites of the present study. Where the strengthening phases are discontinuous (i.e. short fibers), flow of the matrix phases around the end of the fiber may occur. However, the aspect ratio of the silicide phase (>10) is such that the infinitely long fiber assumption is quite reasonable. The analysis also assumes that the stresses supported by the matrix and fiber are uniform within each phase and there is a discontinuous step at the fiber/matrix interface; this can only occur when each phase can deform independently without any interaction with the other phase. This equation contains no explicit parameter that accounts for the microstructural dimensions of the composite. The microstructural dimensions of the individual phases are incorporated implicitly through their constitutive properties, as described by the power law creep expressions.

The constitutive creep equations for the monolithic solid solutions were employed; using the data for the (Nb) and silicide solid solutions shown in Table II. For each calculation an applied stress was selected and the equation solved for the strain rate. Since n does not equal m , the equation had to be solved numerically. The above equation can predict the increase in the creep rate with increasing stress for a given Si concentration in the hypoeutectic regime. However, the model does not incorporate any damage mechanisms in either the (Nb) or the silicide.

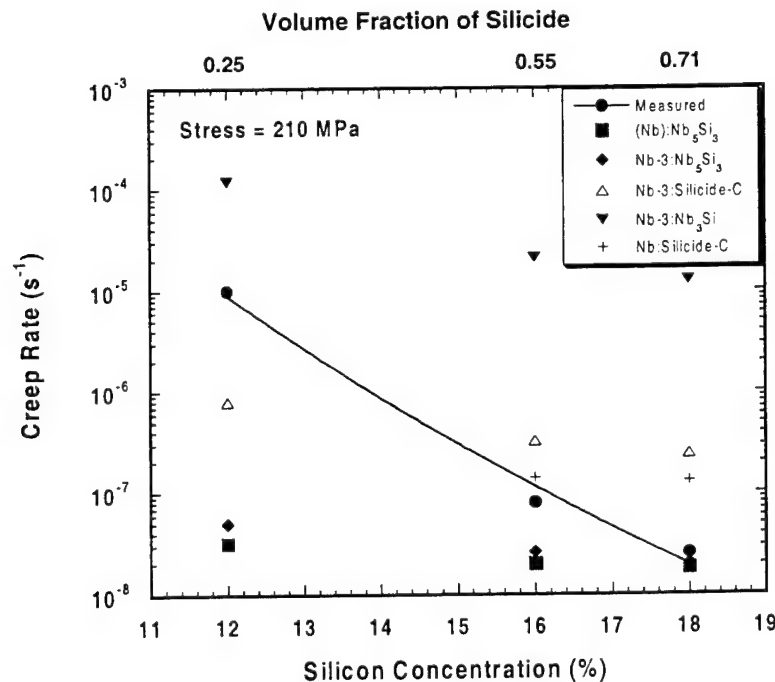


Figure 8. Comparison of the measured and the calculated composite creep rates at 210MPa for the range of (Nb) and silicide solid solutions investigated.

Figure 8 shows the effect of both the type of silicide and the type of (Nb) on the predicted

creep rates. The calculations were performed using Equation (1) in conjunction with the data in Table II at 1200°C for silicides and 1100°C for (Nb). The results show that increasing the alloying content of the (Nb) (Nb-3 vs. Nb-1Si) causes an increase in the predicted creep rate. Of the three silicides considered, the binary Nb₅Si₃ produces the composite with the lowest creep rate, and the Nb₃Si produces the composite with the highest creep rate. In general the predicted creep rates are higher than those measured experimentally. The effect of the (Nb) solid solution is brought about by the difference in the constitutive creep properties of the (Nb), specifically the effect of Ti additions. Figure 7 shows the detrimental effect of Ti on the creep performance of the (Nb).

Figure 8 shows the creep rate at 1200°C and 210MPa as a function of Si concentration for a series of composites that were constructed from the Nb₃Si-C, the binary Nb₅Si₃, and the complex Nb₅Si₃-C silicides. The composites were constructed using the ternary Nb-46Ti-1Si solid solution and the Nb-1Si binary solid solution. The power law constants describing the creep behavior of these individual phases are shown in Table II. The Si concentrations at which the composite creep properties were calculated were 12, 16 and 18%; these correspond to silicide volume fractions of 0.25, 0.55 and 0.71 respectively. The creep behavior was only modelled for composites in the hypoeutectic regime because the damage mechanisms that become operative at Si concentrations higher than ~18% are not represented explicitly by the constitutive model.

The data in Figure 8 illustrates the following points :

- [1] The binary Nb- composites have the lowest creep rates.
- [2] The Nb-3 : Nb₃Si-C composites have the highest creep rates.
- [3] The calculated creep rates decrease with increasing volume fraction of silicide.
- [4] The calculated decrease in creep rate with increasing volume fraction of silicide is lower than the measured trend; this point will be discussed subsequently.
- [5] The constitutive properties of the (Nb) have a significant effect on the composite creep performance; if we consider the Nb₅Si₃ based composite with (Nb), the creep rates are increased ~50% on substitution of Nb-3 for Nb; the increase in the creep rate on adding Ti to the (Nb) is increased as the (Nb) volume fraction is increased. Similarly, if we consider the Nb₅Si₃-C based composite with (Nb), the creep rates are increased ~50% on substitution of Nb-3 for Nb.

The creep rates were calculated for the same composites at 140MPa, and similar trends were observed, as shown in Figure 9.

Figure 10 shows the effect of the type of silicide (at a volume fraction on 0.6) on the creep rate for the Nb₃Si-C, the binary Nb₅Si₃, and the complex Nb₅Si₃ -C silicides at stress levels of 140 and 210MPa. The results of these calculations show the important role of the constitutive behavior of the silicide. The composite based on the binary Nb₅Si₃ has the lowest creep rate at both stress levels.

Figure 11 shows the effect of the chemistry of the (Nb) on the creep rate for composites constructed from the three difference silicides, Nb₃Si-C, the binary Nb₅Si₃, and the

complex $\text{Nb}_5\text{Si}_3\text{-C}$ at a stress level of 140MPa and volume fraction of silicide of 0.6. Again the results show that the creep rates are highest with the $\text{Nb}_3\text{Si-C}$, and lowest with the binary Nb_5Si_3 . In addition, for all silicides, the creep rates were lower with the Nb-1Si than with the Nb-3 (Nb-46Ti-1Si). This suggests that the constitutive behavior of the (Nb) at high temperature can in fact play a bigger role than has previously been suggested [12].

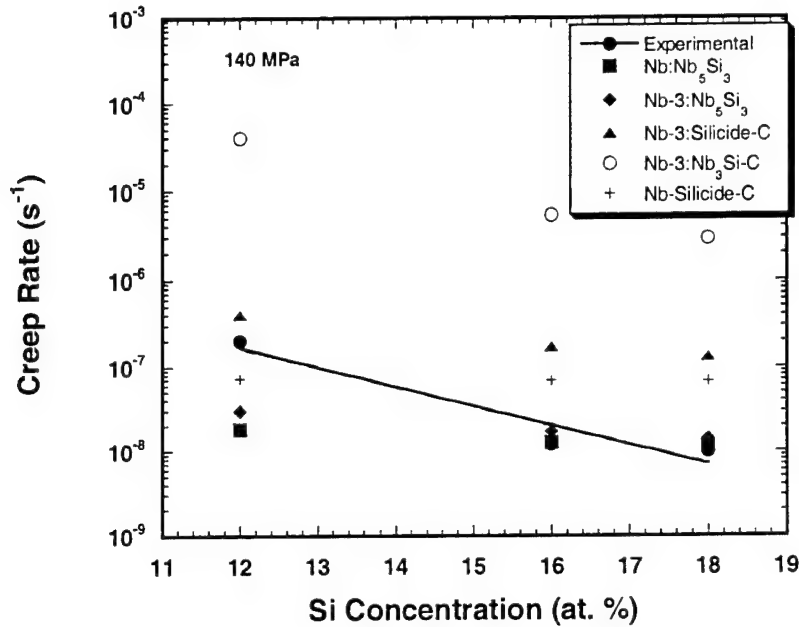


Figure 9. Comparison of the measured and calculated composite creep rates at 140 MPa for the range of (Nb) and silicide solid solutions investigated.

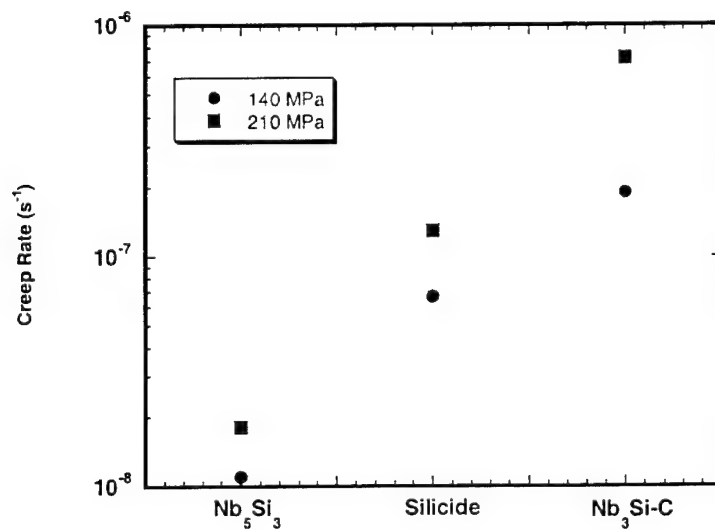


Figure 10. Predicted creep rates for 140 MPa and 210 MPa.

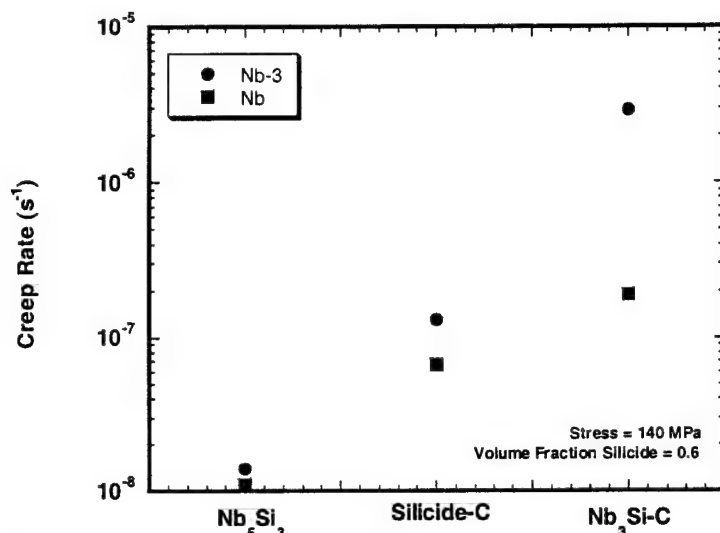


Figure 11. Effect of (Nb) chemistry on composite creep rate.

Figure 8 also shows the effect of silicide volume fraction on creep rate at a stress of 210 MPa. In Figure 8 the measured creep rates are given along with predicted creep rates for various combinations of (Nb) and silicide solid solutions. The measured creep rates decrease between 12 and 18%Si (~0.25 to ~0.7 silicide volume fraction). The calculated creep rates also decrease with increasing Si concentration from 12 to 18 %Si, but the rate at which the predicted creep rates decrease is slower than the rate at which the measured creep rates decrease. There are several possible reasons for this difference. First, in addition to the increase in the volume fraction of silicide, there is probably a change in the continuous matrix phase from (Nb) to silicide at some point between 12 and 18%Si. Second, interface diffusion may play a bigger role in the composites, whereas in the monolithic solid solutions creep was limited by bulk diffusion.

In addition, in the composites that contain Nb₃Si rather than Nb₅Si₃, the calculated creep rates of the Nb₃Si-containing composites were substantially higher than the creep rates that were measured for the DS Nb-8Hf-25Ti-XSi alloys. The measured creep rates of the Nb₃Si-containing composites are closer to the calculated creep rates of the Nb₅Si₃-containing composites.

Stochastic Creep Modeling

The modeling described above takes a continuum approach to describing creep deformation. As such, it provides considerable insight into the problems that are associated with the overall deformation of the composite and allows for one method of prediction of the creep rate. However, the experimental studies also indicate that damage contributes to the measured creep rate and to develop a more complete model of this process we need both the continuum approach and an approach that directly considers microstructure and damage. As part of our research on this program, we have explored

the use of stochastic methods to examine the problem of creep deformation. Such a technique allows one to generate equivalent microstructures and then deform them in selected ways by finite element methods.

The basic approach to generating equivalent microstructures is to perform the following steps:

- 1 An experimental micrograph is scanned and digitized .
- 2 Correlation coefficients are determined from the scanned image that match the volume fraction of the second phase and other specific features of the microstructure.
- 3 An equivalent image is generated that has the same volume fraction of the various phases as the starting microstructure.
- 4 This microstructure is 'annealed' until it reproduces the same correlation coefficients as the starting structure.
- 5 This process can be repeated multiple times generating a series of equivalent images.
- 6 Once these images are obtained they can be used to obtain average mechanical properties.

In our studies to date we have focused on obtaining equivalent microstructures. Figure 12 shows a microstructure that has been scanned and digitized. The scanned image was derived from the left hand side of Figure 2. The digitized image shows a low-resolution discretized rendition of the initial image. Figure 13(a) shows a reconstructed micrograph of Figure 12 after it has been "annealed." Figures 13 (b) shows the two-point correlation function for both the original micrograph and the simulated image. It is clear that they match well; the volume fractions are also similar for the two images. Thus, we have developed capabilities to generate equivalent microstructures.

One of the clear differences in the simulated image and the original micrograph is the detailed features of the two. The simulated image has produced a second phase that is essentially spherical whereas the original image has dendritic features. In future work we may want to impose certain restrictions on the simulated microstructures to make them more equivalent to the experimental images. Also to date we have dealt with only two phase microstructures; clearly for these Nb-silicide based composites it is also important to consider more complex structures.

The next step in this research will be to apply the finite element calculations to these simulated microstructures and to examine the damage that can be generated. For these calculations we will use the mechanical properties of the monolithic intermetallics that have already been investigated in the present study.

Nb-Silicide Crystal Structures

The tI32 structure has an ABAB type structure stacked along the [001]. The structure possesses three types of 'basal' planes; mixed planes that contain Nb and Si atoms, planes that contain only Nb atoms, and planes that contain only Si atoms. In the stacking sequence, an A layer is considered as a unit of 4 planes consisting of : [1] a plane of Nb

and Si atoms, [2] a plane of Nb atoms, [3] a plane of Si atoms, and [4] a second plane of Nb atoms. Similarly, in the B layer, layer 1 consists of Nb and Si atoms, but the Si atoms are rotated 30° with respect to the Si atoms of the first layer of the A layer, plane [2] of the B layer is the same as plane [4] of the A layer, plane [3] of the [B] layer, an all Si layer, is the same as plane [3] of the A layer, and plane [4] of the B layer, an all Nb layer, is the same as plane [2] of the A layer. The ABAB stacking sequence is illustrated in Figure 14.

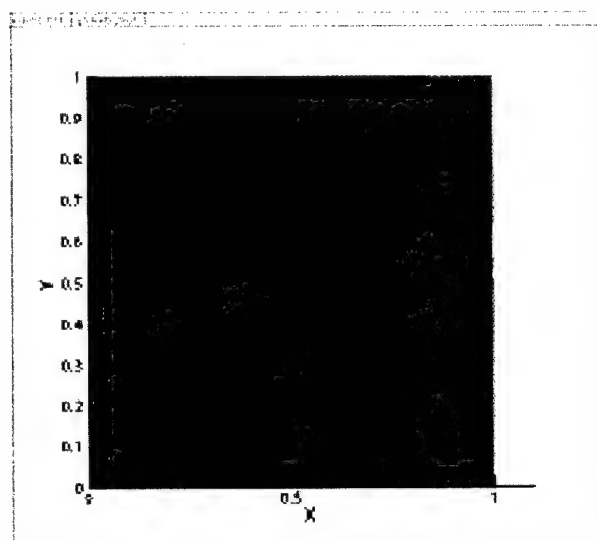


Figure 12. Scanned and digitized microstructure used for the stochastic simulation.

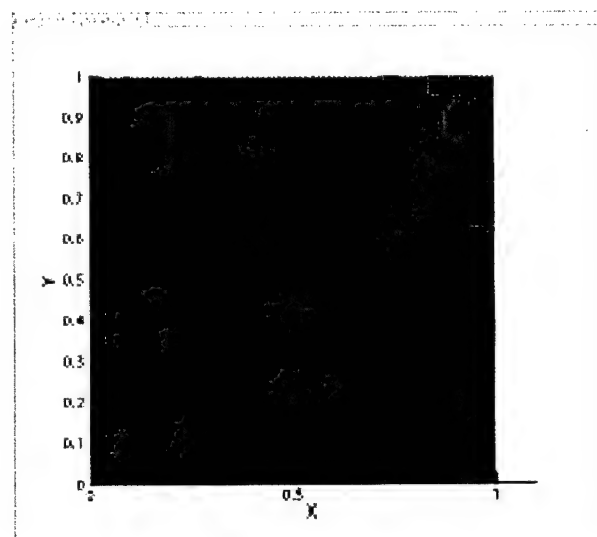


Figure 13(a) Reconstructed micrograph of Figure 12 after simulation "annealing."

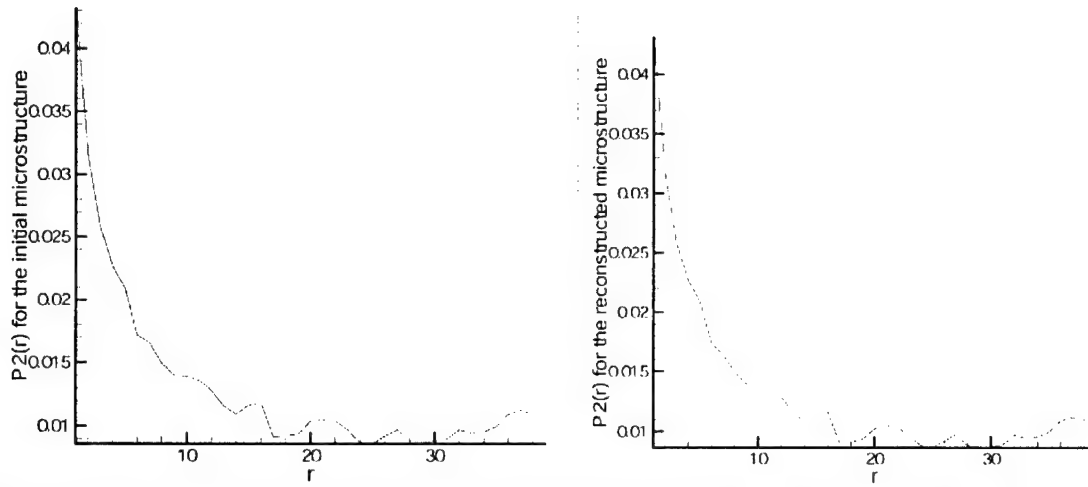


Figure 13(b). Two-point correlation function for the initial and reconstructed plus annealed microstructures.

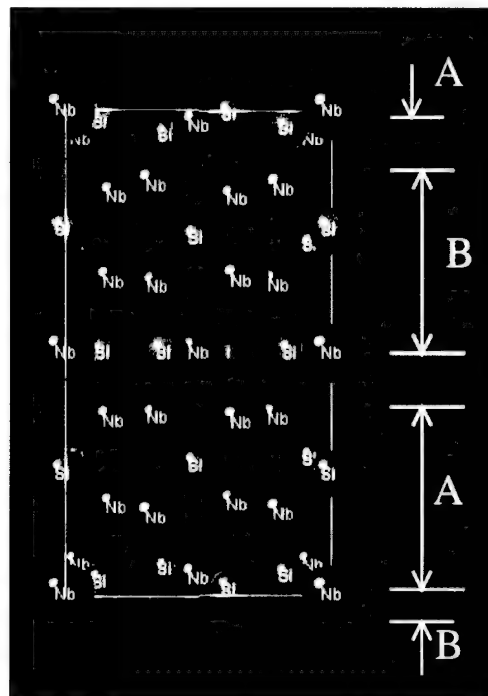


Figure 14. Diagram showing the Nb_5Si_3 $tI32$ crystal structure (low temperature equilibrium form).

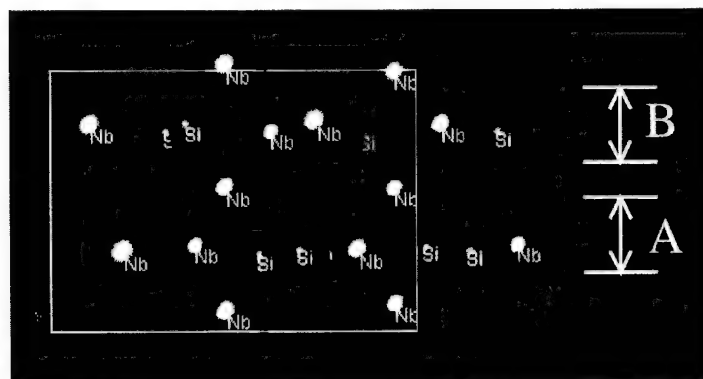


Figure 15. Diagram showing the $(\text{Nb})_5\text{Si}_3$ hP16 crystal structure that is stabilized by additions of Hf and Ti.

The hP16 structure is shown in Figure 15. It consists of a 2 layer type structure stacked along the [0001] direction consisting of Nb-only layers, and mixed layers of Nb and Si atoms. There are no Si-only planes as in the case of the tI32 structure. The A type stacking unit consists of 1 layer of a Nb-only plane and 1 layer of a Nb+Si plane. In the A and B layers the Nb-only planes are the same, but in the mixed plane the Si and Nb atoms fill interstices that are displaced with respect to those in the mixed layer of the A unit. The stacking sequence can again be described by an ABAB type sequence. The crystal structure is much simpler than the tI32 structure and it probably possesses a much smaller Burgers vector.

Microstructural Analyses of the Eutectic Phase Transformation in Complex DS Nb-Silicide In-Situ Composites

The use of Hf and Ti alloying additions to these silicides has also been examined, but there is relatively little data on solid-state phase equilibria. In these systems Nb_5Si_3 has been observed with the hP16 structure when the Hf and Ti concentrations are high. The hP16 structure is shown in Figure 15. The present section describes EBSD analyses of a DS Nb-silicide based composite that experienced a eutectoid transformation.

The microstructure of a composite directionally solidified from a Nb-12.5Hf-33Ti-16Si alloy is shown in Figure 16. In the as-DS condition the microstructure consisted of primary $(\text{Nb})_3\text{Si}$ dendrites and coarse $(\text{Nb})_3\text{Si}$ -(Nb) two-phase cells. There was also a fine-scale intercellular $(\text{Nb})_5\text{Si}_3$ -(Nb) eutectic. After creep testing partial eutectoid decomposition of the eutectic $(\text{Nb})_3\text{Si}$ to $(\text{Nb})_5\text{Si}_3 + (\text{Nb})$ has occurred, as shown in Figure 16(b). This is analogous to the eutectoid phase transformation that occurs in the binary Nb-Si system, where Nb_3Si is metastable and decomposes to Nb and $(\text{Nb})_5\text{Si}_3$ below 1750°C. A typical micrograph showing partial eutectoid phase transformation of Nb-19Si is shown in Figure 17.

EBSD analyses indicate that the complex $(\text{Nb})_3\text{Si}$ has decomposed by a eutectoid reaction, where the products of the reaction are (Nb) and hP16 $(\text{Nb})_5\text{Si}_3$. This is an unexpected result, because the binary and ternary phase diagrams would lead one to

expect $\text{tI32 } (\text{Nb})_5\text{Si}_3$. It is also surprising that the eutectoid has occurred at what are relatively low temperatures for these composites. It appears that in the complex alloy where the Ti and Hf concentrations are high, stabilization of the hP16 occurs in preference to the tI32 structure. The hP16 $(\text{Nb})_5\text{Si}_3$ may offer a lower nucleation energy for the eutectoid hP16 $(\text{Nb})_5\text{Si}_3$ than for the tI32.

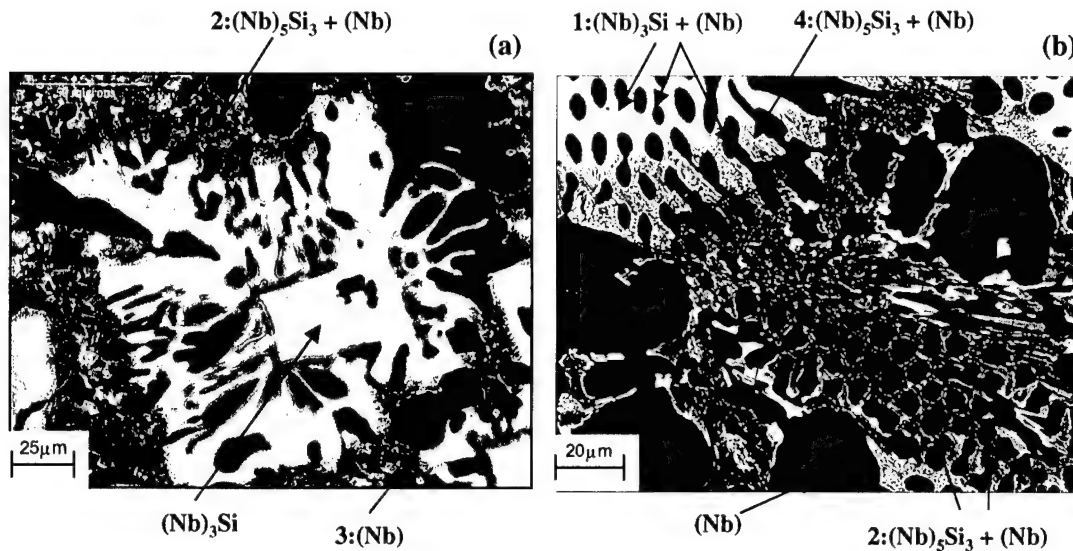


Figure 16. Backscatter electron images (BEI) at (a) low and (b) high magnifications. The figure shows the transverse section of the DS Nb-12.5Hf-33Ti-16Si, showing the primary (Nb) dendrites (1), the primary $(\text{Nb})_3\text{Si}$ dendrites, and the fine-scale $(\text{Nb})_5\text{Si}_3$ - (Nb) interdendritic eutectic (2); the as-DS eutectic $(\text{Nb})_5\text{Si}_3$ has the hP16 structure. The $(\text{Nb})_3\text{Si}$ - (Nb) coarse eutectic can be seen at the upper left corner (1). A eutectoid reaction, $(\text{Nb})_3\text{Si} \leftrightarrow (\text{Nb})_5\text{Si}_3 + (\text{Nb})$, 4, has occurred by nucleation on the interface between the eutectics along the silicide arms; the transformation has proceeded into the $(\text{Nb})_3\text{Si}$.

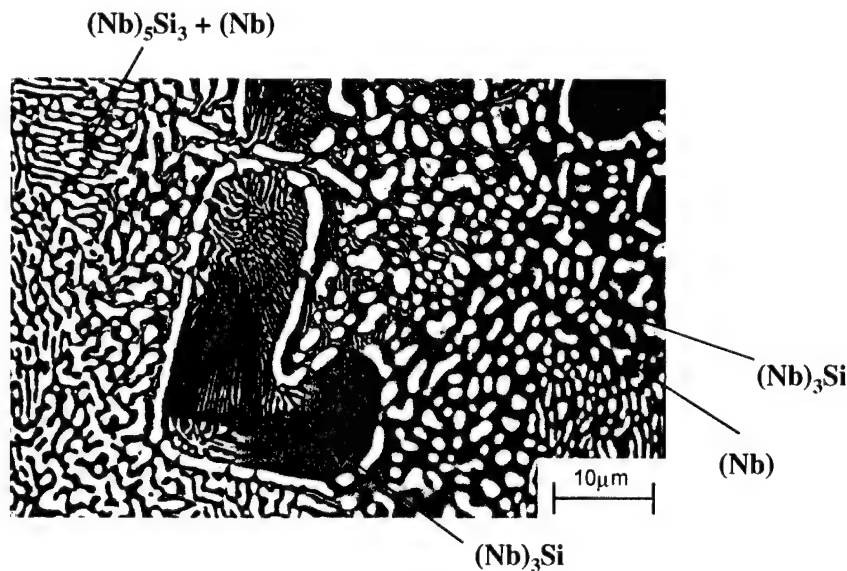


Figure 17. Partial eutectoid phase transformation in binary Nb-19Si.

The following phase orientation relationships were observed: The faceted primary $(\text{Nb})_3\text{Si}$ dendrites at cell cores have the same [001] orientation as eutectic $(\text{Nb})_3\text{Si}$. The $(\text{Nb})_5\text{Si}_3$ in the fine-scale eutectic exhibits a range of orientations in intercellular regions. The [0001] in the hP16 $(\text{Nb})_5\text{Si}_3$ and the [001] $(\text{Nb})_3\text{Si}$ are parallel in several areas. The eutectoid hP16 $(\text{Nb})_5\text{Si}_3$ grows epitaxially with the fine-scale eutectic $(\text{Nb})_5\text{Si}_3$.

4. Summary

This study has described the creep behavior of Nb-silicide based in-situ composites. The creep behavior of composites from model quaternary alloys and monolithic phases has been described. The creep rates of the composites from the quaternary Nb-Hf-Ti-Si alloys decreased with increasing Si concentration from 12 to 18%, and increasing silicide volume fraction from 0.25 to 0.71. At higher Si concentrations, the creep rate increased as a result of crack linking and damage accumulation in the silicides.

Of the intermetallics investigated, the Nb_5Si_3 type silicides had the lowest creep rates. The hP16 silicide phases have higher secondary creep rates than any of the tetragonal silicides, or the T2 phases, at stresses greater than 140 MPa. Analysis of the creep exponents suggests that deformation of the complex Nb_5Si_3 type silicide is probably controlled by Nabarro-Herring type creep, as is the binary Nb_5Si_3 silicide. In contrast, creep of the Nb_3Si silicide appears to be controlled by a dislocation controlled mechanism. The (Nb) solid solutions have creep rates that are more than an order of magnitude higher than either the intermetallics or the composites that were investigated. Ti additions have a significant effect on the (Nb) creep properties.

Modeling results and experimental data from the monolithic silicides and Nb solid solutions indicate that at low Si concentrations the creep deformation is dominated by the (Nb), but as the Si concentration is increased, and the silicide volume fraction is increased, the composite creep performance is controlled by the silicide. However, the model underestimates the effect of increasing volume fraction of the silicide on creep rate.

References:

1. Bewlay, B.P., Lipsitt, H.A., Jackson, M.R., Reeder, W.J., and Sutliff, J.A. (1995). *Mater. Sci. Eng.*, **A192/193**, pp. 534-543.
2. Bewlay, B.P., Jackson, M.R., and Lipsitt, H.A. (1996). *Metall. and Mater. Trans.*, **27A**, pp. 3801-3808.

3. Dimiduk, D.M., Mendiratta, M.G., and Subramanian, P.R. (1993). In *Structural Intermetallics*, Eds. R. Darolia, J.J. Lewandowski, C.T. Liu, P.L. Martin, D.B. Miracle, and M.V. Nathal, TMS Publications, Warrendale, Pa., pp. 619-630.
4. Bewlay, B.P., Lewandowski, J.J. and Jackson, M.R. (1997). *J. of Metals*, **49** (8), pp. 46-48.
5. Subramanian, P.R., Mendiratta, M.G., and Dimiduk, D.M. (1996). *Journal of Metals*, **48** (1), pp. 33-38.
6. Subramanian, P.R., Mendiratta, M.G., Dimiduk, D.M., and Stucke, M.A. (1997). *Mater. Sci. Eng.*, **A239-240**, pp. 1-13.
7. M.G. Mendiratta, J.J. Lewandowski and D.M. Dimiduk, *Metall. Trans.* 22A (1991), pp. 1573-1581.
8. Mendiratta, M.G., and Dimiduk, D.M. (1993). *Metall. Trans. A* **24A**, pp. 501-504.
9. Bewlay, B.P., Bishop, R.R., and Jackson, M.R. (1998). *Journal of Phase Equilibria*, **19** (6), pp. 577-586.
10. Bewlay, B.P., Bishop, R.R., and Jackson, M.R. (1999). *Z. Metallkunde*, **90** (60), pp. 413-422.
11. Bewlay, B.P., Whiting, P., and Briant, C.L. (1999). *MRS Proceedings on High Temperature Ordered Intermetallic Alloys VIII*, pp. KK6.11.1- KK6.11.5.
12. Henshall, G.A., Strum, M.J., Subramanian, P.R., and Mendiratta, M.G. (1995). *Mat. Res. Soc. Symp. Proc.* **364**, pp. 937-942.
13. Subramanian, P.R., Parthasarathy, T.A., Mendiratta, M.G., and Dimiduk, D.M. (1995). *Scripta Met.* **32** (8), pp. 1227-1232.
14. E. Bullock, M.McLean, and D.E. Miles, *Acta Met.*, Vol. 25, pp. 333-344, Pergamon Press, 1977.
15. D.E. Miles, E. Bullock, and M. McLean, *Proc. Conf. In Situ Composites II*, p. 359. Bolton Landing, NY September 1975, Xerox Individualized Publishing, Lexington, MA, 1976.

5.0 Collaborations

Throughout the present program there have been continued interactions with scientists at universities and the AF laboratories. These have included staff at Case Western Reserve University, Brown University, and UES. These interactions have involved regular discussions of the mechanical behavior of composites and the exchange of data.

6.0 Publications

The following articles have been published in refereed journals and conference proceedings during this one year contract.

1. B.P. Bewlay and M.R. Jackson "High-Temperature Directionally Solidified In-Situ Composites : Processing and Properties," in *Comprehensive Composite Materials*, A Kelly and C. Zweben (eds.) Volume 3: Metal Matrix Composites, T.W.Clyne (ed.), Elsevier (2000), Vol 3, Chapter 22, pp. 579-613.
2. J-C. Zhao, B.P. Bewlay, M.R. Jackson and Q. Chen, "Hf-Si Phase Diagram Determination and Thermodynamic Modeling," *Journal of Phase Equilibria*, Vol 21 (1), 2000, pp. 40-45.
3. B.P. Bewlay and S. Sitzman, "Microstructural Response of DS Nb-Hf-Ti-Si In-Situ Composites During High-Temperature Creep Testing," *Microscopy and Microanalysis*, 2000, Vol. 6, Supplement 2, pp. 376-377.
4. B.P. Bewlay, M.R. Jackson, and M.F.X. Gigliotti, "Single Crystals and Directionally Solidified In-Situ Composites For High-Temperature Applications," in *Intermetallic Compounds – Principles and Practice – Vol. 3*, Eds. R.L. Fleischer and J.H. Westbrook, John Wiley, 2001.
5. B.P. Bewlay, C.L. Briant, E.T. Sylven, M.R. Jackson and G. Xiao, "Creep Studies of the Monolithic Phases in Nb-Silicide In-Situ Composites," in the *MRS Proceedings on High Temperature Ordered Intermetallic Alloys IX*, 2000.
6. B.P. Bewlay, C.L. Briant, A.W. Davis and M.R. Jackson, "The Effect of Silicide Volume Fraction on the Creep Behavior of Niobium-Silicide Based In-Situ Composites," in the *MRS Proceedings on High Temperature Ordered Intermetallic Alloys IX*, 2000.
7. J.-C. Zhao, B.P. Bewlay, and M.R. Jackson, "Determination of the Nb-Hf-Si Phase Diagram at 1500°C," submitted to the *Journal of Intermetallics*, January 2001.
8. R.J. Grylls, B.P. Bewlay, H.L. Fraser and H.A. Lipsitt, "Characterization of Silicide Precipitates in Nb-Si and Nb-Ti-Si Alloys," in the *Philosophical Magazine*, August 2000.
9. B.P. Bewlay, C.L. Briant, M.R. Jackson, and P.R. Subramanian, "Recent Advances in Nb-Silicide In-Situ Composites," submitted to the proceedings of the Plansee Seminar, 2001.
10. S. Sitzman and B.P. Bewlay, "Microstructural Analyses of the Eutectoid Phase Transformation in Complex DS Nb-Silicide In-Situ Composites," *Microscopy and Microanalysis*, 2001, to be published.

7.0 Presentations

The following presentations have been given during this one year contract or will be presented subsequently. Both invited and contributed papers are shown.

1. B.P. Bewlay, C.L. Briant, A.W. Davis, G. Xaio and M.R. Jackson, "Creep Studies of the Monolithic Phases in Nb-Silicide In-Situ Composites", presented at the MRS Symposium on High Temperature Ordered Intermetallic Alloys IX, Boston, December 2000.
2. B.P. Bewlay, C.L. Briant, A.W. Davis and M.R. Jackson, "The Effect of Silicide Volume Fraction on the Creep Behavior of Niobium-Silicide Based In-Situ Composites", presented at the MRS Symposium on High Temperature Ordered Intermetallic Alloys IX, Boston, December 2000.
3. B.P. Bewlay, C.L. Briant, M.R. Jackson, J-C Zhao and P.R. Subramanian, "Recent Advances in Nb-Silicide In-Situ Composites", to be presented at the Plansee Seminar, 2001.
4. S.J. Balsone, B.P. Bewlay, M.R. Jackson, J-C Zhao and P.R. Subramanian, "Recent Developments in Very High Temperature Nb-Silicide In-Situ Composites," to be presented at the Aeromat Conference, 2001.
5. J.-C. Zhao, B.P. Bewlay, M.R. Jackson, and L.A. Peluso, "Phase Stability of Laves Phases in Nb-Silicide In-Situ Composites", to be presented at the International Symposium on Structural Intermetallics, Sept, 2001.
6. S.J. Balsone, B.P. Bewlay, M.R. Jackson, J-C Zhao and Subramanian, "Recent Advances in Nb-Silicide In-Situ Composites", to be presented at the International Symposium on Structural Intermetallics, Sept, 2001.

8.0 Technology Transfers and Transitions

The niobium silicide based composites that are being investigated in this program are targeted for aircraft engine applications. The objective of the present research is to develop initial predictive creep modeling capability for these high-strength in-situ composites. The ability to predict the creep rate and the stress sensitivity of creep rate is required.

The predictive creep model developed in the present program has been employed to identify the correct constituent phased for optimization of creep performance. The near-

term application of these composites is for the Integrated High Performance Turbine Engine Technology (IHPTET) joint services (Air Force, Navy, Army, and NASA) program. The team of GE Aircraft Engines and Allison Advanced Development Company has selected these Nb-base silicide intermetallic composites for the proposed full demonstration of IHPTET Phase III goals as the primary material for the high pressure turbine (HPT) blades.

Primary Contact:

Bernard P. Bewlay
GE Corporate Research and Development
PO Box 8
Schenectady, NY12301
Tel: 518 387 6121

High-temperature *In Situ* Composites:
Processing and Properties

B.P. Bewlay and M.R. Jackson

3.22

High-temperature *In Situ* Composites: Processing and Properties

B. P. BEWLAY and M. R. JACKSON
General Electric Company, Schenectady, NY, USA

3.22.1 INTRODUCTION	580
3.22.2 PROCESSING	581
3.22.2.1 Vacuum Arc Melting	582
3.22.2.2 Directional Solidification: Float Zone Processing	582
3.22.2.3 Directional Solidification: Czochralski Methods	583
3.22.2.4 Directional Solidification: Bridgman Methods	583
3.22.3 MICROSTRUCTURE AND PHASE STABILITY	584
3.22.3.1 Microstructures and Phase Chemistries	584
3.22.3.2 Phase Stability Investigations	586
3.22.3.2.1 Nb-Ti-Si phase stability	588
3.22.3.2.2 Nb-Hf-Si ternary phase stability	589
3.22.3.2.3 Quaternary and higher order systems	593
3.22.3.2.4 Precipitation in Nb solid solutions	594
3.22.4 MECHANICAL PROPERTIES	595
3.22.4.1 Fracture Behavior	595
3.22.4.1.1 Effect of Ti additions on fracture toughness	597
3.22.4.2 Fatigue Properties	600
3.22.4.2.1 Thermal fatigue	601
3.22.4.3 High-temperature Strength	601
3.22.4.4 Tensile Creep Properties	602
3.22.4.5 Compression Creep Studies	604
3.22.4.5.1 Nb-Ti-Hf-Si composites	604
3.22.4.5.2 Mo-modified composites	605
3.22.4.5.3 Higher Order Alloy Composites	606
3.22.4.6 Physical and Thermal Properties	607
3.22.4.7 Oxidation Behavior	608
3.22.5 APPLICATIONS/ENGINE MATERIALS ENVIRONMENT	611
3.22.6 FUTURE DIRECTIONS	612
3.22.7 SUMMARY	613
3.22.8 REFERENCES	614

3.22.1 INTRODUCTION

This chapter describes the processing and properties of high-temperature *in situ* composites based on refractory metals and refractory metal silicides. These *in situ* composites consist of high-strength, high melting temperature Nb-based silicides together with a high melting temperature, modest strength, high-toughness Nb-based metallic phase. These composites offer an excellent balance of high- and low- temperature mechanical properties with promising environmental resistance at temperatures above 1000 °C. A range of processing schemes has been used to generate these *in situ* composites including solidification, vapor phase, and thermomechanical processes. Solidification processing techniques that have been used include directional solidification and arc melting. Directional solidification has been performed using Czochralski, Bridgman, and zone refining techniques. Composites have been generated from alloys with melting temperatures up to 2250 °C. Composite characteristics that will be described include microstructures, phase stability, mechanical properties, and oxidation resistance. The high-temperature strength, creep rupture properties, and oxidation behavior of these refractory metal *in situ* composites will be compared with both those of the most recent Ni-based superalloys and material property goals for future aircraft engines.

The efficiency of current gas turbine engines is limited by the maximum turbine inlet temperature (Subramanian *et al.*, 1996; Jackson *et al.*, 1996) that in turn is restricted by the capability of present day Ni-based superalloys. Superalloys are presently used up to maximum surface temperatures of ~1150 °C. For further improvements in thrust to weight ratio, new materials with improved high-temperature properties, such as strength, creep performance, and environmental properties, are required. During the 1990s, the potential of intermetallic compounds with low densities, high elastic moduli, and high melting ranges (Subramanian *et al.*, 1994, 1996, 1997; Jackson *et al.*, 1996; Dimiduk *et al.*, 1993; Mendiratta *et al.*, 1991; Mendiratta and Dimiduk, 1993; Bewlay *et al.*, 1996, 1997a, 1997c; Anton and Shah, 1992) has been explored. However, the poor intrinsic toughness of monolithic intermetallics is such that their application in aircraft engine components is not possible. However, a solution to this problem is to combine intermetallic materials with metallic second phases in order to generate composites with toughness levels that are sufficient for component applications (Subramanian *et al.*, 1994, 1996, 1997; Jackson *et al.*, 1996; Dimiduk *et al.*, 1993; Mendiratta *et al.*,

1991; Mendiratta and Dimiduk, 1993; Bewlay *et al.*, 1996, 1997a, 1997b). This composite approach is being used to improve the low-temperature fracture toughness of intermetallic-based composites and thereby generate a material with a combination of attractive high-temperature properties and acceptable low-temperature properties. In this arena, Nb-Si *in situ* composites that consist of a Nb-based solid solution, (Nb), with Nb₃Si and/or Nb₅Si₃ silicides have been shown to have great potential because of their attractive balance of high and low temperature mechanical properties (Dimiduk *et al.*, 1993; Subramanian *et al.*, 1997; Mendiratta *et al.*, 1991; Mendiratta and Dimiduk, 1993; Bewlay *et al.*, 1996, 1997c). These *in situ* composites also possess long-term morphological and chemical stability at temperatures up to 1500 °C (Subramanian *et al.*, 1994, 1996, 1997; Jackson *et al.*, 1996; Dimiduk *et al.*, 1993; Mendiratta *et al.*, 1991, Mendiratta and Dimiduk, 1993). Unfortunately, the composites from binary Nb-Si alloys have very poor oxidation resistance, and elements that are added to these composites to improve oxidation resistance can compromise high temperature mechanical properties in the case of inappropriate alloy selection (Subramanian *et al.*, 1994, 1996; Jackson *et al.*, 1996; Bewlay, Lewandowski *et al.*, 1997). However, from model binary Nb-Si alloys, whole families of ternary, quaternary, and higher order alloys have been developed to generate *in situ* composites with improved oxidation properties (Subramanian *et al.*, 1994, 1996; Bewlay *et al.*, 1996, 1997a, 1997b).

Historically, developments based on Nb have offered significant gains in temperature capability of aerospace components due to the high melting temperatures of niobium alloys, relatively low densities, low ductile-brittle transition temperature, and stable oxide (Buckman, 1998). There are two principal deficiencies of niobium-based systems at high temperature, first inadequate high-temperature mechanical behavior, and second, catastrophic oxidation resistance (Subramanian *et al.*, 1994; Buckman, 1998). Earlier research has suggested that for Nb alloys to have useful high-temperature strength they will have to be strengthened by both solid solution strengthening elements and dispersoids (Buckman, 1998). However, niobium silicide-based composite approaches have been shown to provide substantial improvements in both high-temperature mechanical behavior and oxidation resistance of niobium-based systems, such that they are now being considered for application in the highest performance gas turbines.

Three decades ago there was intense activity in directionally solidified (DS) eutectics for

structural applications such as jet engine turbine blades (Bibring, 1973). The development of these eutectics relied on a rich knowledge of Ni- and Co-base superalloys for the strong, ductile composite matrices. Strengthening of these crystallographically-oriented matrices was accomplished with both lamellar intermetallic compounds (at Pratt and Whitney/United Technologies Research Center) and fibrous monocarbides TaC, TiC, and NbC (at ONERA and at General Electric) (Lemkey and Thompson, 1971; Khan, 1979; Walter and Kline, 1973; Jackson *et al.*, 1982). ONERA initiated the development of monocarbide-reinforced fiber composite materials, concentrating on Co-base systems with TaC fiber reinforcement. As designs required greater strength at intermediate temperatures, Co was replaced by Ni-based γ' -strengthened matrices.

Aligned eutectics could be produced in chemistries almost as complex as the multielement superalloys, and subsequent studies at ONERA, GE, NASA, and DLR demonstrated that carbide stability in thermal cycling was excellent for a broad range of composite chemistries (Woodford, 1976; Stohr, 1979). Efforts at GE Aircraft Engines (GEAE), GE-CRD, and at ONERA, included alloying with Re, uncommon then in superalloy systems (Smashy, 1974). These eutectics (particularly NiTaC-13, NiTaC-14, and CoTaC 744) were extremely strong (> 120 MPa for 1000 h at 1100 °C), with rupture capability far beyond any superalloy at that time.

Achieving excellent high-temperature strength in the aligned monocarbide eutectics was only the first of many requirements. Through iterative alloy approaches, oxidation and fatigue behaviors were improved, transverse ductility was improved with boron additions, and matrix instability during cyclic thermal exposure was reduced for retention of the excellent eutectic properties (Gigliotti *et al.*, 1982). In production trials of airfoils, melt-mould reactions at 1400–1600 °C during directional solidification caused nucleation of carbide particles at the ceramic-metal interface, which when fractured, created surface cracks. These carbide particles also perturbed the local aligned microstructure that was required for DS eutectic properties. However, by modification of the eutectic chemistry, strong, stable composites were generated with minimal surface reaction.

Although engine tests were successful (Buckman, 1998; Bibring, 1973; Lemkey and Thompson, 1973; Khan, 1979; Walter and Cline, 1973; Jackson *et al.*, 1982; Woodford, 1976; Stohr, 1979; Smashy, 1974; Gigliotti *et al.*, 1982; Bruch *et al.*, 1979; Rabinovitch and Hauser,

1979; Cetel *et al.*, 1979; Menzies *et al.*, 1988), both for solid and hollow blades, at SNECMA with the ONERA CoTaC 744, at GE with NiTaC13 and NiTaC14B, and at Pratt and Whitney with lamellar composites, there were mass production difficulties with these eutectics. The low solidification rates required for aligned growth (typically $< 2 \text{ cm h}^{-1}$) and the small numbers of parts per furnace run, resulted in a large number of furnaces for the necessary production volumes. The furnace investment was too high and the return on investment too low to make this technology an attractive business proposition.

Structural eutectics research was a 15-year development, typical of the development timeframe in structural materials where safety considerations in the final component application are critical. The long-term commitment to the research required great patience on the part of those who performed the studies and on the part of those who funded the efforts. Although eutectic-based superalloys are not actually used in the late 1990s, the spin-offs from the eutectics research in single crystal superalloy chemistry and casting technologies are at the heart of jet engines. The strengths of the DS eutectic alloys from the early 1980s have yet to be exceeded by the best single crystal superalloys, almost two decades later.

The aim of this chapter is to review microstructures, phase chemistries, fracture toughness, oxidation characteristics, high-temperature mechanical behavior, and low-temperature fatigue properties of a new class of *in situ* composites, refractory metal-intermetallic composites (RMICs).

3.22.2 PROCESSING

A range of processing approaches has been used to generate Nb-based RMICs, including arc casting (Subramanian *et al.*, 1994, 1996, 1997; Dimiduk *et al.*, 1993; Mendiratta *et al.*, 1991; Mendiratta and Dimiduk, 1993; Rigney *et al.*, 1994; Weiss *et al.*, 1994a, 1994b), directional solidification (Jackson *et al.*, 1996; Bewlay *et al.*, 1994a, 1995a, 1996, 1997a, 1997e; Pope *et al.*, 1994; Shah *et al.*, 1995; Johnson *et al.*, 1993), physical vapor deposition (Gigliotti *et al.*, 1992), forging (Weiss *et al.*, 1994b), and extrusion (Subramanian *et al.*, 1997; Mendiratta *et al.*, 1991; Mendiratta and Dimiduk, 1993; Bewlay *et al.*, 1996, 1997c). Powder metallurgy (see Chapter 3.25, this volume) and foil-laminate processing (see Chapter 3.24, this volume) (Jackson *et al.*, 1994, 1995, 1996; Rowe *et al.*, 1994; Kajuch *et al.*, 1992,

1995) approaches have also been employed. Each of the above processes provides a characteristic microstructure.

Solid-liquid processing of these high-temperature, reactive materials is severely limited by the availability of suitable mold materials. As a result, cold-crucible methods have been adopted. The most widely used methods for these RMICs include arc melting plus extrusion, and directional solidification. The directional solidification techniques that have been employed include float zone (Pope *et al.*, 1994; Shah *et al.*, 1995; Johnson *et al.*, 1993), Bridgman and Czochralski methods. These two approaches will be described in the following sections.

3.22.2.1 Vacuum Arc Melting

Consumable and nonconsumable vacuum arc melting techniques have been used to produce RMICs from binary Nb-Si and higher order alloys containing Hf, Mo, Ta, Ti, Cr, and Al (Subramanian *et al.*, 1994, 1997; Dimiduk *et al.*, 1993; Mendiratta *et al.*, 1991; Mendiratta and Dimiduk 1993; Bewlay *et al.*, 1997c). Consumable arc melting has been used to produce ingots with diameters up to 75 mm, and up to ~150 mm long. Typically, these materials have been subjected to subsequent consolidation by hot isostatic pressing and/or hot extrusion. The vacuum arc melting approach has the advantages of producing ingots large enough for prototype component manufacture, and it is also compatible with well-established conventional processing techniques. However, it has the disadvantages of possessing poor solidification control, randomly oriented composite structures, and a population of relatively large-scale defects.

RMICs that consist of approximately equiaxed structures of a (Nb) and a (Nb) silicide have been evaluated in the extruded plus heat-treated conditions (Subramanian *et al.*, 1994, 1997; Dimiduk *et al.*, 1993; Mendiratta *et al.*, 1991; Mendiratta and Dimiduk, 1993; Bewlay *et al.*, 1997c). Extrusions have been produced by machining consumable arc melted large castings to a diameter of ~70 mm and placing them in Mo cans with a wall thickness of ~6 mm. Prior to extrusion, the canned ingots were heated in an induction furnace to a temperature between 1400 and 1600 °C and extruded through tool steel dies maintained at 260 °C at extrusion ratios in the range 3–10. This scheme provides a composite microstructure aligned with the extrusion direction and an acceptable process yield. Depending on the Si concentra-

tion, the volume fraction of silicide phase has been adjusted over the range of 0.25–0.45. Extrusion of bar stock for eventual machining of turbine vanes and blades is an approach similar to that used for ODS Ni superalloy airfoils, such as INCO alloys MA754 or MA6000.

3.22.2.2 Directional Solidification: Float Zone Processing

Directional solidification of RMICs has been performed using an optical imaging float zone process (OIFZ) by Pope *et al.* (1994) and Shah *et al.* (1995). This float zone method is derived from the zone melting technique of Pfann (1966) where a small volume of material, in a relatively large rod-type charge, is melted and then the molten zone is translated along the rod. The molten zone is retained in position by surface tension between two co-linear rods of the same alloy, and as a result a crucible is not required to retain the melt. The system described by Pope *et al.* (1994) consists of two 3.5 kw tungsten halogen lamps enclosed in a double ellipsoidal, water-cooled, copper chamber, as shown schematically in Figure 1(a). Pope *et al.* (1994) reported directional solidification of a range of RMICs and monolithic intermetallic compounds using the OIFZ technique.

In addition to the optical imaging heat source, induction heating and electron beam heating sources have been used for directional solidification of high-temperature composite materials (Johnson *et al.*, 1993). Electron beam heating sources are not preferred for high-temperature materials because this heating method requires a high vacuum and it is therefore difficult to use with alloys that contain species with a high vapor pressure. Induction heating float zone processing requires the sample to be a conductor, but it has the advantage that the electromagnetic levitation forces may be used to contain the molten-zone and thereby allow the growth of samples with a larger diameter (Johnson *et al.*, 1993).

Pope *et al.* (1994) also discussed the advantages and disadvantages of the OIFZ approach in more detail. The principal advantages of this approach are that it is very clean and it is capable of working with a range of different materials. There are several disadvantages of the OIFZ technique. First, the specimen size is limited by a compromise between liquid surface tension and the hot zone dimension (in this regard induction heating can also offer additional flexibility). Second, the starting material must possess a high level of homogeneity.

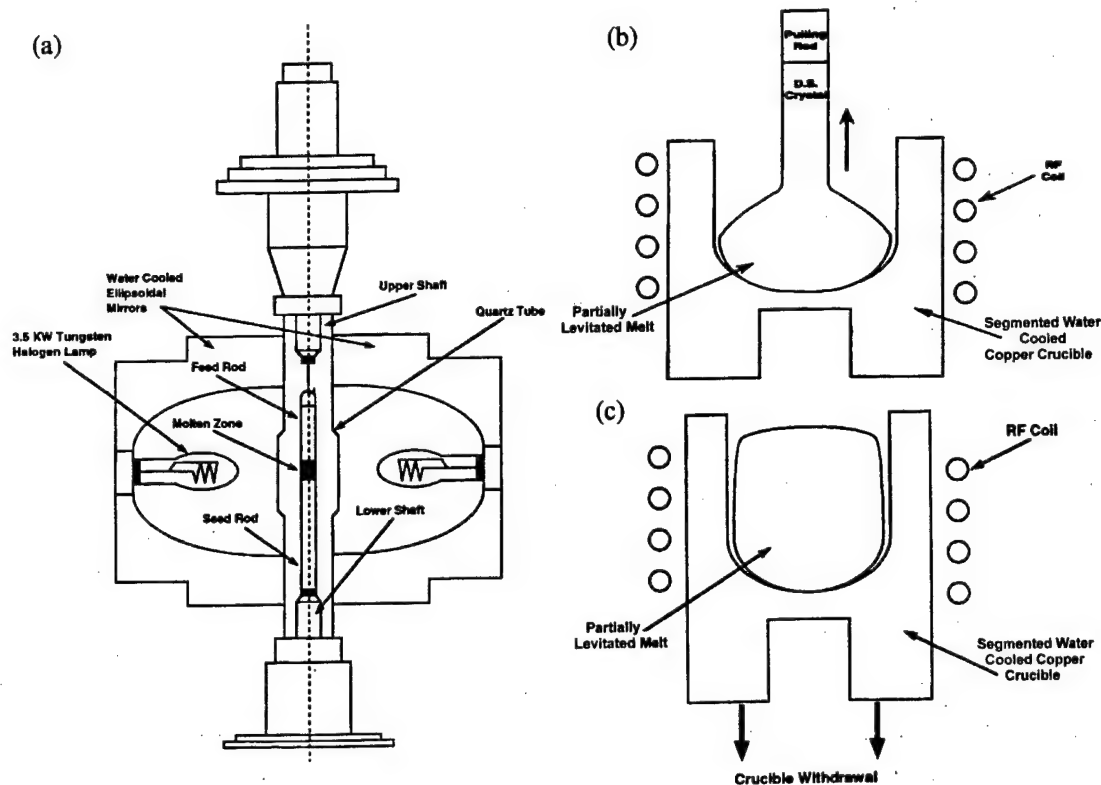


Figure 1 Schematic diagrams of directional solidification approaches for RMICs and recent technological developments. (a) OIFZ processing (Pope *et al.*, 1994), (b) cold crucible Czochralski directional solidification, and (c) cold crucible Bridgman-type directional solidification.

Third, evaporation of volatile species, such as Cr, and condensation on the furnace tube, can lead to attenuation of the heat input from the optical source and destabilization of the directional solidification conditions. For small scale samples the advantages appear to outweigh the disadvantages. However, the scale-up issues for float zone directional solidification of RMICs have not yet been defined.

3.22.2.3 Directional Solidification: Czochralski Methods

DS ingots have been produced using Czochralski crystal growth from an induction levitated melt using growth rates of $0.5\text{--}15\text{ mm min}^{-1}$. This process is shown schematically in Figure 1(b). A broad range of Nb-based RMICs with melting points up to $\sim 2300^\circ\text{C}$ (Bewlay *et al.*, 1994a, 1995a, 1997c; Chang *et al.*, 1992) has been produced. The alloys were induction levitation melted in a segmented water-cooled copper crucible. This is a flexible method and it has been used for high-temperature alloys, such as Nb-Si, Cr-Si, Cr-Nb, Mo-Si and higher order alloys derived from these binary systems. Samples up to $\sim 15\text{ mm}$ diameter and $> 100\text{ mm}$ long have been directionally solidified using the

Czochralski approach. The process has been described in further detail elsewhere (Chang *et al.*, 1992; Bewlay *et al.*, 1994a, 1994b). Typically, high purity elements ($> 99.99\%$) have been used for preparation of these composites, because great attention to the interstitial level is required.

For mechanistic studies of creep behavior (see Chapter 3.14, this volume), directional solidification provides excellent control of microstructure and chemistry in samples with low defect concentration and size. Directional solidification also has great potential as a small solid airfoil manufacturing technique. The ingots can be machined into airfoil configurations, as is the practice for ODS Ni alloys. At present there is limited experience in providing components with cooling channels using this technique.

3.22.2.4 Directional Solidification: Bridgman Methods

Bridgman methods have been used for directional solidification of *in situ* composites using segmented water-cooled copper crucibles. This approach has effectively produced DS ingots with diameters up to 35 mm , although the struc-

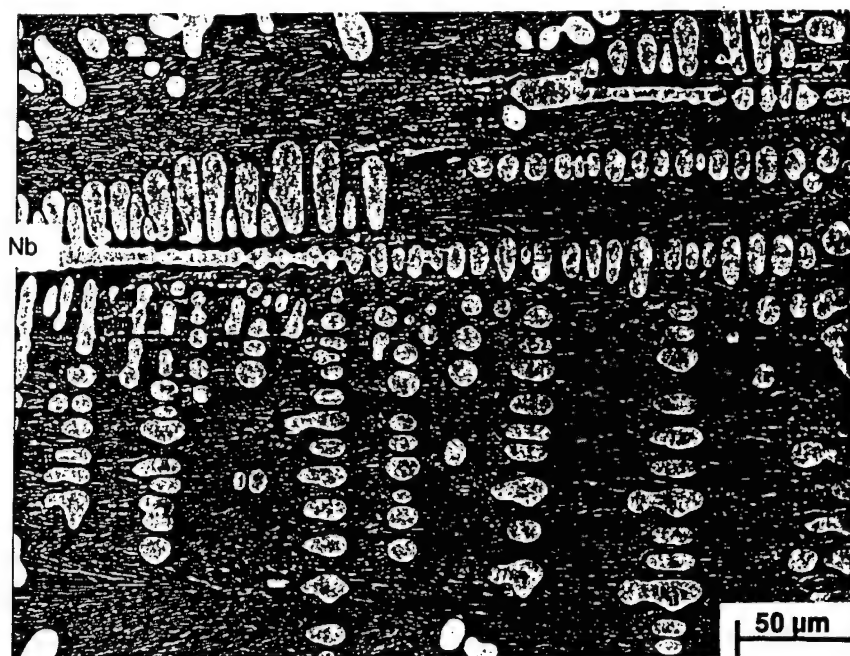


Figure 2 Scanning electron micrograph of the longitudinal section of a DS Nb-silicide based composite Nb-14%Si.

ture is not as consistent as in samples produced using the Czochralski method. In the Bridgman approach the water-cooled copper crucible is withdrawn in a controlled manner through an electromagnetic field that is used to induction levitation melt the alloy charge in the crucible. This process is shown schematically in Figure 1(c).

3.22.3 MICROSTRUCTURE AND PHASE STABILITY

3.22.3.1 Microstructures and Phase Chemistries

The basis for the niobium–niobium–silicide composites is the Nb-rich side of the Nb–Si phase diagram where there is a eutectic between Nb_3Si and (Nb) (Massalski, 1991; Mendiratta and Dimiduk, 1991). This eutectic occurs at 1880°C and 18.2Si. There is also a eutectoid of the form $\text{Nb}_3\text{Si} \rightarrow (\text{Nb}) + \text{Nb}_5\text{Si}_3$ (Massalski, 1991; Mendiratta and Dimiduk, 1991). (Nb)– Nb_3Si and (Nb)– Nb_5Si_3 composites have been prepared by arc-melting, as well as directional solidification, of binary Nb–Si alloys (Bewlay *et al.*, 1995b) with compositions from 10 to 25 Si; all compositions are given in atom percent throughout this chapter. A typical composite from a DS Nb–14 Si alloy is shown in Figure 2. The microstructure consists of (Nb) dendrites with an interdendritic Nb_3Si –(Nb) eutectic. In these high-strength *in situ* compo-

sites the (Nb) provides extrinsic toughening; there is no intrinsic ductility in the silicide at room temperature. The Nb_5Si_3 and Nb_3Si have tI32 and tP32 crystal structures, respectively. Analogous ternary Nb–Ti–Si alloy composites have also been investigated (Subramanian *et al.*, 1997; Bewlay *et al.*, 1994a, 1995b, 1997c); a typical microstructure of a DS ternary Nb–Ti–Si alloy composite is also shown in Figure 3(a) and (b); it consists of interpenetrating dendrites of the (Nb) and Nb_3Si in the composite, with dendrite cross-sections of the order of 5–50 μm wide.

A range of complex Nb–silicide composites has also been generated from multielement Nb alloys. Figure 3(c) shows a typical scanning electron micrograph (backscatter electron (BSE) imaging) of a longitudinal section of a specific metal and silicide composite (MASC) microstructure for which a broad range of properties have been reported (Bewlay *et al.*, 1997b). This composite was derived from the binary Nb–16Si composition (Chang *et al.*, 1992; Bewlay *et al.*, 1994a, 1995b). It contained both metallic and M_3Si intermetallic dendrites, a small amount of an M_5Si_3 intermetallic (where M represents Nb, Ti and Hf), and an interdendritic eutectic of silicide and metal. In this regard, it is entirely analogous to hypereutectic binary Nb–Si and ternary Nb–Ti–Si composites reported previously (Chang *et al.*, 1992). The M_3Si dendrites possessed the distinctive faceted morphology that has been reported previously in the binary hypereutectic

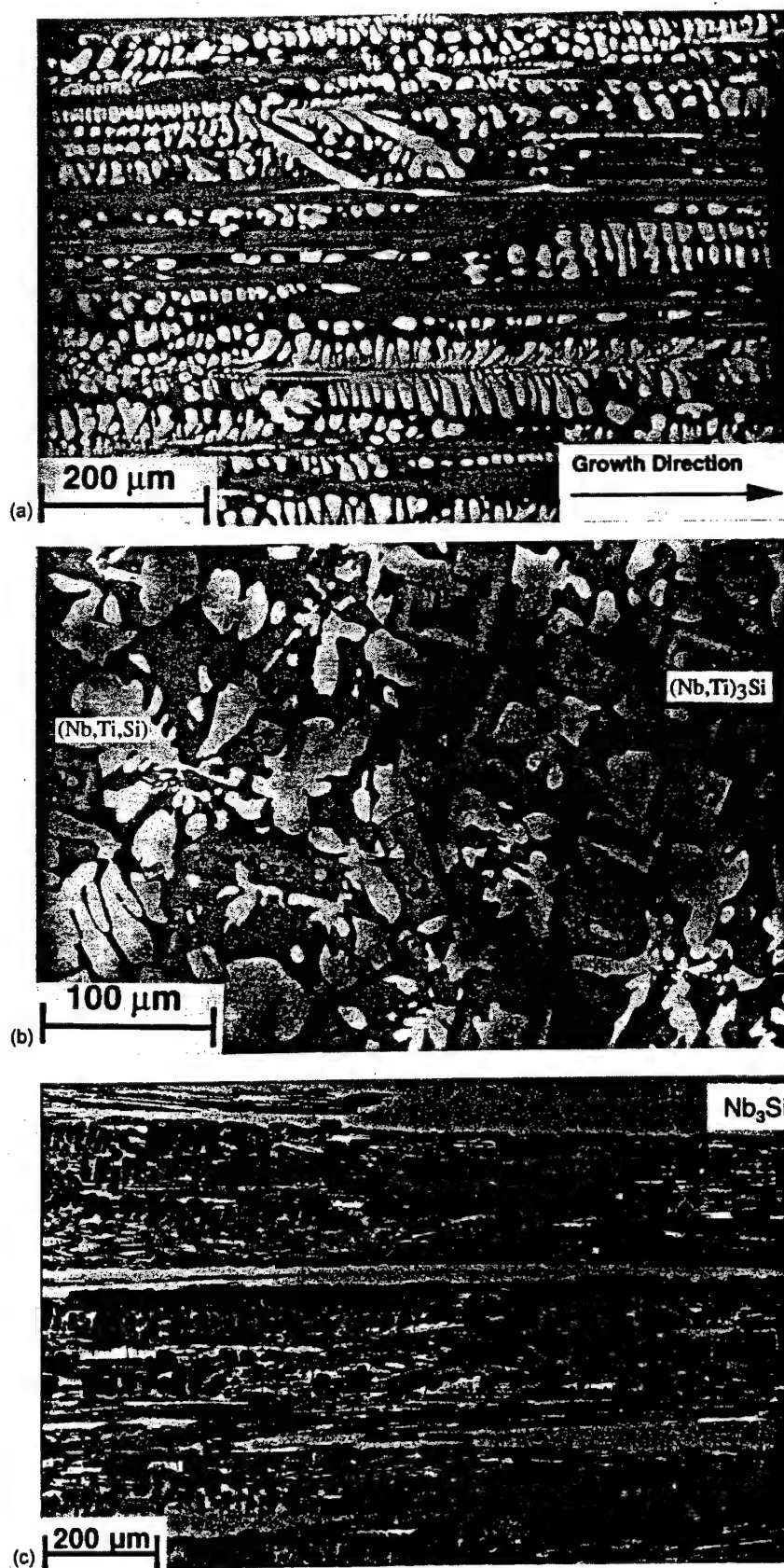


Figure 3 Scanning electron micrographs of (a) the longitudinal section of DS Nb-27Ti-16Si, (b) the transverse section of Nb-27Ti-16Si, (c) the longitudinal section of the DS MASC (after Bewlay, Lewandowski *et al.*, 1997).

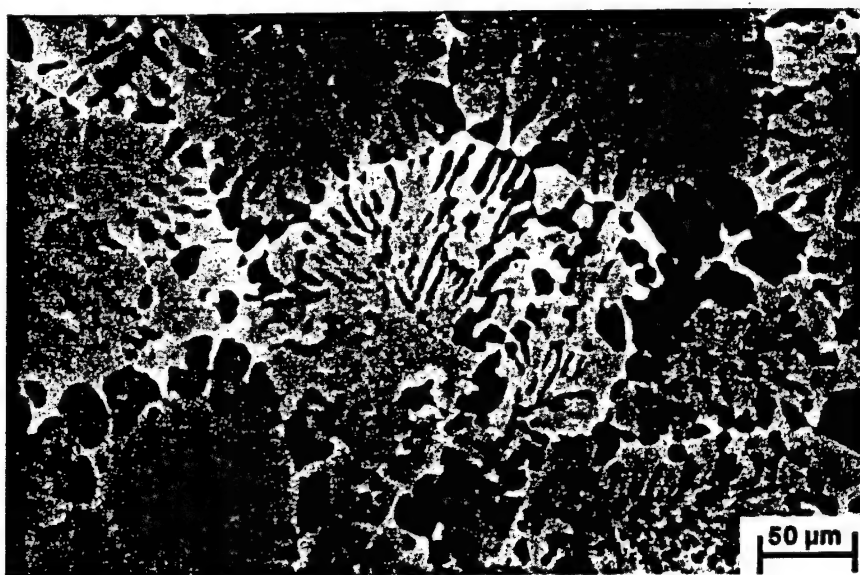


Figure 4 Typical microstructure (BSE image) of the transverse section of a DS composite generated from a quaternary Nb-16Ti-8Hf-16Si alloy at a growth rate of 5 mm min^{-1} . The (Nb) is the dark phase and the M_3Si is the light phase.

binary Nb-Si alloys and the ternary Nb-Ti-Si composites (Bewlay *et al.*, 1995b, 1997b). The metallic and intermetallic dendrites of the MASC were aligned with the growth direction.

There have been several detailed studies of microtexture in Nb-silicide based composites of binary and higher order alloys in the as-extruded and DS conditions (Bewlay and Sutliff, 1998; Sutliff and Bewlay, 1996). Texture of the phases has a significant effect on the mechanical properties of these *in situ* composites. The microtexture of Nb-Si binary composites in the as-DS, DS + heat-treated, and arc-cast + extruded + heat-treated conditions has been determined using the Electron Back Scattering Pattern (EBSP) technique for electron diffraction in the scanning electron microscope. In the DS composite, the primary (Nb) dendrites had little texture, but in the eutectic/eutectoid (Nb) a $[113]$ texture was observed. The $[001]$ of the eutectoid Nb_5Si_3 was perpendicular to the growth direction of the DS composite. In extruded Nb-10 Si the orientation relationships between the (Nb) and Nb_5Si_3 have been investigated by Sutliff and Bewlay (1996). They found that a $[110]$ fiber texture parallel to the extrusion direction was observed in the (Nb) of the single and double extruded composites. In addition, the $[001]$ Nb_5Si_3 was observed to be perpendicular to the extrusion direction. Rigney (1996) reported similar data.

The microstructure of a composite generated from a quaternary Nb-16 Ti-8 Hf-16 Si alloy is shown in Figure 4. The composite consisted of eutectic cells that contained an M_3Si -type phase together with (Nb). At these lower Ti and Hf

concentrations the eutectic is between the tP32 M_3Si and the (Nb). The microstructure of a composite generated from a Nb-9 Mo-22 Ti-8 Hf-16 Si alloy is shown in Figure 5. This composite consisted of eutectic cells of M_5Si_3 with (Nb). The M_5Si_3 possessed the hP16 structure rather than the previously reported tI32 Nb_5Si_3 (Massalski, 1991; Bewlay and Sutliff, 1998). The hP16 structure was stabilized by the high Ti and Hf additions. The scale of the microstructure shown in Figure 5 is significantly finer than that in Figure 4. EMPA analysis indicated that the approximate compositions of the phases were Nb-16 Ti-4 Hf-21 Mo-2 Si and Nb-19 Ti-13 Hf-2 Mo-38 Si.

Selected pole figures from EBSP data are shown in Figure 6 for (a) the Nb_3Si , (b) the Nb type phase in Nb-16 Ti-8 Hf-16 Si, (c) the hP16 M_5Si_3 in the Nb-9 Mo-22 Ti-8 Hf-16 Si, and (d) the (Nb) in the Nb-9 Mo-22 Ti-8 Hf-16 Si. These data indicate that in the Nb-9 Mo-22 Ti-8 Hf-16 Si the $[0001]$ hP16 M_5Si_3 and the $[001]$ of the (Nb) were strongly aligned with the growth direction. In the Nb-16 Ti-8 Hf-16 Si the $[111]$ M_3Si was aligned with the growth direction, but the (Nb) was not strongly textured. Thus, composition has a substantial impact on both the phases generated and the texture of the phases in the DS composite.

3.22.3.2 Phase Stability Investigations

Significant effort has been placed on the definition of liquid-solid and solid-solid phase stability in the Nb-Ti-Si and Nb-Hf-Si

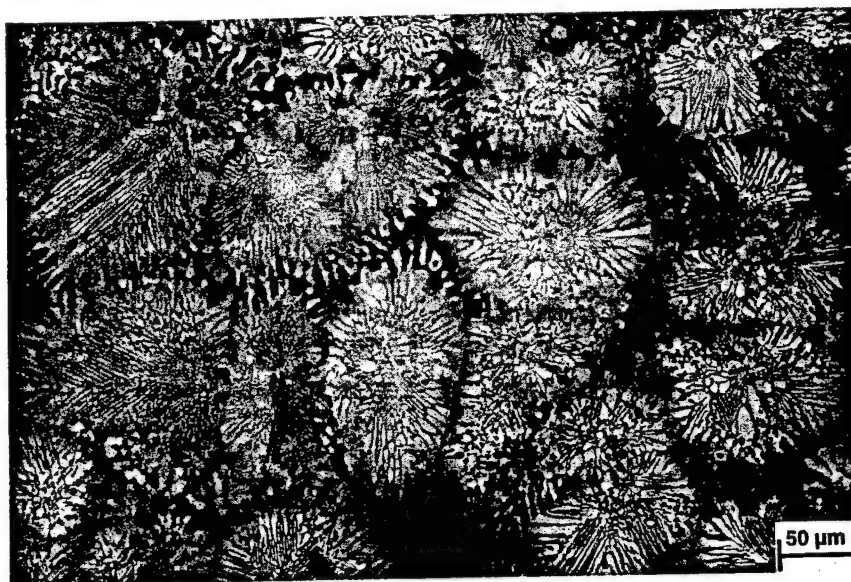


Figure 5 Typical microstructure (BSE image) of the transverse section of a DS composite generated from a Nb-9Mo-22Ti-8Hf-16Si alloy at a growth rate of 5 mm min^{-1} . The composite consists of eutectic cells of (Nb) (light phase) and hP16 M_5Si_3 (dark phase).

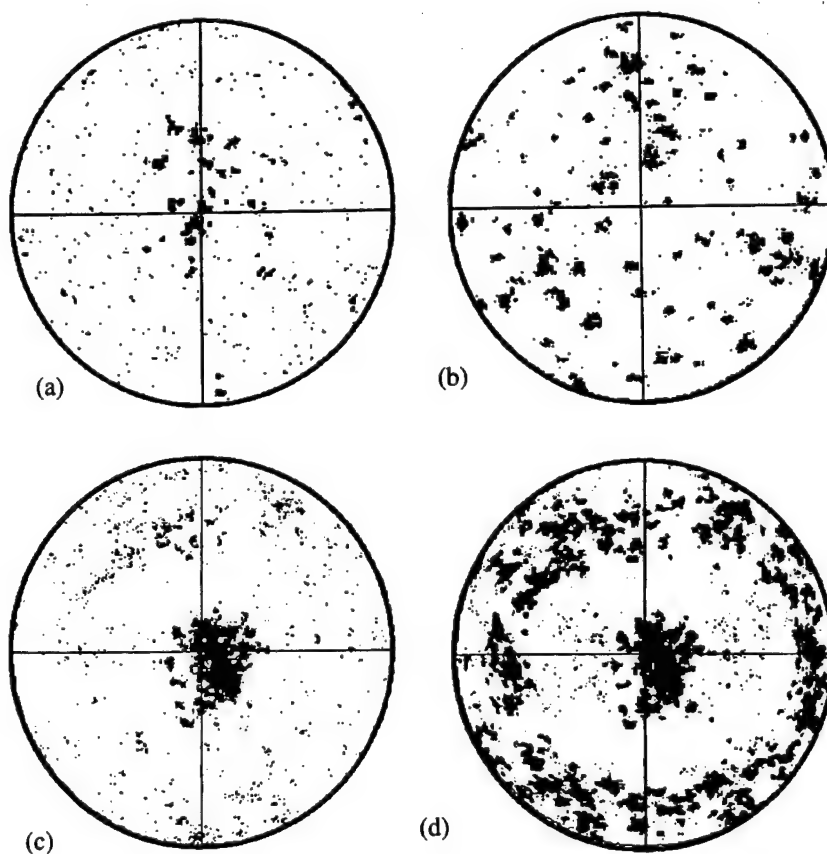


Figure 6 (a) [001] Nb_3Si pole figure in the Nb-16Ti-8Hf-16Si alloy, (b) [001] (Nb) pole figure in the Nb-16Ti-8Hf-16Si alloy, (c) [0001] pole figure of the M_5Si_3 , and (d) {111} pole figure in the Nb-9Mo-22Ti-8Hf-16Si.

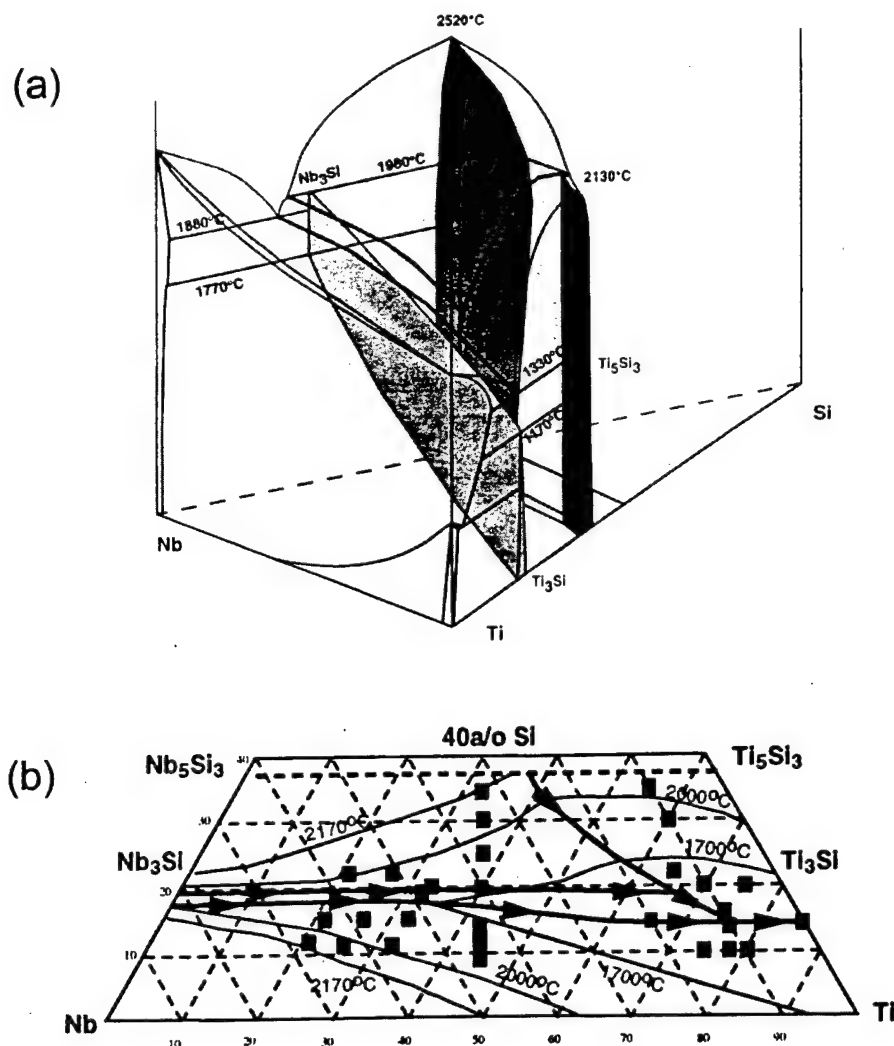


Figure 7 (a) Space diagram of the metal-rich end of the Nb-Ti-Si system. (b) Liquidus surface projection showing the two transition reactions (fine solid lines show temperature contours, and the compositions that were investigated are shown as solid squares).

systems because Ti and Hf additions to Nb-Si based composites have been shown to provide improvements in fracture toughness and oxidation behavior (Subramanian *et al.*, 1994, 1996, 1997; Jackson *et al.*, 1996; Bewlay *et al.*, 1996, 1997b). Subramanian *et al.* (1994) and Jackson *et al.* (1994, 1996) reported that the oxidation resistances of both the single-phase silicide and the metallic phase were improved by partial substitution of Ti for Nb. Hf is added because it is also a strong solid solution strengthener of the (Nb) (Bewlay *et al.*, 1996; Buckman, 1988).

Knowledge of the Nb-Hf-Si liquidus surfaces in ternary and higher order systems is required in order to predict the constituent phases and volume fractions of phases in these *in situ* composites. Thus, phase stability information is a critical requirement for definition of both the manufacture of these high-temperature *in situ* composite systems, and

their stability during service. In the present section phase stability in the Nb-Ti-Si and Nb-Hf-Si ternary systems will be described first, and then phase stability in higher order systems containing Mo, Cr, and Al will be discussed.

3.22.3.2.1 Nb-Ti-Si phase stability

Ternary Nb-Ti-Si phase equilibria have been reported for the metal-rich end of the phase diagram (Bewlay *et al.*, 1997b, 1999a; Liang and Chang, 1999), including liquid-solid and solid-solid phase equilibria. A space diagram of the metal-rich region (up to 37.5% Si) of the Nb-Ti-Si phase diagram is shown in Figure 7(a) (Bewlay *et al.*, 1997b), and a projection of the liquidus surface is shown in Figure 7(b). Figure 7(a) also shows the eutectic between

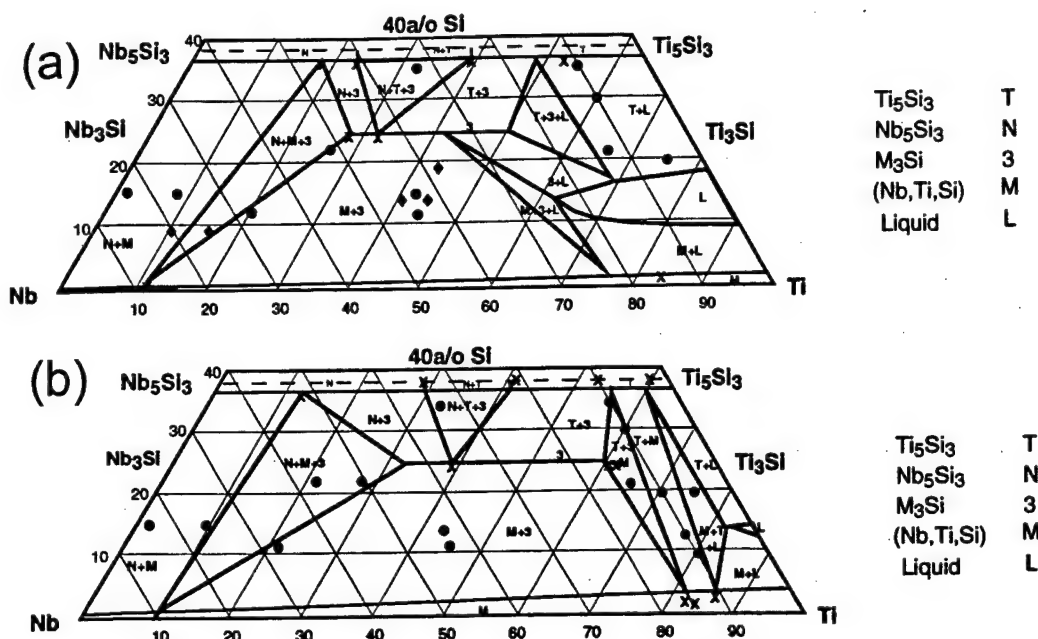


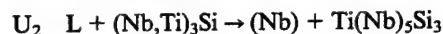
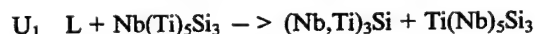
Figure 8 Isothermal sections of the Nb-Ti-Si phase diagram at temperatures of (a) 1500 °C and (b) 1340 °C. The compositions that were heat treated are included as solid bullets. EMPA measurements of phase compositions are shown as Xs. Literature data are also included as diamonds (Subramanian *et al.*, 1996, 1997).

Nb₃Si and (Nb). Isothermal sections at temperatures of from 1650 °C and 1150 °C have been defined and isothermal sections at 1500 °C and 1340 °C are shown in Figure 8(a) and (b). In the Nb-Ti-Si system, phase equilibria involve five phases: (Nb), Nb₃Si, Nb₅Si₃, Ti₅Si₃, and Ti₃Si with particular focus on the first four of these phases for RMICs (Massalski, 1991; Bewlay *et al.*, 1997b, 1999a).

In the present section, the Nb₅Si₃ with Ti in solid solution is referred to as Nb(Ti)₅Si₃, and the Ti₅Si₃ with Nb in solid solution is referred to as Ti(Nb)₅Si₃. The Nb₃Si with Ti in solid solution is referred to as (Nb,Ti)₃Si, because Nb₃Si and Ti₃Si are isomorphous. There are several reactions in the binary Nb-Si and Ti-Si systems which influence the metal-rich end of the ternary system. First, there is the $L \rightarrow \text{Ti}_5\text{Si}_3 + (\text{Ti})$ binary eutectic at 1330 °C (Massalski, 1991). Second, the binary Nb-Si phase diagram (Massalski, 1991) possesses a eutectic of the form $L \rightarrow \text{Nb}_3\text{Si} + (\text{Nb})$ at 1880 °C, and also a peritectic of the form $L + \text{Nb}_5\text{Si}_3 \rightarrow \text{Nb}_3\text{Si}$ at 1980 °C, as described earlier. In the ternary phase diagram a eutectic groove extends between the two binary eutectics, but due to the different binary eutectic reactions there is a change in the nature of the liquidus surface, and the eutectic groove, with decreasing Nb and increasing Ti concentration.

In the liquidus projection shown in Figure 7(b), the peritectic ridge, p_2 , intersects

the peritectic ridge, p_1 , to generate U_1 and the resulting peritectic ridge intersects the eutectic groove, e_1 , to generate U_2 . The two transition reactions are described by Bewlay *et al.* (1997b):



The first of these transition reactions occurs at a composition of approximately Nb-66 Ti-19 Si, and at a temperature of ~1650 °C. The second of these transition reactions occurs at a composition of approximately Nb-76 Ti-13.5Si, and a temperature of ~1350 °C.

The microstructure of a DS composite from Nb-44Ti-12Si heat treated at 1500 °C for 100 h is shown in Figure 9; this composition is from the two-phase field (Nb) + (Nb,Ti)₃Si. It contained large-scale metal dendrites, which had coarsened substantially from the initial solidification structure.

3.22.3.2.2 Nb-Hf-Si ternary phase stability

A space diagram of the Nb-Hf-Si system is shown in Figure 10(a) and the liquidus surface projection is shown in Figure 10(b) (Bewlay *et al.*, 1998). At the metal-rich end of the Nb-Hf-Si ternary phase diagram there is a eutectic trough between the $L \rightarrow \text{Nb}_3\text{Si} + (\text{Nb})$ and

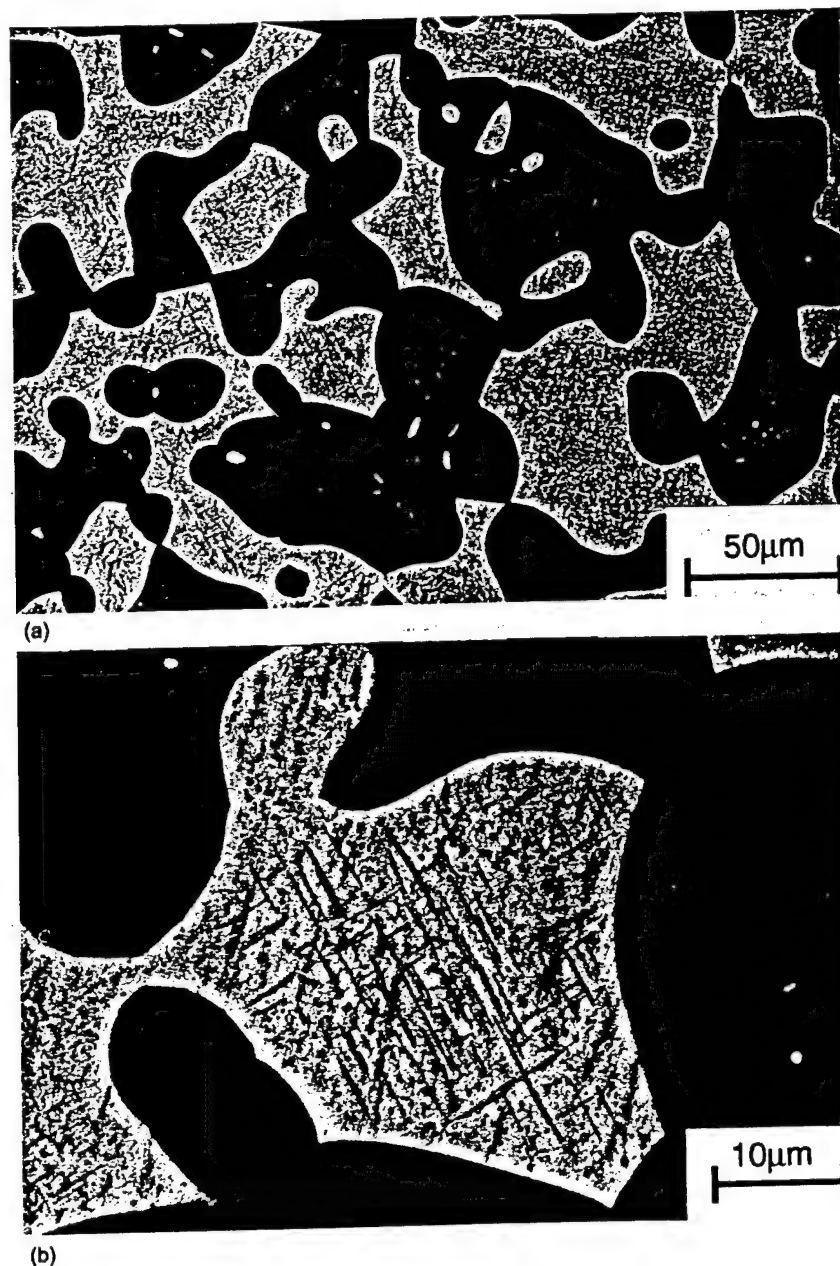


Figure 9 Typical microstructure (BSE image) of the transverse section of a DS Nb-44Ti-12Si alloy heat treated at 1500 °C for 100 h shown at (a) low and (b) high magnifications. The large white dendrites are (Nb) and the interdendritic gray phase is (Nb,Ti)₃Si.

$L \rightarrow \text{Hf}_2\text{Si} + (\text{Hf})$ binary eutectics (Massalski, 1991; Bewlay *et al.*, 1998; Gokhale and Abbaschian, 1989). However, because of the different binary eutectic reactions there is a change in the nature of the liquidus surface, and the eutectic groove, with decreasing Nb and increasing Hf concentration. There is also only a 50 °C difference in temperatures of these two binary eutectics (Massalski, 1991), and the slope of this trough is therefore very shallow. The loci of the peritectic ridge from the $L + \text{Nb}_5\text{Si}_3 \rightarrow \text{Nb}_3\text{Si}$ peritectic, p_2 , the $L + \text{Hf}_5\text{Si}_3 \rightarrow \text{Hf}_2\text{Si}$ peritectic ridge, p_3 , and the Hf-Hf₂Si eutectic groove, e_3 , generate

three invariant reactions in the Nb-Hf-Si system. The locations of these three invariant reactions are pertinent to the generation of high-temperature composites from Nb-Si alloys modified with Hf. In the present section, the Nb₅Si₃ with Hf in solid solution is referred to as Nb(Hf)₅Si₃, the Hf₅Si₃ with Nb in solid solution is referred to as Hf(Nb)₅Si₃, the Hf₂Si with Nb in solid solution is referred to as Hf(Nb)₂Si, and the Nb₃Si with Hf in solid solution is referred to as Nb(Hf)₃Si. The Hf₅Si₃ has the hP16 crystal structure.

The three transition reactions are shown below. In Figure 10(b), the peritectic ridge, p_2 ,

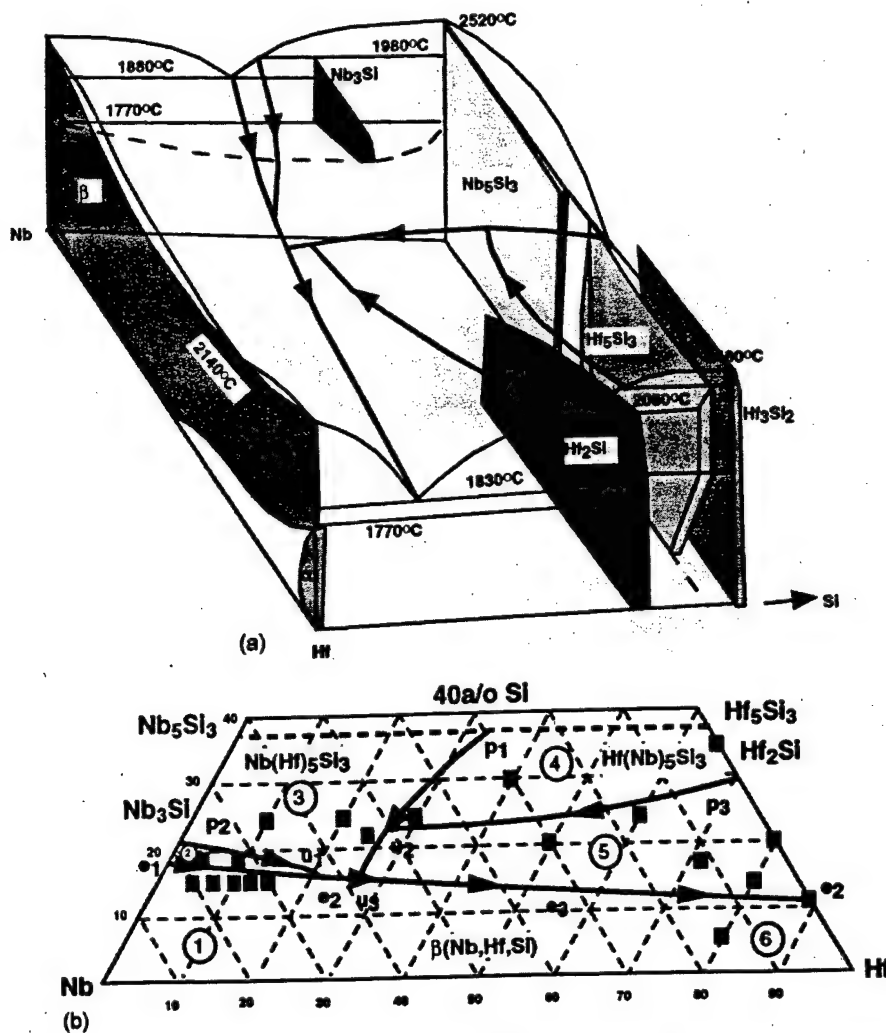
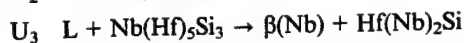
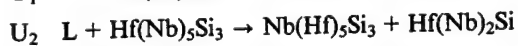
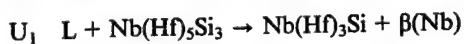


Figure 10 (a) Space diagram of the metal-rich end of the Nb-Hf-Si system. (b) schematic diagram showing the projection of the Nb-Hf-Si liquidus surface. The projection shows the peritectic ridges, p_1 , p_2 , p_3 , the eutectic valleys, e_1 , e_2 , e_3 , and the invariant reactions, U_1 , U_2 , U_3 . The alloy compositions that were investigated are shown as the solid points on the liquidus surface projection.

intersects the eutectic groove, e_1 , to generate U_1 . The peritectic ridges, p_1 and p_3 , intersect to generate U_2 , and the subsequent ridge intersects the eutectic groove, e_1 , to generate U_3 .



The first of these transition reactions occurs at a composition of approximately Nb-21 Hf-16 Si, and at a temperature of $\sim 1850^\circ\text{C}$. The second of these transition reactions occurs at a composition of approximately Nb-27 Hf-22 Si and a temperature of $\sim 2040^\circ\text{C}$. The third transition reaction occurs at Nb-26 Hf-14 Si and a temperature of $\sim 1840^\circ\text{C}$.

Six regimes have been identified on the liquidus surface, as shown in the projection of Figure 10(b). The regimes that are most relevant

to the development of high-temperature composites are 1, 2, and 3. Microstructures of *in situ* composites from regimes 1 and 3 are described below. Composites from regime 1 contained primary $\beta(\text{Nb})$ dendrites with Nb(Hf)₃ Si- $\beta(\text{Nb})$ eutectic. A typical microstructure of the transverse section of the DS Nb-15Hf-16Si composition is shown in Figure 11. The microstructure consisted of a small volume fraction of primary $\beta(\text{Nb})$ dendrites, which are the dark grey phase in the BSE micrograph, together with an interdendritic Nb(Hf)₃ Si- $\beta(\text{Nb})$ cellular eutectic.

Composites from regime 3 contained primary Nb(Hf)₅Si₃ dendrites, peritectic Nb(Hf)₃ Si, and Nb(Hf)₃ Si- $\beta(\text{Nb})$ eutectic. The typical microstructure of the transverse section of the DS Nb-10 Hf-25 Si alloy is shown in Figure 12. The large black phase is Nb(Hf)₅Si₃, and it is surrounded by dark gray peritectic Nb(Hf)₃ Si.

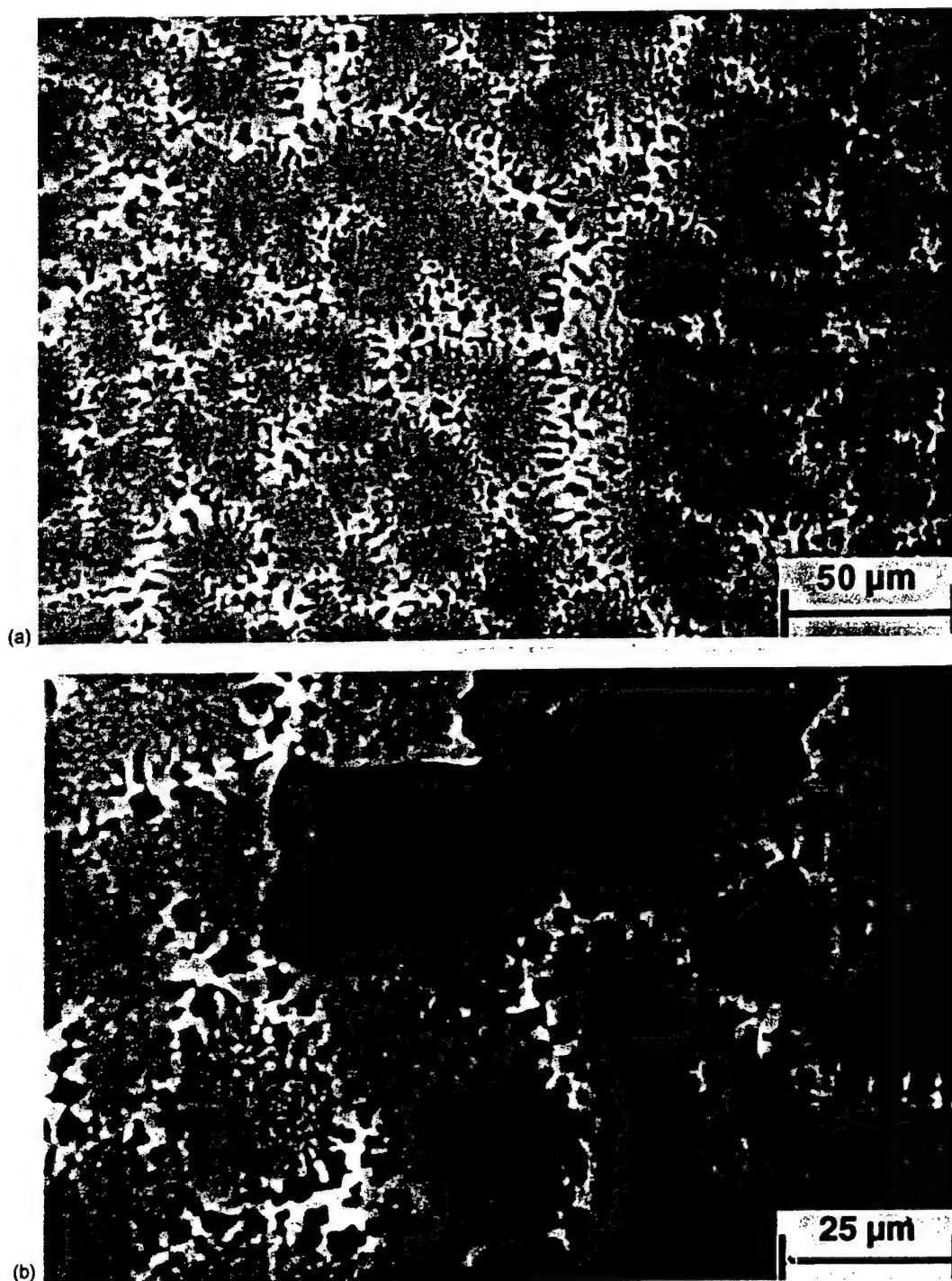


Figure 11 Typical microstructure (BSE image) of the transverse section of a DS Nb-15Hf-16Si alloy at (a) low and (b) high magnifications. There are large-scale dark $\beta(\text{Nb})$ dendrites with interdendritic eutectic cells of $\text{Nb}(\text{Hf})_3\text{Si}$ (light gray) and $\beta(\text{Nb})$. The $\text{Nb}(\text{Hf})_3\text{Si}$ also contained some brighter regions that were Hf rich.

The peritectic and dendritic $\text{Nb}(\text{Hf})_3\text{Si}$ appear to have grown in a coupled manner with the $\beta(\text{Nb})$ dendrites. Hf partitioning between the $\text{Nb}(\text{Hf})_3\text{Si}$ and $\beta(\text{Nb})$ was such that there was little contrast between these two phases.

During solidification of alloys with higher Hf concentrations in regime 3, the composition of

the liquid can also move directly into the eutectic valley, e_2 , and miss the peritectic ridge, p_2 , as well as e_1 and U_1 , thereby generating a two-phase composite of $\beta(\text{Nb})$ and $\text{Nb}(\text{Hf})_5\text{Si}_3$. Thus, judicious selection of Hf additions can have a substantial effect on the phases generated in the *in situ* composites.

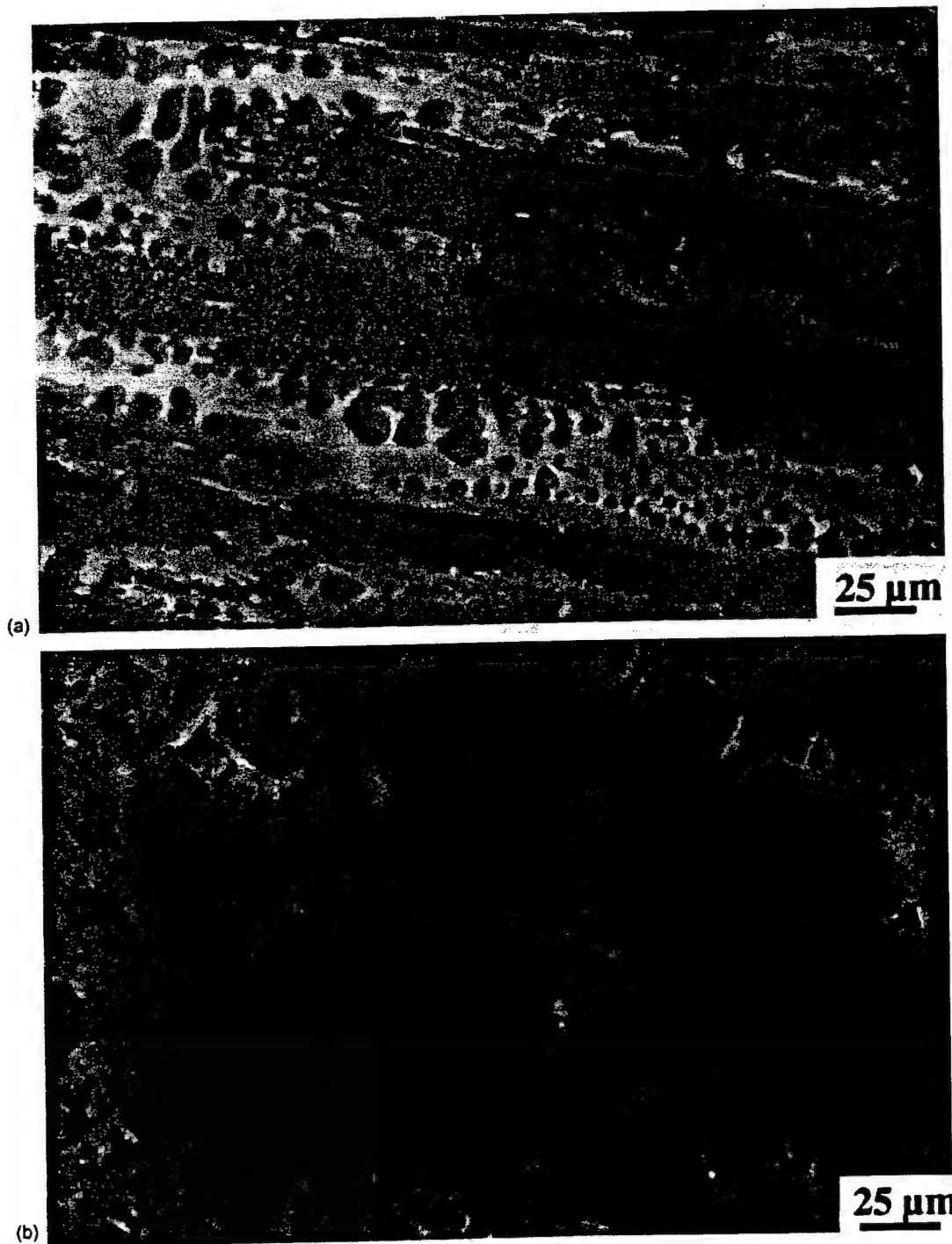


Figure 12 Typical microstructures (BSE images) of (a) the longitudinal section and (b) the transverse section of a DS Nb-10Hf-25Si alloy. The large black phase is $\text{Nb}(\text{Hf})_5\text{Si}_3$, the large dark gray phase is $\text{Nb}(\text{Hf})_3\text{Si}$, and the light gray phase is $\beta(\text{Nb})$.

3.22.3.2.3 Quaternary and higher order systems

Phase stability in Nb-silicide composites of several quaternary and higher order systems has also been investigated. Al and Cr are important alloying additions for oxidation resistance. Mo, Ta, and W have also been con-

sidered but there have been limited evaluations of the effects of these elements on phase stability (Subramanian *et al.*, 1997; Shah *et al.*, 1995). Mo can have a substantial effect on composite phases as indicated by the micrographs in Figures 4 and 5.

Phase stability in the MASC has been described previously. The MASC contained three

Table 1 Composition ranges for the silicide and metallic phases observed in the DS MASC (Nb–24.7Ti–8.2Hf–2.0Cr–1.9Al–16.0Si) and the DS Nb–27Ti–22Si.

Alloy	Phase	Nb	Ti	Hf	Si	Al	Cr
DS MASC	(Nb)	58–61	27.2–29.4	5.0–5.3	0.9–1.3	2.5–3.0	2.8–3.9
	M ₃ Si	48.3–49.0	18.2	7.8	24.7–25.4	0.1	0.1–0.2
	M ₅ Si ₃	25.5–27.9	22.2–23.2	12.5–12.9	35.4–37.5	1.0–1.5	0.4–0.5
Nb–27Ti–22Si	(Nb)	54–69	29–44	–	1.6–2.4	–	–
	(Nb,Ti) ₃ Si	44–54	22–29	–	23–24	–	–
	Nb(Ti) ₅ Si ₃	44–45	19–20	–	35–36	–	–

Source: Bewlay, Jackson *et al.*, 1994a, 1997a.**Table 2** Average phase chemistries for silicide and Laves phases that have been observed in alloys that were heat-treated at 1200 °C before oxidation treatments.

	Nb (at.%)	Al (at.%)	Nb (at.%)	Hf (at.%)	Ti (at.%)	Cr (at.%)	Si (at.%)
M ₅ Si ₃ High Ti	21.2	2.3	21.2	13.6	25.4	1.0	36.5
M ₅ Si ₃ Intermediate Ti	29.5	1.9	29.5	11.4	19.3	1.4	36.5
M ₅ Si ₃ Low Ti	40.5	2.4	40.5	6.5	14.0	0.7	35.9
Metal	51.4	4.1	51.4	3.0	30.2	10.6	0.7
Laves	19.8	1.4	19.8	7.3	12.3	52.6	6.6

Source: Jackson *et al.*, 1994.

phases: a metallic phase containing Nb, Ti, Hf, Si, Al, and Cr, an M₃Si silicide phase, and also an M₅(Si,Al)₃ type phase. The composition ranges for these phases are shown in Table 1. The tP32 M₃Si and hP16 M₅(Si,Al)₃ Nb silicides show extensive solubility for Hf and Ti. The Si concentrations of the M₃Si and M₅Si₃ silicides were close to the stoichiometric values.

Higher Cr additions have also been examined and can lead to the formation of a Laves phase (Subramanian *et al.*, 1997; Jackson *et al.*, 1994). The introduction of the Laves phase can lead to a substantial improvement in the oxidation resistance. Typical compositions of the phases in a Laves phase-containing silicide based *in situ* composite are shown in Table 2. Three M₅Si₃ type phases coexist with a Si-rich Laves phase and (Nb) (Jackson *et al.*, 1994).

3.22.3.2.4 Precipitation in Nb solid solutions

Precipitation in the metallic solid solutions of RMICs can have critical effects on both the low temperature mechanical properties, such as strength and toughness, as well as high temperature performance, such as creep rate and creep rupture behavior. Precipitation strength-

ening of monolithic Nb alloys has received significant attention (Anton *et al.*, 1988; Grylls *et al.*, 1998; Cockeram, Lipsitt *et al.*, 1991a; Cockeram *et al.*, 1992; Cockeram, Saqib *et al.*, 1991b; Grigorovich *et al.*, 1980; Grigorovich and Sheftel', 1983; Sheftel' and Bannykh, 1993). The use of dispersoids has also been considered. Anton *et al.* (1988) reported that the most promising dispersoids are ZrB₂, HfB₂, ZrN, HfN, and Si₃N₄.

Fine-scale precipitates have been reported in (Nb) of the *in situ* composites of both binary Nb–Si and ternary Nb–Ti–Si alloys (Grylls *et al.*, 1998; Cockeram, Lipsitt *et al.*, 1991a; Cockeram, Saqib *et al.*, 1991b; Cockeram, Lipsitt *et al.*, 1992). Typical silicide precipitates within the (Nb) dendrite of the composites are shown in Figure 13. The large precipitates (~0.5 μm) possessed a dendritic morphology with the principal axis of the precipitate parallel to the [010] in the (Nb). An array of fine needle-shaped silicide precipitates within the (Nb) can also be seen in Figure 13. Precipitates can be seen in all three orthogonal directions. The precipitates possessed an ordered orthorhombic structure. In the (Nb) of the Nb–14Si, precipitation was heterogeneous whereas in the (Nb) of the Nb–44Ti–12Si, the precipitation was homogenous (Grylls *et al.*, 1998).

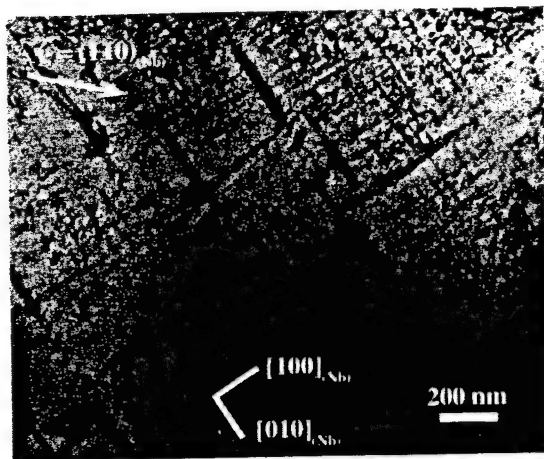


Figure 13 Bright field transmission electron micrograph showing silicide precipitates in the (Nb) of the Nb-42.5Ti-15Si composite heat treated at 1500 °C for 100 h followed by slow cooling to below 800 °C.

The orthorhombic $(\text{Nb,Ti})_3\text{Si}$ precipitates in the Ti-containing composites were metastable with respect to the tP32 structure. The Nb_3Si precipitates in the binary Nb-Si solid solution were metastable with respect to both the stoichiometry and crystal structure of tI32 Nb_5Si_3 . Ordering to the metastable orthorhombic Nb_3Si required a smaller nucleation barrier than to the stable tI32 Nb_5Si_3 , and the close matching of the lattice plane spacing of the matrix and precipitate allowed the interfacial energy to be minimized. The following precipitate-matrix orientation relationships were observed in both the Nb-Si binary and the Nb-Ti-Si ternary alloys for the coherent precipitates.

$$[100]_{\text{Nb}} \parallel [100]_{\text{ppt}}; (001)_{\text{ppt}} \parallel (001)_{\text{Nb}}$$

Mendiratta and Dimiduk (1991) have also reported precipitates of Si-rich particles in binary Nb-Si alloys, and they postulated that these precipitates were generated as a result of the decrease in the solubility of Si in (Nb) with decreasing temperature after a 1500 °C heat treatment. This explanation is consistent with more recent data by Grylls *et al.* (1998) who also examined the formation and stability of precipitates at temperatures as low as 1200 °C. Cockeram and co-workers (Cockeram, Lipsitt *et al.*, 1991a; Cockeram *et al.*, 1992; Cockeram, Saqib *et al.*, 1991b) also provided a characterization of silicide precipitates in Nb-10 Si alloys (Mendiratta *et al.*, 1991).

The reactive metals Zr and Hf together with C and N produce fine precipitates that contribute to the high-temperature strength of Nb alloys. For example, Nb strengthened by only 2% ZrN shows a tensile strength of ~500 MPa at 1200 °C (Buckman, 1988; Grigorovich *et al.*,

1980; Grigorovich and Sheftel', 1983; Sheftel' and Bannykh, 1993). Nb strengthened by only 9% of (group IVa) MC carbides also shows a tensile strength of more than 500 MPa at 1200 °C (Grigorovich *et al.*, 1980; Grigorovich and Sheftel', 1983; Sheftel' and Bannykh, 1993). The carbides, nitrides and borides of Hf, Zr, and Nb have very high decomposition temperatures. In addition, the solubilities of B and C in Nb are quite small at temperatures below about 1500 °C. Therefore, the rate of dispersoid coarsening is probably quite slow at a temperature of 1200 °C. By combining carbide dispersions with large additions of W, Cb-1 remains the strongest Nb base alloy with acceptable workability (Buckman, 1988). The role of carbide and nitride dispersions in strengthening the (Nb) of the RMICs has been explored, but to date there are few reported data.

3.22.4 MECHANICAL PROPERTIES

In the following section, emphasis will be placed on four critical mechanical properties and the development of RMICs towards these property goals: low-temperature damage tolerance (fracture toughness and room temperature fatigue), high-temperature strength, and creep behavior. The progress in the development of RMICs towards these goals will be discussed.

3.22.4.1 Fracture Behavior

Minimum fracture toughness is required to provide damage tolerance in order to make components that can survive the final assembly into turbine engines, and tolerate impact loading in service from events such as foreign object damage. A fracture toughness of 20 $\text{MPa}\sqrt{\text{m}}$ is considered a minimum value for critical components. (General treatments of the fracture toughness characteristics of particulate, fibrous, and layered MMCs are given respectively in Chapters 3.07, 3.08, and 3.11, this volume.) There have been extensive studies of the fracture mechanisms in composites from binary Nb-Si alloys (Subramanian *et al.*, 1996; Jackson *et al.*, 1996; Mendiratta *et al.*, 1991; Mendiratta and Dimiduk, 1993; Bewlay *et al.*, 1995a, 1997c; Ravichandran, 1992; Henshall *et al.*, 1997; Nekkanti and Dimiduk, 1990). Typically fracture toughness measurements have been performed using single edge notched bending specimens (SENB), and the procedures provided by ASTM standard E-399 (1983). Several researchers, typically using procedures described by the ASTM standard

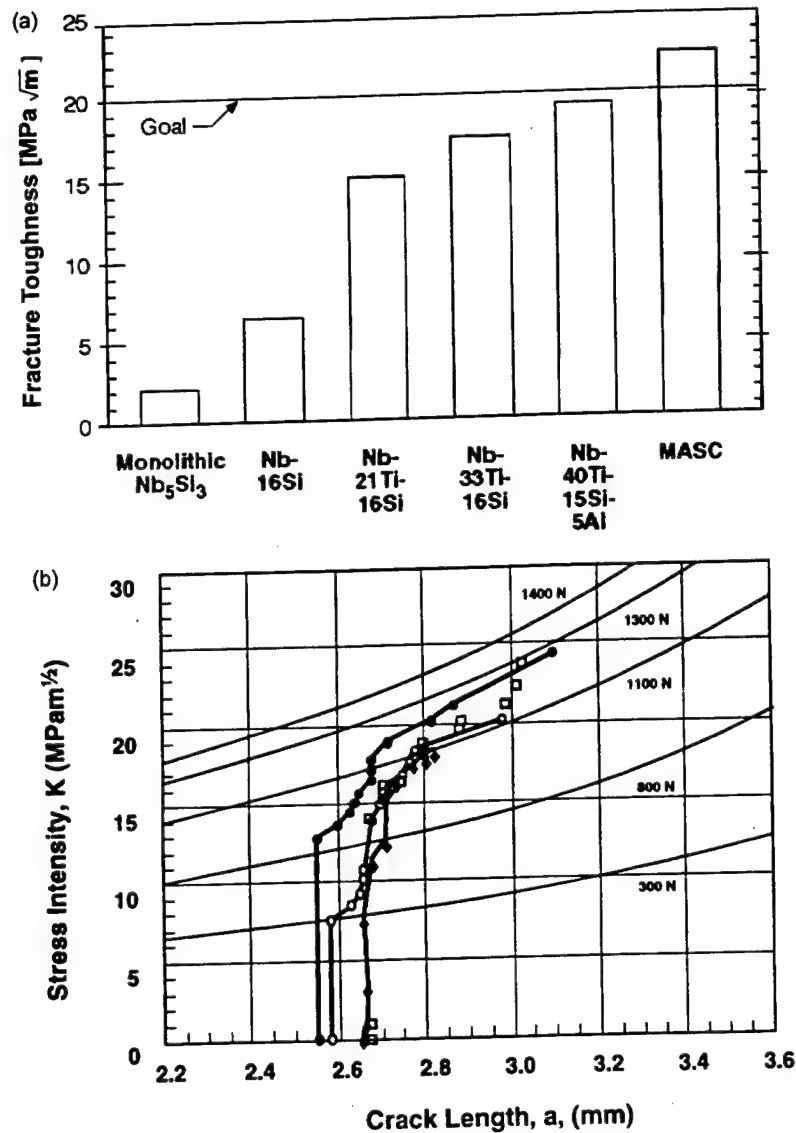


Figure 14 (a) Fracture toughness of (Nb)-toughened silicide-based composites from binary Nb-Si, ternary Nb-Ti-Si and quaternary Nb-Ti-Si-Al alloys, (b) R-curve behavior of the *in situ* composites. Data from the DS MASC (Nb-24.7%Ti-16%Si-8.2%Hf-2.0%Cr-1.9%Al) are also shown.

E-561-94 (1994), have also performed R-curve measurements.

Fracture toughness measurements for a series of Nb-based RMICs are shown in Figure 14(a) (Subramanian *et al.*, 1994, 1996, 1997; Jackson *et al.*, 1996; Dimiduk *et al.*, 1993; Mendiratta *et al.*, 1991; Mendiratta and Dimiduk, 1993; Bewlay *et al.*, 1996, 1997a, 1997c). Early *in situ* composites from binary Nb-Si alloys showed promising levels of toughness. Room temperature fracture toughness measurements are shown in Tables 3-6 for a range of composites from binary, ternary, quaternary, and higher order alloys. The MASC has a toughness of $>20 \text{ MPa}\sqrt{\text{m}}$ (Bewlay *et al.*, 1996); this toughness level has also been

demonstrated recently in a wider range of systems (Bewlay *et al.*, 1997c).

R-curve measurements that have been reported show that the resistance to crack growth increases with increasing crack length, an indication that crack growth occurs in a stable manner. R-curve measurements are shown in Figure 14(b) for the MASC. Typically, the initiation toughness values for the MASC were 7-13 $\text{MPa}\sqrt{\text{m}}$, and the K_{IC} values were 19-22 $\text{MPa}\sqrt{\text{m}}$. The form of these R-curves is similar to those reported previously in binary Nb-10 Si *in situ* composites, which displayed K_{IC} values of $>20 \text{ MPa}\sqrt{\text{m}}$ in the extruded condition (Rigney *et al.*, 1994; Rigney, 1996; Bewlay *et al.*, 1997b).

Table 3 Room temperature fracture toughness of DS ternary Nb-Ti-Si *in situ* composites from compositions in the range 3–33% Ti.

Composition (at.%)	DS constituent phases	Fracture toughness (MPa \sqrt{m})
Nb-16Si	(Nb), Nb ₃ Si	7.8
Nb-33Ti-16Si	(Nb), (Nb,Ti) ₃ Si	11.1
Nb-27Ti-16Si	(Nb), (Nb,Ti) ₃ Si	11.7
Nb-27Ti-12Si	(Nb), (Nb,Ti) ₃ Si	9.8
Nb-21Ti-16Si	(Nb), (Nb,Ti) ₃ Si	11.6
Nb-21Ti-12Si	(Nb), (Nb,Ti) ₃ Si	10.6
Nb-32Ti-19Si	(Nb), (Nb,Ti) ₃ Si, Nb(Ti) ₅ Si ₃	12.4
Nb-42.5Ti-15Si	(Nb), (Nb,Ti) ₃ Si	12.3
Nb-3Ti-16Si	(Nb), (Nb,Ti) ₃ Si	9.7

Source: Bewlay, Jackson *et al.*, 1995a.**Table 4** Room temperature fracture toughness of Nb-16Si composites modified with Hf and Ti.

Composition	Fracture toughness (MPa \sqrt{m})
Nb-7.5Hf-21Ti-16Si	12.2
Nb-10Hf-21Ti-16Si	11.9
Nb-12.5Hf-21Ti-16Si	12.1
Nb-21Ti-16Si	11.6
Nb-7.5Hf-33Ti-16Si	12.6
Nb-10Hf-33Ti-16Si	13.3
Nb-12.5Hf-33Ti-16Si	14.0
Nb-33Ti-16Si	11.1

Table 5 Room temperature fracture toughness of Nb-16Si composites modified with Hf, Ti, Cr and Al. The effects of Hf, Cr, and Si concentrations on fracture toughness are described.

Composition	Fracture toughness (MPa \sqrt{m})
Nb-20Ti-8Hf-2Al-2Cr-16Si	21.0
Nb-30Ti-8Hf-2Al-2Cr-16Si	19.3
Nb-24.6Ti-11Hf-2Al-2Cr-16Si	21.8
Nb-23.6Ti-14Hf-2Al-2Cr-16Si	18.2
Nb-25Ti-8Hf-2Al-2Cr-18Si	20.0
Nb-26.5Ti-8Hf-2Al-10Cr-16Si	18.7
Nb-24.7Ti-8.2Hf-2.0Cr-1.9Al-16.0Si	23.3

Fracture surfaces of both binary Nb-Si and ternary Nb-Ti-Si composites have been reported previously. Generally in those systems with the highest toughness ductile rupture of the (Nb) is observed. Figure 15(a) and (b) show fracture surfaces of the DS MASC. The fracture surfaces were highly convoluted and consistent with a high work of fracture. The higher magnification fractograph shows that (Nb) dendrites failed in a ductile manner, and were pulled out of the matrix. The (Nb) between the silicide dendrites was also pulled to a chisel

Table 6 Room temperature fracture toughness of Mo modified composites.

Composition	Fracture toughness (MPa \sqrt{m})
Nb-8Hf-25Ti-16Si	16.1
Nb-3Mo-8Hf-25Ti-16Si	17.9
Nb-9Mo-8Hf-25Ti-16Si	14.0
Nb-8Ti-8Hf-16Si	12.3
Nb-9Mo-8Hf-16Si	11.9
Nb-9Mo-5Ti-8Hf-16Si	7.7
Nb-9Mo-8Ti-8Hf-16Si	8.7
Nb-9Mo-13Ti-8Hf-16Si	8.8
Nb-9Mo-16Ti-8Hf-16Si	7.4
Nb-9Mo-22Ti-8Hf-16Si	10.0
Nb-15Mo-0Ti-8Hf-16Si	11.4

point, and microcracking of the silicide matrix was observed. Typically, the M₃Si and M₅Si₃ silicide dendrites fail by cleavage. At higher magnifications crack bridging and crack blunting are observed. This suggests that the (Nb) provides the majority of the toughness, although microcracking and interface debonding may also make significant toughening contributions. Crack deflection and crack multiplication also occurs.

3.22.4.1.1 Effect of Ti additions on fracture toughness

The effect of Ti on fracture toughness of a range of DS Nb-Ti-Si composites is shown in Table 3. Considering the effect of Ti on the fracture toughness of the 16% Si alloy, the toughness of the Ti-containing composite is ~50% greater than that of the binary Nb-16% Si composite (7.8 MPa \sqrt{m}) (Bewlay *et al.*, 1994a, 1995b), but there is no systematic increase in the fracture toughness with increasing Ti concentration, for concentrations in the range 21–33% Ti. For both the 27% and 21%

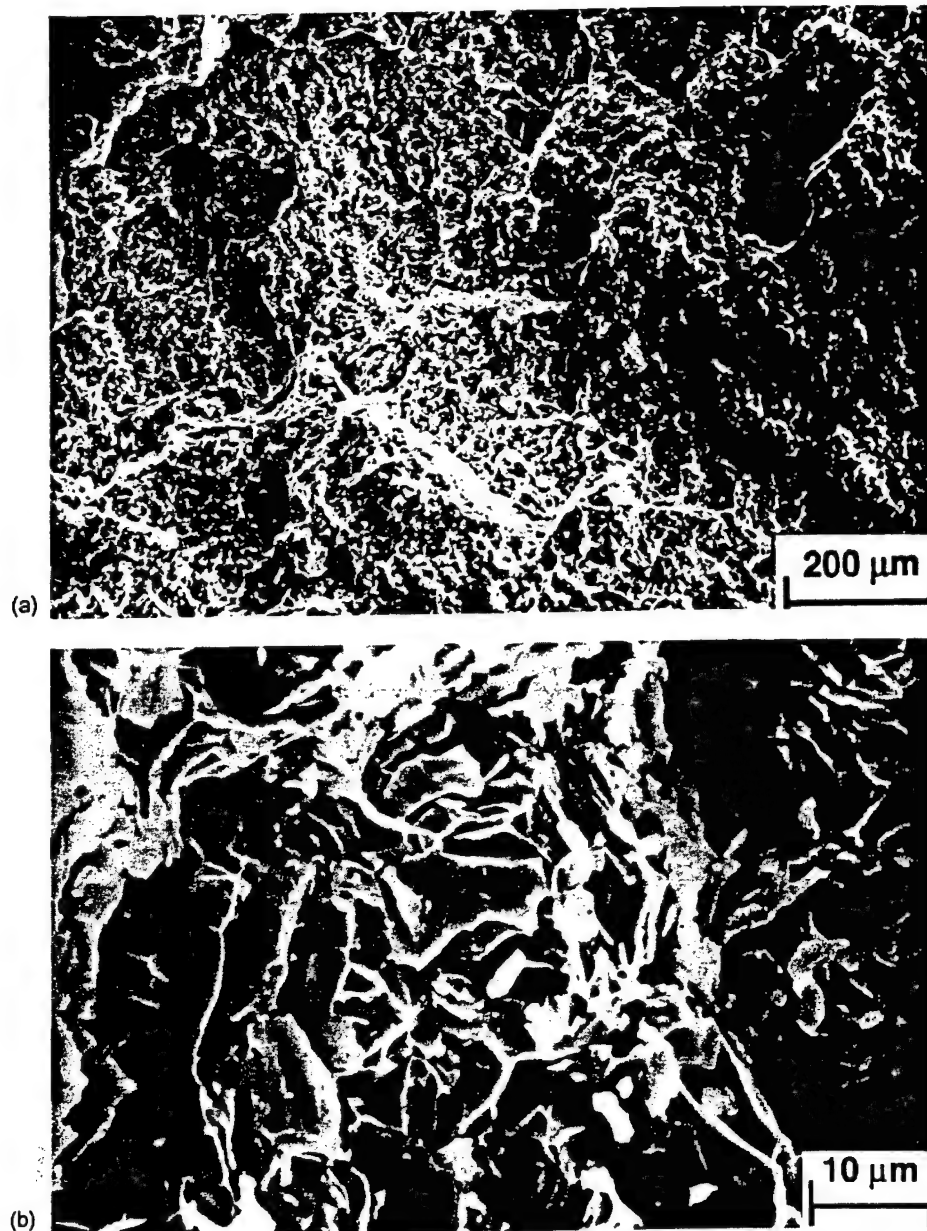


Figure 15 Fracture surfaces of several DS *in situ* composites; the MASC at (a) low and (b) high magnifications, and DS Nb-27Ti-16Si at (c) low and (d) high magnifications.

Ti composites, reducing the Si concentration from 16% to 12% results in slightly smaller fracture toughness values, even though the volume fraction of (Nb) is greater in the 12% alloys. For the 27% Ti composites, the fracture toughness of the 16% Si composites was $11.9 \text{ MPa}\sqrt{\text{m}}$, whereas that of the 12% alloy was $9.8 \text{ MPa}\sqrt{\text{m}}$. This situation is different to that observed in the binary Nb-Si *in situ* composites where the toughness increased with decreasing Si concentration and increasing volume fraction of Nb; decreasing the Si concentration from 18% to 10% increased the Nb volume fraction from ~ 0.35 to ~ 0.7 and the fracture toughness values from 6

to $14 \text{ MPa}\sqrt{\text{m}}$, respectively (Bewlay *et al.*, 1995a). However, given the narrow range of ternary compositions and fracture toughness values, these trends are somewhat speculative.

A fractograph of the transverse section of a DS Nb-27Ti-16Si composite is shown in Figure 15(c). The (Nb) dendrites failed in a ductile manner, as did the fine-scale (Nb) between the $(\text{Nb,Ti})_3\text{Si}$ dendrites, as shown in both Figure 15(c) and (d). Cleavage of the $(\text{Nb,Ti})_3\text{Si}$ occurred on many planes giving rise to complex fracture surfaces. Subramanian *et al.* (1994) also observed plastic stretching and rupture of the (Nb), as well as secondary cracking of the silicide in the Nb-42.5Ti-15Si. There

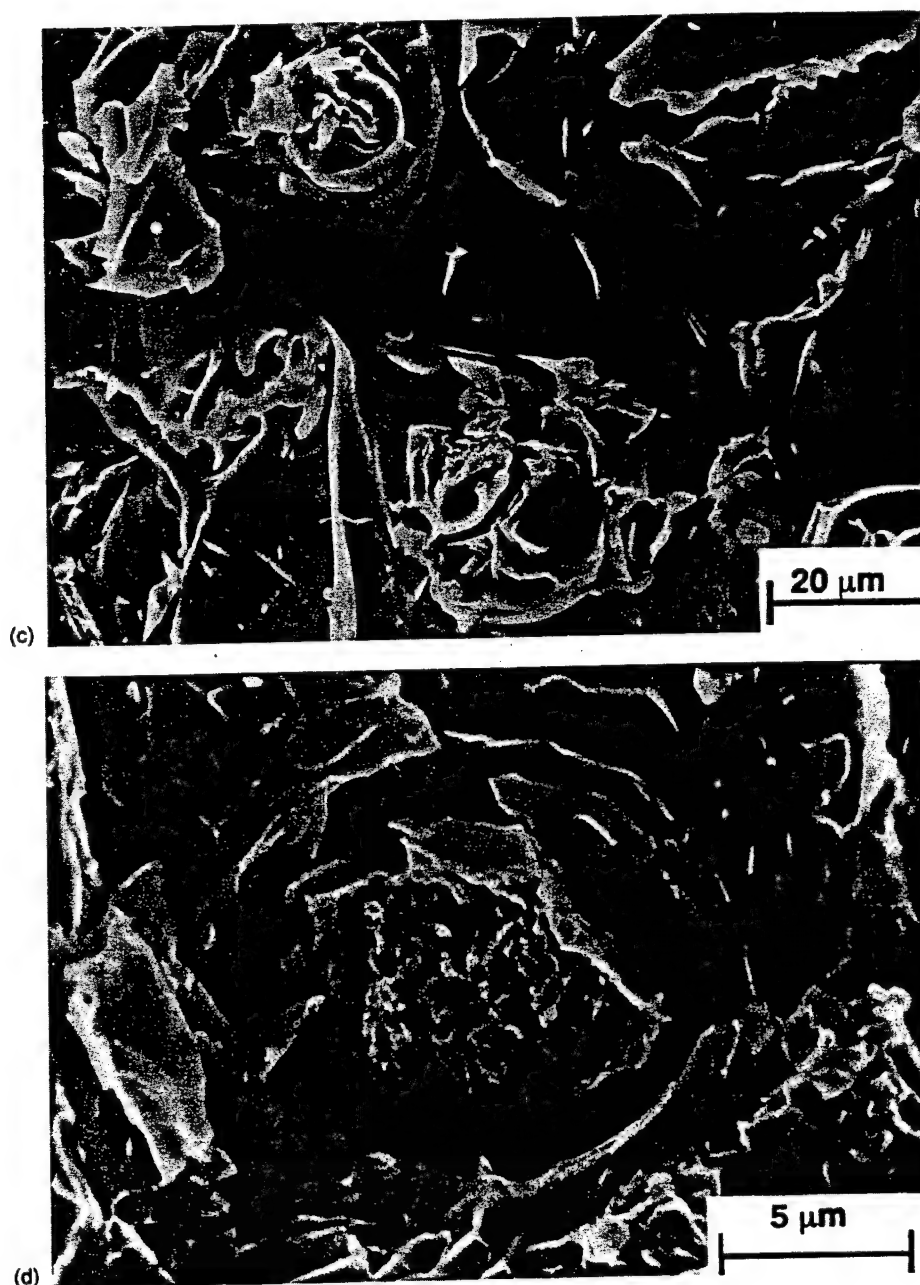


Figure 15 (continued).

are two possible explanations for the toughening enhancement observed in the Nb-Ti-Si composites over that of the binary Nb-Si composite. First, the (Nb) may have greater intrinsic ductility than the (Nb) in the binary two-phase composite. Second, the metallic phase exists only as large-scale (Nb) dendrites, rather than a combination of fine-scale eutectic and large-scale dendritic morphologies as in the binary alloy, and thus the same volume fraction of metallic phase may provide more toughening in the case of the ternary alloy (Bewlay *et al.*, 1994a; Ravichandran, 1992).

The effect of Hf additions on the room temperature fracture toughness has also been ex-

amined, as shown in Table 4 for Nb-16Si modified with Hf compositions of 7.5-12.5 and Ti compositions of 21-33%. Room temperature fracture toughness was relatively insensitive to Hf:Ti composition ratios in the range 0.2-0.6. However, Ti additions appear to have a stronger effect on toughness than Hf additions. The room temperature fracture toughness of composites with 33 Ti was generally higher than those with 21 Ti.

Table 5 shows a range of alloys derived from the base MASC composition (Bewlay *et al.*, 1997c) (last row of Table 5). These data indicate that, for Ti concentrations in the range 20-30%, there is little effect on toughness. The

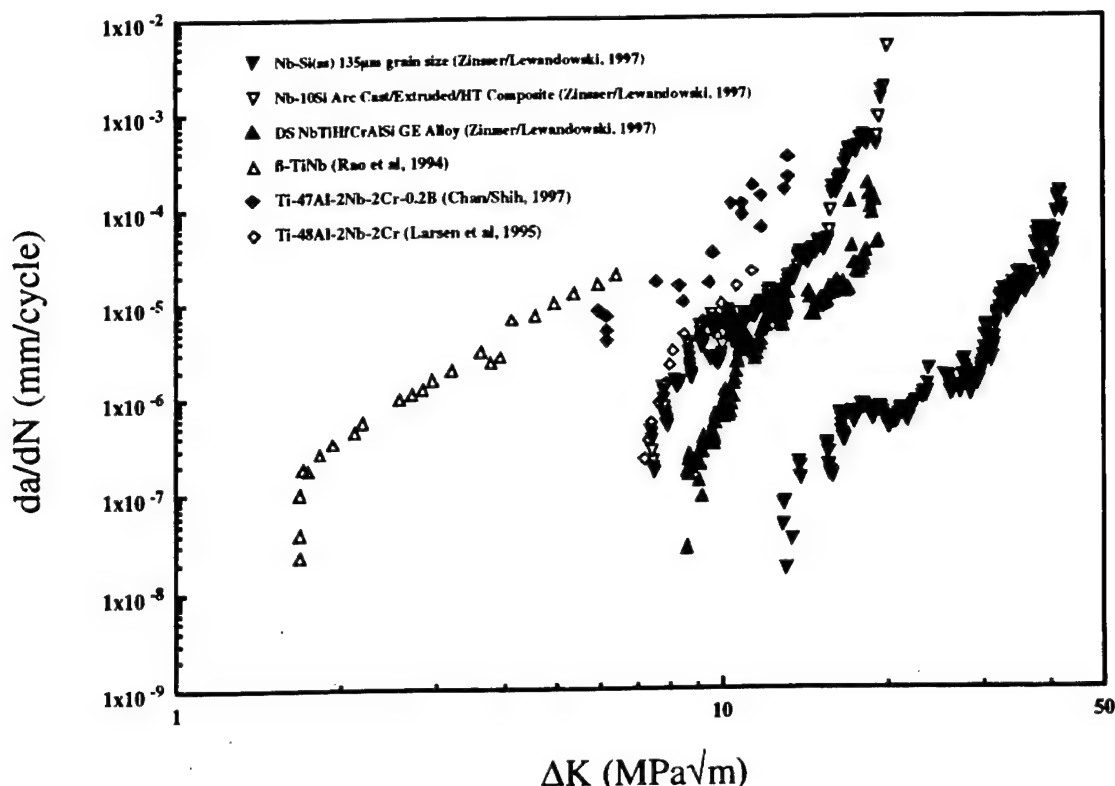


Figure 16 Fatigue crack growth data obtained at room temperature and an R ratio of 0.1 for a number of advanced monolithic and *in situ* composites containing intermetallic materials. The threshold values of Nb-silicide based composites are higher than for other intermetallic systems, and the Paris law coefficients are close to those of monolithic metallic systems.

above data also indicate that the Si concentration of the MASC can be increased to 18% without compromising composite toughness. This is an important observation because the Si concentration controls the volume fraction of silicide and therefore the elevated temperature strength and creep properties. It can also be seen from the fracture toughness data that increasing the Hf from 8% to 14%, or increasing the Cr concentration up to 10% leads to a reduction in toughness. The effect of Mo on fracture toughness is shown in Table 6. Models of ductile phase toughening can provide some insight into toughening mechanisms that are operative in this family of composites. However, they do not completely describe the toughening behavior that has been reported (Bewlay *et al.*, 1994b). In particular, the effect of volume fraction of metallic phase on composite toughness is only partially described by models for ductile phase toughening (Bewlay *et al.*, 1994b).

3.22.4.2 Fatigue Properties

There has been relatively little work on evaluation of the performance of RMICs under cyclic loading conditions (Zinsser and Lewan-

dowski, 1998; Bewlay *et al.*, 1997c). Early work (Rao *et al.*, 1993, 1994) on a variety of intermetallics extrinsically toughened with Nb alloys revealed that, while significant toughness improvements were obtained under monotonic loading conditions, these improvements were often not realized when testing under cyclic loading conditions. In several cases, the fatigue crack growth resistance of the composite showed little improvement over that of the brittle monolithic intermetallic, and the Paris law coefficients that were reported were similar to those of ceramics (Rao *et al.*, 1993, 1994).

The fatigue crack growth behaviors of extrinsically toughened niobium silicide *in situ* composites are more promising, as shown in Figure 16 (Bewlay *et al.*, 1997c; Zinsser and Lewandowski, 1998). Figure 16 shows fatigue crack growth data obtained for a range of RMICs including the cast/extruded Nb-10Si composite (Mendiratta *et al.*, 1991; Bewlay *et al.*, 1997c; Samant and Lewandowski, 1997), the DS MASC (Bewlay *et al.*, 1997c), monolithic cast/extruded Nb-1 Si alloy, and TiAl based intermetallics (Chan and Shih, 1997; Larsen *et al.*, 1995). Figure 16 indicates that the fatigue performance of monolithic Nb-1Si is significantly better than that of the

Table 7 Paris law exponents and fatigue thresholds of a range of Nb-silicide containing composites, and two monolithic Nb alloys.

Material/grain size	Condition	R	Fatigue threshold, ΔK_{th} (MPa \sqrt{m})	Paris law exponent	K_{Ic} (MPa \sqrt{m})
Pure Nb	Equiaxed grains (135 μm)	0.1	10.2	2.8	—
Nb-Si (ss)	Equiaxed grains (135 μm)		13.0	2.3	—
Nb-12Si	DS	0.1	13.2	16.7	18.1
Nb-18.2Si	DS	0.1	3.0	—	6.0
Nb-10Si	Arc cast/extruded/HT	0.1	8.0	5.3	22.3
Nb-10Si	Arc cast/extruded/HT	0.8	4.4	16.9	27.2
Nb-42.5Ti-15Si	DS	0.1	5.5	9.7	10.2
Nb-25Ti-8Hf- 2Cr-2Al-16Si	DS	0.1	8.5	2.9	24.2

Source: Bewlay, Lewandowski *et al.*, 1997c; Zinsser and Lewandowski, 1998.

Nb-silicide based composite (Rao *et al.*, 1994), and suggests that the good fatigue characteristics of the Nb in these systems dominates the composite creep performance due to (i) its intrinsic properties, (ii) its continuity, and (iii) its scale.

Zinsser and Lewandowski (1998) examined the effect of R ratio (0.1 and 0.4) on the room temperature fatigue crack growth behavior of a Nb-10 Si Nb-Nb₅Si₃ composite over a range of ΔK levels. The results were compared with fatigue crack growth behavior for a monolithic Nb-1.2 Si solid solution. Crack growth rates (da/dN) were measured in the range 10^{-2} – 10^{-7} mm cycle⁻¹ in the composite and 10^{-3} – 10^{-8} mm cycle⁻¹ in the Nb(Si). They reported fatigue thresholds ΔK_{th} in the range 5.6–12.9 MPa \sqrt{m} and Paris law slopes in the range 2–5. The ΔK_{th} was higher for the Nb-1 Si than the Nb-Nb₅Si₃ composite and the Paris law slopes were also higher for the Nb-1 Si (5.3 vs. 2.3), as shown in Table 7. In comparison, pure Nb exhibits threshold values for fatigue of ~ 10 MPa \sqrt{m} with Paris law slopes of 4–7; these are similar to those observed for other metallic materials.

Zinsser and Lewandowski (1998) also reported that increasing the R ratio reduces the observed threshold stress intensities, ΔK_{th} , in both the Nb-Nb₅Si₃ composite and the Nb(Si) solid solution. They reported a strong correlation between the amount of cleavage observed on the fracture surface and K_{max} . They proposed that the increase in the amount of cleaved primary Nb in the Nb-Nb₅Si₃ composite during fatigue crack growth was controlled by K_{max} .

3.22.4.2.1 Thermal fatigue

The envisioned applications of RMICs will subject the component to a variety of thermal

fatigue cycles. Although there has not been a significant amount of work to address the behavior of RMICs under thermal cycling conditions, the thermal expansion mismatch between the metal and the intermetallics over the envisioned application temperature range is relatively small (Jackson *et al.*, 1996; Bewlay *et al.*, 1997c; Buckman, 1980). Thus, it is expected that thermal ratcheting between the phases will be negligible, and the interface between composite phases will not suffer excess stress during thermal cycling.

3.22.4.3 High-temperature Strength

There is a limited amount of high-temperature tensile data available for RMICs. However, density-normalized bending strength-temperature data have been reported previously for Nb-42.5Ti-15Si, Nb-40Ti-15Si-5Al (Jackson *et al.*, 1996; Subramanian *et al.*, 1997), and binary Nb-10 Si composites (Mendiratta *et al.*, 1991). The tensile strength of the MASC is shown as a function of temperature in Figure 17. The tensile fracture stress was ~ 800 MPa at room temperature, and the yield stress was 370 MPa at 1200 °C. At room temperature no macroscopic ductility was measured in the tensile tests, but fractographic observations indicated plastic deformation of the metallic phase. Monolithic alloys of similar compositions to the metallic phase of the composite have yield strengths of less than 55 MPa at 1200 °C (Bewlay *et al.*, 1997c). Thus, the composite possesses substantially improved tensile properties. The MASC does possess some flaw sensitivity of the fracture stress at low temperatures. In comparison with monolithic intermetallics, the strength retention of this composite at high temperatures is impressive.

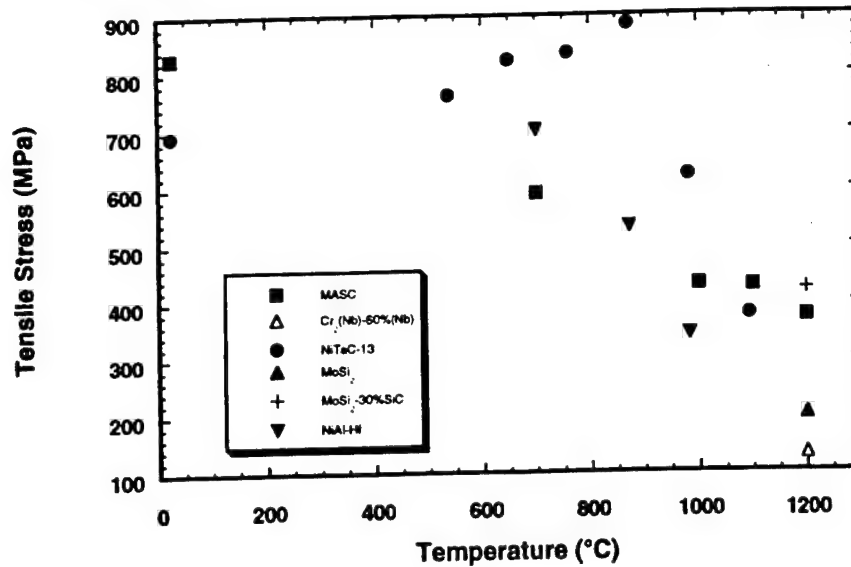


Figure 17 Tensile strength of a range of DS *in situ* composites as a function of temperature showing the improvement of high temperature strength over Nb-silicide based composites in comparison with Ni-based superalloys, NiTiC/COTAC eutectics, and Laves phase-based composite. Literature data for the tensile strength of NiAl modified with Hf, bending strengths of monolithic MoSi₂, and MoSi₂ reinforced with 30% SiC, are also shown (Bewlay *et al.*, 1997c).

The binary Nb-10 Si composite showed bending strength levels at 1200 °C similar to the tensile strengths of the MASC (370 MPa) (Bewlay *et al.*, 1997c). However, the reductions in the high temperature strength levels displayed in ternary Nb-Ti-Si and quaternary Nb-Ti-Si-Al are not experienced by the MASC. Details of the strengthening mechanism are the subject of further research. There are essentially two strengthening mechanisms available for the (Nb). Solid solution strengthening can be affected by the addition of refractory and high modulus elements, and dispersion strengthening can be generated using refractory MC carbides and/or nitrides (e.g., HfN, ZrN). Precipitation mechanisms have been described previously in this chapter, but to date the strength increment to the composite that they offer has not been investigated in detail. The effects of adding elements such as W, Ta, or Mo on solid solution strengthening, room temperature fracture toughness, and high temperature creep have been explored as described in this

chapter. The effect of dispersion strengthening of the (Nb) in these composites on room temperature fracture toughness has received less attention.

3.22.4.4 Tensile Creep Properties

In this section, the tensile creep behavior of the MASC will be described and then more detailed investigations of the creep behavior of these composites will be described.

The secondary tensile creep rates of the MASC are shown in Figure 18 together with those of a range of high temperature alloys, including PWA1480, Mo TZM, and monolithic commercial Nb-based alloys (B-66 and C129Y) at 1100 °C. Tensile creep data of the MASC are also shown in Table 8. The composite creep rates are more than an order of magnitude lower than those of B-66 and C129Y. The stress sensitivity of the creep rate of the MASC is lower than that of Mo TZM, but it is higher

Table 8 Tensile creep data (rupture life, secondary creep rates and strain to failure) of the MASC at 1000 and 1100 °C.

Temperature (°C)	Stress (MPa)	Rupture life (h)	Creep rate (s ⁻¹)	Elongation at failure, ϵ_f (%)
1100	140	35	1.7×10^{-7}	7
1100	105	554	9.3×10^{-9}	10.1
1000	175	171	2.9×10^{-8}	5.3

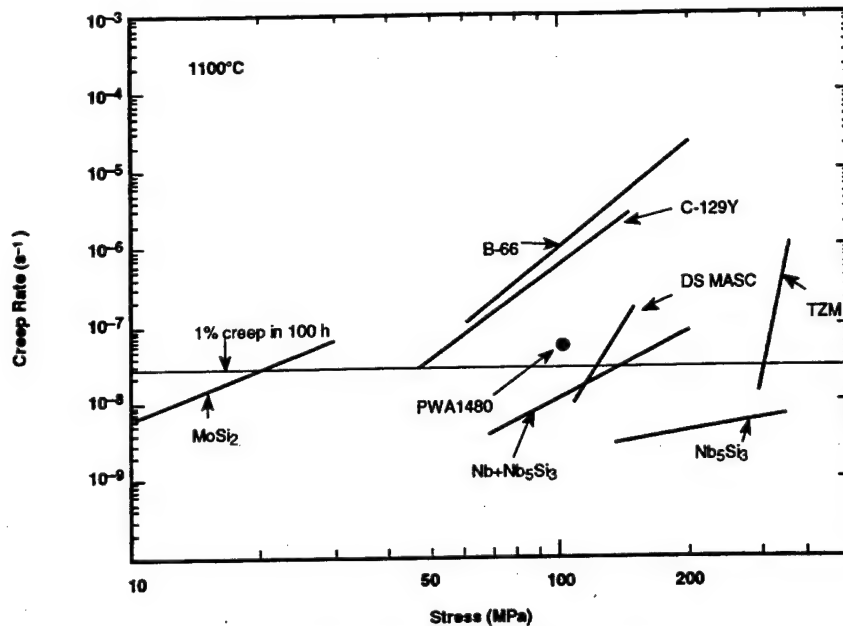


Figure 18 Comparison of secondary tensile creep rates of a DS Nb-silicide *in situ* composite with binary Nb₅Si₃, TzM, PWA1480, and monolithic Nb alloys.

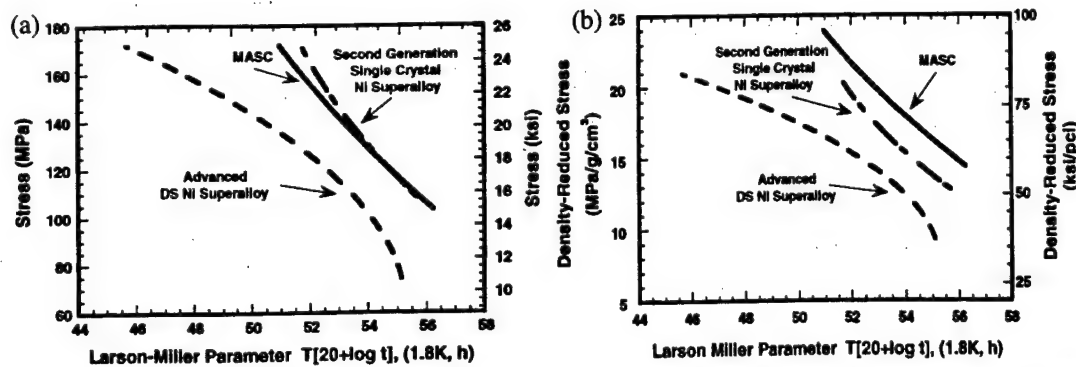


Figure 19 Stress rupture behavior of the DS MASC is compared to that of DS and SX Ni-based superalloys in Larson-Miller plots ($C = 20$) where the temperature-time parameter is plotted against (a) rupture stress and (b) rupture stress/material density.

than that of the compression data shown for the binary Nb-16 Si (Nb)-Nb₅Si₃.

The MASC creep rupture behavior is shown in the Larson-Miller plot in Figure 19(a). Data for an advanced DS Ni-based superalloy, and an advanced generation single-crystal (SX) Ni-based superalloy, are also shown (Bewlay *et al.*, 1997c). At 1100°C and 105 MPa the rupture life was greater than 500 h. Tensile stresses higher than 105 MPa led to shorter rupture times at either 1000 or 1100°C. At low stresses the behavior is similar to that of the SX alloy, but at high stresses it is slightly lower. The density-normalized stress rupture data for the MASC is also compared in Figure 19(b) with those data for the DS and SX Ni-based superalloys. To date, the only tensile stress rupture data that has been reported for RMICs is that of the

MASC. Figure 19(b) illustrates the increase in specific rupture performance that results from the substantial reduction in density of the MASC compared to the third-generation single-crystal superalloy.

The slopes of the Larson-Miller plots in Figure 19 appear to be lower than those of the CMSX alloys, and this may render the maximum operating stress of these materials lower than that of third generation superalloys. The rupture behavior that will be required for future applications will be well beyond any behavior observed thus far. Current estimates are that ultimately an 80-fold increase over current rupture lives may be required for application of the silicide-based composites (Jackson *et al.*, 1996). In summary, the stress rupture behavior of the MASC is similar to that of

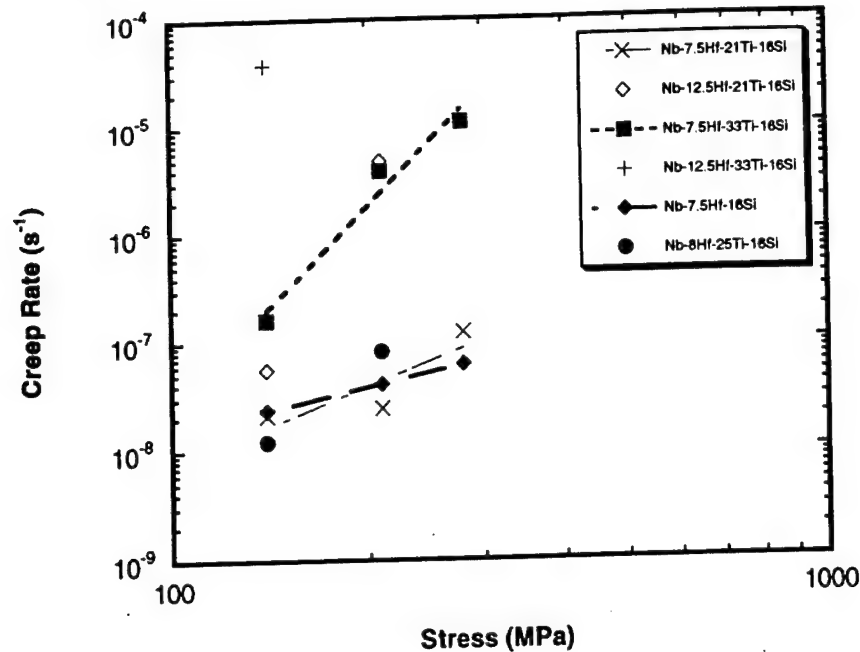


Figure 20 Graph of secondary creep rates at 1200 °C and stresses of 70–280 MPa for a range of quaternary Nb–Hf–Ti–Si alloys.

advanced single crystal Ni-based superalloys and thus, after accounting for the lower density of the MASC, the creep behavior offers great potential.

3.22.4.5 Compression Creep Studies

In order to achieve increases in the creep performance of these niobium silicide based *in situ* composites beyond the present capability, more fundamental investigations of the effects of alloying additions, such as Hf, Ti, Cr, Al, and Mo have been performed (Subramanian *et al.*, 1995; Henshall *et al.*, 1995; Bewlay *et al.*, 1998). These effects will be described in the following sections. Previous work on monolithic Nb₅Si₃ suggests that creep deformation in Nb₅Si₃ is controlled by diffusion of Nb in the Nb₅Si₃ phase (Subramanian *et al.*, 1995). Creep of composites is controlled by a combined function of creep in the silicide and metallic phases. Thus, elements such as Mo and Hf, that have a

large atomic size, may be effective in improving the intrinsic creep performance of the silicide and, therefore, the composite. Parametric modeling has indicated that the creep properties of these composites are insensitive to volume fraction of metallic phase (Henshall *et al.*, 1995); this has yet to be investigated experimentally.

3.22.4.5.1 Nb–Ti–Hf–Si composites

Secondary creep rates are shown in Figure 20 for a series of quaternary DS Nb–Hf–Ti–Si alloys at a temperature of 1200 °C and at stress levels in the range 140–280 MPa. These data are also shown in Table 9, together with data for the DS Nb–16 Si and the Nb–7.5 Hf–16 Si ternary alloys. Hf concentrations in the range 7.5–12.5 and Ti concentrations in the range 21–33 were examined, providing Ti:Hf ratios in the range 1.7–4.4. The microstructures of these composites are similar to those shown in Figure 4.

Table 9 Secondary creep rates at 1200 °C and stresses from 140–280 MPa for a range of Nb–Hf–Ti–Si alloys.

Composition	Constituent phases	140 MPa Creep rate (s ⁻¹)	210 MPa Creep rate (s ⁻¹)	280 MPa Creep rate (s ⁻¹)
Nb–7.5Hf–16Si	(Nb), Nb ₃ Si	2.3×10^{-8}	4.0×10^{-8}	4.8×10^{-8}
Nb–7.5Hf–21Ti–16Si	(Nb), Nb ₃ Si	2.1×10^{-8}	3.2×10^{-8}	1.2×10^{-7}
Nb–7.5Hf–33Ti–16Si	(Nb), Nb ₃ Si, (Ti,Hf) ₅ Si ₃	1.6×10^{-7}	3.9×10^{-6}	1.1×10^{-5}
Nb–12.5Hf–21Ti–16Si	(Nb), Nb ₃ Si, (Ti,Hf) ₅ Si ₃	5.5×10^{-8}	4.8×10^{-6}	Failed
Nb–12.5Hf–33Ti–16Si	(Nb), Nb ₃ Si, (Ti,Hf) ₅ Si ₃	3.8×10^{-5}	Failed	–

Table 10 Secondary creep rates at 1100 °C and stresses from 70–280 MPa for a range of Nb–Hf–Ti–Si alloys modified with Mo.

Composition	70 MPa Creep rate (s^{-1})	140 MPa Creep rate (s^{-1})	210 MPa Creep rate (s^{-1})	280 MPa Creep rate (s^{-1})
Nb–8Hf–25Ti–16Si	1.6×10^{-9}	2.0×10^{-9}	–	2.9×10^{-9}
Nb–3Mo–8Hf–21Ti–16Si	5.2×10^{-9}	1.2×10^{-8}	1.3×10^{-8}	1.4×10^{-8}
Nb–9Mo–8Hf–21Ti–16Si	–	2.0×10^{-9}	1.4×10^{-8}	6.0×10^{-8}
Nb–8Hf–25Ti–2Al–2Cr–16Si	1.2×10^{-8}	5.0×10^{-8}	1.0×10^{-6}	Fail

Table 11 Secondary creep rates at 1200 °C and stresses from 70–280 MPa for a range of Nb–Hf–Ti–Si alloys modified with Mo.

Composition	70 MPa Creep rate (s^{-1})	140 MPa Creep rate (s^{-1})	210 MPa Creep rate (s^{-1})	280 MPa Creep rate (s^{-1})
Nb–7.5Hf–16Si	–	2.3×10^{-8}	4.0×10^{-8}	4.8×10^{-8}
Nb–8Hf–25Ti–16Si	6.3×10^{-9}	1.2×10^{-8}	8.0×10^{-8}	Fail
Nb–3Mo–8Hf–21Ti–16Si	1.4×10^{-8}	2.5×10^{-8}	6.4×10^{-8}	Fail
Nb–9Mo–8Hf–21Ti–16Si	2.6×10^{-8}	2.2×10^{-7}	4.5×10^{-6}	Fail
Nb–8Hf–25Ti–2Al–2Cr–16Si	9.1×10^{-8}	Fail	–	–
Nb–16Si	1.7×10^{-9}	1.5×10^{-8}	4.9×10^{-8}	–

The creep data indicate that the Nb–7.5 Hf–16 Si and the Nb–16Si composites possessed the lowest creep rates, and that at any selected stress level and Hf concentration the creep rate increased with increasing Ti concentration. Clearly, Ti and Hf additions can have a significant effect on the creep performance. For example, at 7.5 Hf increasing the Ti concentration from 21% to 33% increased the creep rate from $2.1 \times 10^{-8} s^{-1}$ to $1.6 \times 10^{-7} s^{-1}$ at 140 MPa. At stress levels of 210 MPa and below there is little difference between the secondary creep rates of the Nb–16 Si, the Nb–7.5 Hf–16 Si, and the Nb–7.5 Hf–21 Ti–16 Si compositions. At higher stress levels, the Ti additions have a detrimental effect on creep performance. Similarly, at Hf concentrations of 12.5 and stress levels of 140 MPa, increasing the Ti concentration from 21% to 33% increases the creep rate from $5.5 \times 10^{-8} s^{-1}$ to $3.8 \times 10^{-5} s^{-1}$. At higher stress levels the effect of increasing the Ti concentration led to premature failure; under these conditions the composites could not support steady-state creep, and they proceeded rapidly from the primary to the tertiary creep regime, and failed prematurely.

At any selected stress level, increasing the Hf concentration leads to an increase in the creep rate. For example, at a stress level of 140 MPa and Ti concentration of 21%, increasing the Hf concentration from 7.5% to 12.5% increases the creep rate from $2.1 \times 10^{-8} s^{-1}$ to $5.5 \times 10^{-8} s^{-1}$, but there is a strong stress sensitivity of this effect, so that at 210 MPa the creep rates are $3.2 \times 10^{-8} s^{-1}$ and $4.8 \times 10^{-6} s^{-1}$, i.e., Hf

concentrations higher than 7.5% provide a strong sensitivity of the secondary creep rate to stress. However, the creep rates of the Nb–7.5 Hf–21 Ti–16 Si are similar to those of the Nb–7.5 Hf–16 Si, and the stress sensitivity of the creep rates are also similar.

These creep data suggest that the Ti:Hf ratio should be maintained at a level less than 3 and the Ti concentration should be kept below 21%. The mechanisms that lead to increased creep rates at higher Ti, higher Hf, or higher (Hf + Ti) concentrations are still under investigation. One of the effects that is significant is that at high (Ti + Hf) concentrations the hP16 Ti_5Si_3 type silicide is stabilized in preference to the tI32 Nb_5Si_3 type or tP32 Nb_3Si type silicides (Bewlay *et al.*, 1995b; Sutliff and Bewlay, 1998). The Nb_5Si_3 has a higher melting temperature than either the Ti_5Si_3 or the Hf_5Si_3 , and thus it probably contributes to the improved creep resistance.

3.22.4.5.2 Mo-modified composites

Secondary creep rates are shown in Table 10 and 11 and Figure 21 for temperatures of 1100 °C and 1200 °C for the baseline Nb–8Hf–25Ti–16Si, as well as alloys containing 3% and 9% Mo (substituting Mo for Nb). The microstructures of the Mo-modified composites are similar to those in Figure 4 at low Mo concentrations (up to 3%), but at higher Mo concentrations the microstructures are similar to that shown in Figure 5.

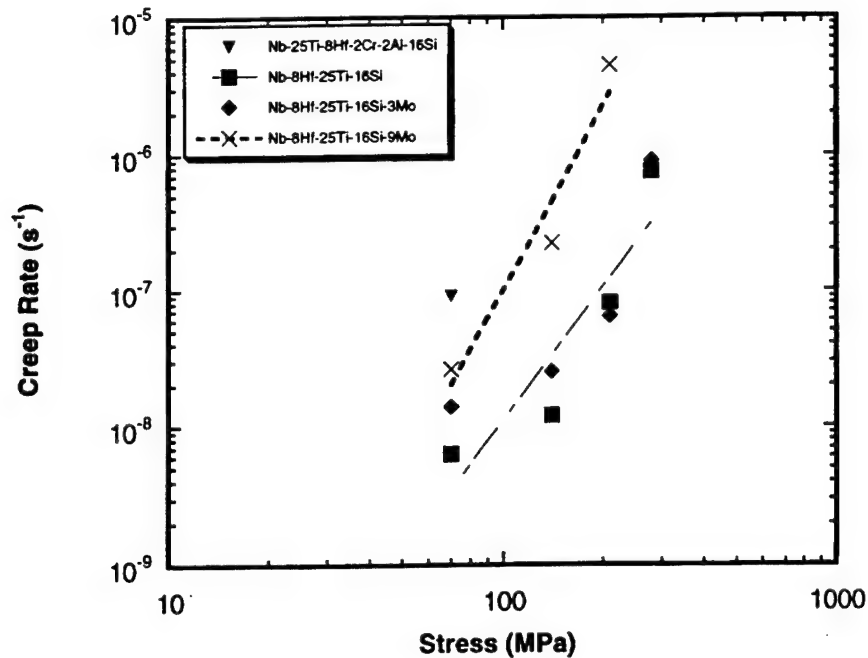


Figure 21 Graph of secondary creep rates at 1200 °C and stresses of 70–280 MPa for a range of Nb–Hf–Ti–Si alloys modified with Mo.

It can be seen that the performance of the Nb–7.5 Hf–16 Si and the Nb–8 Hf–25 Ti–16 Si are similar to the Nb–16Si, but at Mo concentrations greater than 3% the creep rates are increased for temperatures of both 1100 and 1200 °C. In comparison with the Nb–8 Hf–25 Ti–2 Cr–2 Al–16 Si, the Mo additions have a less detrimental effect on the creep rate than the Cr and Al additions. However, unlike the Mo additions, the Cr and Al additions are required for oxidation resistance (they also appear to provide some toughening). It appears therefore that there is no major benefit associated with substitution of Mo for Nb, even though Mo additions may also increase the strength of the (Nb). However, it is not clear why the substitution of Mo for Nb leads to an increase in the creep rate. Mo may stabilize the Nb₃Si phase in preference to Nb₅Si₃, and it may also lead to an increase in the volume fraction of the metallic

phase. Both of these effects could have a detrimental effect on creep performance.

3.22.4.5.3 Higher Order Alloy Composites

Starting with the MASC as the baseline composition, the effects of increasing Hf, Ti, and Cr (substituting for Nb) have been examined. Secondary creep rates are shown at 1200 °C and stress levels in the range 70–280 MPa in Table 12 and Figure 22 for a range of composites.

Figure 22 shows three effects. First, the creep rate increased with increasing Ti concentration from 20% to 30%. This may have been due in part to the larger volume fraction of Hf₅Si₃ type phase in the composite, as well as the lower melting temperature of the metallic phase. Second, increasing the Si concentration from 16%

Table 12 Secondary creep rates at 1200 °C and stresses from 70 to 280 MPa for a range of Nb–Hf–Ti–Si–Cr–Al alloys.

Composition	70 MPa Creep rate (s ⁻¹)	140 MPa Creep rate (s ⁻¹)	210 MPa Creep rate (s ⁻¹)	280 MPa Creep rate (s ⁻¹)
Nb–7.5Hf–16Si	–	2.3×10^{-8}	4.0×10^{-8}	4.8×10^{-8}
Nb–8Hf–20Ti–2Al–2Cr–16Si	1.1×10^{-7}	5.0×10^{-7}	2.7×10^{-6}	Fail
Nb–8Hf–30Ti–2Al–2Cr–16Si	2.4×10^{-6}	Fail	–	–
Nb–11Hf–25Ti–2Al–2Cr–16Si	2.2×10^{-6}	Fail	–	–
Nb–8Hf–24Ti–2Al–2Cr–16Si	7.6×10^{-7}	Fail	–	–
Nb–8Hf–24Ti–2Al–2Cr–18Si	4.7×10^{-7}	Fail	–	–
Nb–16Si	1.7×10^{-9}	1.5×10^{-8}	4.9×10^{-8}	–

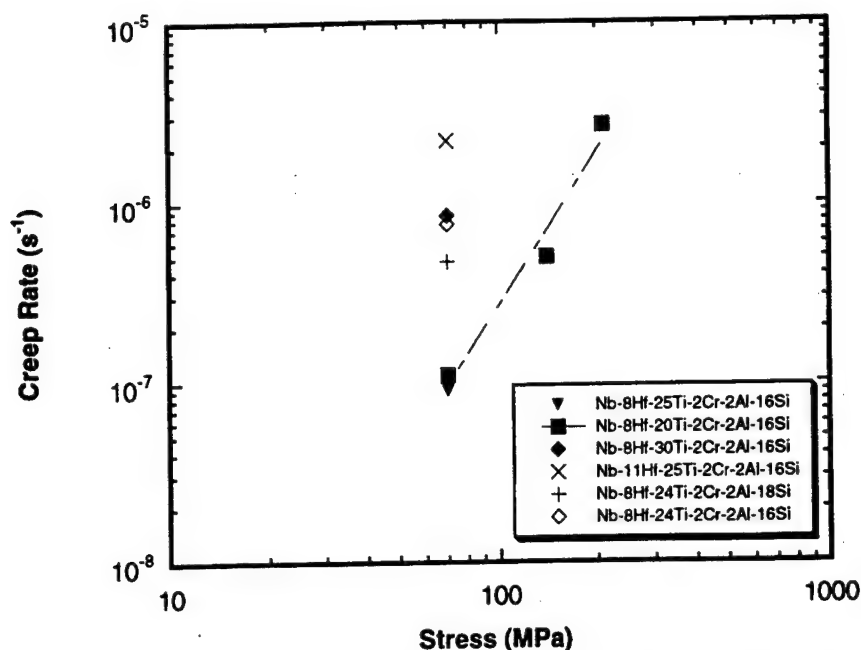


Figure 22 Graph of secondary creep rates at 1200 °C for a range of Nb-Hf-Ti-Si-Cr-Al alloys. All alloys except the low Ti alloy failed rapidly at stresses greater than 70 MPa and the creep rates could not be determined.

to 18% (substituting Si for Nb) led to a slight reduction of creep rate at 1200 °C and 70 MPa from $7.6 \times 10^{-7} \text{ s}^{-1}$ to $4.7 \times 10^{-7} \text{ s}^{-1}$. Third, substituting Hf for Nb appears to have a detrimental effect on the secondary creep rate; increasing the Hf concentration from 8% to 11% led to a change in the creep rate from $7.6 \times 10^{-7} \text{ s}^{-1}$ to $2.2 \times 10^{-6} \text{ s}^{-1}$ at 70 MPa and 1200 °C. This was probably due to the increase in the volume fraction of the Hf_5Si_3 type silicide. It appears that all the six element alloys have creep rates at 1200 °C that are at least an order of magnitude higher than those of the composite generated from the binary Nb-16Si alloy.

These observations regarding the effects of Ti and Hf in these complex alloy composites are all consistent with those that were reported for the quaternary Nb-Hf-Ti-Si alloys. The creep rates of these composites at 1100 °C are acceptable, but at 1200 °C the creep rates are lower than the goals. Further optimization of alloy composition, microstructure, and texture is required to reduce composite creep rates.

Subramanian *et al.* (1995) have also examined compression creep behavior at 1100 °C and 1200 °C for stress levels of 70–210 MPa for a range of complex composites similar to the MASC. They considered MASC type composites modified with up to 10Ta, 5Ge, and 14Cr. In general the secondary creep rates were slightly higher than those of the MASC (which was similar to that of the composite from the Nb-10Si alloy).

The creep exponents for the Nb-7.5 Hf-16 Si and the Nb-8 Hf-25 Ti-16 Si were ~ 1 and ~ 2 , respectively. At higher Hf and/or Ti concentrations the exponents were increased substantially. For the Nb-3 Mo-8 Hf-25 Ti-16 Si the creep exponent was ~ 1 but at 9Mo the exponent was ~ 5 . These data suggest that at higher alloying levels the creep rate is controlled less by the behavior of the monolithic silicide for which the creep exponent is ~ 1 (Subramanian *et al.*, 1995).

In summary, the fundamental studies on quaternary Nb-Hf-Ti-Si alloys and those on higher order alloys indicate that the addition of Ti, Hf, and Mo have a substantial effect on composite secondary creep rates. The threshold Hf, Ti, and Mo concentrations above which the creep performance degenerates beyond that of the Nb-16 Si composite have been defined, together with the appropriate stress levels for possible component operations. For example, the data indicate that the creep performance of the Nb-8Hf-25Ti-16Si is compatible with the creep goals at temperatures up to 1200 °C.

3.22.4.6 Physical and Thermal Properties

There has been relatively little work on investigating the elastic moduli of this family of composite materials. However, dynamic elastic moduli at room temperature, and at temperatures up to 1200 °C have been reported by Bewlay *et al.* (1996) for the MASC. The

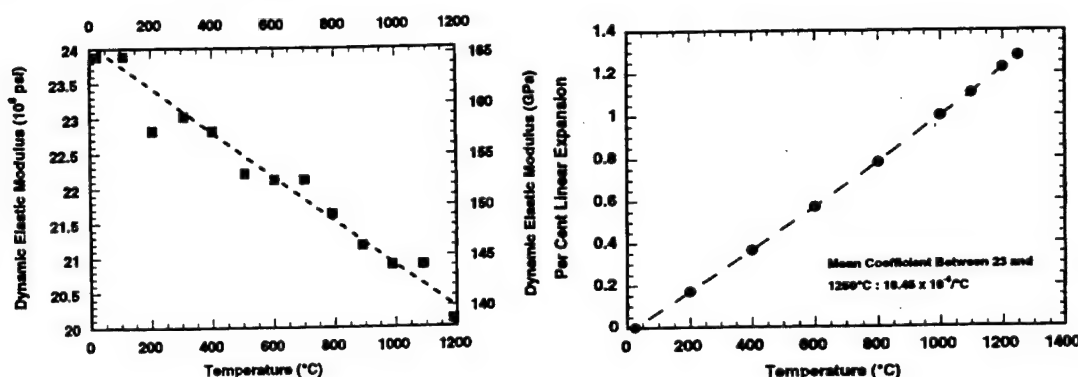


Figure 23 (a) The modulus of the MASC from room temperature to 1250°C; the modulus decreased approximately linearly with increasing temperature to 140 GPa at 1200°C, (b) The total expansion from room temperature to 1250°C of the MASC; the thermal expansion of the MASC is approximately linear over this temperature range with a coefficient of $10.45 \times 10^{-6} \text{ } ^\circ\text{C}^{-1}$.

modulus at room temperature was 165 GPa and it decreased approximately linearly with increasing temperature to 140 GPa at 1200°C, as shown in Figure 23(a). In comparison, monolithic Nb_5Si_3 has been reported to have a modulus of 170–210 GPa at room temperature (Bewlay *et al.*, 1996). Thus, the modulus of 140 GPa for the composite at 1200°C is very promising. Typical modulus values for a third generation Ni based superalloy at 1100°C are 75–83 GPa in the $\langle 001 \rangle$ and 210 GPa in the $\langle 111 \rangle$. Although the specific modulus of the MASC at 1200°C is probably greater than that of Ni-based superalloys, the anisotropy of the composite modulus needs to be investigated in further detail. There has been little work on thermal diffusivity.

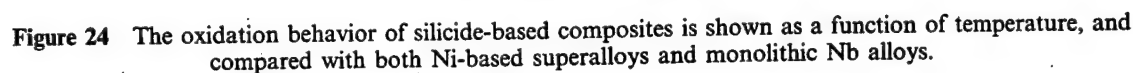
The total expansion of the MASC to 1250°C is shown in Figure 23(b). The thermal expansion of the MASC is approximately linear over this temperature range with a coefficient of $10.45 \times 10^{-6} \text{ } ^\circ\text{C}^{-1}$. Previously, monolithic binary Nb_5Si_3 and ternary $(\text{Nb,Ti})_5\text{Si}_3$ silicides were reported to have expansion coefficients of $\sim 9.0 \times 10^{-6} \text{ } ^\circ\text{C}^{-1}$ over this temperature range (Jackson *et al.*, 1994). Typically, the thermal expansion of a monolithic alloy of a similar composition to the metallic phase of this composite is $\sim 9.4 \times 10^{-6} \text{ } ^\circ\text{C}^{-1}$. These results suggest that the expansion mismatch between the metal and the silicides over this temperature range is relatively small. Thus, it is expected that the thermal ratcheting between the phases will be negligible, and the interface between composite phases will not experience excess stress during thermal cycling.

3.22.4.7 Oxidation Behavior

Unfortunately, the composites from binary Nb–Si alloys have very poor oxidation resis-

tance, as shown in Figure 24. The oxidation resistance at 1200 and 1300°C of silicide based composites toughened with (Nb) is substantially improved over that of binary (Nb)– Nb_5Si_3 composites by additions such as Ti, Hf, Al, and Cr (Subramanian *et al.*, 1996; Jackson *et al.*, 1996), as shown in Figure 24. External and internal oxidation are the two principal concerns. With regard to external and internal oxidation, additions of Hf are also used to reduce oxygen solubility and diffusivity and thereby slow embrittlement at elevated temperatures resulting from internal oxidation and oxygen dissolution (Subramanian *et al.*, 1996; Jackson *et al.*, 1996; Wlodek, 1961).

A comparison of oxidation performance for the DS MASC and Ni-based superalloys is shown in Figure 24 (Bewlay *et al.*, 1996). The DS MASC shows material losses at rates intermediate between the rapid losses of an older superalloy like IN 738, and the improved oxidation behavior of third-generation single crystal superalloys. Subramanian *et al.* (1996, 1997) have reported similar oxidation performance. The dashed lines in Figure 24 indicate the goal behavior where component surface temperatures may be 1315°C. This goal is derived from current superalloy capability. If superalloys can survive with surface temperatures of 1150°C, then the rate of metal loss for the best superalloys at that temperature, $\sim 25 \mu\text{m}/100 \text{ h}$, is a reasonable goal for the refractory metal *in situ* composites at their anticipated maximum surface temperature. These oxidation data at 1200°C show a substantial improvement over that of binary (Nb)– Nb_5Si_3 composites (Jackson *et al.*, 1996, but the oxidation resistance of this composite requires further improvement. Pesting behavior (oxidation resistance dependent on stress and the defect content of the test sample, particularly at intermediate temperatures) does not appear to be a major problem



A study has been performed to examine the response of oxidation resistance at 1200°C (2200 F) and 1315°C (2400 F) to several variables, including the volume fractions of each phase, and the bulk Ti and Hf concentrations (Jackson *et al.*, 1994). A range of additions was investigated, including Al, B, Ge, W, Mo, and V, and the following trends were observed: increasing the volume fraction of (Nb) leads to a reduction in the oxidation resistance.

Boron has been shown to improve the oxidation resistance of a number of monolithic silicides (Thom *et al.*, 1993, 1994), such as Mo_5Si_3 and Ti_5Si_3 compounds, as first reported by Thom *et al.* (1994) and Akinc and co-workers (Thom *et al.*, 1993). Boron additions of 6% have also been found to improve oxidation of the Nb-silicide based composites. B can occupy interstitial sites in the M_5Si_3 lattice (where $\text{M} = \text{Mo}, \text{Ti}, \text{Nb}, \text{Cr}$, etc), up to a solubility limit that varies depending on the alloying elements, but it can approach 11% B. B acts to improve oxidation behavior, possibly by

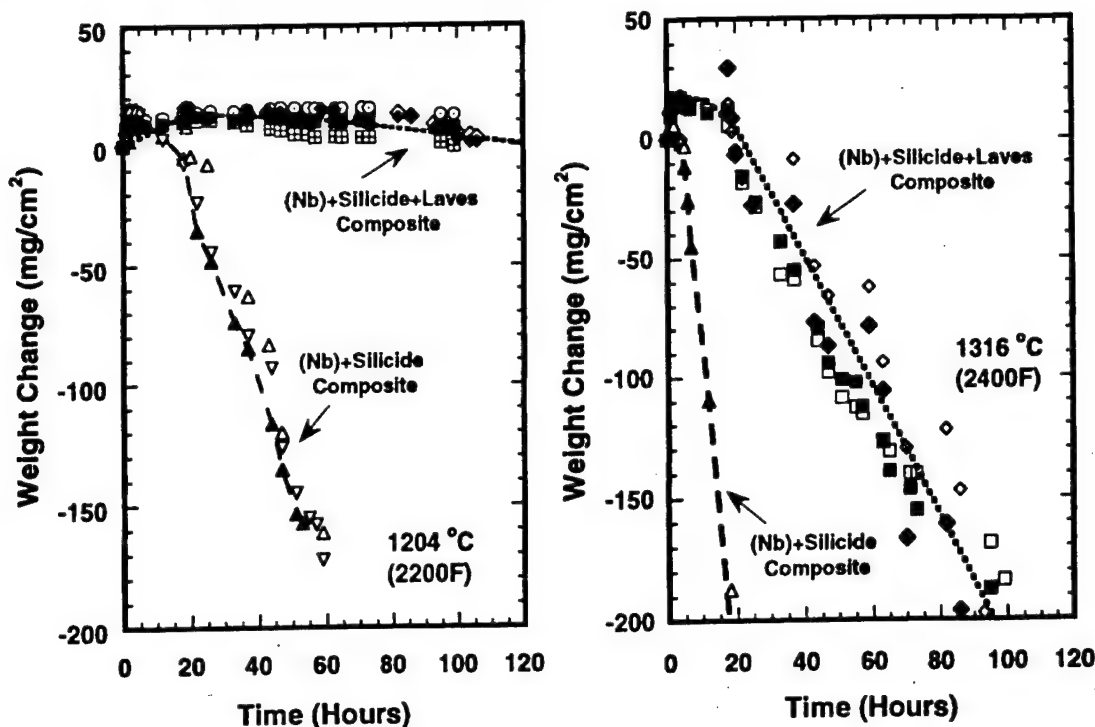


Figure 25 Comparison of 2200 F and 2400 F oxidation resistance of Nb-18Ti-7Hf-20Cr-2Al-18Si to the MASC behavior. Data (a) for four samples of baseline composition and four of the Laves phase modified alloy at 2200 F, (b) two samples of baseline composition and four of the Laves phase modified alloy at 2400 F.

changing kinetics of silica formation, affecting the viscosity of the oxide through glass-like formation, or by simply offering up additional atomic species available for oxidation as a stable scale. Additions of 6% B can reduce spallation. Bulk B concentrations of 3% and less have little effect on the oxidation performance. Solubilities of B and C in M_5Si_3 can extend almost to Nowotny-type M_5Si_3B and M_5Si_3C . However, in the (Nb,Ti,Hf) $_5Si_3$ system, B concentrations in M_5Si_3 in equilibrium with the (Nb) and the Laves are generally very low (<1%). B additions can also lead to stabilization of the T2 and M_5B_2Si type phases. Ge additions to SiO_2 increase the expansion behavior of that oxide to near-equality with expansion of Nb-base refractory alloys and they may therefore offer potential. Germanium additions of up to 4% have also been examined, but at this level they did not have a beneficial effect on oxidation resistance. The effect of strengthening elements, such as W, Mo, V, Ta, and Zr on oxidation was also examined. W, Mo, and V had a highly detrimental effect on the oxidation resistance. Ta and Zr also had a detrimental effect but it was not as severe as for W, Mo, and V.

These oxidation data have been characterized by regression analyses for major element effects (Nb, Ti, Hf, Cr, Si, and Al), and by direct comparison for other addition elements (B, Ge, Ta, Zr, Mo, W, and V) (Jackson and

Bewlay, 1998). No systematic difference was observed for data sets of samples that were cycled every hour vs. those that were exposed isothermally overnight and cyclically during the day. The following trends were observed:

(i) Analysis of the effect of the major alloying elements on weight loss showed that Cr and Si are the most beneficial, with Al increasing in importance as oxidation temperature increased. It appeared that there was a negative impact of Hf on oxidation, particularly at 2400 F, this was unexpected and contrary to previous reports (Jackson *et al.*, 1994, 1996). No significant elemental-interaction effects were observed.

(ii) The analysis of volume fraction effects showed that reducing the volume fraction of (Nb) increased the oxidation resistance. There is an optimum balance between Laves volume fraction and silicide volume fraction, for a given (Nb) volume fraction. Higher nominal-Ti silicide phases tend to reduce oxidation loss.

(iii) Studies of the effects of B, Ge, and refractory element additions indicate: (a) boron, especially at levels > 3a/o, offers a benefit to the oxidation performance of the composite; (b) Ge as a partial Si replacement does not benefit oxidation due to the absence of a continuous protective silica layer; and (c) Ta and Zr are the strengthening elements that are most likely to help balance oxidation and strength.

A regression analysis of the 2200 F/100 h weight change data was performed for the elements Ti, Hf, Cr, Si, and Al, using only linear effects, because the statistical evaluation of the interaction plots indicated that there were not any strong interaction pairs. The mass loss per unit area can be described by an equation of the form:

$$\Delta \text{wt}/A|_{1200\text{C}} = -491 + 7.54X_{\text{Ti}} + 7.40X_{\text{Cr}} + 10.6X_{\text{Si}} - 0.04X_{\text{Hf}} + 4.16X_{\text{Al}} \text{ (in mg cm}^{-2}\text{)}$$

where the mass loss per unit area is in mg cm^{-2} and the compositions are in atom percent. The coefficients from the individual compositions indicate that all elements except Hf have a significant effect on the mass loss. Thus, if the data are re-analyzed without Hf, the equation is essentially unchanged.

A regression analysis of the 2400 F/100 h weight change data was performed for the elements Ti, Hf, Cr, Si, and Al, using only linear effects, providing the following equation:

$$\Delta \text{wt}/A|_{1315\text{C}} = -1940 + 23.5X_{\text{Ti}} + 30.1X_{\text{Cr}} + 33.6X_{\text{Si}} - 9.3X_{\text{Hf}} + 33.8X_{\text{Al}} \text{ (in mg cm}^{-2}\text{)}$$

The coefficients of the individual compositions indicate significance for all terms but Ti and Hf. For the range of values selected, Cr, Al, and Si are most important in determining weight change at 2400 F, while Ti has a smaller positive benefit than at 2200 F and Hf has a larger negative effect than at 2200 F. In Nb-based alloys, it has been reported previously that Hf has a beneficial effect on oxidation rate, and also a strong positive effect on reducing the depth of internal oxidation.

The key issue with regard to Laves phase additions is whether or not the balance of high and low temperature mechanical properties can be maintained with these relatively high volume fractions of Laves phase. The previous oxidation studies suggest that a minimum volume fraction of Laves phase is required in order to provide the composite with adequate oxidation resistance. Although oxidation behavior of those alloys was substantially better than binary Nb-Si composites, they do not quite meet the oxidation goal of $25 \mu\text{m}$ lost in 100 h. The major-element analyses suggest that a good baseline chemistry for further improvement in oxidation resistance can be achieved and be balanced against fracture toughness by concentrating on Cr, Si, and Al concentrations, maintaining Ti and Hf levels for their effects on toughness, density, and internal oxidation.

Even if the goal of $<25 \mu\text{m}$ loss/100 h at 1315°C is met, the RMICs will need protective

coatings, just as do today's superalloys. The role of RMIC coatings has therefore also been considered previously (Jackson *et al.*, 1996; Subramanian *et al.*, 1997; Cockeram, 1994; Cockeram and Rapp, 1997). Pack-siliciding of the DS MASC has been reported to provide a further improvement in the oxidation behavior (Jackson *et al.*, 1996). In addition, considerable research has also been performed on Mo-based silicide coatings alloyed with W, B, and Ge (Jackson *et al.*, 1996; Cockeram, 1994; Cockeram and Rapp, 1997), that have shown potential for providing protection to 1400°C . A likely coating goal for Nb-based RMICs is therefore $\sim 10 \mu\text{m}$ loss/100 h in 1315°C oxidation, extrapolating the behavior for coatings on superalloys at 1150°C .

3.22.5 APPLICATIONS/ENGINE MATERIALS ENVIRONMENT

High-pressure turbine blade temperatures have increased by 125°C since the 1960s as a result of both controlled solidification to form single crystal Ni-based superalloy components, and the use of substantial additions of Re, W, Ta, and Mo. The Nb-based RMICs (Subramanian *et al.*, 1996, 1997; Jackson *et al.*, 1996) have much higher potential application temperatures, because of their dramatically increased melting temperatures. The estimated maximum temperature capability is $\sim 200^\circ\text{C}$ higher than that of current single crystal superalloys. Designs using these RMICs will result in service at much higher bulk and surface temperatures than can be achieved with superalloys (Jackson *et al.*, 1996).

Goals for these RMICs are summarized in Table 13. The density goal for the RMICs is $<7 \text{ g cm}^{-3}$ (25% lower than for third-generation single crystal superalloys $\sim 9.1 \text{ g cm}^{-3}$) (Jackson *et al.*, 1996); a density of 7.35 g cm^{-3} has already been demonstrated for the MASC (Bewlay *et al.*, 1996). Other composites of this family are reported to have densities as low as 6.5 g cm^{-3} (Subramanian *et al.*, 1997). The toughness goal for these materials is $>20 \text{ MPa } \sqrt{\text{m}}$, together with stable crack growth behavior.

The goal for creep performance is 1% in 100 h. If there is minimal primary creep this corresponds to a secondary creep rate of $3 \times 10^{-8} \text{ s}^{-1}$. This has been demonstrated in binary Nb-Si, ternary Nb-Ti-Si, and quaternary Nb-Ti-Hf-Si composites, but not in higher order systems. However, anisotropy of creep properties has not been examined and requires further consideration. In addition, although the

Table 13 Property goals and present capability for Nb-silicide based composites.

	Property goal	Present capability
Density	$< 7.0 \text{ g cm}^{-3}$	7.3 g cm^{-3}
1400°C phase stability	Total stability	Demonstrated in silicide-based composites
RT fracture toughness	$> 20 \text{ MPa}\sqrt{\text{m}}$	$> 20 \text{ MPa}\sqrt{\text{m}}$
Fatigue-Paris law slope	< 5	2-5
ΔK_{th}	$> 10 \text{ MPa}\sqrt{\text{m}}$	6-13 $\text{MPa}\sqrt{\text{m}}$
Creep rupture	100 F improvement	Similar to CMSX10
Creep rate (s^{-1}) at 1200°C	3×10^{-8}	1.2×10^{-8} : Nb-8Hf-25Ti-16Si (140 MPa) 1.5×10^{-8} : Nb-16Si (140 MPa)
Oxidation	$\sim 25 \mu\text{m}/100 \text{ h}$	$\sim 250 \mu\text{m}/100 \text{ h}$

effect of volume fraction of (Nb) on toughness has been well defined (Bewlay *et al.*, 1995a; Henshall *et al.*, 1997), the effect of volume fraction (Nb) on creep performance is less well understood.

Although solid components are attractive for early engine testing of the RMICs, due to the simplicity of machining from stock to final part, applications in hollow parts will take greatest advantage of the RMIC high temperature capability. The cooling techniques presently used for precision-cast Ni-based superalloy single crystals will be required for RMICs in order to achieve their potential 200°C gains. At present there is little experience in using RMICs in conjunction with advanced airfoil cooling schemes.

Joining methods can be used to produce hollow, cooled components in order to exploit the potential of selecting the optimum processing method for different parts of the turbine component. For example, an EB-PVD airfoil wall could be joined to an extruded turbine blade spar or root. This hybrid structure can tailor the chemistry and microstructure to optimize properties in the different regions of the component, and it can also take advantage of process economics for thin-wall vs. thick-section regions of the component. The economics of the processes and the optimization of properties will decide which is ultimately the optimum method for airfoil manufacture.

Hollow RMIC airfoils will require both internal and external coatings to prevent loss of material by oxidation/corrosion, and to avoid embrittlement and subsequent reduction in fracture toughness. Although coating systems have been developed which resist oxidation at temperatures as high as 1400°C (Jackson *et al.*, 1996; Cockeram, 1994; Cockeram and Rapp, 1996), defects in the coating or foreign object damage of the coating can result in localized coating failure, and rapid catastrophic attack of the underlying substrate. Chemical vapor deposition (CVD), PVD, thermal spray, plating, and slurry coating are all processes that may

find application for forming protective coatings on RMICs. It may be possible to deposit internal coatings before joining sections of the hollow structures. For PVD processed sections of components, EB-PVD coating may become integral to formation of the load-bearing structure.

3.22.6 FUTURE DIRECTIONS

For the further development of Nb silicide-based composites, fracture toughness no longer appears to be a major barrier, provided that further alloying additions do not reduce the present toughness levels. The levels of toughness measured, the crack growth characteristics, and the ability to perform common cutting, grinding, and machining tasks with standard practices, suggest that further improvements in toughness are unnecessary at present.

Initial fatigue data have been obtained at room temperature; elevated temperature testing is also required. Although earlier data on the toughness of RMICs did not show a significant change in toughness at temperatures up to 500°C, this issue needs to be considered in more detail. Threshold values ΔK_{th} of $> 10 \text{ MPa}\sqrt{\text{m}}$, will be required with Paris law slopes not greater than five for component applications.

Further evaluation of the effects of both alloying and processing modifications on the properties outlined in the present review is necessary in order to achieve the required oxidation and creep goals. Alloying additions that are introduced to improve one specific property must maintain a full balance of properties. Process developments are required to enhance RMIC properties and to establish the capability to manufacture complex articles of these composites. Process developments will probably include cold wall casting schemes and vapor deposition approaches. Vapor deposition of

RMICs offers exciting potential in terms of designing composite microstructures and complex component articles such as hollow blades and vanes. However, a sufficient combination of chemistry and microstructure control has to be developed to provide the required balance of high and low temperature mechanical properties.

In the area of oxidation (see Chapter 3.17, this volume), a further improvement in the base composite performance of a factor of 15 is required in order to achieve the goal of $<25\text{ }\mu\text{m}$ loss per 100 h for component surface temperatures of $1315\text{ }^{\circ}\text{C}$ ($2400\text{ }^{\circ}\text{F}$). The role and performance of coatings for RMICs are still in their infancy. Commercial silicide coatings, such as R512E (20Cr–20Fe–60Si) have been explored (Jackson *et al.*, 1996; Cockeram, 1994; Cockeram and Rapp, 1997). However, further basic research and applied development is required for this area to proceed. In addition, the effect of coatings on the mechanical properties of the base composite needs to be examined.

3.22.7 SUMMARY

This overview has described the state of the art in niobium silicide based *in situ* composites. This materials system offers exciting potential for structural applications up to $1200\text{ }^{\circ}\text{C}$. Microstructure, phase equilibria, mechanical behavior, and oxidation performance have been described.

Inadequate fracture toughness has been a major barrier to the use of intermetallic-based systems commercially. However, fracture toughness values in excess of $20\text{ MPa}\sqrt{\text{m}}$ have been reported in silicide-based composites toughened by (Nb), in combination with oxidation resistances and rupture lives comparable to those of single crystal superalloys for temperatures up to $1150\text{ }^{\circ}\text{C}$. Creep performance and environmental resistance require further improvement.

Phase equilibria data are required to predict composite volume fractions and stability during service. Phase equilibria of these *in situ* composites can be influenced significantly by minor element additions, so that a careful strategy of balancing alloying additions to produce the desired structures for strength, toughness, and oxidation resistance may provide considerable flexibility in achieving further improvements in both mechanical properties and oxidation resistance in subsequent alloy iterations.

Design rules for alloy selection for oxidation performance have been described. The beneficial effects of additions of a Cr_2Nb type Laves

phase on oxidation resistance have also been described. The lowest (Nb) phase volume fraction results in lower oxidation losses; for a constant 37% by volume of (Nb), there appears to be an optimum in the proportions of Laves and silicide phases. Lowering the fraction of (Nb) is generally beneficial to oxidation behavior. There appears to be an optimum balance between Laves volume fraction and silicide volume fraction for a given (Nb) volume fraction. Additions of B, especially at levels greater than 3%, increase the oxidation resistance of the composite system. Although the evidence of oxide chemistry indicates that silica is not formed over the entire oxidizing surface, so that much of the surface is unaffected by B in the silicide, the addition of B does slow the overall rate of oxidation. Some of the B participates in a $\text{T2 M}_5\text{B}_2\text{Si}$ phase formation, rather than in the silicides.

Fundamental studies on quaternary Nb–Hf–Ti–Si alloys and those on higher order alloys indicate that the addition of Ti, Hf, and Mo have a substantial effect on composite secondary creep rates. The threshold Hf, Ti, and Mo concentrations above which the creep performance degenerates beyond that of the Nb–16Si composite have been defined, together with the appropriate stress levels for possible component operations. For example, the data indicate that the creep performance of the Nb–8Hf–25Ti–16Si is compatible with a creep rate $5 \times 10^{-8}\text{ s}^{-1}$ and stress levels of up to 140 MPa for temperatures up to $1200\text{ }^{\circ}\text{C}$.

Oxidation and creep remain the most serious issues for the future use of the Nb-based RMICs. Although alloying additions to Nb-based RMICs have increased oxidation resistance substantially, considerable further improvement is needed. Material loss rates due to oxidation are still only comparable with the best current superalloys. Where superalloys operate with maximum surface temperatures of $1150\text{ }^{\circ}\text{C}$, the RMICs will be expected to operate equally successfully at $1315\text{ }^{\circ}\text{C}$. Thus, advanced airfoil designs may require up to a $200\text{ }^{\circ}\text{C}$ improvement in the oxidation properties, and an increase in the stress rupture behavior of up to three Larson–Miller parameters from the present levels.

ACKNOWLEDGMENTS

The authors would like to thank D. J. Dalpe, J. A. Sutliff, R. R. Bishop, W. J. Reeder, L. A. Peluso, P. Whiting, A. W. Davis, S. Sitzman, W. Zinsser, and E. H. Hearn for their contributions to the experimental work. This research

was partially sponsored by AFOSR under contracts #F49 620-96-C-0022 and #F49 620-93-C-0007 with Dr. C. H. Ward and Dr. S. Wu as Program Managers. The authors are also grateful to Dr. M. G. Mendiratta, Dr. P. R. Subramanian, Dr. D. M. Dimiduk, AFWL, Dr. H. A. Lipsitt, Dr. R. J. Grylls, Prof. J. J. Lewandowski, Prof. C. L. Briant, and Prof. H. L. Fraser for very helpful discussions.

3.22.8 REFERENCES

- D. L. Anton and D. M. Shah, *Mat. Res. Soc. Symp. Proc.*, 1991, **213**, 733-738.
- D. L. Anton and D. M. Shah, *Mat. Sci. Eng.*, 1992, **A153**(1-2), 410-415.
- D. L. Anton, D. B. Snow and A. F. Giamei, AFOSR Annual Report, May 1988.
- B. P. Bewlay, R. R. Bishop and M. R. Jackson, *J. Phase Equilibria*, 1999a, **20**(2), 109-112.
- B. P. Bewlay, R. R. Bishop and M. R. Jackson, *Z. Metallkunde*, 1999b, **90**(6), 413-422.
- B. P. Bewlay, M. R. Jackson and H. A. Lipsitt, *Metall. Mater. Trans.*, 1996, **27**(12), 3801-3808.
- B. P. Bewlay, M. R. Jackson and H. A. Lipsitt, in 'Processing and Design Issues in High Temperature Materials', eds. N. S. Stoloff and R. H. Jones, TMS Publications, Warrendale, PA, 1997a, pp. 247-262.
- B. P. Bewlay, M. R. Jackson and H. Lipsitt, *J. Phase Equilibria*, 1997b, **18**(3), 264-278.
- B. P. Bewlay, M. R. Jackson, W. J. Reeder and H. A. Lipsitt, in 'MRS Proceedings on High Temperature Ordered Intermetallic Alloys VI', MRS, Pittsburgh, PA, 1994a, pp. 943-948.
- B. P. Bewlay, M. R. Jackson, W. J. Reeder and H. A. Lipsitt, in 'MRS Symposium Proceedings 364', MRS, Pittsburgh, PA, 1995a, pp. 943-948.
- B. P. Bewlay, J. J. Lewandowski and M. R. Jackson, *J. Metals*, 1997c, **49**(8), 46-48.
- B. P. Bewlay, H. A. Lipsitt, M. R. Jackson, W. J. Reeder and J. A. Sutliff, *Mater. Sci. Eng.*, 1995b, **A192**/193, 534-543.
- B. P. Bewlay, H. A. Lipsitt, W. J. Reeder, M. R. Jackson and J. A. Sutliff, in 'Processing and Fabrication of Advanced Materials for High Temperature Applications III', Chicago IL, eds. V. A. Ravi, T. S. Srivatsan J. J. Moore, TMS Publications, Warrendale, PA, 1994b, pp. 547-565.
- B. P. Bewlay and J. A. Sutliff, *Microscopy and Microanalysis*, 1998, **288**, 278-279.
- B. P. Bewlay, J. A. Sutliff and R. R. Bishop, *J. Phase Equilibria*, 1998, **20**(2), 109-112.
- B. P. Bewlay, P. Whiting and C. L. Briant, submitted to the MRS Proceedings on High Temperature Ordered Intermetallic Alloys VIII, 1998.
- H. Bibring, in 'Conference on *in situ* Composites-I', eds. F. D. Lemkey and E. R. Thompson, National Academy of Science NMAB-308II, Washington, DC, 1973, pp. 1-69.
- C. A. Bruch, R. W. Harrison, M. F. X. Gigliotti, M. F. Henry, R. C. Haubert and C. A. Gay, in 'Conference on *in situ* Composites-III', Boston MA, eds. J. L. Walter, M. F. X. Gigliotti, B. F. Oliver and H. Bibring, Ginn Custom Publishers, Lexington, MA, 1979, pp. 258-267.
- R. W. Buckman, Jr. et al., in 'Alloying of Refractory Metals in Alloying', eds. J. L. Walter, M. R. Jackson and C. T. Sims, ASM International, Metals Park, OH, 1988, pp. 419-445.
- A. D. Cetel, M. Gell and J. W. Glatz, in 'Conference on *in situ* Composites-III', Boston MA, eds. J. L. Walter, B. F. Oliver, M. F. X. Gigliotti and H. Bibring, Ginn Custom Publishers, Lexington, MA, 1979, pp. 292-302.
- K. S. Chan and D. S. Shih, *Metall. Trans. A*, 1997, **28A**, 79-90.
- K.-M. Chang, B. P. Bewlay, J. A. Sutliff and M. R. Jackson, *J. Metals*, 1992, **44**(6), 59-63.
- B. V. Cockeram, Ph.D. Thesis, Ohio State University, 1994.
- B. V. Cockeram, H. A. Lipsitt, R. Srinivasan and I. Weiss, *Scripta Met. Mater.*, 1991a, **25**, 2109-2114.
- B. V. Cockeram, H. A. Lipsitt, R. Srinivasan, and I. Weiss, *Scripta Met. Mater.*, 1992, **26**, 755-760.
- B. V. Cockeram and R. A. Rapp, in 'Processing and Design Issues in High Temperature Materials', eds. N. S. Stoloff and R. H. Jones, TMS Publications, Warrendale, PA, 1996, pp. 391-402.
- B. V. Cockeram, M. Saqib, R. Omlor, R. Srinivasan, L. E. Matson and I. Weiss, *Scripta Met. Mater.*, 1991b, **25**, 393-398.
- D. M. Dimiduk, M. G. Mendiratta and P. R. Subramanian, in 'Structural Intermetallics', eds. R. Darolia, J. J. Lewandowski, C. T. Liu, P. L. Martin, D. B. Miracle and M. V. Nathal, TMS Publications, Warrendale, PA, 1993, pp. 619-630.
- M. F. X. Gigliotti, M. R. Jackson, S. W. Yang, M. F. Henry and D. A. Woodford, in 'Conference on *in situ* Composites-IV', Boston, MA, eds. F. D. Lemkey, H. E. Cline and M. McLean, North Holland, Amsterdam, 1982, pp. 21-29.
- A. Gokhale and R. Abbaschian, *Bulletin of Alloy Phase Diagrams*, 1989, **4**(10), 390-393.
- V. G. Grigorovich and E. N. Sheftel', *Met. Sci. Heat Treatment*, 1983, **24**(7-8), 472-478.
- V. G. Grigorovich, E. N. Sheftel' and G. Sh. Usmanova, *Izv. Akad. Nauk SSSR, Met.*, 1980, **6**.
- R. J. Grylls, B. P. Bewlay, H. L. Fraser and H. A. Lipsitt, *Philosophical Magazine*, August 1998, accepted.
- G. A. Henshall, M. J. Strum, B. P. Bewlay and J. A. Sutliff, *Metall. Mater. Trans.*, 1997, **28A**, 2555-2564.
- G. A. Henshall, M. J. Strum, P. R. Subramanian and M. G. Mendiratta, *Mat. Res. Soc. Symp. Proc.*, 1995, **364**, 937-942.
- M. R. Jackson and B. P. Bewlay, USAF Delivery order report, AFML, Sept 1998.
- M. R. Jackson, B. P. Bewlay, R. G. Rowe, D. W. Skelly and H. A. Lipsitt, *J. Metals*, 1996, **48**(1), 39-44.
- M. R. Jackson, M. F. X. Gigliotti, S. W. Yang and J. L. Walter, in 'Conference on *in situ* Composites-IV', Boston, MA, eds. F. D. Lemkey, H. E. Cline and M. McLean, North Holland, Amsterdam, 1982, pp. 155-165.
- M. R. Jackson, R. G. Rowe and D. W. Skelly, Annual Report, WRDC Contract #F33 615-91-C-5613, 1994.
- M. R. Jackson, R. G. Rowe and D. W. Skelly, *Mat. Res. Soc. Symp. Proc.*, 1995, **364**, 1339-1344.
- D. R. Johnson, S. M. Joslin, R. D. Reviere, B. F. Oliver and R. D. Noebe, in 'Processing and Fabrication of Advanced Materials for High Temperature Applications II', eds. V. A. Ravi and T. S. Srivatsan, TMS Publications, Warrendale, PA, 1993, pp. 77-90.
- J. Kajuch, J. Short and J. J. Lewandowski, *Acta Metall. Mater.*, 1995, **43**(5), 1955-1967.
- J. Kajuch, J. D. Rigney and J. J. Lewandowski, *Mat. Sci. Eng.*, 1992, **A155**, 59-65.
- T. Khan, in 'Conference on *in situ* Composites-III', eds. J. L. Walter, M. F. X. Gigliotti, B. F. Oliver and H. Bibring, Ginn Custom Publishers, Lexington, MA, 1979, pp. 378-388.
- J. M. Larsen, B. D. Worth, S. J. Balsone and J. W. Jones, in 'Gamma Titanium Aluminides', eds. Y. W. Kim, R. Wagner and M. Yamaguchi, TMS, Warrendale, PA, 1995, pp. 821-834.

- F. D. Lemkey and E. R. Thompson, *Metall. Trans.*, 1971, 2, 1537-1546.
- H. Liang and Y. A. Chang, *Intermetallics*, 1999, 7, 561-570.
- T. B. Massalski, 'Binary Alloy Phase Diagrams', ASM, Metals Park, OH, 1991.
- M. G. Mendiratta and D. M. Dimiduk, *Metall. Trans.*, 1993, A24A, 501-504.
- M. G. Mendiratta, J. J. Lewandowski and D. M. Dimiduk, *Metall. Trans.*, 1991, 22A, 1573-1583.
- R. G. Menzies, C. A. Bruch, M. F. X. Gigliotti, J. A. Smith and R. C. Haubert, in 'Superalloys 1988', The Metallurgical Society/AME, Warrendale, PA, 1988, pp. 1573-1581.
- R. M. Nekkanti and D. M. Dimiduk, *Mat. Res. Soc. Symp. Proc.*, 1990, 194, 175-182.
- W. G. Pfann, 'Zone Refining', Wiley, New York, 1966.
- D. P. Pope, D. M. Shah, W. Romanow and M. Huntley, *Mat. Res. Soc. Symp. Proc.*, 1994, 322, 461-472.
- M. Rabinovitch and J.-M. Hauser, in 'Conference on *in situ* Composites-III', Bolton Landing, NY, eds. J. L. Walter, M. F. Gigliotti, B. F. Oliver and H. Bibring, Ginn Custom Publishers, Lexington, MA, 1979, pp. 246-257.
- K. T. Rao, G. R. Odette and R. O. Ritchie, *Acta Metall. Mater.*, 1994, 42(3), 893-911.
- K. T. Rao, W. O. Soboyejo and R. O. Ritchie, *Metall. Trans. A*, 1993, 23A, 95-104.
- K. S. Ravichandran, *Scripta Met.*, 1992, 26, 1389-1393.
- J. D. Rigney, Ph.D. Thesis, Case Western Reserve University, 1993.
- J. D. Rigney and J. J. Lewandowski, *Metall. Trans. A*, 1996, 27A, 3292-3306.
- J. D. Rigney, P. R. Singh and J. J. Lewandowski, *Mat. Res. Soc. Symp. Proc.*, 1994, 322, 502-509.
- R. G. Rowe, D. W. Skelly, M. Larsen, J. Heathcote, G. Lucas and G. R. Odette, *Mat. Res. Soc. Symp. Proc.*, 1994, 322, 461-472.
- A. Samant and J. J. Lewandowski, *Metall. Trans. A*, 1997, 28A, 389-399.
- D. M. Shah, D. L. Anton, D. P. Pope and S. Chin, *Mater. Sci. Eng.*, 1995, A192/193, 658-672.
- E. N. Sheftel and O. A. Bannykh, in 'Proceedings of the 13th International Plansee Seminar Reutte Austria', eds. H. Bildstein and R. Eck, 1993, pp. 43-69.
- R. W. Smashey, *USPat.* 3 904 402 (1974).
- 'Standard Practice for R-Curve Determination', ASTM STP E 561-94, American Society for Testing and Materials, Philadelphia, PA, 1994.
- 'Standard Test Method for Plane-Strain Fracture Toughness of Metallic Materials', ASTM STP E-399, American Society for Testing and Materials, Philadelphia, PA, 1983, pp. 488-512.
- J.-F. Stohr, in 'Conference on *in situ* Composites-III', eds. J. L. Walter, M. F. Gigliotti, B. F. Oliver and H. Bibring, Ginn Custom Publisher, Lexington, MA, 1979, pp. 130-140.
- P. R. Subramanian, M. G. Mendiratta and D. M. Dimiduk, *Mat. Res. Soc. Symp. Proc.*, 1994, 322, 491-502.
- P. R. Subramanian, M. G. Mendiratta and D. M. Dimiduk, *J. Metals*, 1996, 48(1), 33-38.
- P. R. Subramanian, M. G. Mendiratta, D. M. Dimiduk and M. A. Stucke, *Mater. Sci. Eng.*, 1997, A239-240, 1-13.
- P. R. Subramanian, T. A. Parthasarathy, M. G. Mendiratta and D. M. Dimiduk, *Scripta Met.*, 1995, 32(8), 1227-1232.
- J. A. Sutliff and B. P. Bewlay, in 'Proceedings of the 54th Annual Meeting of the Microscopy Society of America', eds. G. W. Bailey, J. M. Corbett, R. V. W. Dimlich, J. R. Mical, and, N. J. Zalusey, San Francisco Press, CA, 1996.
- A. J. Thom, Y. M. Kim and M. F. Akinc, in 'High Temperature Ordered Intermetallic Alloys-V', eds. I. Baker, R. Darolia, J. D. Whittenberger and M. H. Yoo, Materials Research Society, Pittsburgh, PA, 1993, pp. 1037-1042.
- A. J. Thom, M. K. Meyer, Y. Kim and M. Akinc, in 'Processing and Fabrication of Advanced Materials-III', eds. V. A. Ravi, T. S. Srivatsan and J. J. Moore, TMS, Warrendale, PA, 1994, pp. 413-438.
- J. L. Walter and H. E. Cline, in 'Conference on *in situ* Composites-I', Lakefield, CT, eds. F. D. Lemkey and E. R. Thompson, Natl. Acad. Sci. NMAB-3081, Washington, 1973, pp. 61-74.
- I. Weiss, M. Thirukkonda and R. Srinivasan, in 'Advances in Hot Deformation Textures and Microstructures', eds. J. J. Jonas, T. R. Bieler and K. J. Bowman, TMS, Warrendale, PA, 1994a, pp. 559-578.
- I. Weiss, M. Thirukkonda and R. Srinivasan, *Mat. Res. Soc. Symp. Proc.*, 1994b, 322, 377-386.
- S. T. Wlodek, in 'Columbium Metallurgy', eds. D. L. Douglas and F. W. Kruz, Interscience, New York, 1961, vol. 10, pp. 175-205.
- D. A. Woodford, in 'Conference on *in situ* Composites-II', Bolton Landing, NY, eds. M. R. Jackson, J. L. Walter, F. D. Lemkey and R. W. Hertzberg, Xerox Ginn, Lexington, MA, 1976, pp. 211-221.
- W. A. Zinsser and J. J. Lewandowski, *Mat. Trans.*, 1998, submitted.

Hf-Si Binary Phase Diagram Determination and Thermodynamic Modeling

J.-C. Zhao, B.P. Bewlay, M.R. Jackson, and Q. Chen

Journal of Phase Equilibria, 2000

Hf-Si Binary Phase Diagram Determination and Thermodynamic Modeling

J.-C. Zhao, B.P. Bewlay, M.R. Jackson, and Q. Chen

(Submitted 20 May 1999; in revised form 17 August 1999)

A new version of the Hf-Si binary phase diagram has been constructed and it includes recent confirmation of the existence of the Hf_5Si_3 phase and observation of the following eutectoid reaction: $\text{Hf}_5\text{Si}_3 \leftrightarrow \text{Hf}_2\text{Si} + \text{Hf}_3\text{Si}_2$ at $1925 \pm 25^\circ\text{C}$. The peritectic reaction, $\text{L} + \text{Hf}_3\text{Si}_2 \leftrightarrow \text{Hf}_5\text{Si}_3$ at $\sim 2360 \pm 30^\circ\text{C}$, was proposed with consideration of Brukl's incipient melting results. Thermodynamic modeling of the binary Hf-Si system was performed via Thermo-Calc with existing phase diagram data, the experimental results described in this paper, and the reported enthalpies of formation for Hf silicides. A complete thermodynamic description of the Gibbs energies of all stable phases in the binary system was developed and was consistent with the majority of the phase diagram and thermochemistry data.

1. Introduction

Niobium silicide-based composites show high promise for application as the next generation turbine airfoil materials with significantly higher operating temperatures than current generation advanced Ni-base superalloys [1989Men, 1996Jac, 1996Sub, 1997Bew]. Hafnium is an important alloying element for strength, toughness, and oxidation resistance of these composites [1996Jac, 1997Bew]. Thus, the phase stability and thermochemistry of the Hf-Si system, especially the stability of the Hf_5Si_3 phase, is of great interest to the development of the Nb silicide-based composites. This work is part of an effort [1999Lia] to build a thermodynamic database for predictive modeling of phase equilibria in complex Nb silicide systems.

The Hf-Si phase diagram has been assessed by Gokhale and Abbaschian [1989Gok]. It was mostly based on the experimental results of Brukl [1968Bru]. Five intermetallic compounds, Hf_2Si , Hf_3Si_2 , Hf_3Si_4 , HfSi , and HfSi_2 , have been included in the assessed phase diagram. The crystal structures of these silicides are listed in Table 1. A Hf_5Si_3 phase with the Mn_5Si_3 (*hP16*, *P6₃/mmc*) crystal structure was identified by [1958Now, 1969Kar]. Several investigators included this phase in their phase diagrams based on their observations [1960Now, 1960Vic, 1971Shu]. The Hf_5Si_3 phase was originally thought to be stabilized by interstitial impurities by [1968Bru, 1989Gok] and was not included in the assessed phase diagram of Gokhale and Abbaschian. Recently, Bewlay *et al.* [1999Bew] found that the Hf_5Si_3 phase existed in a Hf-35 at.% Si alloy containing very low interstitial impurities (total O, N, and C concentrations less than 100 weight ppm); thus, O, N, or C was not required to stabilize this phase. In fact, Brukl found the Hf_5Si_3 phase, although he attributed its existence to interstitial impurities. However, Brukl found that the elimination of the Hf_5Si_3 phase in Hf_2Si

containing alloys was not possible even by careful arc melting (to remove interstitial impurities). As an interesting comparison, Brukl also attributed the existence of a Zr_5Si_3 phase in Zr-Si alloys to interstitial impurities; however, the phase was included in the assessed Zr-Si phase diagram of Okamoto [1990Oka] and also in the thermodynamic modeling of Gueneau *et al.* [1994Gue] based on the evidence of other investigations. The Hf-Si and Zr-Si phase diagrams are similar.

In addition to the direct evidence for the existence of the Hf_5Si_3 phase [1999Bew], there were also other indications that Hf_5Si_3 was a stable phase in the Hf-Si binary system. Shurin and Todorov [1971Shu] found that the Hf_5Si_3 phase decomposed eutectoidally when annealed at 1500 and 1600 $^\circ\text{C}$, while it remained stable at 2000 $^\circ\text{C}$. Brukl [1968Bru] also reported that this phase started to decompose at temperatures lower than 1600 $^\circ\text{C}$. All these results are consistent with the fact that Hf_5Si_3 is a stable phase in the Hf-Si binary system.

The upper stability temperature of the Hf_5Si_3 phase was estimated at $2360 \pm 30^\circ\text{C}$, based on the incipient melting and collapsing data of Brukl [1968Bru]. The incipient melting and collapsing data exhibited a small plateau in the phase diagram while there was an invariant reaction, as shown in Fig. 1. It seems that there was a plateau at about $2360 \pm 30^\circ\text{C}$ in the composition region close to Hf_5Si_3 ; thus, this temperature was tentatively accepted for the peritectic reaction, $\text{L} + \text{Hf}_3\text{Si}_2 \leftrightarrow \text{Hf}_5\text{Si}_3$. The lower stability (eutectoid) temperature has been determined experimentally in the present investigation.

The remainder of the Hf-Si phase diagram used for the present thermodynamic modeling was based on Brukl [1968Bru], which agreed with the assessment of Gokhale and Abbaschian [1989Gok]. There were very little data on the liquidus. The invariant reactions and their temperatures are listed in Table 2.

The only available thermochemistry data for the Hf-Si binary system were the enthalpies of formation for the Hf silicides [1957Smi, 1971Gol, 1976Bon, 1980Sam, 1988Boe, 1990Top, 1998Mes], as shown in Table 3. The data of [1971Gol, 1976Bon] will be discussed in more detail after the thermodynamic modeling.

J.-C. Zhao, B.P. Bewlay, and M.R. Jackson, General Electric Company, Corporate Research and Development, Schenectady, NY 12301; and Q. Chen, Department of Materials Science and Engineering, Royal Institute of Technology, S-10044 Stockholm, Sweden.

Table 1 Crystal structures of the Hf silicides

Phase	Prototype	Space group	Lattice parameters, nm	Reference
Hf ₂ Si	Al ₃ Cu	<i>I4/mcm</i>	$a = 0.6553, c = 0.5186$	[1972Hav, 1991Vil]
Hf ₃ Si ₃	Mn ₃ Si ₃	<i>P6₃/mcm</i>	$a = 0.7844, c = 0.5492$	[1969Kar, 1991Vil]
Hf ₂ Si ₂	U ₃ Si ₂	<i>P4/mbm</i>	$a = 0.6988, c = 0.3675$	[1969Kar, 1991Vil]
Hf ₂ Si ₄	Zr ₂ Si ₄	<i>P4₁2₁2</i>	$a = 0.7039, c = 1.283$	[1969Kar, 1991Vil]
HfSi	FeB	<i>Prma</i>	$a = 0.6889, b = 0.3772, c = 0.5223$	[1969Kar, 1991Vil]
HfSi ₂	ZrSi ₂	<i>Cmcm</i>	$a = 0.3672, b = 1.457, c = 0.3641$	[1969Kar, 1991Vil]

Table 2 Invariant reactions of the Hf-Si binary system

Reaction	Type	Temperature (experimental), °C [1968Bru]	Temperature (calculated), °C	Liquid composition (experimental), at.% Si [1968 Bru]	Liquid composition (calculated), at.% Si
$L \leftrightarrow \text{bcc (Hf)} + \text{Hf}_2\text{Si}$	Eutectic	1831 ± 5	1828	11.5 ± 1	11.1
$\text{Bcc (Hf)} + \text{Hf}_2\text{Si} \leftrightarrow \text{hcp (Hf)}$	Peritectoid	1743 (for Hf)	1743
$L + \text{Hf}_2\text{Si}_2 \leftrightarrow \text{Hf}_2\text{Si}$	Peritectic	2083 ± 12	2086	...	17.9
$L + \text{Hf}_2\text{Si}_2 \leftrightarrow \text{Hf}_2\text{Si}_3$	Peritectic	2360 ± 30(a)	2357	...	27.7
$\text{Hf}_2\text{Si}_2 \leftrightarrow \text{Hf}_2\text{Si} + \text{Hf}_2\text{Si}_3$	Eutectoid	1925 ± 25(b)	1924
$L \leftrightarrow \text{Hf}_2\text{Si}_2$	Congruent	2480 ± 20	2480	40	40
$\text{Hf}_2\text{Si}_2 + L \leftrightarrow \text{Hf}_2\text{Si}_3$	Peritectic	2320 ± 15	2313	...	54.6
$\text{Hf}_2\text{Si}_2 + L \leftrightarrow \text{HfSi}$	Peritectic	2142 ± 15	2133	...	62.8
$\text{HfSi} + L \leftrightarrow \text{HfSi}_2$	Peritectic	1543 ± 8	1546	...	80.8
$L \pm \text{HfSi}_2 + \text{diamond}_A\text{ (Si)}$	Eutectic	1330 ± 8	1325	91 ± 2	90.8

(a) Estimated in the present study. (b) Measured in the present study

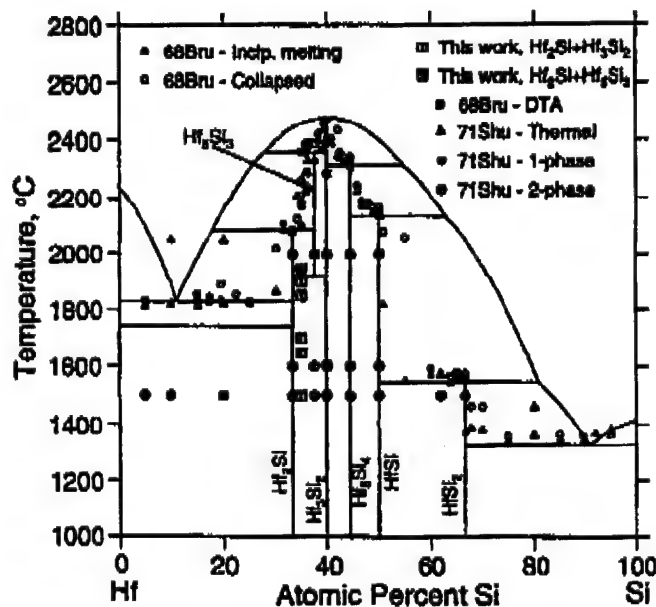


Fig. 1 Comparison of the calculated phase diagram with the experimental data. See Table I for invariant reaction temperatures and their comparison with experimental data [1968Bru].

The aim of this paper is to measure the eutectoid decomposition temperature of Hf₂Si₃ and to perform thermodynamic modeling of the binary system.

2. Experimental Procedures and Results

A binary Hf-35 at.% Si alloy was prepared from >99.9% Hf (not including Zr) and 99.999% Si by induction levitation melting in a segmented water-cooled copper crucible. The alloy was triple melted. The interstitial levels of the Hf were C < 11, O < 52, and N < 22 weight ppm. Chemical analyses were performed on the starting materials but not on the final cast alloy. However, it has been shown previously that the cold crucible melting system prevents any increase in the interstitial levels from those in the starting elements [1997Hen]. There is indigenous Zr in essentially all commercially available Hf. The Zr content in the cast alloy was estimated at ~2 at.%. Fortunately, the Zr₂Si₃ phase has stability very similar to Hf₂Si₃; this can be appreciated by the similarity of the Hf-Si and Zr-Si binary phase diagrams. For this reason, Zr does not significantly affect the results for the Hf-Si alloy.

The as-cast microstructure consisted of primary Hf₂Si₃, peritectic Hf₂Si, and a eutectic of Hf₂Si and a Hf-Si solid solution (Hf). Detailed characterization of the as-cast structure was described in [1999Bew]. According to the phase diagram shown in Fig. 1, the primary phase for the Hf-35 at.% Si alloy should be Hf₂Si₃. However, since the cooling rate during solidification was low and the peritectic ($L + \text{Hf}_2\text{Si}_2 \leftrightarrow \text{Hf}_2\text{Si}_3$) reaction temperature was very high (2360 ± 30 °C), it is probable that the primary Hf₂Si₂ phase transformed to Hf₂Si₃.

Section I: Basic and Applied Research

Table 3 Enthalpies of formation for the Hf silicides at 25 °C (298 K) of the Hf-Si system in kJ/(mole of atoms)

Phase	Enthalpy of formation	Reference and comments
Hf ₂ Si	-62.7	[1980Sam]
	-72.0	[1988Boe] - predicted(a)
	-63.8	This work - modeling
Hf ₃ Si ₂	-70.2 ± 3.3	[1971Gol]
	-70.2	[1980Sam]
	-79.0	[1988Boe] - predicted(a)
	-68.5	This work - modeling
Hf ₅ Si ₃	-83.0	[1988Boe] - predicted(a)
	-80.0 ± 4.7	[1990Top] at 1473 ± 2 K
	-76.8	This work - modeling
Hf ₃ Si ₄	-75.0	This work - modeling
HfSi	-71.1 ± 4.6	[1971Gol]
	-71.1	[1980Sam]
	-91.0	[1988Boe] - predicted(a)
	-70.9 ± 2.0	[1998Mes] at 1473 ± 2 K
	-73.0	This work - modeling
HfSi ₂	-55.7 to -69.7	[1957Smi] - estimated from volume contraction
	-75.2	[1980Sam]
	-74.0	[1988Boe] - predicted(a)
	-69.7	This work - modeling

(a) Predicted using semiempirical Miedema model [1988Boe]

The as-cast samples were cut into pieces and wrapped in Nb foil (for heat treatment temperatures <1700 °C) or Ta foil (for heat treatment temperatures >1700 °C) and heat treated at 1500 °C (100 h), 1650 °C (50 h), 1700 °C (100 h), 1800 °C (20 h), 1900 °C (20 h), and 1950 °C (5 h), respectively. The annealing time for each temperature was selected to minimize interstitial contamination from the furnace atmosphere.

All of the samples were examined by backscatter electron (BSE) imaging using scanning electron microscopy (SEM). Phase identification was also performed using an electron backscatter pattern (EBSP) technique for electron diffraction in SEM. This technique allowed easy selection of microstructural features using BSE imaging for rapid diffraction pattern collection and analysis. A CamScan CS44 scanning electron microscope (CamScan Electron Optics, Ltd., Cambridge, England) was operated using a 40 kV, ~10 nA electron beam, and the sample surface normal was tilted 70° away from the beam axis. A Nordiff (Jarle Hjelen Ltd., Trondheim, Norway) CCD-based EBSP detector was used. Positive phase identification was accomplished by direct comparison of the location and character of the diffraction bands in the experimental pattern with those calculated from simulated patterns generated using the possible structure types and lattice parameters.

The microstructure of the Hf-35at.%Si annealed at 1950 °C consisted mostly of the Hf₃Si₂ and Hf₂Si, as shown in Fig. 2. These phases were identified using EBSP, as shown in Fig. 3 and 4. It is clear that the primary Hf₃Si₂ phase did not decompose at 1950 °C.

At temperatures ≤1900 °C, the primary Hf₃Si₂ phase underwent a eutectoid decomposition into Hf₂Si and Hf₅Si₃, as shown

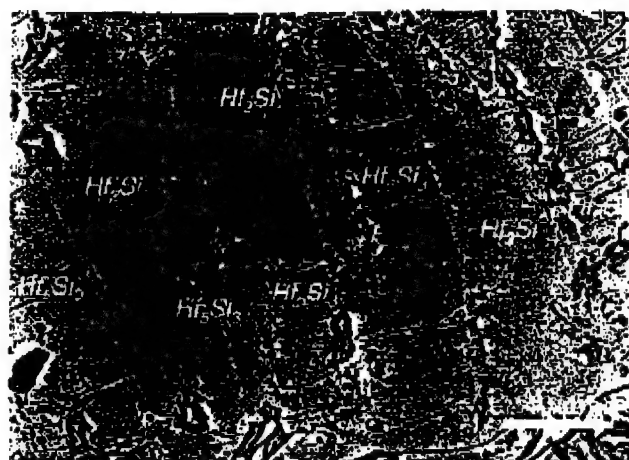


Fig. 2 BSE image of a Hf-35at.%Si alloy heat treated at 1950 °C for 5 h. The darker phase with cracks is Hf₃Si₂, and the lighter phase is Hf₂Si. Note that the Hf₃Si₂ phase was stable at this temperature.

in Fig. 5. The two-phase region in Fig. 5 was the eutectoid decomposition product of the primary Hf₃Si₂ phase. Again, the crystal structure of the phases was identified using EBSP. The EBSP pattern of the Hf₅Si₃ phase is shown in Fig. 6.

Based on the above data, it is clear that the eutectoid reaction, Hf₃Si₂ ↔ Hf₂Si + Hf₅Si₃, exists at 1925 ± 25 °C.

3. Thermodynamic Modeling Procedures and Results

Thermo-Calc [1985Sun] was employed for optimizing the thermodynamic parameters and also for the calculation of the phase diagram and enthalpies. The pure elemental data for Hf and Si were taken from the Scientific Group Thermodata Europe (SGTE) database [1991Din].

The solubility of Si in Hf (both the bcc and hcp phases) was estimated at <1 at.%; similarly, the solubility of Hf in Si was also very low [1968Bru]. Thus, the three solid solution phases, bcc, hcp, and diamond_A4, were treated as pure substances. The Gibbs energy of the liquid phase in terms of 1 mole of atoms was treated as a disordered solution with a subregular solution model:

$$G_m^L = x_{\text{Hf}} G_{\text{Hf}}^L + x_{\text{Si}} G_{\text{Si}}^L + RT(x_{\text{Hf}} \ln x_{\text{Hf}} + x_{\text{Si}} \ln x_{\text{Si}}) + x_{\text{Hf}} x_{\text{Si}} \Sigma^L (x_{\text{Hf}} - x_{\text{Si}})^n$$

where x_i and G_i^L are the mole fraction and the liquid phase molar Gibbs energy of element i ($i = \text{Hf}, \text{Si}$). R is the gas constant, and T is temperature. The last term in the above equation is the excess Gibbs energy with interaction parameters expressed in Redlich-Kister polynomials [1948Red]. All the Hf silicides were treated as having stoichiometric compositions and their Gibbs energies were described by

$$G_{\text{Hf}_i\text{Si}_j} = x_{\text{Hf}} G_{\text{Hf}}^{\text{hcp}} + x_{\text{Si}} G_{\text{Si}}^{\text{diamond}} + \Delta G_f$$

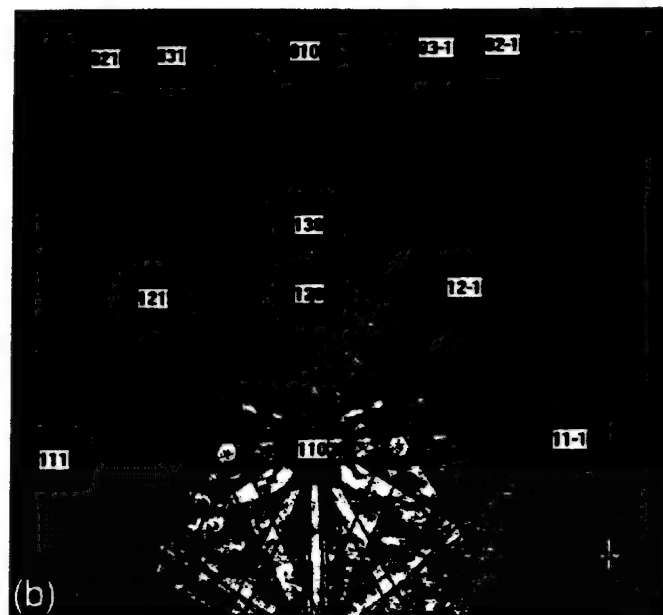
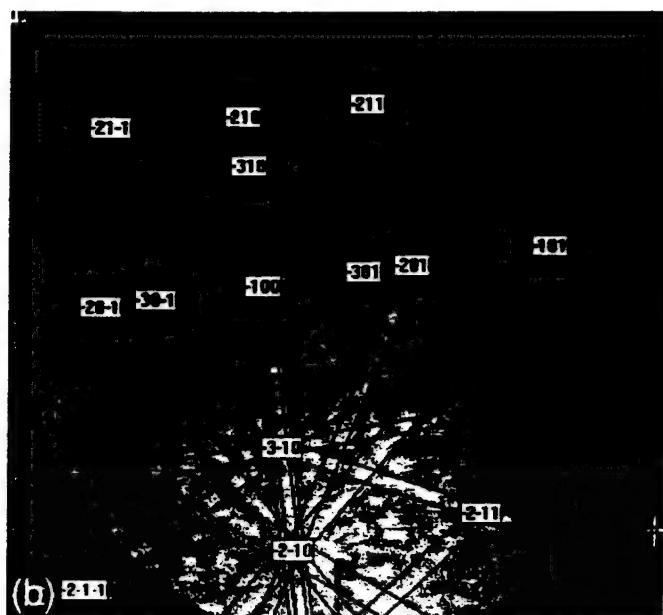
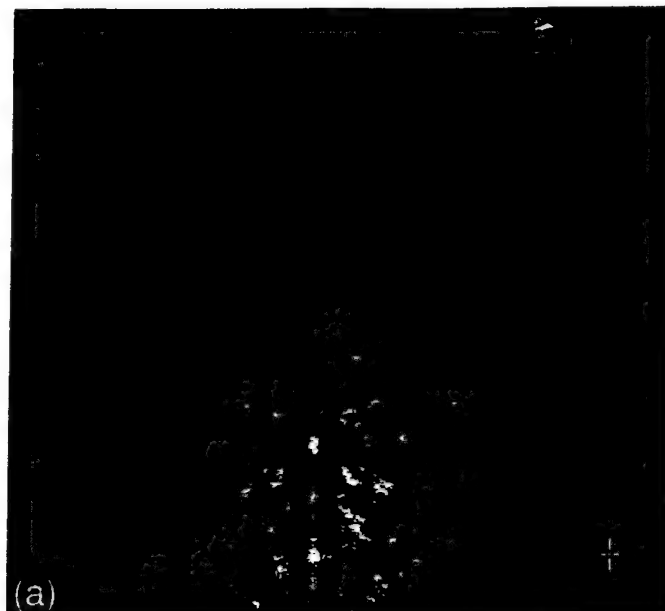
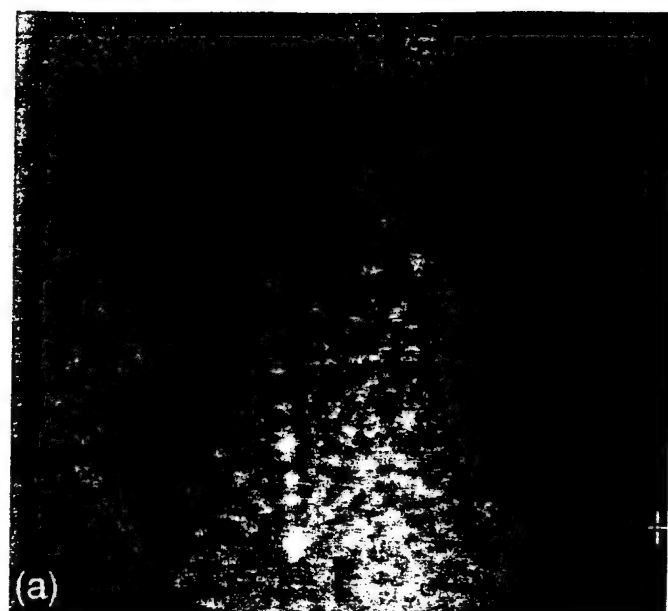


Fig. 3 EBSP of Hf₅Si₃ (a), with the indexed pattern shown in (b).

Fig. 4 EBSP of Hf₅Si (a), with the indexed pattern shown in (b).

where $\Delta G_f = a + bT$ is the molar Gibbs energy of formation of the compound, and a and b are constants generated by the optimization.

The model parameters were optimized from the experimental phase diagram information, especially the invariant reaction temperatures, as well as the enthalpy of formation data of the silicides (Table 3).

The modeled thermodynamic parameters are listed in Table 4. The calculated phase diagram is shown in Fig. 1. It can be seen from Fig. 1 and Tables 2 and 3 that the calculated phase diagram and enthalpies agree well with the majority of the experimental data. All the invariant temperatures were within the error of the experimental measurements. The enthalpies of formation of Samsonov and Vinitskii [1980Sam] agree best with

our assessed values, as shown in Fig. 7 and Table 3. The enthalpies of formation predicted by Boer *et al.* [1988Boe] were lower than both the experimentally determined data and our assessed values. The enthalpies of formation data of Golutvin and Maslennikova [1971Gol] showed wide scatter, especially in the composition range of ~40 to ~65 at.% Si. This is partly due to the fact that some alloys may have been in non-equilibrium states; for instance, their 42.4 at.% Si alloy contained three phases (Hf₃Si₂ + Hf₅Si₄ + Hf₅Si₃), whereas at equilibrium, there should be Hf₃Si₂ + Hf₅Si₄ (two-phase state) according to the phase diagram. Due to the wide scatter, the enthalpy data of [1971Gol] were not included in the present modeling.

The temperature variation of the enthalpy of a Hf-66.7 at.% Si alloy with the HfSi₂ phase at 298 K as a reference

Table 4 Thermodynamic parameters for the phases in the Hf-Si binary system(a)

Liquid: ${}^0L^L = -177,631 + 6.42546T$ ${}^1L^L = -1830$
Hf_2Si : $G_{\text{Hf}_2\text{Si}} = 0.667 {}^0G_{\text{Hf}}^{\text{hcp}} + 0.333 {}^0G_{\text{Si}}^{\text{diamond}} - 63,785 + 1.5413T$
Hf_3Si_3 : $G_{\text{Hf}_3\text{Si}_3} = 0.625 {}^0G_{\text{Hf}}^{\text{hcp}} + 0.375 {}^0G_{\text{Si}}^{\text{diamond}} - 68,537 + 0.8153T$
Hf_3Si_2 : $G_{\text{Hf}_3\text{Si}_2} = 0.600 {}^0G_{\text{Hf}}^{\text{hcp}} + 0.400 {}^0G_{\text{Si}}^{\text{diamond}} - 76,772 + 2.8296T$
Hf_3Si_4 : $G_{\text{Hf}_3\text{Si}_4} = 0.556 {}^0G_{\text{Hf}}^{\text{hcp}} + 0.444 {}^0G_{\text{Si}}^{\text{diamond}} - 74,987 + 2.0556T$
HfSi : $G_{\text{HfSi}} = 0.500 {}^0G_{\text{Hf}}^{\text{hcp}} + 0.500 {}^0G_{\text{Si}}^{\text{diamond}} - 73,013 + 1.9597T$
HfSi_2 : $G_{\text{HfSi}_2} = 0.333 {}^0G_{\text{Hf}}^{\text{hcp}} + 0.667 {}^0G_{\text{Si}}^{\text{diamond}} - 69,725 + 10.480T$

(a) All values are in SI units and for 1 mole of atoms. The thermodynamic data for pure Hf and Si were adopted from SGTE and can be found in [1991Din].

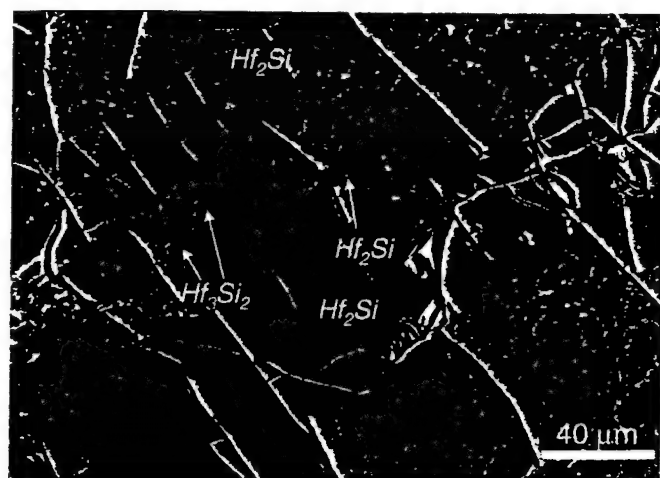


Fig. 5 BSE image of a Hf-35 at.% Si alloy heat treated at 1800 °C for 20 h. The large gray dendrites are Hf_2Si . The dendrites are separated by two-phase regions of Hf_2Si (lighter) and Hf_3Si_2 (darker) phases, which are products of the eutectoid decomposition of the primary Hf_3Si_3 phase.

state is shown in Fig. 8. The calculated results agree well with the experimental data of Bondarenko [1976Bon].

4. Conclusions

A new version of the Hf-Si binary phase diagram was constructed in which the Hf_3Si_3 phase was included as a stable phase in the binary system. A complete thermodynamic description of the Gibbs energies of all stable phases in the system was developed. This was consistent with the majority of the phase diagram and thermochemistry data. The calculated invariant reaction temperatures were within 9 °C of the experimental data of Brukl [1968Bru]. The global optimization of both phase diagram and thermochemistry data has been used to check the reliability of the experimental results. The enthalpy of formation data of [1976Bon, 1980Sam, 1990Top, 1998Mes] agree well with one another and they also agree well with the optimized results. The current assessment takes into account the existence of the Hf_3Si_3 phase and the eutectoid reaction, $\text{Hf}_3\text{Si}_3 \leftrightarrow \text{Hf}_2\text{Si} + \text{Hf}_3\text{Si}_2$, at 1925 ± 25 °C.

Acknowledgments

The authors would like to thank D.J. Dalpe for melting the alloy and S.D. Sitzman and J.A. Sutliff for the EBSP. This re-

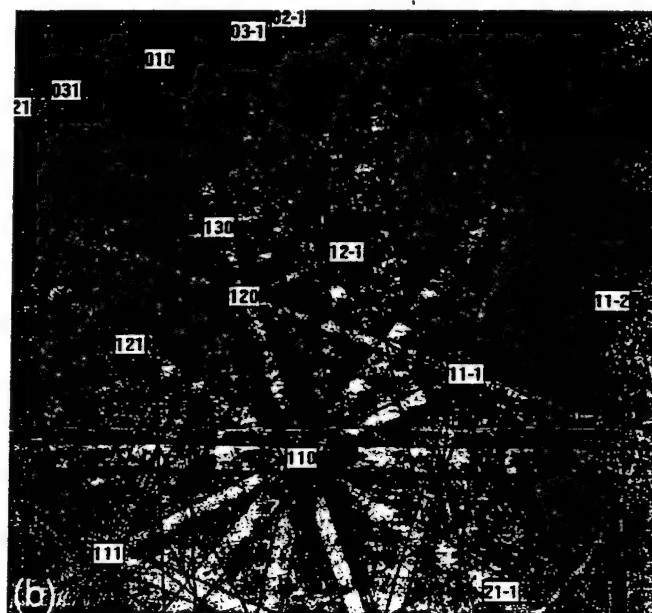
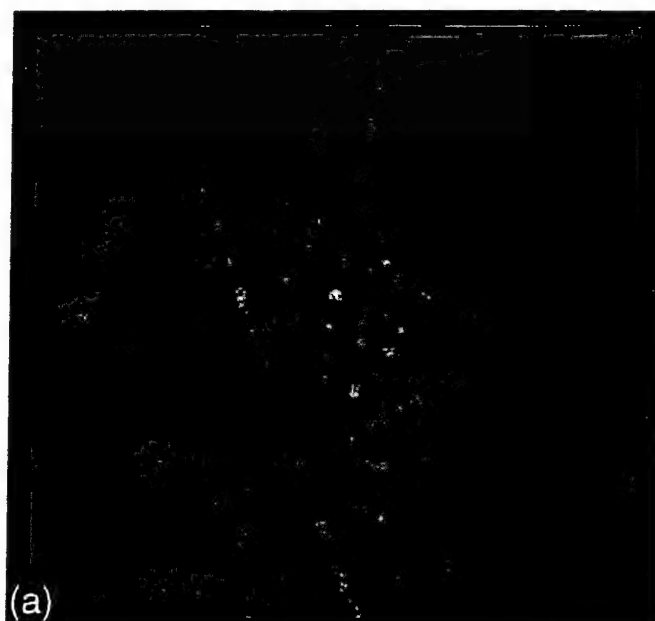


Fig. 6 EBSP of Hf_3Si_2 (a), with the indexed pattern shown in (b).

search was partially sponsored by the AFOSR under Contract No. F49620-96-C-0022 with Dr. Spencer Wu as Program Manager.

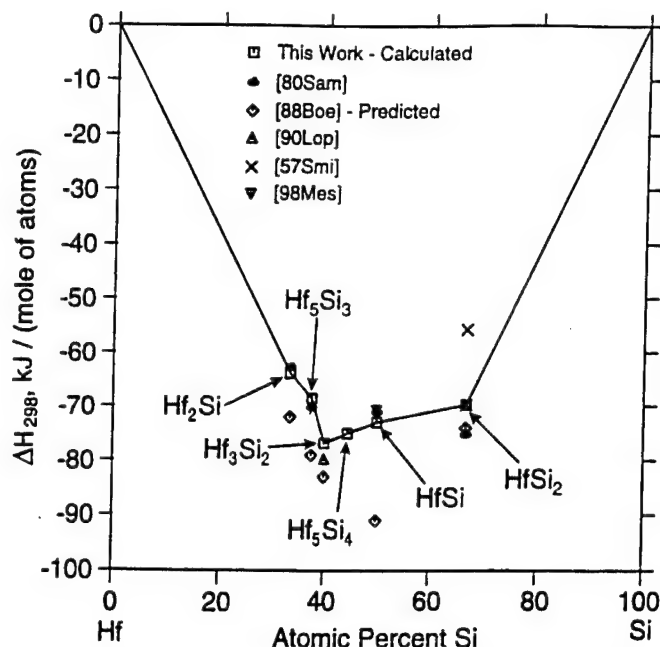


Fig. 7 Comparison of calculated and experimental enthalpies of formation of the Hf silicides at 25 °C (298 K).

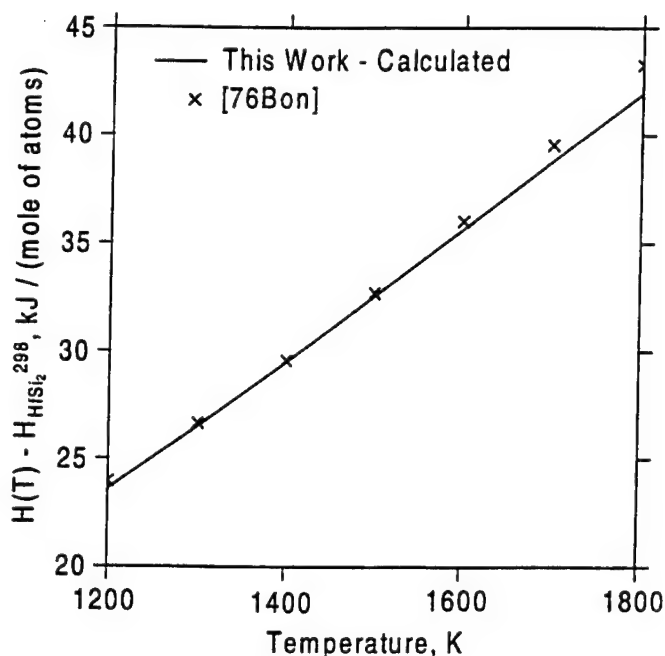


Fig. 8 Comparison of calculated and experimental $H(T) - {}^0H_{\text{HfSi}_2}^{298}$ for a Hf-66.7 at.% Si alloy

References

- 1948Red: O. Redlich and A. Kister: *Ind. Eng. Chem.*, Vol 40, 1948, p 345-48.
- 1957Smi: J.F. Smith and D.M. Bailey: *Acta Crystallogr.*, Vol 10, 1957, p 341-42.
- 1958Now: H. Nowotny, E. Laube, R. Kieffer, and F. Benesovsky: *Monatsh. Chem.*, Vol 89, 1958, p 701-07.
- 1960Now: H. Nowotny, H. Braun, and F. Benesovsky: *Radex Rundsch.*, Vol 6, 1960, p 367-72.
- 1960Vic: R.C. Vickery and H.M. Muir: "Refractory Gd and Hf Compound." Technical Report on Research Chemicals, No. RC-145, AD258218, Department of the Navy, Bureau of Ships, Washington, DC, 1960.
- 1968Bru: C.E. Brukl: "Ternary Phase Equilibria in Transition Metal-B-C-Si Systems. Part I. Binary System, Vol. 13. The Zr-Si and Hf-Si Systems." Technical Report AFML-TR-65-2, Air Force Materials Laboratory, WPAFB, OH, 1968.
- 1969Kar: O.G. Karpinsky and B.A. Evseyev: *Russ. Metall.*, Vol 3, 1969, p 128-30.
- 1971Gol: Y.M. Golutvin and E.G. Maslennikova: *Izv. Akad. Nauk SSSR Metall.*, Vol 13 (1), 1971, p 174-80.
- 1971Shu: A.K. Shurin and N. Todorov: *Metallofizika*, Vol 33, 1971, p 100-02.
- 1972Hav: E.E. Havinga, H. Damsma, and P. Hokkeling: *J. Less-Common Met.*, Vol 27, 1972, p 169-86.
- 1976Bon: V.P. Bondarenko: *Sov. Powder Metall. Met. Ceram.*, Vol 15, 1976, p 938-41.
- 1980Sam: G.V. Samsonov and I.M. Vinitskii: *Handbook of Refractory Compounds*, IFI/Plenum, New York, NY, 1980.
- 1985Sun: B. Sundman, B. Jansson, and J.O. Anderson: *CALPHAD*, Vol 9, 1985, p 153-90.
- 1988Boe: F.R. de Boer, R. Boom, W.C.M. Mattens, A.R. Miedema, and A.K. Niessen: *Cohesion in Metals*, North-Holland, Amsterdam, 1988.
- 1989Gok: A.B. Gokhale and G.J. Abbaschian: *Bull. Alloy Phase Diagrams*, Vol 10, 1989, p 390-93.
- 1989Men: M.G. Mendiratta and D.M. Dimiduk: *Mater. Res. Soc. Symp. Proc.*, Vol 133, 1989, p 441-46.
- 1990Oka: H. Okamoto: *Bull. Alloy Phase Diagrams*, Vol 11, 1990, p 513-19.
- 1990Top: L. Topor and O.J. Kleppa: *J. Less-Common Met.*, Vol 167, 1990, p 91-99.
- 1991Din: A.T. Dinsdale: *CALPHAD*, Vol 15, 1991, p 317-415.
- 1991Vil: P. Villars and L.D. Calvert: *Pearsons Handbook of Crystallographic Data for Intermetallic Phases*, 2nd ed., ASM International, Materials Park, OH, Vol 1-4, 1991.
- 1994Gue: C. Gueneau, C. Servant, I. Ansara, and N. Dupin: *CALPHAD*, Vol 18, 1994, p 319-27.
- 1996Jac: M.R. Jackson, B.P. Bewlay, R.G. Rowe, D.W. Skelly, and H.A. Lipsitt: *JOM*, Vol. 48, 1996, p 39-44.
- 1996Sub: P.R. Subramanian, M.G. Mendiratta, and D.M. Dimiduk: *JOM*, Vol 48, 1996, p 33-38.
- 1997Bew: B.P. Bewlay, J.J. Lewandowski, and M.R. Jackson: *JOM*, Vol 49, 1997, p 44-45.
- 1997Hen: G.A. Henshall, M.J. Strum, B.P. Bewlay, and J.A. Sutliff: *Metall. Mater. Trans., A* Vol 28A, 1997, p 2555-64.
- 1998Mes: S.V. Meschel and O.J. Kleppa: *J. Alloys Compounds*, Vol 280, 1998, p 231-39.
- 1999Bew: B.P. Bewlay, M.R. Jackson, and R.R. Bishop: *J. Phase Equilibria*, Vol. 20, 1999, p 109-12.
- 1999Lia: H. Liang and Y.A. Chang: *Intermetallics*, Vol 7, 1999, p 561-70.

Microstructural Response of DS Nb-Silicide In-Situ Composites During High-Temperature Creep Testing

B.P. Bewlay and S.D. Sitzman

Microscopy and Microanalysis, 2000

MICROSTRUCTURAL RESPONSE OF DS Nb-SILICIDE IN-SITU COMPOSITES DURING HIGH-TEMPERATURE CREEP TESTING

B.P. Bewlay and S.D. Sitzman

General Electric Corporate Research and Development, Schenectady, New York 12301

Directionally solidified (DS) in-situ composites based on (Nb) and Nb silicides, such as Nb_5Si_3 and Nb_3Si , are being investigated for high-temperature structural applications [1, 2]. The use of alloying additions, such as Hf, Ti and Mo, to these silicides is required to enhance their properties. The present paper describes the microstructural response of a DS Nb-silicide based composite to creep testing.

The composites investigated were directionally solidified from a molten alloy using the Czochralski method as described previously [2]. Creep tests were conducted at 1200°C to strains of up to 50%. Microstructure and microtexture characterizations were performed using scanning electron microscopy, electron microprobe analysis (EMPA), and electron backscatter diffraction pattern analysis (EBSP).

Microstructures of the longitudinal section of a DS composite generated from a Nb-12.5Hf-33Ti-16Si alloy are shown in Figure 1 in the as-DS (left hand side) and the DS+creep tested conditions (right hand side). The as-DS microstructure possessed elongated faceted primary dendrites and a fine-scale eutectic. EBSP identified the faceted dendrites as M_3Si -type t132 (where M denotes Nb, Hf and Ti), and the fine-scale eutectic as M_5Si_3 (hP16 crystal structure) and (Nb). In the phase colored images of the second row of Figure 1, the M_3Si is blue, the M_5Si_3 is green and the (Nb) is red. The $[001]$ Nb_3Si and the $[0001]$ $(\text{Hf,Ti})_5\text{Si}_3$ were parallel to the growth direction.

The creep deformed DS composite displayed bent M_3Si dendrites and break-up/refinement of the eutectic M_5Si_3 and (Nb). Quantitative characterization of the strain within the phases was performed using EBSP. Orientation images and a corresponding $\langle 001 \rangle$ pole figure of the M_3Si dendrites and a $[0001]$ pole figure of the M_5Si_3 eutectic are shown. The colors in the orientation images correspond with the individual pole colors on the pole figures. The DS direction and the creep deformation directions are also shown. The $[001]$ M_3Si and the $[0001]$ M_5Si_3 have rotated such that they are almost perpendicular to the deformation direction.

References

1. B.P. Bewlay, M.R. Jackson, and P.R. Subramanian, JOM, April 1999 Vol 51(4), pp. 32-36.
2. B.P. Bewlay, M.R. Jackson and H.A. Lipsitt, *Metall. and Mater. Trans.*, 279 (1996)3801-3808.

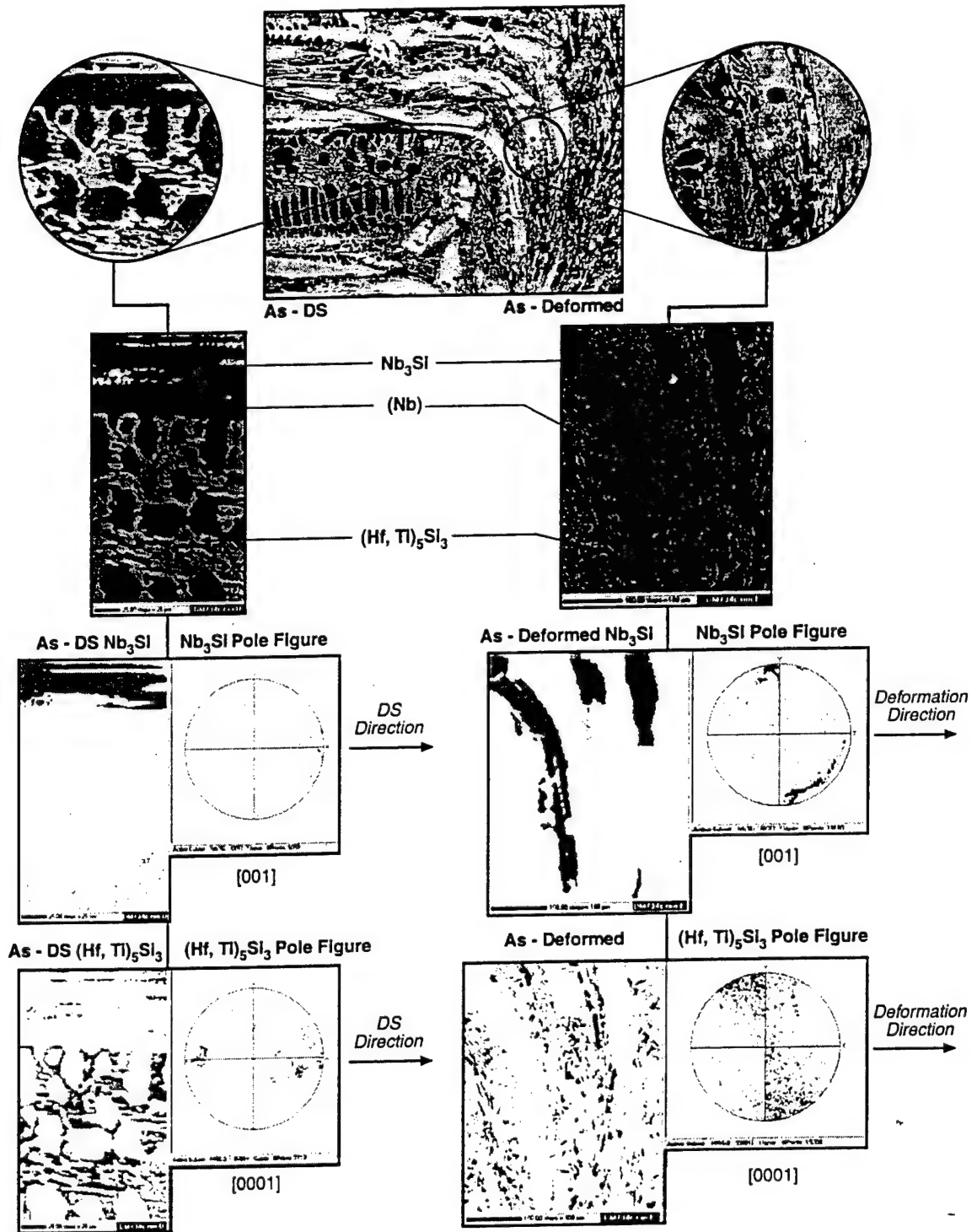


FIG. 1. Microstructures of the longitudinal section of a Nb-12.5Hf-33Ti-16Si composite before and after creep deformation at 1200 °C. The left-hand side figures show the microstructure and EBSD orientation images of a DS region. The [001] Nb₃Si and the [0001] (Hf,Ti)₅Si₃ were parallel to the growth direction. The right-hand side figures show the microstructure and EBSD orientation images of a region after creep deformation. The [001] Nb₃Si and the [0001] (Hf,Ti)₅Si₃ have rotated such that they are almost perpendicular to the deformation direction.

Creep Studies of the Monolithic Phases in Nb-Silicide
In-Situ Composites

B.P. Bewlay, C.L. Briant, E.T. Sylven, M.R. Jackson, and G. Xiao

Proceedings on High Temperature Ordered Intermetallic Alloys IX, 2000

Creep Studies of Monolithic Phases in Nb-Silicide Based In-Situ Composites

B.P. Bewlay¹, C.L. Briant², E.T. Sylven², M.R. Jackson¹ and G. Xiao²

¹GE Corporate Research and Development, Schenectady, NY 12301, USA

²Division of Engineering, Brown University, Providence, RI 02912, USA

ABSTRACT

Nb-silicide composites combine a ductile Nb-based solid solution with high-strength silicides, and they show great promise for aircraft engine applications. Previous work has shown that the silicide composition has an important effect on the creep rate. If the Nb:(Hf+Ti) ratio is reduced below ~1.5, the creep rate increases significantly. This observation could be related to the type of silicide present in the material. To understand the effect of each phase on the composite creep resistance, the creep rates of selected monolithic phases were determined. To pursue this goal, monolithic alloys with compositions similar to the Nb-based solid solution and to the silicide phases, Laves, and T2 phases, were prepared. The creep rates were measured under compression at 1100 and 1200°C. The stress sensitivities of the creep rates of the monolithic phases were also determined. These results allow quantification of the load bearing capability of the individual phases in the Nb-silicide based in-situ composites.

INTRODUCTION

Nb-silicide based in-situ composites are being explored for structural applications at very high temperatures [1-4]. These composites consist of Nb₅Si₃ and Nb₃Si type silicides toughened with a Nb solid solution (abbreviated by (Nb) in the present paper). More recent Nb-silicide based in-situ composites are highly alloyed with elements such as Cr, Ti, Hf, B and Al. These in-situ composites have demonstrated a promising combination of high-temperature strength, creep resistance, and room-temperature fracture toughness [1-3]. With the appropriate combination of alloying elements it is possible to achieve the required balance of room temperature toughness and high temperature creep resistance. Alloying elements such as Cr and B have beneficial effects on oxidation resistance, stabilizing Laves phases and T2 niobium borosilicide phases, respectively. The Nb₅Si₃ and Nb₃Si have the tI32 and tP32 ordered tetragonal structures with 32 atoms per unit cell. The unit cells also possess large lattice parameters; the large Burgers vectors and complex dislocation cores associated with these structures would suggest that dislocation creep makes only a small contribution to creep deformation in these silicides. When Nb₅Si₃ is alloyed with Ti and Hf, the less complex hP16 structure can also be stabilized [1, 6]. The Laves phases typically have C14, C15, or more complex structures of a hexagonal form [3].

The present study was performed to determine the creep rates of monolithic intermetallic phases and to develop the constitutive creep laws for these phases. These creep laws are also required to perform predictive modeling of more complex two-phase and multi-phase systems [7]. The monolithic phases described in this paper were produced by directional solidification, or arc melting, followed by homogenization heat treatments. Previous work indicated that creep deformation in binary Nb₅Si₃ is controlled by bulk diffusion of Nb in the Nb₅Si₃ [4]. The aim of the present paper is to describe high-temperature creep behavior of the monolithic intermetallic phases that exist in Nb-silicide in-situ composites.

EXPERIMENTAL

The samples were prepared using directional solidification [1, 3] or multiple arc melting. The starting charges were prepared from high purity elements (>99.99%). The samples were examined using scanning electron microscopy and Electron Back-Scatter Diffraction in the SEM (EBSD).

The compositions of the monolithic phases that were investigated are shown in Table I. The compositions of these monolithic alloys were selected on the basis of electron microprobe analyses (EMPA) of the phases in multi-phase composites [1, 3]. The monolithic phases that were generated from ternary alloys were given the post-script 3, for example, the Nb_5Si_3 modified with 10% Ti was described by silicide-3. The monolithic phases that were generated from quaternary and higher-order alloys were given the post-script C, such as silicide-C. The hP16-3 composition was based on EMPA of the hP-16 in previous studies [8]. The hP16-C composition was based on analyses of the hP16 phase in complex composites [1]. The (Nb) compositions were based on EMPA data from binary Nb-Si, ternary Nb-Ti-Si [8] and higher order alloys [1].

The microstructure of hP16-3 consisted principally of the hP16 phase, as confirmed using EBSD, and a volume fraction of ~0.05 of residual bcc (Nb). The homogenization treatment was not completely effective in removing the eutectic (Nb) associated with solidification. The microstructure of the hP16-C was similar to that of the hP16-3. The grain size of the hP16 phase for both alloys was ~100 μm . The other monolithic alloys were essentially single phase with only minor volume fractions of phases emanating from solidification segregation.

Compression creep tests were performed at a temperatures of 1100 and 1200°C, and at stress levels in the range 70-280 MPa. The cylindrical specimens that were used were 7.6 mm in diameter and up to 30 mm in length. The samples were machined by EDM to final dimensions. In each test the sample was placed between two 18.7 mm diameter silicon nitride platens to prevent breakage of the graphite rams. Pure niobium foil was placed at the interface between the platens and the sample to prevent any contamination of the sample or reaction with the platens. Creep testing was performed in a vacuum of ~4x10⁻⁵ Torr.

Table I : Compositions of the monolithic phases that were investigated (the compositions are given in atom per cent). The silicide phases are both Nb_5Si_3 -based.

PHASE	Nb	Ti	Hf	Si	Cr	Al	B
Laves-C	21.0	11.0	5.5	8.5	53.0	1.0	
Laves-3	30.0			15.0	55.0		
Silicide-C	38.5	16.0	6.0	37.0	1.0	1.0	0.5
Silicide-3	53.0	10.0		37.0			
T2-C	41.5	13.0	3.0	12.5	4.0	0.5	25.5
T2-3	62.5			12.5			25.0
hP16-3	20	44		36.0			
hP16-C	25.5	25.5	13	36.0			
(Nb) ₃ Si-C	49.0	18.2	7.8	25.0			
(Nb)-C	63.1	27	5	0.9	2	2	
Nb-1Si	99			1			
Nb-46Ti-1Si	53	46		1			

In order to perform a creep experiment, a sample was loaded at temperature to the first stress level of 70 MPa and held at that level for 24 hours. The creep rate was determined by analysis of the creep curves. After the 24-hour test, the sample dimensions were determined and the load was increased. This process was continued until the test was terminated or the sample failed.

RESULTS AND DISCUSSION

Creep Behavior at 1100°C

The data for the creep tests at 1100°C are shown in Figure 1. The data are not complete for all compositions, as will be discussed below. The data are well behaved for the ternary Nb_5Si_3 silicide-3 and the $\text{Nb}_3\text{Si-C}$. There is some scatter in the $\text{Nb}_5\text{Si}_3\text{-C}$ data; the highest creep rate that was measured was $2 \times 10^{-8} \text{ s}^{-1}$ at 210 MPa, and all other measurements were below this value. At creep rates $< 10^{-8} \text{ s}^{-1}$ there is generally more scatter in the data because these rates are very close to the measurement limit for the creep system that was employed ($\sim 5 \times 10^{-9} \text{ s}^{-1}$); this limit was governed by the dilatometer resolution, mechanical stability, and electrical noise. The silicide-3 and silicide-C have creep rates that are close to those of the binary Nb_5Si_3 at 1200°C, but they are slightly higher. The ternary Nb_5Si_3 with Ti substituted for Nb has a lower creep rate than the $\text{Nb}_5\text{Si}_3\text{-C}$. The $\text{Nb}_3\text{Si-C}$ has the highest creep rates. At 1100°C the creep rate of the T2 phase was $\sim 3 \times 10^{-8} \text{ s}^{-1}$, but there was little sensitivity of the creep rate to stress in the range studied.

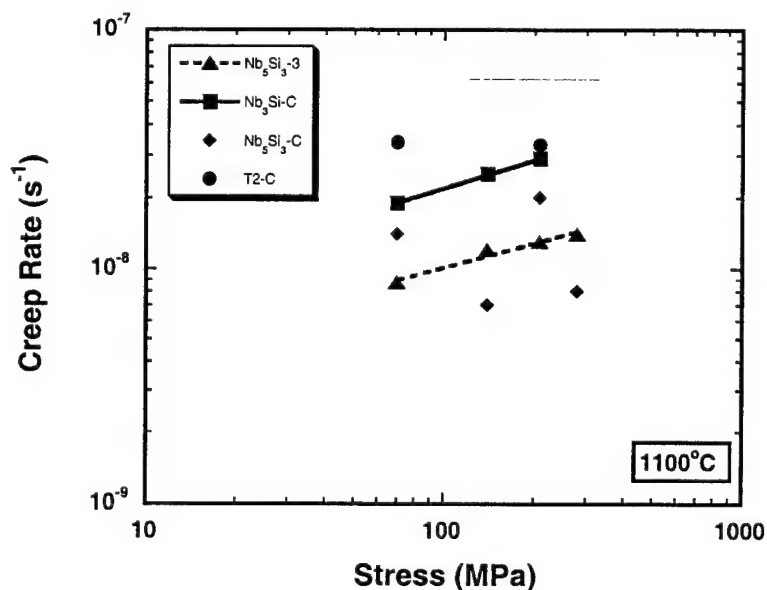


Figure 1 : Secondary creep rates at 1100°C for the monolithic phases that were investigated.

Due to limited ductility of some of the phases at 1100°C, cracking occurred in some cases during the creep test, and this led to some difficulties/inconsistencies in some creep strain measurements. For some of the alloys, such as Laves-3 and Laves-C, the creep rates were very low ($< 5 \times 10^{-9} \text{ s}^{-1}$) at low stresses (70 MPa), and increasing the stress led to cracking prior to creep. This behavior

was observed for the Laves-C at both 1100°C and 1200°C. Thus, there are no data in Figure 1 for the Laves phases and the T2-3 phase. The microstructures of the creep samples were analyzed after the creep test in order to investigate the type of cracking that occurred.

Creep data for the binary Nb_5Si_3 at 1200°C, as reported by Subramanian et al. [4], indicate that even at 1200°C the creep rate of the binary Nb_5Si_3 is less than that of any of the other phases at 1100°C. In order to determine the stress sensitivity of the creep rate, the creep rate ($\dot{\epsilon}$) and stress (σ) were related using a power law equation, $\dot{\epsilon} = B \sigma^n$; where n is the stress exponent and B is a constant at any specific temperature. The grain size of all the materials was large and similar in each case ($\sim 100\mu\text{m}$), and in this analysis no attempt was made to incorporate any grain size dependence. The constants obtained from these analyses are shown in Table II.

The monolithic (Nb) alloys have exponents of ~ 3 and in these systems deformation is probably controlled by dislocation creep. These exponents are similar to those reported previously for Nb-1.25Si [7]. At 1100°C further analysis of the exponents for the intermetallics is limited by the small data set. Exponents for the silicide-3 and Nb_3Si -C were determined, but they had values less than unity. This would suggest that there is some creep threshold, or other complicating factor, controlling creep deformation in these phases.

Table II : Power law constants for creep of the monolithic phases that were investigated.

Phase	Stress Range (MPa)	Temperature (°C)	Constant	Exponent
Nb_5Si_3	100-280	1200	6.16×10^{-11}	1.0
Nb-10Si	70-140	1200	6.57×10^{-12}	1.9
Silicide-C	70-140	1200	3.84×10^{-11}	1.5
Nb_3Si -C	70-140	1200	1.07×10^{-14}	3.6
Laves-3	70-140	1200	1.11×10^{-9}	1
T2-C	70-140	1200	2.15×10^{-9}	0.9
(Nb)-3	3-80	1100	1.9×10^{-10}	3.3
(Nb)	3-80	1100	4.7×10^{-14}	2.9

Creep Behavior at 1200°C

The data for the creep tests at 1200°C are shown in Figure 2. The data are well behaved for all alloys. Figure 2 also shows data for the binary monolithic Nb_5Si_3 and the Nb_5Si_3 -Nb composite prepared from the binary Nb-10Si alloy [7]. The binary Nb_5Si_3 possessed the lowest creep rates and the Nb_3Si -C displayed the highest creep rates of the tetragonal phases. The hP16 phases have creep rates similar to the T2-C phase at stresses up to 140 MPa. However, on increasing the stress above 140MPa the creep rate of the hP16-C increases dramatically to a level of $3 \times 10^{-5} \text{s}^{-1}$ at 210MPa, as shown in Figure 2. This behavior suggests a change in the creep mechanism with increasing stress. The hP16 phases have the worst performance, and at high stresses are beyond the scale of Figure 2.

The silicide-3 and silicide-C have creep rates that are slightly higher than those of the binary Nb_5Si_3 . The ternary Nb_5Si_3 with Ti has a lower creep rate than the Nb_5Si_3 -C. The T2-C creep

curve was higher than those of the Nb_5Si_3 type silicides, although it is lower than that of the Nb_3Si -C. The creep rate of the T2-3 was $\sim 1 \times 10^{-8} \text{ s}^{-1}$, but there was little sensitivity of the creep rate to stress. The T2-3 also has a lower creep rate than the T2-C; the addition of Ti, Hf, Cr and Al led to an increase in the creep rate of the T2. The Laves-3 possessed creep rates similar to those of the silicide-3.

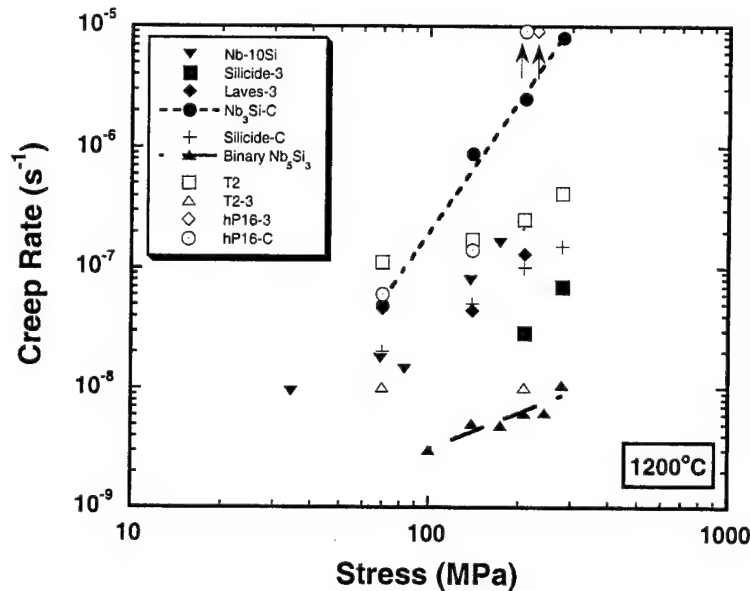


Figure 2 : Secondary creep rates at 1200°C for the monolithic silicides, Laves phases, hP16 and T2 phases that were investigated.

Of the phases studied, the Nb_3Si -C has the highest creep rate. Unfortunately, data for binary Nb_3Si was not obtained because this phase is generated by a peritectic reaction during solidification of hypereutectic alloys and it is extremely difficult to prepare in the bulk form as a metastable single phase. At 1200°C several of the monolithic phases, including the Laves phase and the Nb_3Si -C, have creep performance only equal to, or inferior to, that of the Nb_5Si_3 -Nb composite from the binary Nb-10Si alloy. The Nb_3Si -C has creep rates almost an order of magnitude higher than the Nb-10Si, and the stress exponent is almost two times higher. The hP16-C creep rates were also significantly higher than in the Nb-10Si composite.

The stress exponents were obtained and are shown in Table II. In the case of the Nb_5Si_3 , the stress exponent was almost one and the mechanism for creep deformation was reported to be Nabarro-Herring creep, the creep deformation being limited by Nb diffusion [4]. In the cast and heat treated conditions the dislocation densities in the monolithic phases investigated in the present study were very low and Harper-Dorn creep probably did not make a significant contribution to creep. The potential creep mechanisms are Nabarro-Herring, grain boundary sliding, or power law creep. Examination of the creep exponents in Table II indicates that the creep deformation of the monolithic phases is controlled by a range of mechanisms. For example, the T2-C, Laves-3, and silicide-C have exponents close to unity, as is the case for binary Nb_5Si_3 . At present there are insufficient data to establish a stress exponent for the silicide-3. Deformation of the silicide-C is

probably also controlled by Nabarro-Herring type creep, but the diffusing species that control deformation are still being investigated. The Nb_3Si -C displays a high stress sensitivity with a creep exponent of ~ 3.6 . This high stress exponent suggests that creep deformation is controlled by dislocation glide, as is the case for pure metals, despite the fact that the dislocation structures in this intermetallic are complicated.

CONCLUSIONS

The (Nb) solid solutions have creep rates at 1100°C and 1200°C that are more than an order of magnitude higher than the intermetallics investigated. Of the intermetallics investigated, the Nb_5Si_3 type silicides had the lowest creep rates. The complex Nb_3Si -C type silicide had the highest creep rate of the tetragonal silicides investigated. The hP16 silicide phases have higher secondary creep rates than any of the tetragonal silicides, or the T2 phases, at stresses greater than 140 MPa. At lower stresses, the hP16 silicide has creep rates similar to those of the T2 phase. Analysis of the creep exponents suggests that deformation of the complex Nb_5Si_3 type silicide is probably controlled by Nabarro-Herring type creep, as is the binary Nb_5Si_3 silicide. In contrast, creep of the Nb_3Si silicide appears to be controlled by a dislocation controlled mechanism.

ACKNOWLEDGMENTS

The authors would like to thank D.J. Dalpe for the directional solidification, C. Bull for assistance with creep testing, and Dr. V. Smentkowski for the EBSD. The authors would also like to thank Dr. P.R. Subramanian for his comments. This research was partially sponsored by AFOSR under contract #F49620-00-C-0014 with Dr. C.S. Hartley and Dr. S. Wu as Program Managers.

REFERENCES

- [1] B.P. Bewlay, M.R. Jackson and H.A. Lipsitt, *Metall. and Mater. Trans.*, 1996, Vol 279, pp. 3801-3808.
- [2] M.G. Mendiratta, J.J. Lewandowski and D.M. Dimiduk, *Metall. Trans. 22A* (1991), pp. 1573-1581.
- [3] P.R. Subramanian, M.G. Mendiratta, D.M. Dimiduk and M.A. Stucke, *Mater. Sci. Eng.*, A239-240, 1997, pp. 1-13.
- [4] P.R. Subramanian, T.A. Parthasarathy, M.G. Mendiratta and D.M. Dimiduk, *Scripta Met. and Mater.*, Vol. 32(8), 1995, pp. 1227-1232.
- [5] B.P. Bewlay, M.R. Jackson and H.A. Lipsitt, *Journal of Phase Equilibria*, Vol 18(3), 1997, pp. 264-278.
- [6] B.P. Bewlay, R.R. Bishop and M.R. Jackson, *Z. Metallkunde*, 1999, Vol 90, pp. 413-422.
- [7] G.A. Henshall, M.J. Strum, P.R. Subramanian, and M.G. Mendiratta, *Mat. Res. Soc. Symp. Proc.* 364, 1995, pp. 937-942.
- [8] B.P. Bewlay, R.R. Bishop and M.R. Jackson, *Journal of Phase Equilibria*, Vol 19(6), 1998, pp. 577-586.

The Effect of Silicide Volume Fraction on the Creep Behavior of Niobium-Silicide Based In-Situ Composites

B.P. Bewlay, C.L. Briant, A.W. Davis and M.R. Jackson

Proceedings on High Temperature Ordered Intermetallic Alloys IX, 2000

The Effect of Silicide Volume Fraction on the Creep Behavior of Nb-Silicide Based In-Situ Composites

B.P. Bewlay¹, C.L. Briant², A.W. Davis² and M.R. Jackson¹

¹GE Corporate Research and Development, Schenectady, NY 12301, USA

²Division of Engineering, Brown University, Providence, RI 02912, USA

ABSTRACT

This paper will describe the creep behavior of high-temperature Nb-silicide in-situ composites based on quaternary Nb-Hf-Ti-Si alloys. The effect of volume fraction of silicide on creep behavior, and the effects of Hf and Ti additions, will be described. The composites were tested in compression at temperatures up to 1200°C and stress levels in the range 70 to 280 MPa. At high (Nb) phase volume fractions the creep behavior is controlled by deformation of the (Nb) and, as the volume fraction of silicide is increased, the creep rate is reduced. However, at large silicide volume fractions (>0.7) damage in the silicide begins to degrade the creep performance. The creep rate has a minimum at a volume fraction of ~0.6 silicide. The creep performance of the monolithic and silicide phases will also be discussed.

INTRODUCTION

Nb-silicide based in-situ composites are potential candidates for use in high temperature structural applications. These composites consist of a Nb-based solid solution, denoted (Nb), strengthened by Nb₃Si and/or Nb₅Si₃ based silicides. Previous work has shown that these materials exhibit a good combination of room temperature fracture toughness and high temperature strength [1-3]. However, the high-temperature creep performance has been found to be highly dependent on the alloy composition and constituent phases. Two of the most common alloying additions are Ti and Hf, and these elements can adversely increase the creep rate to $>10^{-7} \text{ s}^{-1}$ at stress levels greater than 100 MPa, if they are present in concentrations greater than ~30 and 8 percent, respectively [4]. The composite creep rate may also be increased because increasing Ti and Hf stabilizes a hexagonal silicide [5]. In contrast, Nb₃Si and tetragonal Nb₅Si₃ are beneficial to creep behavior provided their volume fraction and distribution within the composite are controlled.

The aim of the present paper is to describe the effect of volume fraction of silicide on the creep rate of Nb-silicide based in-situ composites. Alloys were prepared with Si concentrations from 12 to 22 atomic percent (all compositions are given in atom percent in the present paper). These alloys provided a broad range of silicide volume fractions. The Ti and Hf concentrations were held constant at 25 and 8 atomic percent, respectively.

EXPERIMENTAL

All samples were prepared using Czochralski cold crucible growth [3]. Composites were directionally solidified from quaternary alloys with compositions of Nb-8Hf-25Ti-XSi, where X was

adjusted from 12 to 22%. The directional solidification procedure has been described in more detail previously [3]. Monolithic Nb alloys were also prepared with compositions of Nb-1Si, Nb-46Ti-1Si, and Nb-27Ti-5Hf-2Al-2Cr-0.9Si (denoted as Nb-C in the present paper), in order to determine the creep performance of the Nb solid solution in the in-situ composites at elevated temperatures.

All the creep data reported in the present paper were obtained in compression. Compression creep tests were performed at a temperature of 1200°C, and at stress levels in the range 70-280 MPa. The cylindrical specimens that were used were 7.6 mm in diameter and 15 mm long, and they were machined from DS samples such that the loading axis of the creep sample was parallel to the growth direction. In order to perform the creep test, the sample was first heated to the test temperature. A load was then applied to the sample, and it was maintained at a constant value for 24 hours. During this 24 hour period the strain was monitored and the creep rate was obtained through analysis of these data. A vacuum of approximately 5×10^{-5} Torr was maintained throughout the test. The sample was measured after each test and then used for the tests at higher stresses.

Detailed metallographic information was obtained using both optical microscopy and scanning electron microscopy before and after the creep test. Electron back scatter diffraction pattern analysis (EBSD) and orientation imaging in the scanning electron microscope were used to identify the phases and their crystallographic orientations.

RESULTS AND DISCUSSION

The typical microstructure of the composites with Si concentrations of 20% and less is shown in Figure 1. The microstructure consisted of large-scale $(\text{Nb})_3\text{Si}$ tP32 phase (the grey phase) with large-scale (Nb) dendrites (the light phase). Both the $(\text{Nb})_3\text{Si}$ and the (Nb) possess substantial amounts of Hf and Ti in solid solution [5, 6]. There was some segregation in the (Nb) which led to varying BSE contrast at the interface between the (Nb) and the $(\text{Nb})_3\text{Si}$. EPMA and EBSD data indicated that this was a result of Ti segregation and Hf/Nb depletion in these regions.

A typical microstructure of the composites with Si concentrations greater than 20% is shown in Figure 2. In addition to the faceted $(\text{Nb})_3\text{Si}$ and (Nb) phases observed in the composites from lower Si concentrations, the Nb_5Si_3 tI32 phase was also observed as the primary solidification phase. The $(\text{Nb})_5\text{Si}_3$ was the large-scale, dark, faceted phase in the micrograph of Figure 2.

Figure 3 shows the creep rate at 1200°C as a function of Si concentration for the Nb-25Ti-8Hf-XSi composites, where X was varied from 12 to 22 atomic percent. Data are shown for stresses of 70 to 280 MPa. As the Si concentration was increased from 12% to 18%, the volume fraction of $(\text{Nb})_3\text{Si}$ increased from 0.25 to 0.62. There is a broad range of compositions for which the creep rate is less than $3 \times 10^{-8} \text{ s}^{-1}$.

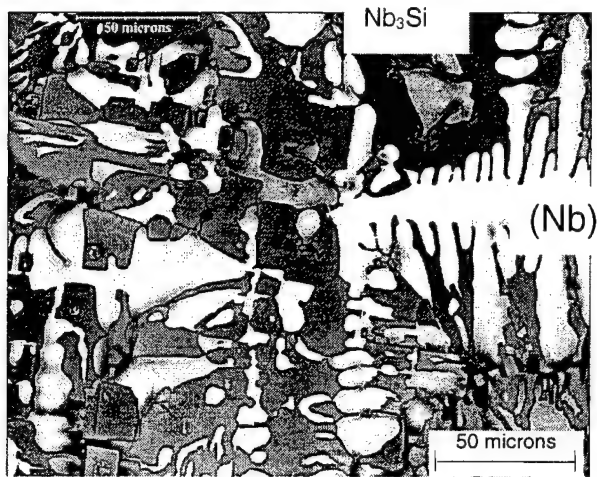


Figure 1. Typical microstructure (BSE image) of the transverse section of a DS composite generated from a quaternary Nb-25Ti-8Hf-16Si alloy. The (Nb) is the light phase and the $(\text{Nb})_3\text{Si}$ is the grey faceted phase.

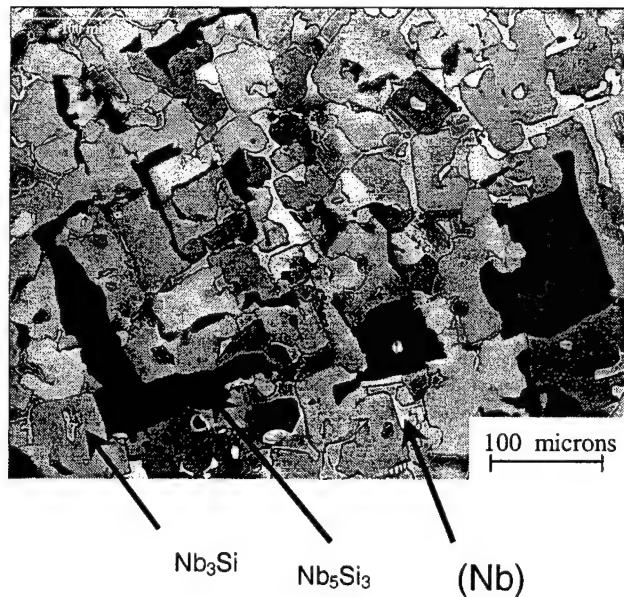


Figure 2. Typical microstructure (BSE image) of the transverse section of a DS composite generated from a quaternary Nb-25Ti-8Hf-22Si alloy. The (Nb) is the light phase, the $(\text{Nb})_3\text{Si}$ is the grey faceted phase, and the $(\text{Nb})_5\text{Si}_3$ the dark phase.

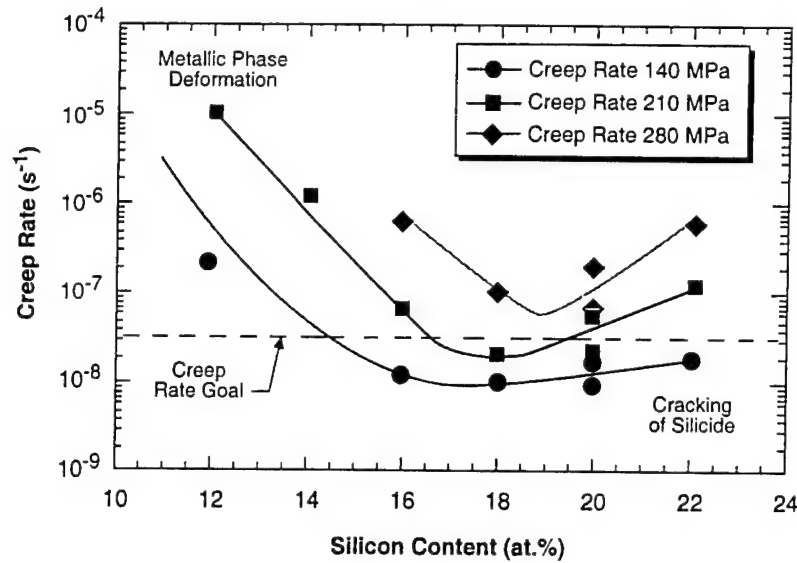


Figure 3. The effect of Si concentration and volume fraction of (Nb) and silicide on the secondary creep rate at 1200°C for stresses of 140-280 MPa.

These data reveal several important points. First, for a constant Si concentration, the creep rate increased with increasing applied stress. Second, the creep rate possessed a minimum value at approximately 18 %Si. At higher Si concentrations the creep rate increased again. Microstructural analysis of the samples after the creep test indicated that at low Si concentrations, deformation was controlled by creep of the (Nb) and at high Si concentrations, composite deformation was controlled by cracking of the silicide.

In order to interpret these results further, the creep behavior of the (Nb) was investigated. Figure 4 shows the creep rate of the Nb-1Si, Nb-46Ti-1Si, and Nb-C at 1100°C and 1200°C as a function of stress. The compositions of these alloys cover the compositions of the Nb-based solid solutions in the composites that have been generated previously from ternary, quaternary, and higher-order alloys. The results at 1200°C show that the creep rate of the (Nb) is greater than 10^{-7} s^{-1} even at stresses as low as 70 MPa. The creep rates of the Nb-C, Nb-1Si and Nb-46Ti-1Si are similar to those of the composites from the low Si (less than 14%) quaternary alloys shown in Figure 3. These results also show that the creep rate of the Nb-Si solid solution is very sensitive to additions of Ti. In order to determine the stress sensitivity of the creep rate, the creep rate ($\dot{\epsilon}$) and stress (σ) for the three alloys at 1100°C and 1200°C were fitted to a power law creep expression, $\dot{\epsilon} = B \sigma^n$; where n is the stress exponent and B is a constant at any specific temperature.

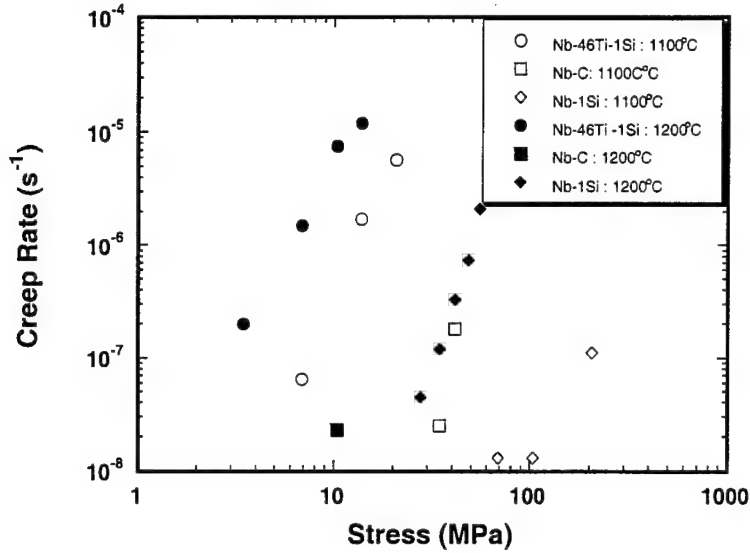


Figure 4. Secondary creep rates as a function of stress at 1100°C and 1200°C for binary Nb-Si, ternary Nb-Ti-Si, and complex Nb-based monolithic solid solutions. The effect of alloying additions on creep rate is shown.

The second set of creep data that must be considered are those for the Nb_5Si_3 silicide [7]. The Nb_5Si_3 creep rates are much lower than those for the Nb-based solid solutions and are similar to those for the high-Si quaternary alloys. In order to develop a better understanding of the response of the composite to increasing silicide volume fraction and increasing stress, the constitutive behavior of the composite was simulated using the expressions provided by Henshall et al. [8, 9], where σ_A is the applied stress, n is the stress exponent for the silicide (1.0), and m is the stress exponent for the Nb (2.9). V_s and V_w are the volume fractions of the silicide and Nb, respectively. A_s and A_w are the pre-exponents in the power law creep expressions for the silicide and Nb, respectively.

$$\sigma_A = V_s \left[\frac{1}{A_s^{1/n}} \right] \dot{\epsilon}^{1/n} + V_w \left[\frac{1}{A_w^{1/m}} \right] \dot{\epsilon}^{1/m}$$

The creep data for the Nb-1Si solid solution were used together with those for the binary monolithic Nb_5Si_3 [8]. This equation can predict the increase in the creep rate with increasing stress for a given Si concentration, as will be published subsequently [10]. However, this equation does not predict as strong a dependence on the silicide volume fraction as was observed experimentally. This difference may arise because the power law creep parameters used were those for Nb-1Si, rather than those for the actual quaternary (Nb) alloys of the composites tested. In addition, the damage accumulation that occurs at Si concentrations greater than 18% is at present not modeled. Thus, the results from the monolithic silicide and the (Nb) studies suggest that at low Si concentrations the creep rate is dominated by the (Nb), but that as the Si concentration is increased, and the silicide volume fraction is increased, the creep rate decreases.

CONCLUSIONS

The creep rates of the composites from the quaternary Nb-Hf-Ti-Si alloys decreased with increasing Si concentration from 12 to 18%. At higher Si concentrations, the creep rate increased as a result of crack linking and damage accumulation in the silicides. The composite creep rate increased with increasing stress, and at each stress level there was a minimum in the creep rate at ~18Si. The Nb solid solutions have creep rates at 1100°C and 1200°C that can be more than an order of magnitude higher than those of the composites.

Modeling results and experimental data from the monolithic silicides and Nb solid solutions indicate that at low Si concentrations the creep deformation is dominated by the (Nb), but as the Si concentration is increased, and the silicide volume fraction is increased, the composite creep performance is controlled by the silicide. However, the model underestimates the effect of increasing volume fraction of the silicide on the creep rate. The model is currently being extended to improve the predictive capability.

ACKNOWLEDGMENTS

The authors would like to thank D.J. Dalpe for the directional solidification, and C. Bull for assistance with creep testing. This research was partially sponsored by AFOSR under contract #F49620-00-C-0014 with Dr. C.S. Hartley and Dr. S. Wu as Program Managers.

REFERENCES

- [1] P.R. Subramanian, M.G. Mendiratta, D.M. Dimiduk and M.A. Stucke, *Mater. Sci. Eng.*, A239-240, 1997, pp. 1-13
- [2] P.R. Subramanian, M.G. Mendiratta and D.M. Dimiduk, *Mat. Res. Soc. Symp. Proc.*, 322 (1994), pp. 491-502.
- [3] B.P. Bewlay, M.R. Jackson and H.A. Lipsitt, *Metall. and Mater. Trans.*, 1996, Vol 279, pp. 3801-3808.
- [4] B.P. Bewlay, P. Whiting and C.L. Briant, *MRS Proceedings on High Temperature Ordered Intermetallic Alloys VIII*, 1999, pp. KK6.11.1- KK6.11.5.
- [5] B.P. Bewlay, M.R. Jackson and H.A. Lipsitt, *Journal of Phase Equilibria*, Vol 18(3), 1997, pp. 264-278.
- [6] B.P. Bewlay, R.R. Bishop and M.R. Jackson, *Journal of Phase Equilibria*, Vol 19(6), 1998, pp. 577-586.
- [7] P.R. Subramanian, T.A. Parthasarathy and M.G. Mendiratta and D.M. Dimiduk, *Scripta Met. and Mater.*, Vol. 32(8), 1995, pp. 1227-1232.
- [8] G.A. Henshall and M.J. Strum, *Scripta Metall.*, Vol 30(7), 1994, pp. 845-850
- [9] G.A. Henshall, M.J. Strum, P.R. Subramanian, and M.G. Mendiratta, *Mat. Res. Soc. Symp. Proc.* 364, 1995, pp. 937-942.
- [10] C.L. Briant and B.P. Bewlay, to be published.

Determination of Nb-Hf-Si Phase Equilibria

J.C. Zhao, B.P. Bewlay, M.R. Jackson

submitted to *Journal of Intermetallics*, 2001

Determination of Nb-Hf-Si Phase Equilibria

J.-C. Zhao*, B.P. Bewlay, M.R. Jackson

General Electric Company, Corporate Research and Development,

P.O. Box 8, Schenectady, New York 12301.

Abstract

Phase equilibria of Nb-Hf-Si at 1500 °C have been investigated for the metal-rich end of the ternary phase diagram using scanning electron microscopy, electron probe microanalysis, and electron backscatter diffraction analysis. An isothermal section at 1500 °C was constructed for this ternary system based on experimental data from 11 alloys heat treated at 1500 °C for 100 hrs. Phase equilibria between the following silicides, Nb(Hf)₅Si₃, Hf(Nb)₅Si₃, Nb(Hf)₃Si, Hf(Nb)₂Si, Hf(Nb)₃Si₂, Hf(Nb)₅Si₄, Hf(Nb)Si, Nb(Hf)Si₂, and two metal-rich solid solutions, β (Nb,Hf,Si) and α (Hf,Nb,Si) are described.

Keywords: A. Composite (based on silicides); B. Phase diagram; D. microstructure (as-cast); G. aero-engine components.

* Corresponding author. Tel.: 1-518-387-4103; fax: 1-518-387-6232. E-mail address: ZhaoJC@crd.ge.com

1. Introduction

Niobium silicide based in-situ composites are potential candidates for turbine airfoil materials in advanced aircraft engines [1-4]. Phase stability in these composites is required to define the optimum compositions and microstructures for property improvements and high temperature stability. This work defines phase equilibria in the binary and ternary systems [5-9] that are required to understand phase stability in the multicomponent composites. Hf has been added to improve oxidation resistance and strength [2, 10]. However, there is presently incomplete knowledge of the Hf-Si binary system and there is little existing information on the Nb-Hf-Si ternary system. In this regard, previous work has been conducted to investigate the stability of the Hf-Si binary system [8,9] and the liquid-solid phase equilibria of the Nb-Hf-Si system using directionally solidified alloys [7]. This paper reports the isothermal section of the Nb-Hf-Si system at 1500 °C. This is required to define phase stability of the composites during service. This temperature was selected because it is below the eutectoid decomposition temperature of Nb₃Si, but high enough for fast decomposition kinetics. The phase equilibria at 1500 °C are likely to be very similar to those at the potential service temperature, 1200 to 1400 °C.

A schematic three-dimensional (3-D) projection of the metal-rich region of the Nb-Hf-Si phase diagram (all compositions are in at.% throughout this paper) is shown in Fig. 1. The binary Nb-Hf system is based on an assessment by Fernandez-Guillermé [11]; the Nb-Si system is based on the assessments of Schlesinger, et al. [12] and Liang and Chang [13]; and the Hf-Si binary is based on a recent assessment [9]. Experimental results supporting the Nb-Hf-Si ternary phase diagram will be presented in the present article.

A total of 10 phases are discussed in this paper. Their crystal structures are listed in Table 2 [14, 15]. The Nb₃Si with Hf in solid solution is referred to as Nb(Hf)₃Si; the Nb₅Si₃ with Hf in solid solution, Nb(Hf)₅Si₃; the NbSi₂ with Hf in solid solution, Nb(Hf)Si₂; the HfSi with Nb in solid solution, Hf(Nb)Si; the Hf₅Si₄ with Nb in solid

solution, $\text{Hf}(\text{Nb})_5\text{Si}_4$; the Hf_3Si_2 with Nb in solid solution, $\text{Hf}(\text{Nb})_3\text{Si}_2$; the Hf_5Si_3 with Nb in solid solution, $\text{Hf}(\text{Nb})_5\text{Si}_3$; the Hf_2Si with Nb in solid solution, $\text{Hf}(\text{Nb})_2\text{Si}$. None of these silicides are isomorphous. In addition, there were two Nb-Hf solid solutions containing small amounts of Si for which the hcp phase is given the prefix α and the bcc phase is given the prefix β .

The aim of the present paper is to describe the 1500 °C isothermal section of the metal-rich end of the Nb-Hf-Si phase diagram.

2. Experimental procedures

The samples were prepared using either cold crucible directional solidification (DS) [2, 16] after triple melting the starting charges from high purity elements ($> 99.99\%$), or induction skull melting (ISM). The DS procedure has been described in more detail previously [16]. The as-cast microstructures of the corresponding alloys have been described in detail elsewhere [7]. The sum of the concentrations of the interstitials (O, N, and C) of the starting elements was less than 80 wt. ppm. Table 1 shows the range of nominal compositions that was investigated. Samples for heat treatment were wrapped in Nb foil and heat treated at 1500 °C for 100 hours in a vacuum ($<10^{-5}$ Torr) furnace. All of the samples were examined using scanning electron microscopy (SEM) backscatter electron (BSE) imaging and energy dispersive spectrometry (EDS).

Phase compositions were measured on selected samples using electron probe microanalysis (EPMA) which was performed on a JEOL 733 microprobe operating at 15 kV, 20 nA, and $\sim 1 \mu\text{m}$ beam diameter. Pure Nb, pure Hf and stoichiometric Hf_2Si were used as standards for Nb, Hf and Si, respectively. There is indigenous Zr in essentially all commercially available Hf. The Zr content in the cast alloys was estimated at $\leq 2 \text{ at.}\%$. Zr analysis was performed along with the other three elements and the Zr concentration in all the phases was less than $\sim 3 \text{ at.}\%$. In consideration of the similarity of Zr and Hf –

which can be appreciated by the similarity of the Hf-Si and Zr-Si phase diagrams [9, 17], Zr concentration was added to Hf concentration for each EPMA measurement.

Phase identification of selected compositions was also performed using the electron backscatter diffraction (EBSD) technique in SEM [18,19]. This technique allows easy selection of microstructural features using BSE imaging for rapid diffraction pattern collection and analysis. A CamScan CS44 SEM (Cam Scan Electron Optics, Ltd., Cambridge, England) was operated using a 40 kV, ~10 nA electron beam. Positive phase identification was accomplished by direct comparison of the location and character of the diffraction bands in the experimental pattern with those calculated from simulated patterns generated using the possible structure types and lattice parameters.

3. Results and discussion

The microstructure, phase composition and crystal structure data obtained from selected samples are summarized in the isothermal section shown in Fig. 2, and in Table 1. These will be described in more detail below:

Nb-10Hf-16Si:

The equilibrium microstructure was three-phase $\beta(\text{Nb,Hf,Si}) + \text{Nb}(\text{Hf})_5\text{Si}_3 + \text{Hf}(\text{Nb})_2\text{Si}$. Typical BSE micrographs are shown in Fig. 3. The bright phase was $\text{Hf}(\text{Nb})_2\text{Si}$, the light gray phase was $\text{Hf}(\text{Nb})_2\text{Si}$, the darker gray phase was $\text{Nb}(\text{Hf})_5\text{Si}_3$, and the darkest phase was $\beta(\text{Nb,Hf,Si})$. The crystal structures of these phases were confirmed using EBSD. Most of the eutectic $\text{Nb}(\text{Hf})_3\text{Si}$ phase in the as-DS alloy (the as-DS microstructure consisted of $\beta(\text{Nb,Hf,Si})$ dendrites with interdendritic cells of $\text{Nb}(\text{Hf})_3\text{Si}$ and $\beta(\text{Nb,Hf,Si})$, see, Ref. 7) underwent the eutectoid decomposition to $\beta(\text{Nb,Hf,Si})$ and $\text{Nb}(\text{Hf})_5\text{Si}_3$ during the 1500 °C annealing. In addition, because of the inhomogeneous nature of the as-DS alloys, there were $\text{Hf}(\text{Nb})_2\text{Si}$ and $\text{Hf}(\text{Nb})_5\text{Si}_3$ phases formed in Hf-rich interdendritic regions. Thus, four phases were observed in the 1500°C sample, and this made it possible to define two three-phase regions: $\beta(\text{Nb,Hf,Si}) + \text{Nb}(\text{Hf})_5\text{Si}_3 +$

Hf(Nb)₂Si and Nb(Hf)₅Si₃ + Hf(Nb)₂Si + Hf(Nb)₅Si₃. The solubility of Hf in the Nb(Hf)₅Si₃ phase is ~16%. The solubility of Nb in Hf(Nb)₅Si₃ and Hf(Nb)₂Si are ~36% and ~47%, respectively. After 100 hrs, the alloy had still not reached full equilibrium. On prolonged annealing, the Hf(Nb)₅Si₃ phase would be expected to transform to Hf(Nb)₂Si (and/or Nb(Hf)₅Si₃) as more Nb diffused into the region (and Hf and Si diffused out). In addition, there were regions where the Nb(Hf)₃Si was still experiencing the eutectoid decomposition process, as shown in Fig. 3(b).

Nb-10Hf-18.5Si:

The annealed microstructure was similar to that of Nb-10Hf-16Si. Again the Nb(Hf)₃Si phase underwent partial eutectoid decomposition into β (Nb,Hf,Si) and Nb(Hf)₅Si₃ and the decomposition process was not fully complete.

Nb-10Hf-25Si:

The equilibrium structure was two-phase β (Nb,Hf,Si) + Nb(Hf)₅Si₃. The Nb(Hf)₃Si phase in the as-DS alloy underwent partial eutectoid decomposition to β (Nb,Hf,Si) and Nb(Hf)₅Si₃ after the 1500 °C heat treatment as shown in Fig. 4. The eutectic regions in as-DS condition were richer in Hf and there was some Hf(Nb)₅Si₃ formed after the 1500°C treatment. Again the alloy had not fully equilibrated after 100 hrs. Some regions were still in the decomposition process, as shown in Fig. 4(b). EPMA from regions where decomposition appeared complete yielded an average composition of 95.3Nb-4.2Hf-0.5Si for the metal (bcc) phase, 55.2Nb-10.5Hf-34.3Si for the Nb(Hf)₅Si₃, and 36.7Nb-26.1Hf-37.2Si for Hf(Nb)₅Si₃.

Nb-30Hf-25Si:

The microstructure consisted predominately of two-phases, β (Nb,Hf,Si) + Hf(Nb)₂Si, as shown in Fig. 5 and the equilibrium microstructure was these two phases. The primary Hf(Nb)₅Si₃ in as-DS alloy had transformed into the equilibrium Hf(Nb)₂Si phase on annealing. The β (Nb,Hf,Si) and Hf(Nb)₂Si had compositions of 81Nb-18.5Hf-0.5Si and 33.5Nb-32.8Hf-31.7Si respectively. In some areas the Hf(Nb)₂Si phase possessed a

higher Hf concentration (24.4Nb-42.5Hf-33.1Si); this was probably the result of compositional inhomogeneity (dendrites vs eutectic regions) in the as-DS structures. There was also some $\alpha(\text{Nb,Hf,Si})$, which was probably also the result of inhomogeneity.

Nb-40Hf-30Si:

The equilibrium microstructure also consisted of two phases, $\beta(\text{Nb,Hf,Si}) + \text{Hf}(\text{Nb})_2\text{Si}$, but the volume fraction of the $\text{Hf}(\text{Nb})_2\text{Si}$ phase was much higher, as shown in Fig. 6. The primary $\text{Hf}(\text{Nb})_5\text{Si}_3$ in as-DS alloy had transformed into the equilibrium $\text{Hf}(\text{Nb})_2\text{Si}$ phase after annealing. The compositions of $\beta(\text{Nb,Hf,Si})$ and $\text{Hf}(\text{Nb})_2\text{Si}$ were 68.4Nb-30.7Hf-0.9Si and 23.2Nb-44.1Hf-32.7Si respectively. The Hf concentrations of both phases are higher than those of the Nb-30Hf-25Si alloy; this is consistent with the phase diagram shown in Fig. 2. Some areas had $\text{Hf}(\text{Nb})_2\text{Si}$ with a higher Hf concentration (18.8Nb-48Hf-33.2Si), again this was probably the result of compositional inhomogeneity (dendrites vs eutectic regions) in the as-DS structures.

Nb-60Hf-25Si:

The microstructure also consisted predominately of two phases, $\beta(\text{Nb,Hf,Si}) + \text{Hf}(\text{Nb})_2\text{Si}$, as shown in Fig. 7, and these were the equilibrium phases. The primary $\text{Hf}(\text{Nb})_5\text{Si}_3$ in the as-DS alloy had transformed into the equilibrium $\text{Hf}(\text{Nb})_2\text{Si}$ phase after annealing. The compositions of $\beta(\text{Nb,Hf,Si})$ and $\text{Hf}(\text{Nb})_2\text{Si}$ were 34.0Nb-63.9Hf-2.1Si and 9.0Nb-58.0Hf-33.0Si respectively. There were also some small Hf-rich particles (Fig. 7(b)) that were too small to be identified using SEM, EBSD, or EMPA. These particles were either remnant of some Hf-rich regions during decomposition or precipitates that formed during cooling. There were also some larger scale ($\sim 20 \mu\text{m}$ s) Hf-rich $\alpha(\text{Hf,Nb,Si})$ particles with average compositions varying from 4.6Nb-92.2Hf-3.2Si to 10.9Nb-86.3Hf-2.8Si (Fig. 7(a)). These phases were non-equilibrium and they would have been homogenized out at longer annealing times.

Nb-73Hf-17Si:

Two different interpretations of the microstructure (Fig.8) are possible. The first scenario is that the equilibrium microstructure was two-phase $\beta(\text{Nb,Hf,Si}) + \text{Hf}(\text{Nb})_2\text{Si}$. The white, lath/plate-like precipitates were transformed $\alpha(\text{Hf,Nb,Si})$ formed from the high temperature $\beta(\text{Nb,Hf,Si})$ phase on cooling from 1500 °C, which can be appreciated by looking at the Nb-Hf binary phase diagram [11] (see Fig. 1). There were also some $\alpha(\text{Hf,Nb,Si})$ phase precipitates formed at 1500 °C in Hf-rich regions, but these had some precipitates in them, probably $\text{Hf}(\text{Nb})_2\text{Si}$. The average composition for the $\text{Hf}(\text{Nb})_2\text{Si}$ phase was 3.8Nb-62.6Hf-33.7Si. It was difficult to measure the $\beta(\text{Nb,Hf,Si})$ phase composition at 1500 °C because of the $\beta \rightarrow \alpha$ transformation. The transformed β and α compositions were 23.4Nb-74.1Hf-2.5Si and 3.3Nb-93.7Hf-3.0Si respectively. The original $\beta(\text{Nb,Hf,Si})$ phase composition was probably close to the average of the two, based on a near 50:50 mixture in Fig. 8. The tie-line was not drawn due to uncertainty in the β -phase composition.

The second interpretation is that the equilibrium microstructure was three-phase: $\alpha(\text{Hf,Nb,Si}) + \beta(\text{Nb,Hf,Si}) + \text{Hf}(\text{Nb})_2\text{Si}$ in which the $\alpha(\text{Nb,Hf,Si})$ and $\beta(\text{Nb,Hf,Si})$ phase had a composition of 3.3Nb-93.7Hf-3.0Si and 23.4Nb-74.1Hf-2.5Si, respectively. The $\beta(\text{Nb,Hf,Si})$ phase composition, however, seems inconsistent with that projected from the Nb-Hf binary phase diagram.

Nb-80Hf-5Si:

The equilibrium microstructure could be two-phase $\beta(\text{Nb,Hf,Si}) + \text{Hf}(\text{Nb})_2\text{Si}$, or three-phase $\alpha(\text{Hf,Nb,Si}) + \beta(\text{Nb,Hf,Si}) + \text{Hf}(\text{Nb})_2\text{Si}$. The amount of $\text{Hf}(\text{Nb})_2\text{Si}$ was very small. The $\beta(\text{Nb,Hf,Si})$ phase transformed to $\beta(\text{Nb,Hf,Si})$ and $\alpha(\text{Hf,Nb,Si})$ on cooling from 1500 °C, Fig. 9. There were also precipitates, probably $\beta(\text{Nb,Hf,Si})$, formed during cooling in the original $\alpha(\text{Hf,Nb,Si})$ phase, Fig. 9(b). No EPMA was performed on this sample. This alloy was probably in a two-phase region.

Nb-90Hf-5Si:

The equilibrium microstructure probably consisted of three-phase $\beta(\text{Nb,Hf,Si}) + \alpha(\text{Nb,Hf,Si}) + \text{Hf}(\text{Nb})_2\text{Si}$, Fig. 10. The light gray phase was $\alpha(\text{Hf,Nb,Si})$ with an average composition of 3.1Nb-93.1Hf-3.8Si. The dark gray phase had an average composition of 21.7Nb-75.6Hf-2.7Si and was $\beta(\text{Nb,Hf,Si})$. The original $\beta(\text{Nb,Hf,Si})$ phase further transformed to $\beta(\text{Nb,Hf,Si})$ and $\alpha(\text{Hf,Nb,Si})$ on cooling from 1500 °C and appeared as a two-phase structure in Fig. 10. The average composition of the two-phase region obtained via area-average scanning mode in EMPA was 11.3Nb-85.0Hf-3.7Si which probably represents the original $\beta(\text{Nb,Hf,Si})$ phase composition at 1500 °C. The dark phase in Fig. 10 was $\text{Hf}(\text{Nb})_2\text{Si}$ with a composition of 2.0Nb-64.4Hf-33.6Si.

Nb-50Hf-37.5Si:

The ISM ingot was very inhomogeneous. After the 1500 °C anneal, part of the sample displayed a well-defined three-phase structure, as shown in Fig. 11(a). The three phases were identified as $\text{Hf}(\text{Nb})\text{Si}$, $\text{Hf}(\text{Nb})_5\text{Si}_4$, and $\text{Nb}(\text{Hf})\text{Si}_2$ with compositions of 4.7Nb-45.9Hf-49.4Si, 21.6Nb-34.4Hf-44.0Si, and 26.2Nb-9.4Hf-64.4Si, respectively. In other areas, two-phase regions were observed. They were $\beta(\text{Nb,Hf,Si})$ (68.0Nb-30.9Hf-1.1Si) and $\text{Hf}(\text{Nb})_2\text{Si}$ (20.2Nb-46.4Hf-33.4Si), as shown in Fig. 11(b). The crystal structures of all these phases were confirmed using EBSD. The dramatic difference in microstructure of the two areas arose because the ISM ingot was difficult to homogenize.

Nb-55Hf-37.5Si:

The equilibrium state of this alloy was probably single-phase $\text{Hf}(\text{Nb})_5\text{Si}_3$. The microstructure after the 1500 °C-100 hr anneal consisted mostly of $\text{Hf}(\text{Nb})_5\text{Si}_3$ with a composition of 6.9Nb-55.3Hf-37.8Si, as shown in Fig. 12. Due to the inhomogeneity of the original cast structure, there were also small amounts of $\text{Hf}(\text{Nb})_3\text{Si}_2$ (6.5Nb-53.8Hf-39.7Si), $\text{Hf}(\text{Nb})_2\text{Si}$ (7.9Nb-58.6Hf-33.6Si) and $\beta(\text{Nb,Hf,Si})$ (38.7Nb-59.1Hf-2.2Si), respectively. The atomic number contrast was very low between the three silicides in this alloy, which made the contrast difference in the BSE image (Fig. 12) very low. The phases were therefore identified using EBSD.

4. Conclusions

The microstructures generated in the ternary Nb-Hf-Si alloys investigated contained a total of 10 phases: $\beta(\text{Nb,Hf,Si})$, $\alpha(\text{Hf,Nb,Si})$, $\text{Nb}(\text{Hf})_5\text{Si}_3$, $\text{Hf}(\text{Nb})_5\text{Si}_3$, $\text{Nb}(\text{Hf})_3\text{Si}$, $\text{Hf}(\text{Nb})_2\text{Si}$, $\text{Hf}(\text{Nb})_3\text{Si}_2$, $\text{Hf}(\text{Nb})_5\text{Si}_4$, $\text{Hf}(\text{Nb})\text{Si}$, and $\text{Nb}(\text{Hf})\text{Si}_2$. The isothermal section of the Nb-Hf-Si system at 1500 °C has been defined.

The Nb solubility is ~46% in $\text{Hf}(\text{Nb})_2\text{Si}$, ~36% in $\text{Hf}(\text{Nb})_5\text{Si}_3$, >6.5% in $\text{Hf}(\text{Nb})_3\text{Si}_2$, $\geq 22\%$ in $\text{Hf}(\text{Nb})_5\text{Si}_4$, and, 5% in $\text{Hf}(\text{Nb})\text{Si}$. The Hf solubilities in $\text{Nb}(\text{Hf})_5\text{Si}_3$ and $\text{Nb}(\text{Hf})\text{Si}_2$ are ~16% and 9.4%, respectively. Four three-phase regions, $\beta(\text{Nb,Hf,Si}) + \text{Nb}(\text{Hf})_5\text{Si}_3 + \text{Hf}(\text{Nb})_2\text{Si}$, $\text{Nb}(\text{Hf})_5\text{Si}_3 + \text{Hf}(\text{Nb})_2\text{Si} + \text{Hf}(\text{Nb})_5\text{Si}_3$, $\beta(\text{Nb,Hf,Si}) + \alpha(\text{Hf,Nb,Si}) + \text{Hf}(\text{Nb})_2\text{Si}$, and $\text{Nb}(\text{Hf})\text{Si}_2 + \text{Hf}(\text{Nb})_5\text{Si}_3 + \text{Hf}(\text{Nb})\text{Si}$ have been defined. The $\text{Nb}(\text{Hf})_3\text{Si}$ phase was unstable at 1500 °C and decomposed by an eutectoid transformation to $\beta(\text{Nb,Hf,Si})$ and $\text{Nb}(\text{Hf})_5\text{Si}_3$.

Acknowledgments

The authors would like to thank D.J. Dalpe for the directional solidification, and J.A. Sutliff and S.D. Sitzman for the EBSD, and D. Wark for microprobe analysis. This research was partially sponsored by AFOSR under contract #F49620-96-C-0022 and #F49620-99-C-0026 with Dr. S. Wu and Dr. C. Hartley as Program Managers.

References

1. Mendiratta MG, Dimiduk DM. Mat. Res. Soc. Symp. Proc. 1989;133:441.
2. Jackson MR, Bewlay BP, Rowe RG, Skelly DW, Lipsitt, HA. JOM 1996;48:39.
3. Subramanian PR, Mendiratta MG, Dimiduk DM. JOM 1996;48:33.
4. Bewlay BP, Lewandowski JJ, Jackson MR. JOM 1997;49:44.
5. Bewlay BP, Jackson MR, Lipsitt HA. J Phase Equilibria 1997;18:264.
6. Bewlay BP, Jackson MR, Bishop RR. J Phase Equilibria 1998;19:577.
7. Bewlay BP, Bishop RR, Jackson MR. Z Metallkde 1999;90:413.
8. Bewlay BP, Sutliff JA, Bishop RR. J Phase Equilibria 1999;20:109.
9. Zhao J-C, Bewlay BP, Jackson MR, Chen Q. J Phase Equilibria 2000;21:40.
10. Subramanian PR, Mendiratta MG, Dimiduk DM. Mat. Res. Soc. Symp. Proc. 1994;322:491.
11. Fernandez Guillermet A. J Alloys Compounds 1996;234:111.
12. Schlesinger ME, Okamoto H, Gokhale AB, Abbaschian R. J Phase Equilibria, 1993;14:502.
13. Liang H, Chang YA. Intermetallics 1999;7:561.
14. Villars P, Calvert LD, editors. Pearsons handbook of crystallographic data for intermetallic phases. 2nd ed., vol. 1-4, Materials Park. ASM International, 1991.
15. Karpinsky OG, Evseyev BA. Russ Metall 1969;3:128.
16. Bewlay BP, Jackson MR, Reeder WJ, Lipsitt HA. Mat. Res. Soc. Symp. Proc., 1994;364:943.
17. Okamoto H. Bull Alloy Phase Diagrams 1990;11:513.
18. Harland CJ, Akhter P, Bewick A. J Phys 1981;E14:175.
19. Michael JR, Schienger ME, Goehner RP, Microscopy and Microanalysis 1997;3 (suppl.2):879.

FIGURE CAPTIONS

Fig. 1. Schematic 3-D projection phase diagram of the metal-rich end of the Nb-Hf-Si ternary system.

Fig. 2. Isothermal section of the estimated equilibrium Nb-Hf-Si phase diagram at 1500 °C. The bulk alloy compositions are shown as solid squares. EPMA measurements of phase compositions are shown as open circles. The tie-triangles constructed in dashed lines were estimated.

Fig. 3. SEM BSE images of the Nb-10Hf-16Si alloy after heat treatment at 1500 °C for 100 hours. The bright phase is $\text{Hf}(\text{Nb})_5\text{Si}_3$, the light gray phase is $\text{Hf}(\text{Nb})_2\text{Si}$, the dark gray phase is $\text{Nb}(\text{Hf})_5\text{Si}_3$, and the dark phase is $\beta(\text{Nb},\text{Hf},\text{Si})$. The area shown in a circle in (b) is non-equilibrium and is $\text{Nb}(\text{Hf})_3\text{Si}$ that was decomposing to $\text{Nb}(\text{Hf})_5\text{Si}_3$ and $\beta(\text{Nb},\text{Hf},\text{Si})$.

Fig. 4. SEM BSE images of the Nb-10Hf-25Si alloy after heat treatment at 1500 °C for 100 hours: (a) low magnification image and (b) high magnification image. The white phase is $\text{Hf}(\text{Nb})_5\text{Si}_3$ that resulted from segregation in the original as-DS structure.

Fig. 5. SEM BSE image of the Nb-30Hf-25Si alloy after heat treatment at 1500 °C for 100 hours. The white phase is $\alpha(\text{Hf},\text{Nb},\text{Si})$ which was probably the result of inhomogeneity in the as-DS sample. The gray and dark phases are $\text{Hf}(\text{Nb})_2\text{Si}$ and $\beta(\text{Hf},\text{Nb},\text{Si})$ respectively.

Fig. 6. SEM BSE image of the Nb-40Hf-30Si alloy after heat treatment at 1500 °C for 100 hours. The gray and dark phases are $\text{Hf}(\text{Nb})_2\text{Si}$ and $\beta(\text{Hf},\text{Nb},\text{Si})$ respectively.

Fig. 7. SEM BSE images of the Nb-60Hf-25Si alloy after heat treatment at 1500 °C for 100 hours: (a) low magnification and (b) high magnification. The dark phase is $\text{Hf}(\text{Nb})_2\text{Si}$ and the contrast in it was probably due to different grain orientations. The gray phase is $\beta(\text{Nb},\text{Hf},\text{Si})$. The light gray phase inside $\beta(\text{Nb},\text{Hf},\text{Si})$ shown in (b) is probably $\alpha(\text{Nb},\text{Hf},\text{Si})$ formed during cooling from 1500 °C. The white phase is $\alpha(\text{Nb},\text{Hf},\text{Si})$, very rich in Hf, which was probably the result of inhomogeneity in the as-DS structure.

Fig. 8. SEM BSE image of the Nb-73Hf-17Si alloy after heat treatment at 1500 °C for 100 hours. The dark phase is $\text{Hf}(\text{Nb})_2\text{Si}$. The two-phase region was $\beta(\text{Nb},\text{Hf},\text{Si})$ at 1500 °C and it transformed into $\beta(\text{Nb},\text{Hf},\text{Si}) + \alpha(\text{Nb},\text{Hf},\text{Si})$ during cooling. There was a very small amount of $\alpha(\text{Nb},\text{Hf},\text{Si})$ present at 1500 °C.

Fig. 9. SEM BSE images of the Nb-80Hf-5Si alloy after heat treatment at 1500 °C for 100 hours: (a) low magnification and (b) high magnification. The dark phase is $\text{Hf}(\text{Nb})_2\text{Si}$. The two-phase region was original $\beta(\text{Nb},\text{Hf},\text{Si})$ at 1500 °C and it transformed into $\beta(\text{Nb},\text{Hf},\text{Si}) + \alpha(\text{Nb},\text{Hf},\text{Si})$ during cooling. The light gray phase is $\alpha(\text{Nb},\text{Hf},\text{Si})$ which was present at 1500 °C.

Fig. 10. SEM BSE image of the Nb-90Hf-5Si alloy after heat treatment at 1500 °C for 100 hours. The darkest phase is $\text{Hf}(\text{Nb})_2\text{Si}$. The white phase is $\alpha(\text{Hf},\text{Nb},\text{Si})$. The two-phase region was original $\beta(\text{Nb},\text{Hf},\text{Si})$ at 1500 °C and it transformed into $\beta(\text{Nb},\text{Hf},\text{Si}) + \alpha(\text{Nb},\text{Hf},\text{Si})$ during cooling.

Fig. 11. SEM BSE images of the Nb-50Hf-37.5Si alloy after heat treatment at 1500 °C for 100 hours. These images (a) and (b) were from different regions of the sample which was inhomogeneous. The darkest phase in (a) is $\text{Nb}(\text{Hf})\text{Si}_2$; the dark gray phase is $\text{Hf}(\text{Nb})_5\text{Si}_4$; and the light gray phase is $\text{Hf}(\text{Nb})\text{Si}$. The white lines shown in (a) were cracks in the sputtered carbon coating on the surface of the sample. The region in (b) consisted of two phases: $\beta(\text{Nb},\text{Hf},\text{Si})$ (darker) and $\text{Hf}(\text{Nb})_2\text{Si}$ (brighter).

Fig. 12. SEM BSE image of the Nb-55Hf-37.5Si alloy after heat treatment at 1500 °C for 100 hours. There were three phases, but there was little contrast between them. EBSD was used for phase identification. The white dots in the micrograph are imperfections in the surface carbon coating. The darkest lines and areas were cracks and pores in the sample.

Table 1. Compositions and constituent phases of the alloys investigated.

Composition	Phases in as-DS condition	Phases after 1500 °C / 100 hrs heat treatment.
Nb-15%Hf-16%Si Nb-10%Hf-16%Si	Primary $\beta(\text{Nb,Hf,Si})$ dendrites with $\text{Nb}(\text{Hf})_3\text{Si}$ - $\beta(\text{Nb,Hf,Si})$ eutectic	$\beta(\text{Nb,Hf,Si})$, $\text{Nb}(\text{Hf})_5\text{Si}_3$, $\text{Hf}(\text{Nb})_2\text{Si}$, and $\text{Hf}(\text{Nb})_5\text{Si}_3^*$
Nb-5%Hf-19%Si Nb-10%Hf-18.5%Si	Primary $\text{Nb}(\text{Hf})_3\text{Si}$ with $\text{Nb}(\text{Hf})_3\text{Si}$ - $\beta(\text{Nb,Hf,Si})$ eutectic	$\beta(\text{Nb,Hf,Si})$ and $\text{Nb}(\text{Hf})_5\text{Si}_3$
Nb-10%Hf-25%Si	Primary $\text{Nb}(\text{Hf})_5\text{Si}_3$, peritectic $\text{Nb}(\text{Hf})_3\text{Si}$, $\text{Nb}(\text{Hf})_3\text{Si}$ - $\beta(\text{Nb,Hf,Si})$ eutectic	$\beta(\text{Nb,Hf,Si})$, $\text{Nb}(\text{Hf})_5\text{Si}_3$, and $\text{Hf}(\text{Nb})_5\text{Si}_3^*$
Nb-30%Hf-25%Si	Primary $\text{Hf}(\text{Nb})_5\text{Si}_3$, peritectic $\text{Hf}(\text{Nb})_2\text{Si}$, $\text{Hf}(\text{Nb})_2\text{Si}$ - $\beta(\text{Nb,Hf,Si})$ eutectic	$\text{Hf}(\text{Nb})_2\text{Si}$ and $\beta(\text{Nb,Hf,Si})$, and $\alpha(\text{Nb,Hf,Si})^*$
Nb-60%Hf-25%Si Nb-40%Hf-30%Si	Primary $\text{Hf}(\text{Nb})_2\text{Si}$ with $\text{Hf}(\text{Nb})_2\text{Si}$ - $\beta(\text{Nb,Hf,Si})$ eutectic	$\text{Hf}(\text{Nb})_2\text{Si}$ and $\beta(\text{Nb,Hf,Si})$, and $\alpha(\text{Nb,Hf,Si})^*$
Nb-80%Hf-14%Si Nb-73%Hf-17%Si	Primary $\text{Hf}(\text{Nb})_2\text{Si}$, $\text{Hf}(\text{Nb})_2\text{Si}$ - $\beta(\text{Nb,Hf,Si})$ eutectic: $\beta \rightarrow \beta + \alpha$	$\text{Hf}(\text{Nb})_2\text{Si}$ and $\beta(\text{Nb,Hf,Si})$; $\beta \rightarrow \beta + \alpha$
Nb-80%Hf-5%Si	Primary $\beta(\text{Nb,Hf,Si})$ with $\text{Hf}(\text{Nb})_2\text{Si}$ - $\beta(\text{Nb,Hf,Si})$ eutectic	$\text{Hf}(\text{Nb})_2\text{Si}$ and $\beta(\text{Nb,Hf,Si})$; $\beta \rightarrow \beta + \alpha$
Nb-90Hf-5Si	Induction skull melted	$\text{Hf}(\text{Nb})_2\text{Si}$, $\beta(\text{Nb,Hf,Si})$, and $\alpha(\text{Nb,Hf,Si})$; $\beta \rightarrow \beta + \alpha$
Nb-50Hf-37.5Si	Primary $\text{Hf}(\text{Nb})_5\text{Si}_3$, peritectic $\text{Hf}(\text{Nb})_2\text{Si}$, and eutectic $\text{Hf}(\text{Nb})_2\text{Si}$ and $\beta(\text{Nb,Hf,Si})$	Inhomogeneous sample. First area: $\text{Hf}(\text{Nb})\text{Si} + \text{Hf}(\text{Nb})_5\text{Si}_4 + \text{Nb}(\text{Hf})\text{Si}_2$; the second area: $\beta(\text{Nb,Hf,Si}) + \text{Hf}(\text{Nb})_2\text{Si}$
Nb-55Hf-37.5Si	Induction skull melted	Single phase $\text{Hf}(\text{Nb})_5\text{Si}_3$. Small amounts of $\text{Hf}(\text{Nb})_3\text{Si}_2$, $\text{Hf}(\text{Nb})_2\text{Si}$ and $\beta(\text{Nb,Hf,Si})$ due to inhomogeneity.

* formed due to inhomogeneity in the as-DS structure.

Table 2. Crystal structures of the phases observed in the Nb-Hf-Si ternary system together with the lattice parameters are for binary compounds and solid-solution phases.

Phase	Prototype	Space group	Lattice parameters, nm	Ref.
Nb(Hf) ₃ Si	PTi ₃	P4 ₂ /n	a = 1.0224, c = 0.5189	[14]
Nb(Hf) ₅ Si ₃	Cr ₅ B ₃	I4/mcm	a = 0.6570, c = 1.1884	[14]
Nb(Hf)Si ₂	CrSi ₂	P6 ₄ 22	a = 0.4794, c = 0.6589	[14]
Hf(Nb)Si	FeB	Pnma	a = 0.6889, b = 0.3772, c = 0.5223	[14,15]
Hf(Nb) ₅ Si ₄	Zr ₅ Si ₄	P4 ₁ 2 ₁ 2	a = 0.7039, c = 1.283	[14,15]
Hf(Nb) ₃ Si ₂	U ₃ Si ₂	P4/mbm	a = 0.6988, c = 0.3675	[14,15]
Hf(Nb) ₅ Si ₃	Mn ₅ Si ₃	P6 ₃ /mcm	a = 0.7844, c = 0.5492	[14,15]
Hf(Nb) ₂ Si	Al ₂ Cu	I4/mcm	a = 0.6553, c = 0.5186	[14,15]
β(Nb,Hf,Si)	W	Im ⁻ ₃ m	a = 0.33007 to 0.3610	[14]
α(Hf,Nb,Si)	Mg	P6 ₃ /mmc	a = 0.31946, c = 0.5058	[14]

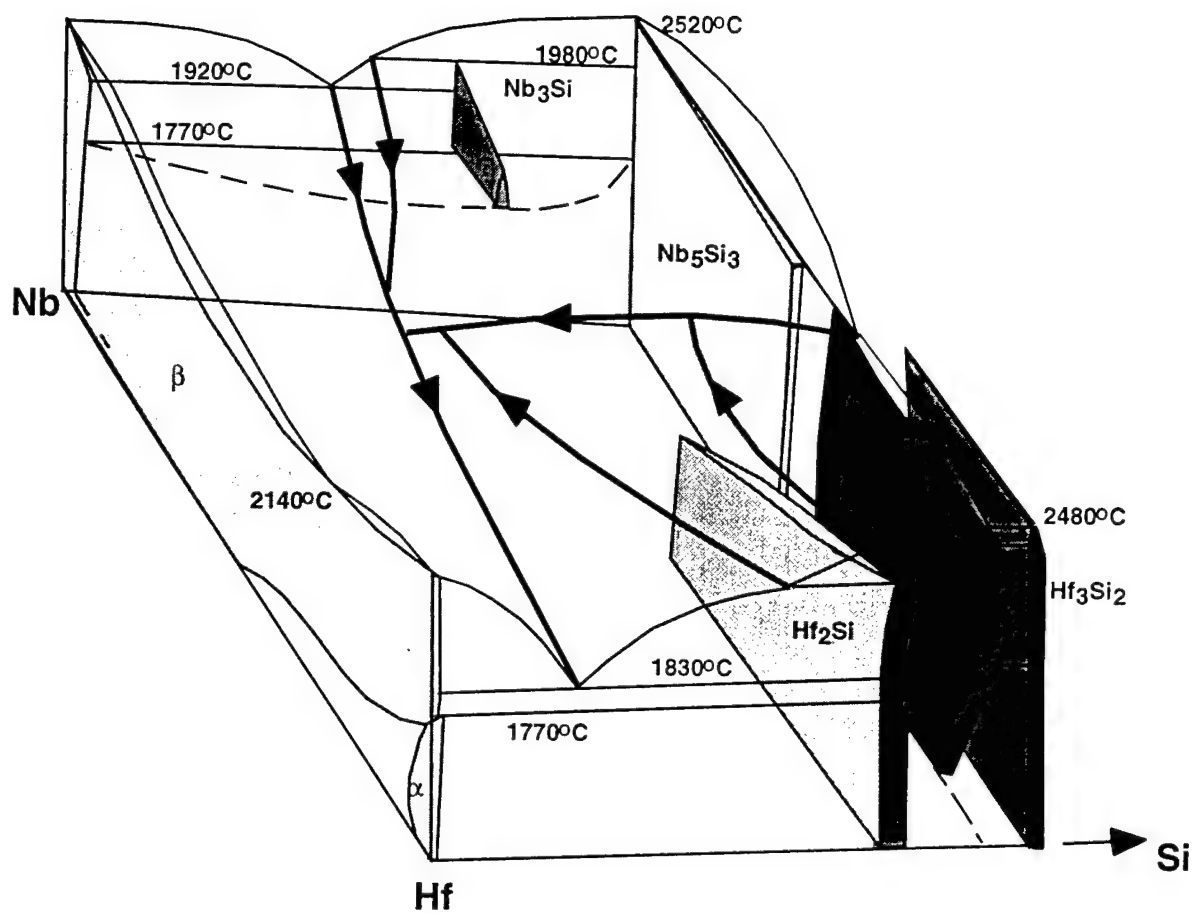


Fig. 1. Schematic 3-D projection phase diagram of the metal-rich end of the Nb-Hf-Si ternary system.

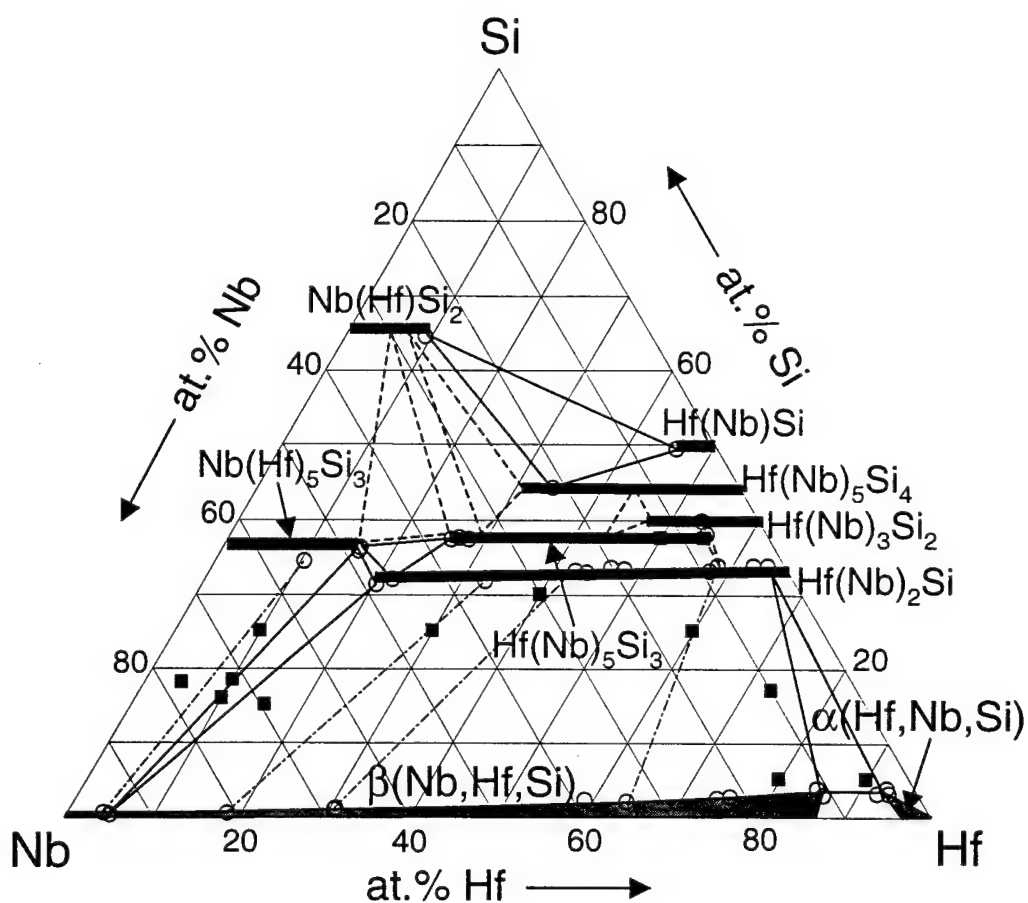


Fig. 2. Isothermal section of the estimated equilibrium Nb-Hf-Si phase diagram at 1500 °C. The bulk alloy compositions are shown as solid squares. EPMA measurements of phase compositions are shown as open circles. The tie-triangles constructed from dashed lines were estimated.

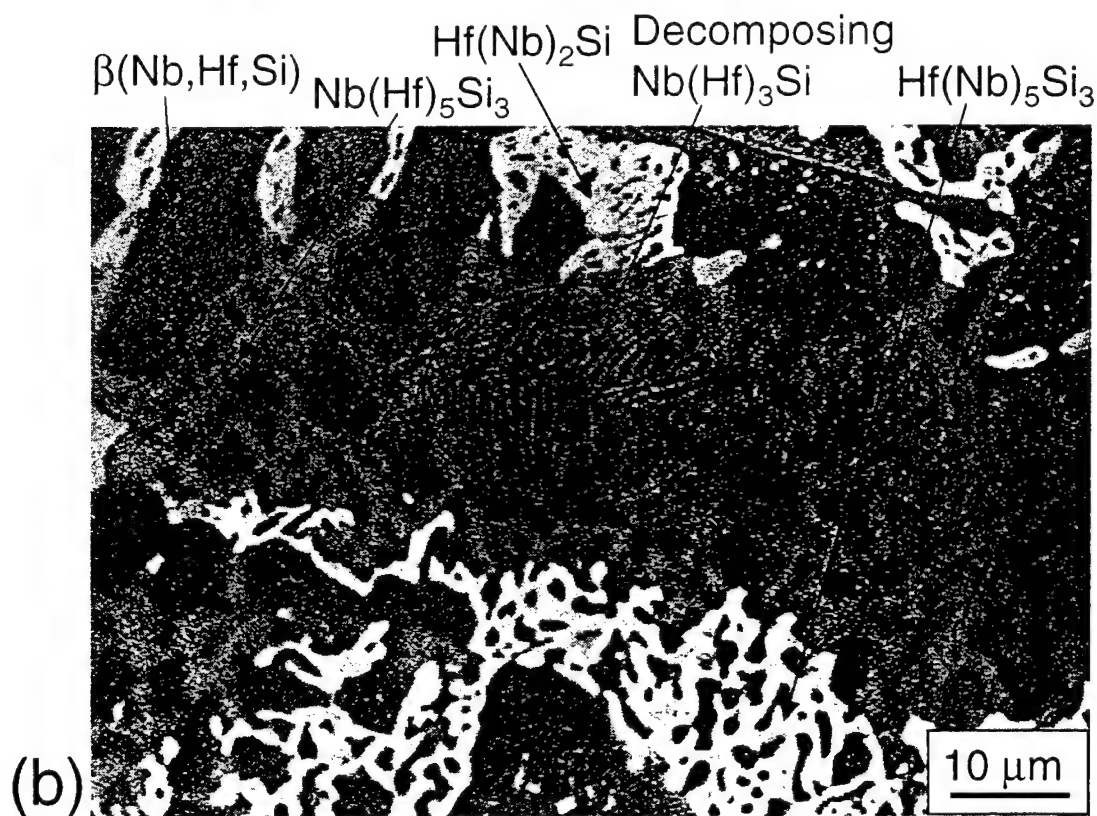
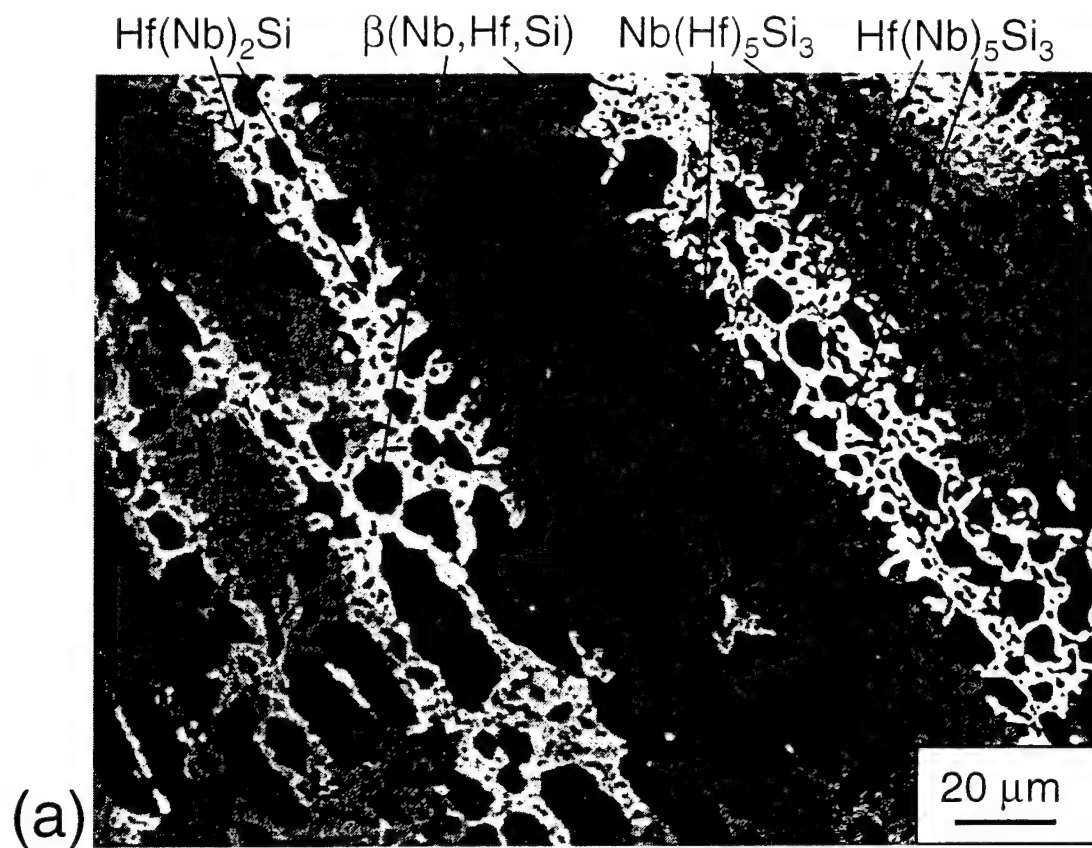


Fig. 3. SEM BSE images of the Nb-10Hf-16Si alloy after heat treatment at 1500 °C for 100 hours. The bright phase is $\text{Hf(Nb)}_5\text{Si}_3$, the light gray phase is $\text{Hf(Nb)}_2\text{Si}$, the dark gray phase is $\text{Nb(Hf)}_5\text{Si}_3$, and the dark phase is $\beta(\text{Nb,Hf,Si})$. The area shown in a circle in (b) is non-equilibrium and is $\text{Nb(Hf)}_3\text{Si}$ that is decomposing to $\text{Nb(Hf)}_5\text{Si}_3$ and $\beta(\text{Nb,Hf,Si})$.

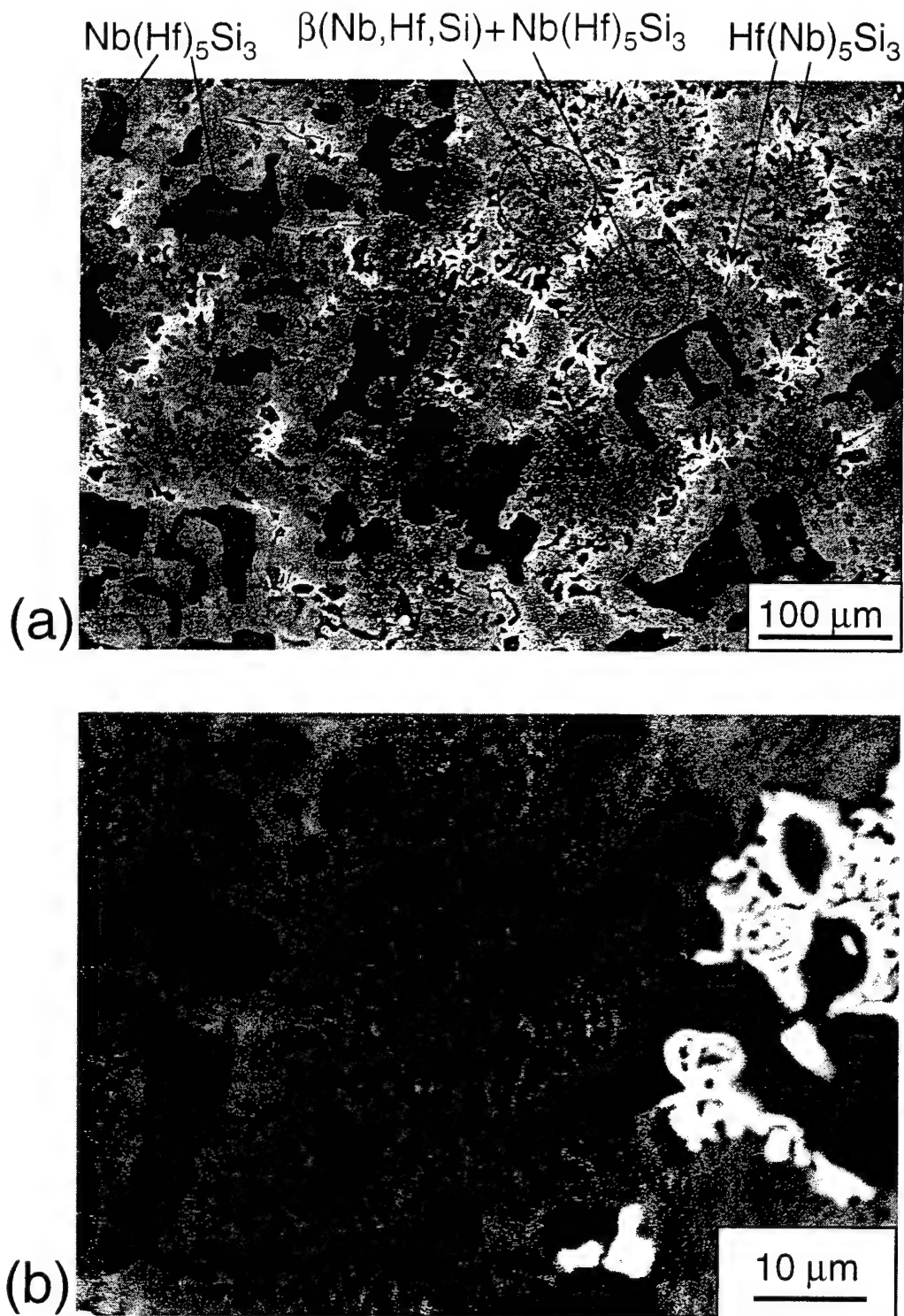


Fig. 4. SEM BSE images of the Nb-10Hf-25Si alloy after heat treatment at 1500 °C for 100 hours: (a) low magnification image and (b) high magnification image. The white phase is $\text{Hf(Nb)}_5\text{Si}_3$ that resulted from segregation in the original as-DS structure.

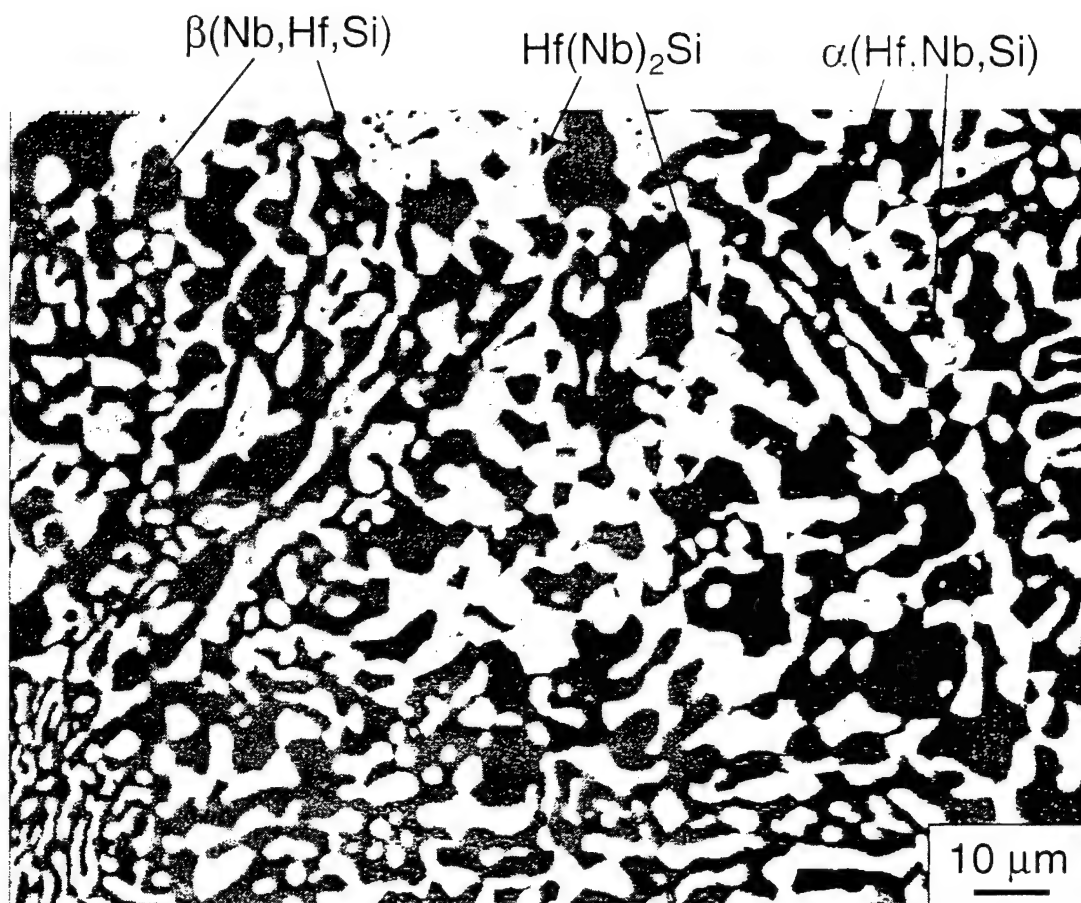


Fig. 5. SEM BSE image of the Nb-30Hf-25Si alloy after heat treatment at 1500 °C for 100 hours. The white phase is $\alpha(\text{Hf}, \text{Nb}, \text{Si})$ which was probably the result of inhomogeneity in the as-DS sample. The gray and dark phases are $\text{Hf}(\text{Nb})_2\text{Si}$ and $\beta(\text{Nb}, \text{Hf}, \text{Si})$ respectively.

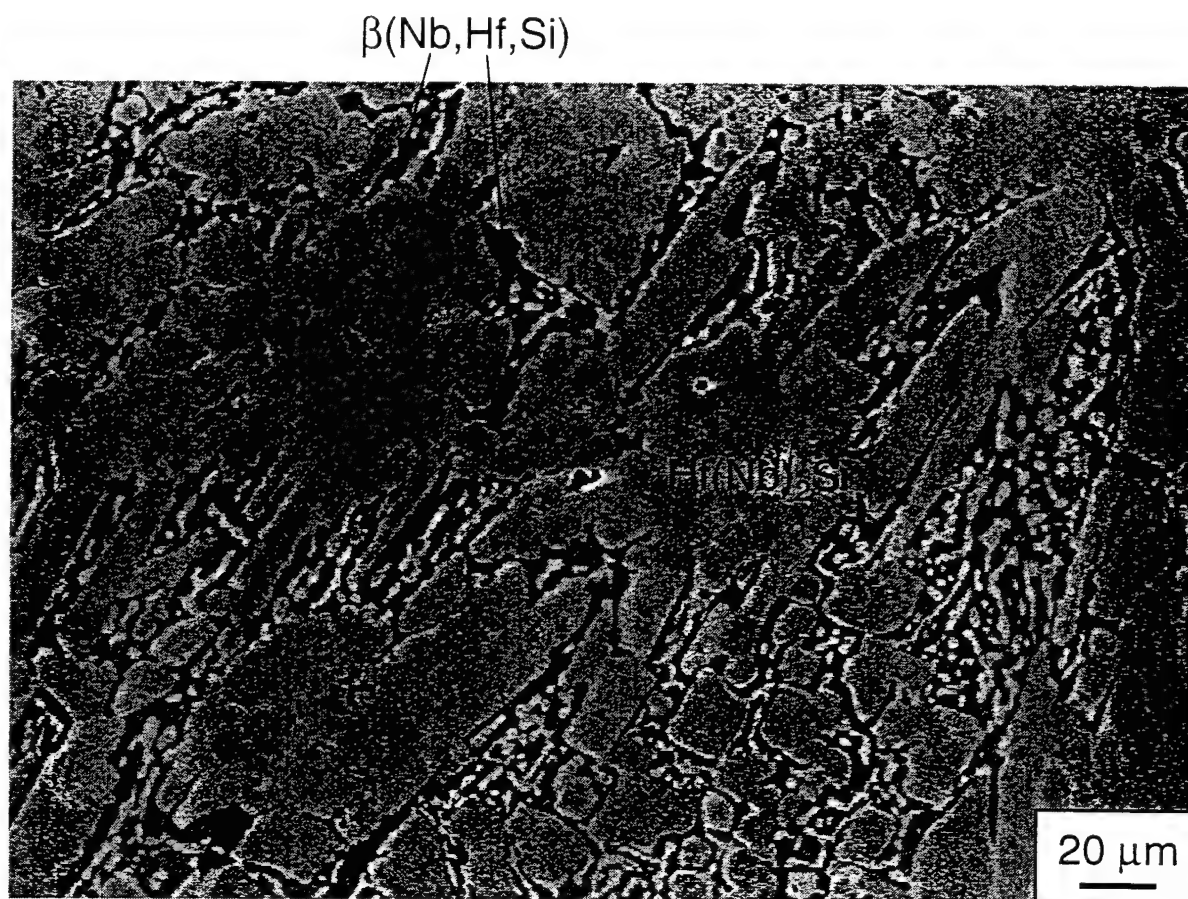


Fig. 6. SEM BSE image of the Nb-40Hf-30Si alloy after heat treatment at 1500 °C for 100 hours. The gray and dark phases are $\text{Hf}(\text{Nb})_2\text{Si}$ and $\beta(\text{Hf,Nb,Si})$ respectively.

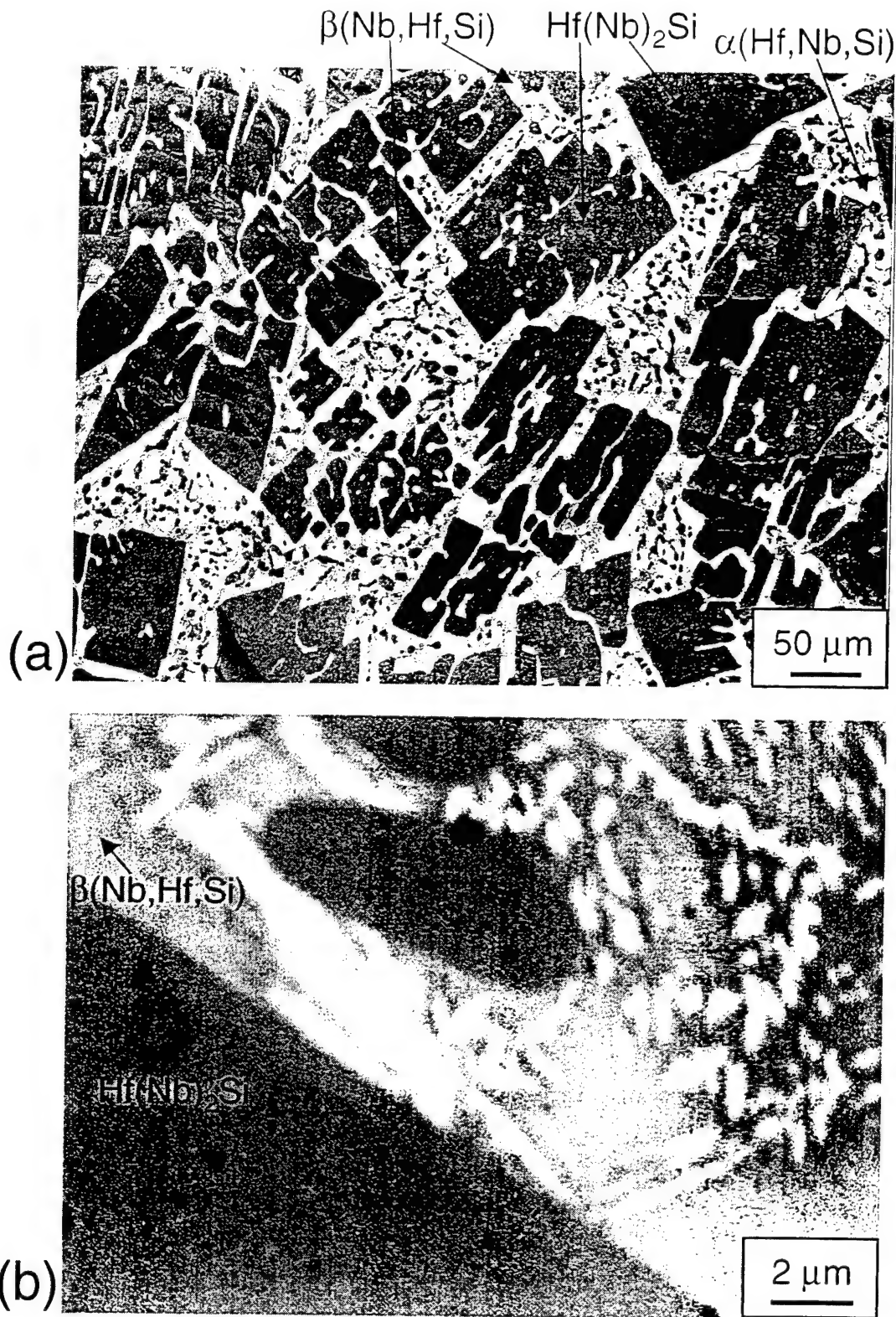


Fig. 7. SEM BSE images of the Nb-60Hf-25Si alloy after heat treatment at 1500 °C for 100 hours: (a) low magnification and (b) high magnification. The dark phase is $\text{Hf}(\text{Nb})_2\text{Si}$ and the contrast in it was probably due to different grain orientations. The gray phase is $\beta(\text{Nb,Hf,Si})$. The light gray phase inside $\beta(\text{Nb,Hf,Si})$ shown in (b) is probably $\alpha(\text{Hf,Nb,Si})$ formed during cooling from 1500 °C. The white phase is $\alpha(\text{Hf,Nb,Si})$, very rich in Hf, which was probably the result of inhomogeneity in the as-DS structure.

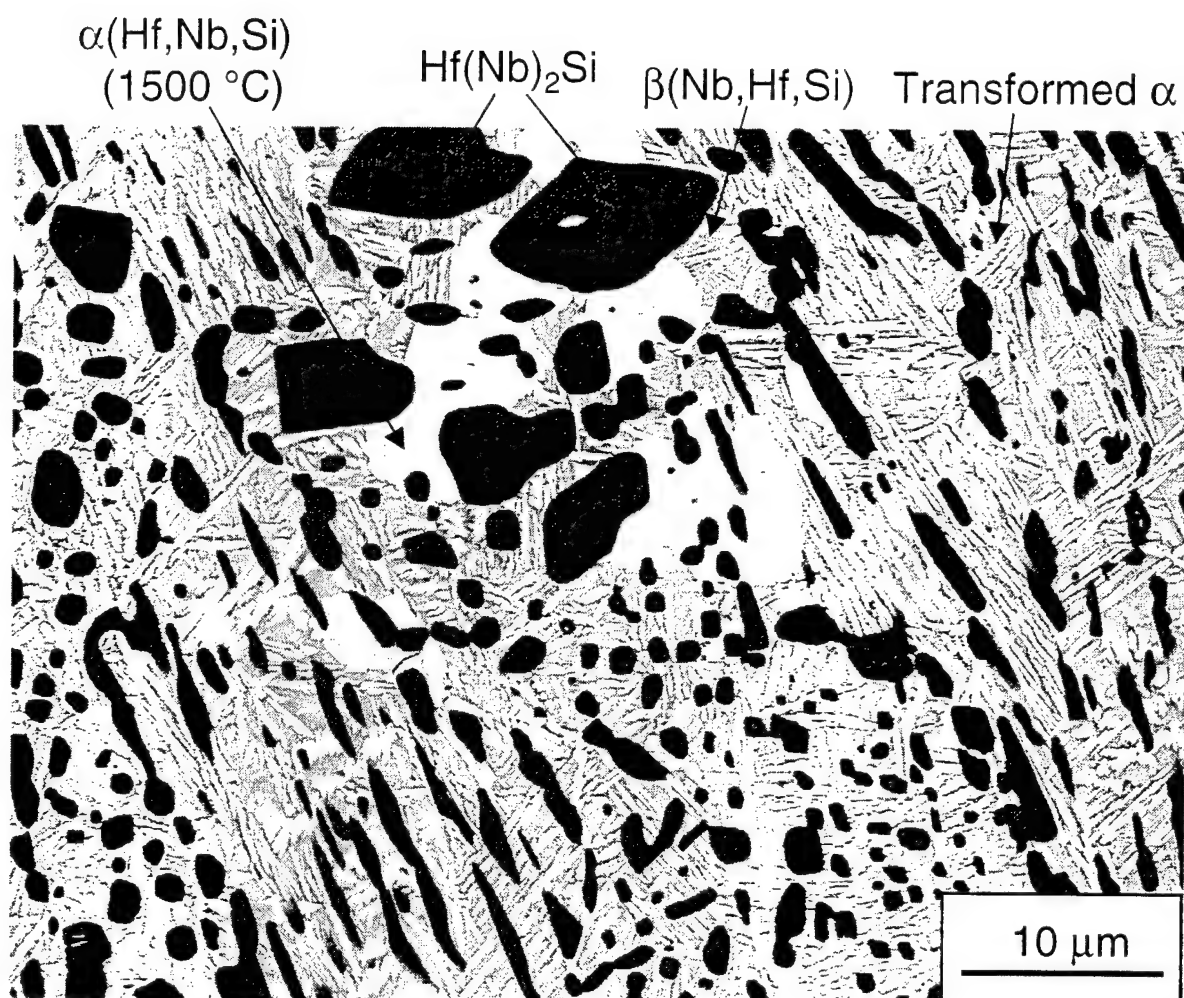


Fig. 8. SEM BSE image of the Nb-73Hf-17Si alloy after heat treatment at 1500 °C for 100 hours. The dark phase is $\text{Hf(Nb)}_2\text{Si}$. The two-phase region was $\beta(\text{Nb,Hf,Si})$ at 1500 °C and it transformed into $\beta(\text{Nb,Hf,Si}) + \alpha(\text{Hf,Nb,Si})$ during cooling. There was a very small amount of $\alpha(\text{Hf,Nb,Si})$ present at 1500 °C.

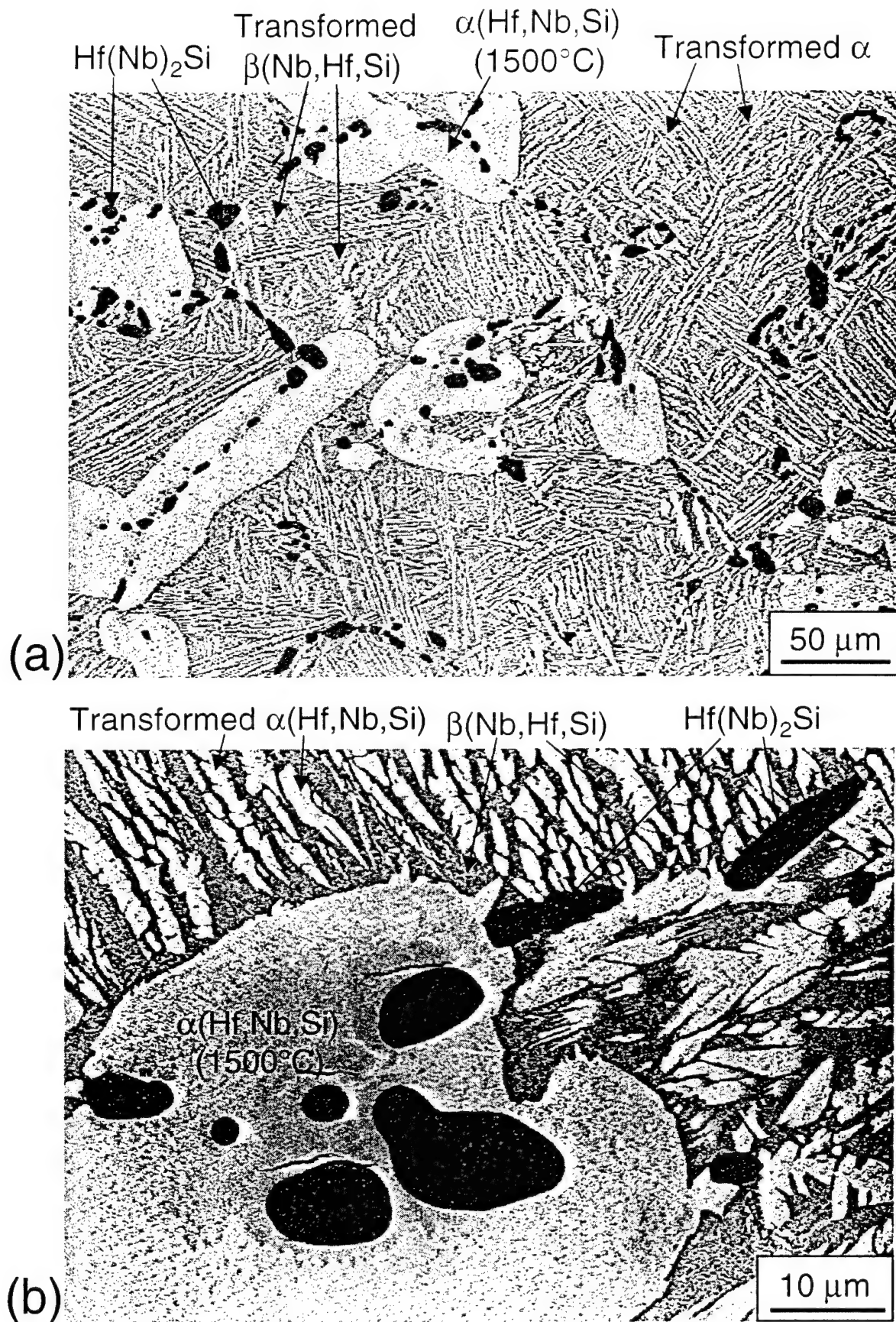


Fig. 9. SEM BSE images of the Nb-80Hf-5Si alloy after heat treatment at 1500 °C for 100 hours: (a) low magnification and (b) high magnification. The dark phase is $\text{Hf(Nb)}_2\text{Si}$. The two-phase region was original $\beta(\text{Nb,Hf,Si})$ at 1500 °C and it transformed into $\beta(\text{Nb,Hf,Si}) + \alpha(\text{Hf,Nb,Si})$ during cooling. The light gray phase is $\alpha(\text{Hf,Nb,Si})$ which was present at 1500 °C.

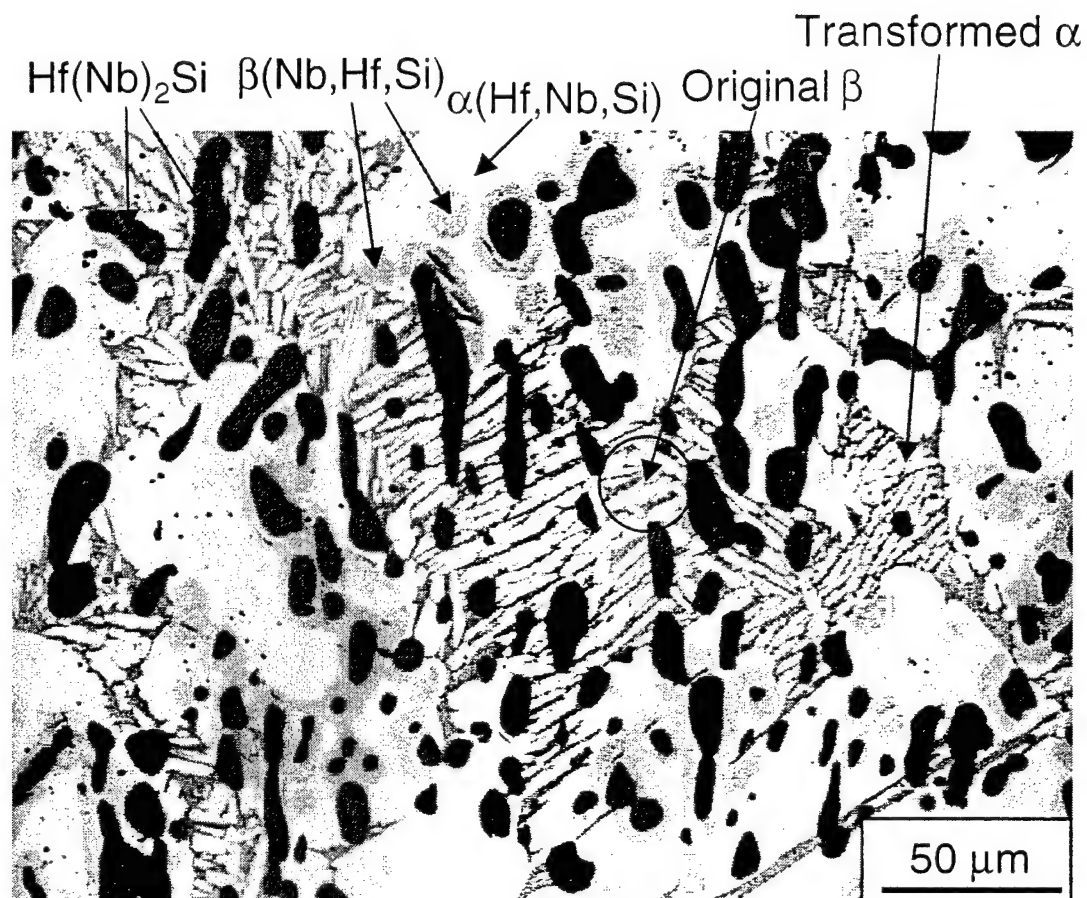


Fig. 10. SEM BSE image of the Nb-90Hf-5Si alloy after heat treatment at 1500 °C for 100 hours. The darkest phase is $\text{Hf(Nb)}_2\text{Si}$. The white phase is $\alpha(\text{Hf,Nb,Si})$. The two-phase region was original $\beta(\text{Nb,Hf,Si})$ at 1500 °C and it transformed into $\beta(\text{Nb,Hf,Si}) + \alpha(\text{Hf,Nb,Si})$ during cooling.

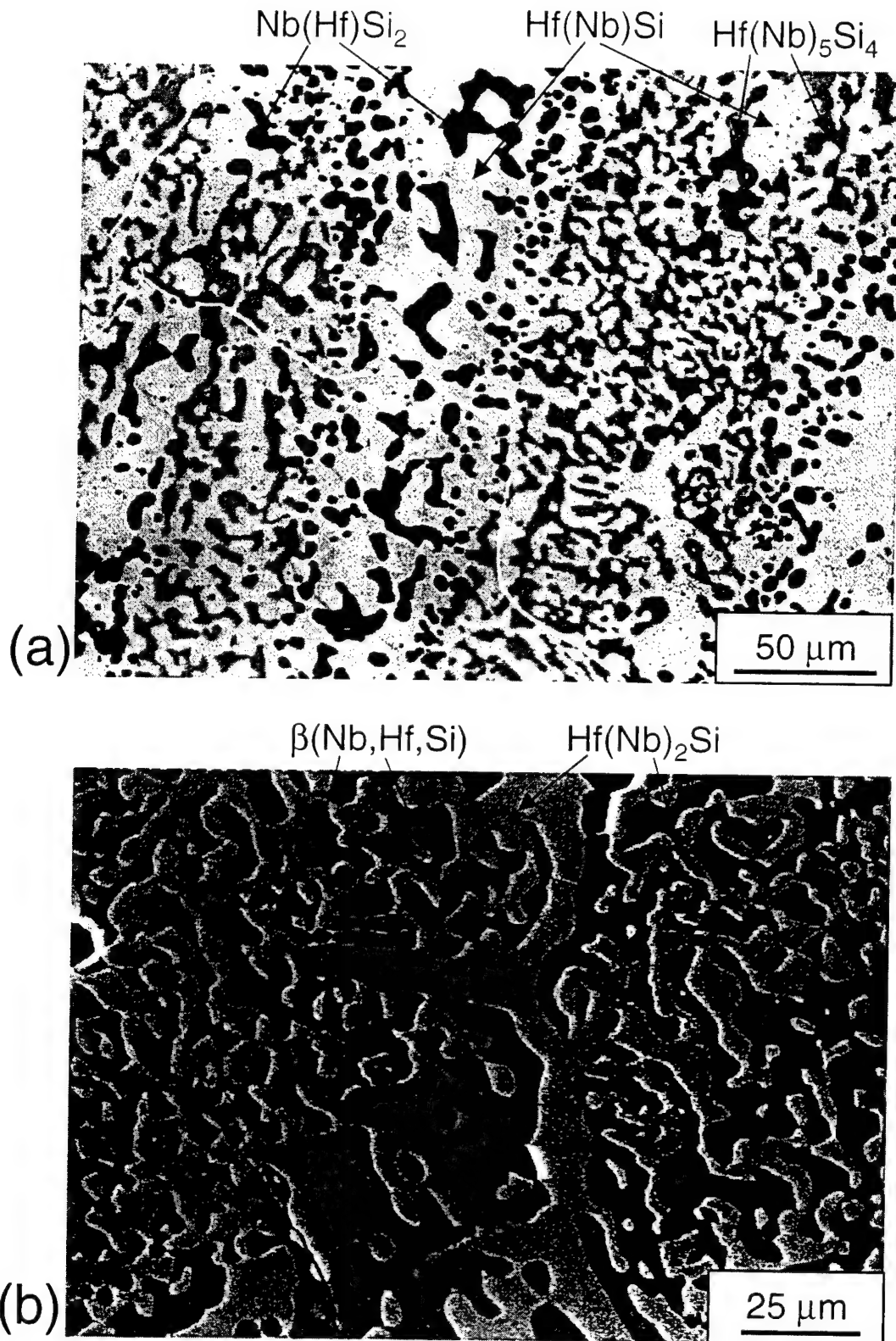


Fig. 11. SEM BSE images of the Nb-50Hf-37.5Si alloy after heat treatment at 1500 °C for 100 hours. These images (a) and (b) were from different regions of the sample which was inhomogeneous. The darkest phase in (a) is Nb(Hf)Si_2 ; the dark gray phase is $\text{Hf(Nb)}_5\text{Si}_4$; and the light gray phase is Hf(Nb)Si . The white lines shown in (a) were cracks in the sputtered carbon coating on the surface of the sample. The region in (b) consisted of two phases: $\beta(\text{Nb,Hf,Si})$ (darker) and $\text{Hf(Nb)}_2\text{Si}$ (brighter).

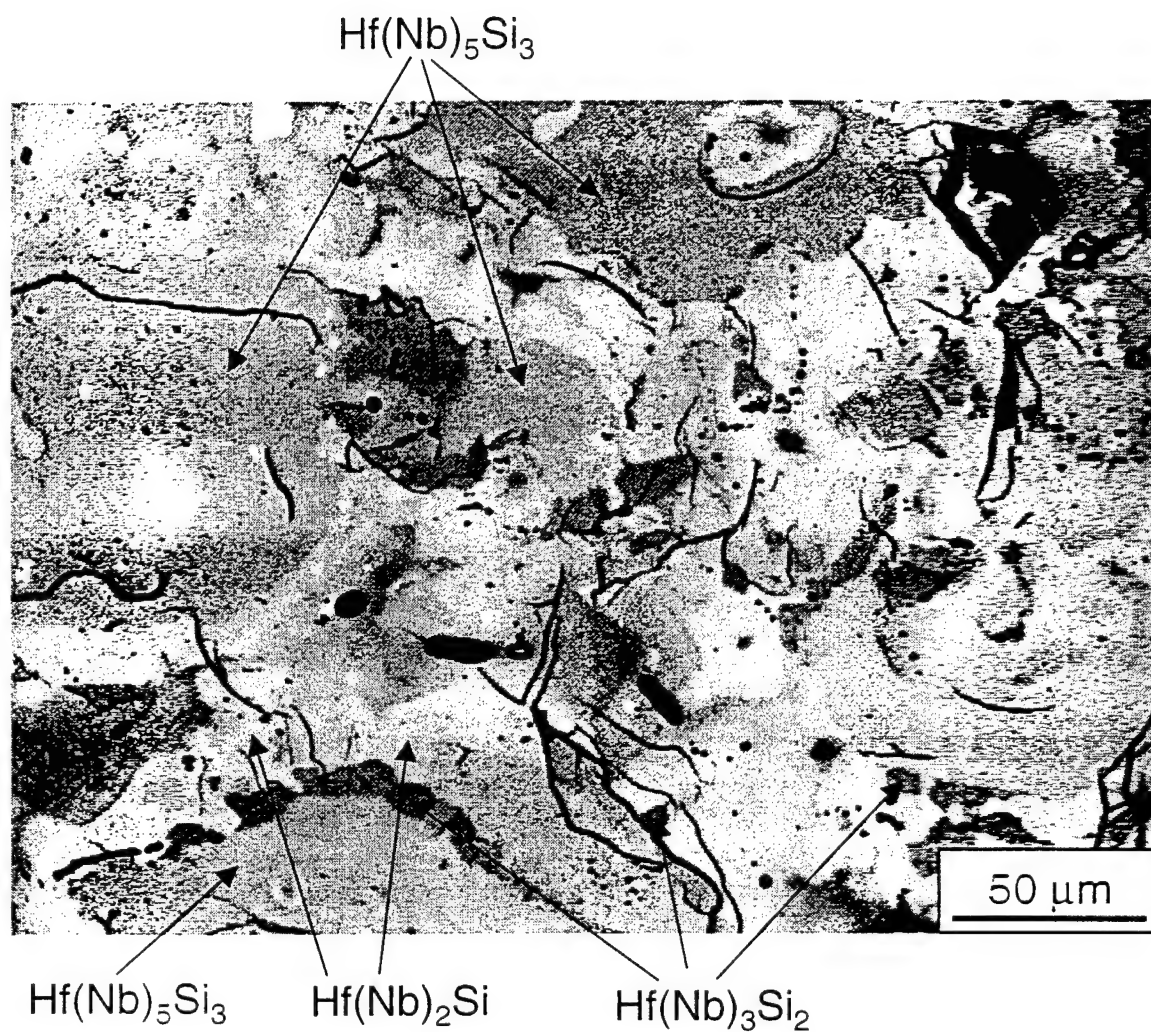


Fig. 12. SEM BSE image of the Nb-55Hf-37.5Si alloy after heat treatment at 1500 °C for 100 hours. There were three phases, but there was little contrast between them. EBSD was used for phase identification. The white dots in the micrograph are imperfections in the surface carbon coating. The darkest lines and areas were cracks and pores in the sample.

Characterization of silicide precipitates
in Nb-Si and Nb-Ti-Si alloys

R.J. Grylls, B.P. Bewlay, H.A. Lipsitt, and H.L. Fraser

Philosophical Magazine, 2000

Characterization of silicide precipitates in Nb-Si and Nb-Ti-Si alloys

By R.J. GRYLLS¹, B.P. BEWLAY², H.A. LIPSITT¹ and H.L. FRASER¹

¹Department of Materials Science and Engineering, The Ohio State University,
Columbus, OH 43210, U.S.A.

²General Electric Company, Corporate Research and Development,
Schenectady, NY 12301, U.S.A.

ABSTRACT

The present paper describes the morphology, chemistry and crystallography of silicide precipitates that were observed in Nb-Si and Nb-Ti-Si solid solutions. Although the stable structure of Nb₃Si is tetragonal (tP32), within the body-centered-cubic (bcc) Nb solid solution fine-scale Nb₃Si precipitates were observed with a metastable orthorhombic crystal structure. These precipitates were observed with an acicular morphology, and with sizes ranging from 2nm to 1μm in the as-solidified condition. The orientation relationship between these precipitates and the Nb matrix is (100)//(100) [010]//[010]. It is suggested that the metastable orthorhombic structure forms due to ease of nucleation of this structure in the bcc Nb matrix. The crystallography of these precipitates is described, and these findings are compared with previous data on the Nb-Si system.

1. INTRODUCTION

Recent studies of Nb-Si in-situ composites have shown a promising combination of high-temperature strength, creep resistance and room-temperature fracture toughness (Mendiratta and Dimiduk 1989, Mendiratta *et al.* 1991, Dimiduk *et al.* 1993, Jackson *et al.* 1996, Cockeram *et al.* 1991a). These composites consist of a Nb-silicide toughened with a Nb solid solution (the Nb-Si solid solution is abbreviated by (Nb) in the present paper). The (Nb) may also contain a dispersion of silicide precipitates (Mendiratta *et al.* 1991, Cockeram *et al.* 1991b, Cockeram *et al.* 1992). The purpose of the present paper is to describe the chemistry and crystallography of precipitates that are generated in Nb solid solutions of directionally solidified (DS) composites of binary Nb-Si and ternary Nb-Ti-Si alloys.

The Nb-rich side of the Nb-Si phase diagram contains a eutectic reaction $\text{liquid} \rightarrow (\text{Nb}) + \text{Nb}_3\text{Si}$ at 1880°C and 18.2% Si (Bewlay *et al.* 1997) (compositions are given in atom percent throughout this paper), and a eutectoid reaction $\text{Nb}_3\text{Si} \rightarrow (\text{Nb}) + \text{Nb}_5\text{Si}_3$ at 1770°C (Mendiratta and Dimiduk 1991, Massalski 1992). These eutectic and eutectoid reactions represent the basis for the in-situ composites that have been investigated previously (Mendiratta and Dimiduk 1989, Jackson *et al.* 1996). Nb_3Si forms by a peritectic reaction between liquid of composition Nb-20%Si and Nb_5Si_3 . The eutectoid decomposition kinetics of Nb_3Si to (Nb) and Nb_5Si_3 are very slow (Subramanian *et al.* 1994), and in as-cast alloys with Si concentrations less than the liquid composition at the peritectic temperature, only Nb_3Si and no primary Nb_5Si_3 is observed. The Nb_5Si_3 and Nb_3Si have tI32 (space group I4/mcm) and tP32 (space group P4₂/n) crystal structures, respectively.

Mendiratta and Dimiduk (1989) have previously observed Si-rich particles in binary Nb-Si alloys, and they postulated that these precipitates were generated as a result of the decrease in the solubility of Si in (Nb) with decreasing temperature on cooling after a 1500°C heat treatment. Cockeram *et al.* (1991a, 1991b) also characterized silicide precipitates seen in a Nb-10Si alloy. The assessed Nb-Si phase diagram (APD) (Massalski 1992) indicates that Nb has a maximum silicon solubility of 3.5% at the eutectic temperature (1880°C) and it decreases to 0.5% at

1770°C. These data can therefore account for the precipitation that has been reported. Mendiratta and Dimiduk (1991) reported the following Si concentrations in Nb as a function of temperature: 1.31% at 1700°C, 0.61% at 1500°C and 0.60% at 1300°C. These data indicate a very sharp decrease in the Si solubility from 3.5% at 1880°C to 1.31% at 1700°C, but there is a smaller decrease from 1700°C to 1300°C. Below 1200°C the solubility of Si in Nb is < 0.1% (Massalski 1992). It should be noted that the recently-reported data regarding solubility of Si in Nb (Mendiratta and Dimiduk 1991) differs from the APD.

Cockeram *et al.* (1991b) characterized precipitates that were found in arc melted Nb-10Si. They used electron diffraction and Energy Dispersive X-ray Spectroscopy (EDS) in the Transmission Electron Microscope (TEM) to identify precipitates in primary (Nb) dendrites. They claimed that the precipitates possessed the Nb₃Si stoichiometry, and that they had the stable tP32 structure. Based on the volume fraction of Nb₃Si precipitates that they observed in the (Nb), they suggested that the maximum solubility of Si in (Nb) at the eutectic temperature was 4.4%.

Phase stability in the ternary Nb-Ti-Si system has been investigated recently and two-phase composites with a wide range of microstructures have been reported (Bewlay *et al.* 1997, Subramanian *et al.* 1994, Bewlay *et al.* 1994). For Ti concentrations up to ~50% and Si concentrations less than 16% the eutectic reaction between (Nb) and Nb₃Si still occurs. In this system the Nb₃Si with Ti in solid solution is referred to as (Nb,Ti)₃Si, because Nb₃Si and Ti₃Si are isomorphous. Similarly, the Nb with Ti and Si in the bcc solid solution is referred to as (Nb,Ti). The (Nb,Ti) solid solution was previously found to contain up to 1.2% Si (Bewlay *et al.* 1997). Silicide precipitates have also been observed in the metallic phase of the (Nb,Ti)-(Nb,Ti)₃Si composites (Bewlay *et al.* 1998). However, there has been no previous examination of the crystallography of these precipitates or their orientation relationship with the (Nb,Ti) matrix.

The present paper describes characterization of silicide precipitates in the Nb solid solutions of composites generated from binary Nb-Si and ternary Nb-Ti-Si alloys. These findings are compared with previous data on the Nb-Si system.

2. EXPERIMENTAL PROCEDURES

Binary Nb-Si and ternary Nb-Ti-Si alloys were prepared from >99.99% purity elements by induction levitation melting in a segmented water-cooled copper crucible. The alloys were triple melted and then directionally solidified using a modified Czochralski method in order to generate two-phase in-situ composites, as has been described in more detail elsewhere (Jackson *et al.* 1996, Bewlay *et al.* 1994).

TEM foils were electro-discharge-machined perpendicular to the growth direction of the DS composites. Samples were ground to 100 μ m thickness, mechanically dimpled to 35 μ m thickness, then perforated using a Gatan DuoMill ion-mill. Samples were examined using a Philips XL-30 Field Emission Gun Scanning Electron Microscope (FEGSEM), a Philips CM200 TEM and a Philips CM300 FEGTEM. Electron microdiffraction was used to determine the crystallography of the silicide precipitates and their orientation relationship with the (Nb) matrix. EDS was performed in order to determine the precipitate chemistry.

3. RESULTS

3.1. Binary Nb₃Si precipitates

The Nb-14%Si hypoeutectic alloy contains (Nb) dendrites and an inter-dendritic eutectic of (Nb) and Nb₃Si, as has been described previously (Bewlay *et al.* 1993, Bewlay *et al.* 1994). Figure 1 shows the typical microstructure of the alloy, with (Nb) as the light phase, and Nb₃Si as the dark phase. Nb₃Si is continuous within the eutectic portion of the microstructure. The typical microstructure of the (Nb) of the DS composite as seen in the TEM is shown in figure 2. Each (Nb) dendrite is essentially a single crystal: no subgrains have been observed.

Heterogeneous precipitation of large-scale silicide precipitates was observed. These precipitates are indicated in figure 2, and a typical group of large-scale silicide precipitates within the (Nb) dendrite of the Nb-14Si composite is shown in more detail in figure 3. These silicides possess Nb_3Si stoichiometry, as will be shown later. The principal axis of the large ($\sim 500\text{nm}$ long), central precipitate is parallel to the $[100]$ direction of the (Nb). Secondary precipitates have grown off the large central precipitate in directions parallel to the $[010]$ and $[001]$ of the (Nb). Precipitate-free zones $\sim 100\text{nm}$ wide were observed in the (Nb) around the silicide precipitates. In the (Nb) dendrite away from the large-scale silicide precipitates contrast was observed from fine-scale ($\sim 50\text{nm}$ long) acicular silicide precipitates, as indicated in figure 3. These precipitates are distributed homogeneously throughout the dendrite, except in the precipitate-free-zones, where they are absent.

Precipitate-free-zones, typically $1\mu\text{m}$ wide, are also found at the boundaries of the (Nb) dendrites. Cockeram *et al.* (1991b) also reported precipitate free zones $0.6\text{--}1.3\mu\text{m}$ wide in the primary (Nb) dendrites. No precipitates are found in the eutectic (Nb). This is expected, since the width of the eutectic (Nb) ligaments is less than the width of the precipitate-free-zone seen in the (Nb) dendrite.

Electron microdiffraction patterns, shown in figure 4, indicate that the eutectic Nb_3Si possesses the stable tP32 structure. However, the silicide precipitates within the (Nb) were found to possess a different crystal structure, as will be shown.

The silicide precipitate chemistry was determined using TEM EDS, as described below. Several precipitate compositions were compared to the composition of the eutectic Nb_3Si using EDS measurements taken from very thin regions at the edge of the foil, where any spectral interference from the (Nb) matrix is minimized. Measurements were taken using the CM300 FEGTEM to make use of the fine probe size and high intensity afforded by the FEG source. Assuming that the eutectic Nb_3Si has the exact 3:1 stoichiometry, and thus using it to determine k-factors, the composition of the precipitates was determined to be in the range Nb-24%Si to Nb-

27%Si. This is sufficiently small scatter that it may be concluded that the composition of the precipitates is based on the stoichiometry Nb₃Si.

Diffraction data obtained in the present study, and shown in figure 5, show that these large-scale silicide precipitates possess an orthorhombic crystal structure. Extensive tilting experiments were performed to determine the point group and lattice parameters. The diffraction patterns in figure 5 were obtained using the high-tilt stage of the CM200 TEM, where it was possible to tilt 90° from one <100> pole to the next. Thus it was possible to determine unequivocally that the structure was orthorhombic. Approximate lattice parameters were obtained by assuming that the lattice parameter of the (Nb) matrix was 3.30Å. Thus the lattice parameters were determined to be $a = 9.3\text{\AA}$, $b = 15.9\text{\AA}$, $c = 3.4\text{\AA}$, which approximately corresponds to factors of 3, 5, and 1 times that of the (Nb) lattice parameter. The point group was determined to be mmm, and, based solely on the reflections observed to be absent in the microdiffraction patterns, it is suggested that the space group is Immm.

The following orientation relationship was observed between the precipitates and the (Nb) matrix:

$$[100]_{\text{Nb}} \parallel [100]_{\text{ppt}} ; (001)_{\text{Nb}} \parallel (001)_{\text{ppt}}.$$

The precipitates described by Cockeram *et al.* (1992) possessed a rod/plate-like morphology (0.05-0.2µm). Cockeram *et al.* (1991b) reported that the diffraction patterns from the silicide precipitates observed in that study were consistent with a tetragonal structure with lattice parameters of $a = 10.224\text{\AA}$ and $c = 5.189\text{\AA}$.

Certain diffraction patterns obtained from the silicide precipitates in the (Nb) of the DS composites observed in the present study appear identical to those published by Cockeram *et al.* (1991b), where they are identified as originating from tetragonal Nb₃Si. Re-examination of the precipitate diffraction patterns published previously indicates that the diffraction spots in figure 3c (Cockeram *et al.* 1991b) are of approximately the correct spacing, but the angles between

reflections are inconsistent with those expected for the $\langle 311 \rangle$ poles* of tetragonal Nb_3Si . Essentially, the Zero-Order-Laue-Zone (ZOLZ) in figure 3c (Cockeram *et al.* 1991b) appears to show 2mm symmetry, which the $\langle 311 \rangle$ poles of tetragonal Nb_3Si do not possess. Furthermore, the proposed orientation relationship of $[113]_{\text{Nb}_3\text{Si}} \parallel [001]_{\text{Nb}}$; $(\sim 110)_{\text{Nb}_3\text{Si}} \parallel (100)_{\text{Nb}}$ is inconsistent with the claim that the $\langle 311 \rangle$ poles are parallel to $\langle 001 \rangle_{\text{Nb}}$ directions, since the angle between $[113]$ and $[311]$ or $[131]$ is $\sim 44^\circ$, not 90° , and no $\langle 311 \rangle$ pole is at 90° to any $\langle 113 \rangle$ pole. In fact the poles shown in figures 3c and 4a (Cockeram *et al.* 1991b) correspond very well to the $[010]$ and $[100]$ poles shown in figure 5 of the present study. These slight inconsistencies in the analysis by Cockeram *et al.* (1991b) probably arose because the precipitates observed were small ($< 100\text{nm}$ in width) and the inter-particle spacing was small ($< 100\text{nm}$). The diffraction patterns seen in (Cockeram *et al.* 1991b) and in the present study appear identical, and so it is concluded that the precipitates observed in the previous study of Nb-10Si were also orthorhombic.

The fine-scale precipitates, shown in detail in figure 6, were found to have the same structure as the large-scale precipitates. Figure 7 shows the three $\langle 001 \rangle$ poles of the orthorhombic structure taken from precipitates such as those shown in figure 6. The precipitates are faceted, with facet faces parallel to $\{110\}_{\text{ppt}}$, as is shown in figure 6. Precipitates have an acicular morphology, with $[001]_{\text{ppt}}$ parallel to the axis of the needle.

3.2. Ternary $(\text{Nb,Ti})_3\text{Si}$ precipitates

The microstructure of the as-DS Nb-42.5Ti-15Si consisted of non-faceted (Nb,Ti) dendrites ($20\text{-}50\mu\text{m}$), which are the lighter phase in the BSE micrograph in figure 8, together with large-scale ($\sim 50\mu\text{m}$) faceted $(\text{Nb,Ti})_3\text{Si}$ dendrites. The microstructure showed good alignment of both non-faceted (Nb,Ti) dendrites and faceted $(\text{Nb,Ti})_3\text{Si}$ dendrites with the growth direction.

* The mixed notation $\{hkl\}$ and $\langle uvw \rangle$ is used to differentiate the first two indices from the third index, both in the case of the tetragonal structure *and* the orthorhombic structure.

A typical array of silicide precipitates within a (Nb,Ti) dendrite is shown in figure 9. The precipitates are elongated in the $[001]_{\text{ppt}}$ direction, and all possible orientational variants with the matrix are seen. Precipitation is generally homogeneous, as shown in figure 10, with groups of heterogeneously-nucleated precipitates surrounded by a precipitate-free zone, as shown in figure 9. The binary alloy discussed earlier also exhibited a bimodal precipitate distribution, although it is yet to be confirmed that the bimodal array in both alloys is formed by a similar precipitation mechanism.

The silicide precipitates in the (Nb,Ti) have the same orthorhombic crystal structure and orientation relationship with the (Nb,Ti) matrix as found in the binary alloy, and to within the limits of the TEM diffraction measurements, the same lattice parameters. The precipitates are faceted, with facet faces parallel to $\{110\}_{\text{ppt}}$ as found for the binary alloy. Typically, the homogeneous precipitates had a width of $\sim 10\text{nm}$ (facet-to-facet) in the as-DS condition. Again, EDS identified these silicide precipitates as $(\text{Nb,Ti})_3\text{Si}$ -type rather than $\text{Nb}(\text{Ti})_5\text{Si}_3$ type. While the details of these precipitates are reported for the (Nb,Ti) of the Nb-42.5Ti-15Si, similar precipitates have also been observed in Nb-44Ti-12Si, Nb-1Si and other Nb-Ti-Si alloys in the DS condition, as well as after various heat treatments. Work is continuing to establish the precipitation kinetics at various temperatures, and to examine the effect of these precipitates on mechanical properties.

4. DISCUSSION

In the (Nb,Ti) it was expected that the precipitates would be the Nb_3Si type because additions of $\geq 17\%$ Ti stabilize Nb_3Si in preference to Nb_5Si_3 (Bewlay *et al.* 1997, Subramanian *et al.* 1994). However in the binary alloy Nb_3Si is unstable below 1770°C . Thus in the binary alloy not only is the precipitate *composition* metastable with respect to Nb_5Si_3 , but the *crystal structure* is also metastable with respect to the stable tP32 structure of Nb_3Si .

Therefore, why is the orthorhombic phase observed in these alloys? Simply from considerations of the mismatch between precipitate and matrix, it can be seen that the interface

between matrix and orthorhombic precipitate will require one extra plane of atoms present only when the precipitate reaches ~5nm in size. Thus the interphase interface would be expected to be coherent up to a certain size of precipitate, and semi-coherent for larger sizes. Although the atomic structure of the precipitates has not been determined, diffraction evidence suggests that the orthorhombic precipitates may be body-centered in structure, and thus may nucleate easily by ordering of the bcc matrix, which could make the barrier to nucleation quite low. No simple lattice match exists between the (Nb) matrix and either tP32 Nb₃Si or tI32 Nb₅Si₃ (Cockeram *et al.* 1991a). This suggests that the barrier to nucleation of orthorhombic Nb₃Si may be significantly lower than the barrier to nucleation of either of the stable structures. Therefore it is thought that the orthorhombic structure is seen because of close lattice matching of the precipitate and matrix, and so the orthorhombic precipitates are able to form at a lower undercooling than either of the stable structures. Work is continuing to establish the heat-treatment conditions whereby the orthorhombic structure transforms to the stable phase.

The ordered orthorhombic (Nb,Ti)₃Si and Nb₃Si are thus considered to be metastable precipitates that may be nucleated by ordering of Si atoms within the (Nb). In the case of (Nb,Ti)₃Si the orthorhombic structure is intermediate to the stable tP32 (Nb,Ti)₃Si. However, Nb₃Si is intermediate to the stable tI32 Nb₅Si₃.

5. CONCLUSIONS

Precipitates were observed in (Nb) and (Nb,Ti) of the in-situ composites of both binary Nb-Si and ternary Nb-Ti-Si alloys. The precipitates possess an ordered orthorhombic structure, with lattice parameters $a = 9.3\text{\AA}$, $b = 15.9\text{\AA}$, $c = 3.4\text{\AA}$. The following precipitate-matrix orientation relationships were observed in both the Nb-Si binary and the Nb-Ti-Si ternary alloys:

$$[100]_{\text{Nb}} \parallel [100]_{\text{ppt}} ; (001)_{\text{Nb}} \parallel (001)_{\text{ppt}}$$

The precipitates exhibited a bimodal distribution, and it is suggested that the large-scale precipitates nucleate heterogeneously and finer-scale homogeneously. However, all precipitates showed the same crystal structure, orientation relationships and acicular morphology, with

$[001]_{\text{ppt}}$ being parallel to the principal axis of the precipitate. The bulk Nb_3Si in the binary Nb-Si and the bulk $(\text{Nb,Ti})_3\text{Si}$ in the Nb-Ti-Si alloys possess the stable tP32 structure.

The $(\text{Nb,Ti})_3\text{Si}$ precipitates are metastable with respect to the tP32 structure, but they possess the stable stoichiometry. The Nb_3Si precipitates are metastable with respect to both the stoichiometry and crystal structure of tI32 Nb_5Si_3 . Ordering to the metastable orthorhombic Nb_3Si requires a smaller nucleation barrier than to the stable tI32 Nb_5Si_3 and the close matching of the lattice plane spacing of the matrix and precipitate allows the interfacial energy to be minimized.

The interphase interfaces are semi-coherent for the large-scale precipitates and are expected to be coherent for very fine precipitates ($\sim 5\text{nm}$ in size). Incoherent orthorhombic precipitates were not observed.

ACKNOWLEDGMENTS

The authors would like to thank D.J. Dalpe for preparation of the initial DS samples. Grateful thanks are extended to Suqin Meng for the often difficult TEM sample preparation. This research was partially sponsored by AFOSR under contract #F49620-96-C-0022 with Capt. C.H. Ward and Dr. S. Wu as Program Managers.

REFERENCES

- Bewlay, B.P., Lipsitt, H.A., Reeder, W.J., Jackson, M.R., and Sutliff, J.A., 1993, *Processing and Fabrication of Advanced Materials for High Temperature Applications III*, edited by V.A. Ravi, T.S. Srivatsan, and J.J. Moore (Warrendale Pennsylvania, The Minerals Metals and Materials Society) p. 547.
- Bewlay, B.P., Jackson, M.R., Reeder, W.J., and Lipsitt, H.A., 1994, *High Temperature Ordered Intermetallic Alloys VI*, Materials Research Society Symposium Proceedings, **364**, edited by J.A. Horton, I. Baker, S. Hanada, R.D. Noebe, and D.S. Schwartz (Pittsburgh, Pennsylvania: Materials Research Society) p. 943.
- Bewlay, B.P., Jackson, M.R., and Lipsitt, H.A., 1997, *J. phase equil.*, **18**, 264.
- Bewlay, B.P., Bishop, R.R., and Jackson, M.R., 1998, submitted to *J. phase equil.*
- Cockeram, B., Lipsitt, H.A., Srinivasan, R. and Weiss, I., 1991a, *Scripta metall. mater.*, **25**, 2109.
- Cockeram, B., Saqib, M., Omlor, R., Srinivasan, R., Matson, L.E. and Weiss, I., 1991b, *Scripta metall. mater.*, **25**, 393.
- Cockeram, B., Lipsitt, H.A., Srinivasan, R. and Weiss, I., 1992, *Scripta metall. mater.*, **26**, 755.
- Dimiduk, D.M., Mendiratta, M.G., and Subramanian, P.R., 1993, *Structural Intermetallics*, edited by R. Darolia, J.J. Lewandowski, C.T. Liu, P.L. Martin, D.B. Miracle, and M.V. Nathal (Warrendale Pennsylvania, The Minerals Metals and Materials Society) p. 619.
- Jackson, M.R., Bewlay, B.P., Rowe, R.G., Skelly, D.W., and Lipsitt, H.A., 1996, *J. Metals*, **48**, 38.
- Massalski, T.B., 1992, *Binary Alloy Phase Diagrams* (ASM Metals Park, Ohio), **3**, 2764.
- Mendiratta, M.G., and Dimiduk, D.M., 1989, *High Temperature Ordered Intermetallic Alloys III*, Materials Research Society Symposium Proceedings, **133**, edited by C.T. Liu, A.I. Taub, N.S. Stoloff and C.C. Koch (Pittsburgh, Pennsylvania: Materials Research Society) p. 441.
- Mendiratta, M.G., and Dimiduk, D.M., 1991, *Scripta metall. mater.*, **25**, 237.



Figure 1 Backscattered Electron (BSE) scanning electron micrograph showing a transverse section through the as-DS binary composite. The (Nb) dendrite is surrounded by a eutectic mixture of Nb_3Si and (Nb). (Nb) is the lighter phase.



Figure 2 Many-beam bright-field transmission electron micrograph showing the typical distribution of precipitate groups within a (Nb) dendrite. Each group consists of many precipitates. Beam direction \underline{B} is close to $\langle 001 \rangle_{(\text{Nb})}$.

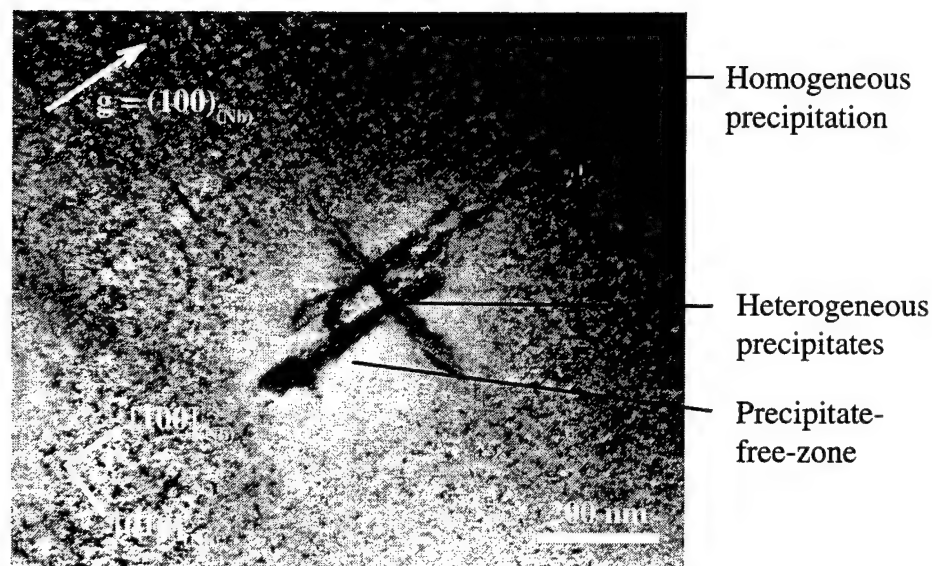


Figure 3 Two-beam bright-field transmission electron micrograph showing a typical group of heterogeneously-nucleated precipitates within a (Nb) dendrite. A precipitate-free zone can be seen around the group. Outside this zone, fine-scale, homogeneously-nucleated acicular precipitates are seen, as shown in more detail in Figure 6. **B** is close to $[001]_{(Nb)}$.

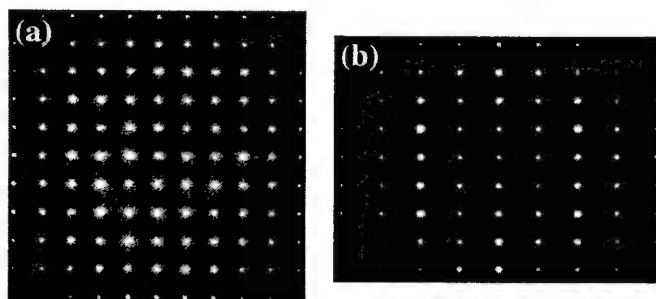


Figure 4 Microdiffraction patterns showing the (a) $[001]$ and (b) $[110]$ poles of the continuous Nb_3Si phase formed during eutectic solidification. All poles and angles between poles are consistent with the stable tP32 structure of Nb_3Si .

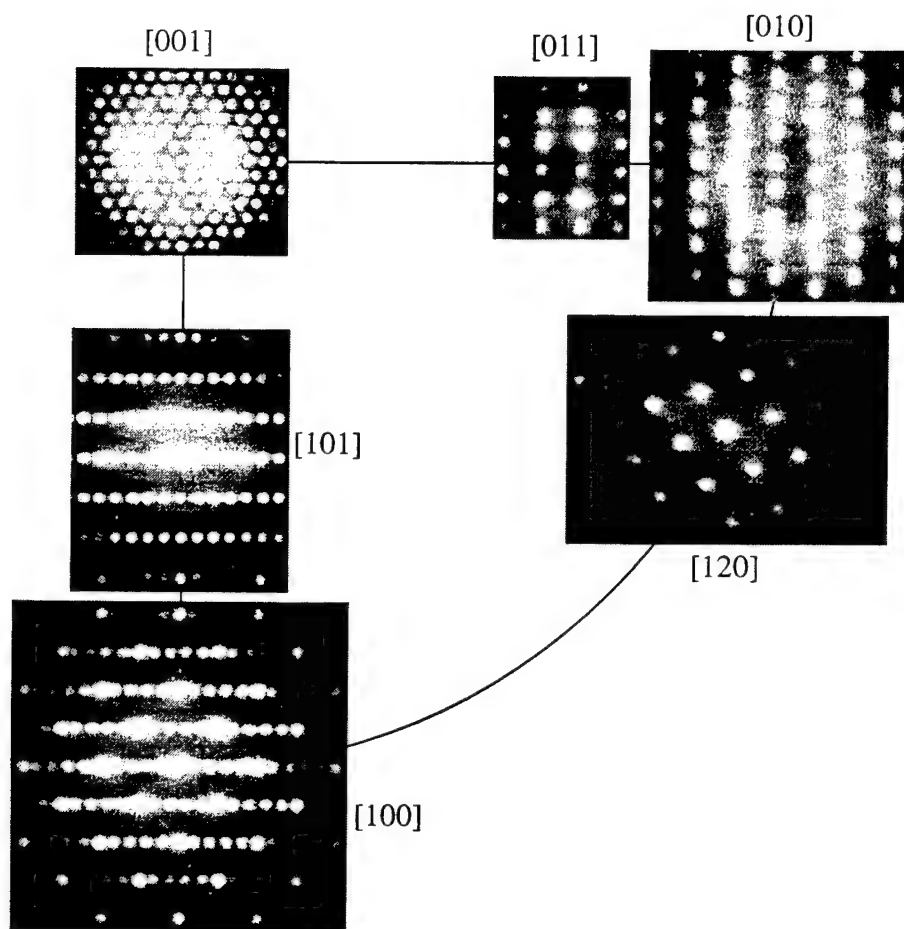


Figure 5 Microdiffraction patterns taken from large-scale Nb_3Si precipitates within a (Nb) dendrite. All poles and angles between poles are consistent with an orthorhombic structure, point group mmm , with lattice parameters $a = 9.3\text{\AA}$, $b = 15.9\text{\AA}$, $c = 3.4\text{\AA}$.

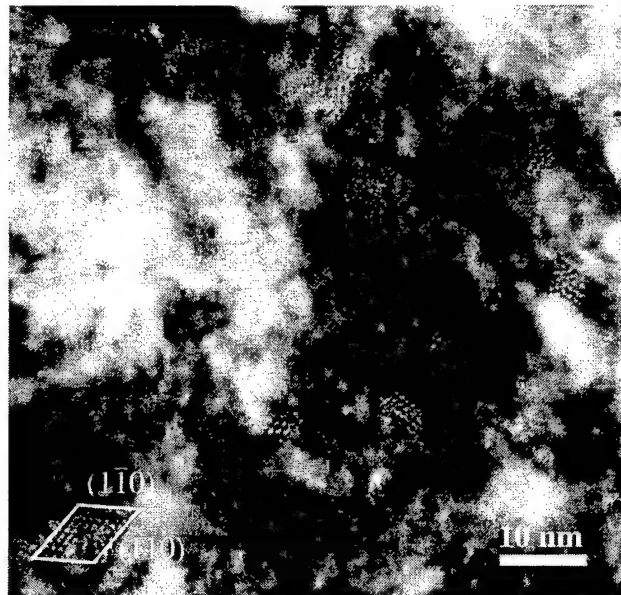


Figure 6 Many-beam bright-field transmission electron micrograph showing fine orthorhombic precipitates. The precipitates tend to be faceted, with facet faces parallel to $\{110\}_{\text{ppt}}$. Only precipitates with $[001]$ parallel to the beam direction are imaged in this case. Precipitates lying in the plane of the foil are essentially invisible. One precipitate has been outlined, and the faceted planes identified. $\mathbf{B} = \langle 001 \rangle_{(\text{Nb})}$.

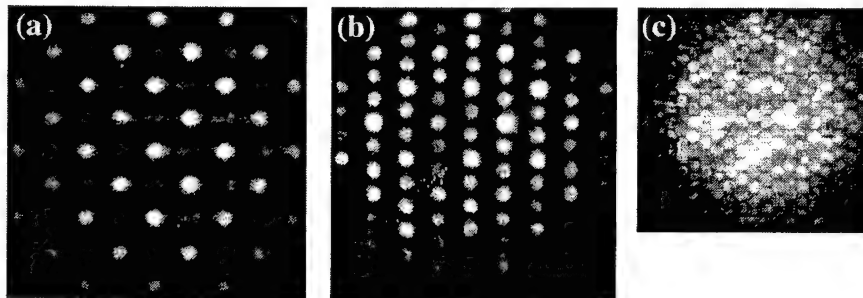


Figure 7 Microdiffraction patterns taken from the very fine Nb_3Si precipitates shown in Figure 6. The zone-axis is in each case $\langle 100 \rangle_{\text{Nb}}$, and the diffraction patterns obtained are entirely consistent with the mmm orthorhombic structure. (a) $[100]$ (b) $[010]$ (c) $[001]$.

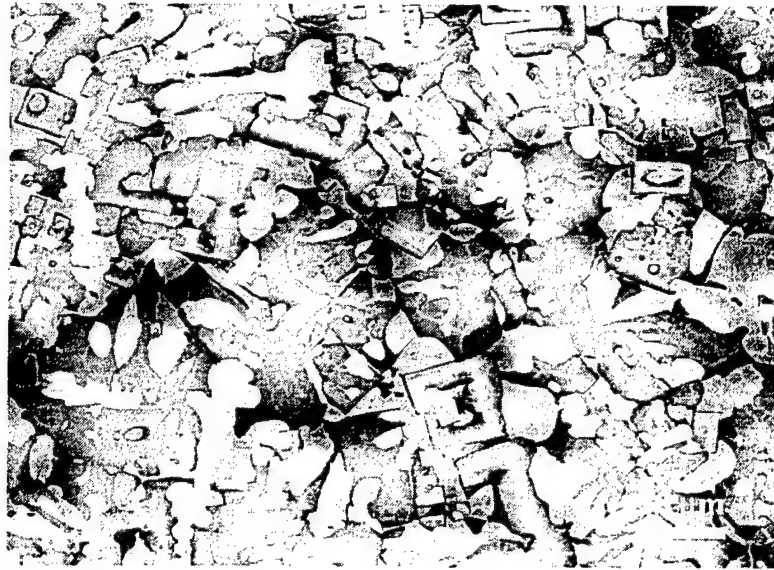


Figure 8 BSE scanning electron micrograph showing a transverse section through the as-DS ternary composite. (Nb,Ti) is the lighter phase, with $(\text{Nb,Ti})_3\text{Si}$ the darker phase.

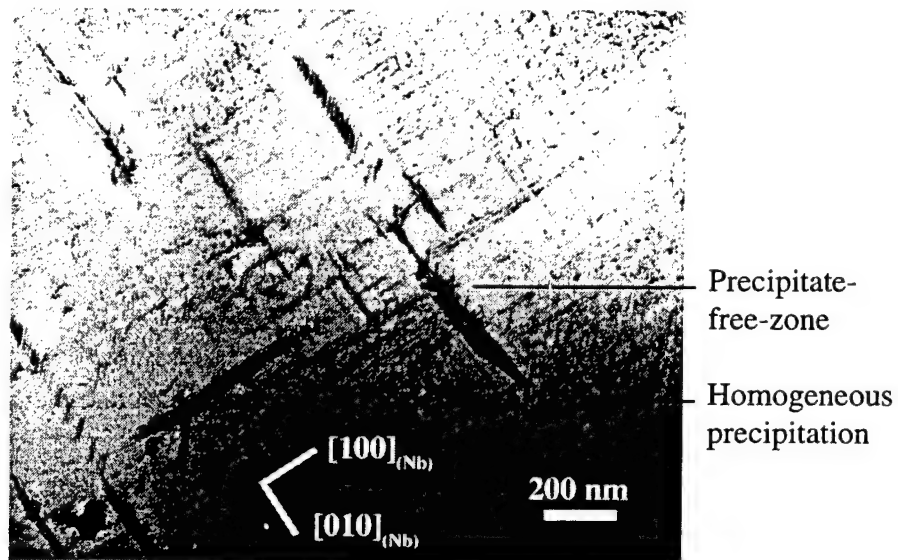


Figure 9 Two-beam bright-field transmission electron micrograph showing typical groups of precipitates within a (Nb,Ti) dendrite. Precipitate-free zones can be seen around the larger precipitates. Outside this zone, fine-scale, homogeneously-nucleated acicular precipitates are seen, as shown in Figure 10. \mathbf{B} is close to $[001]_{(\text{Nb})}$.



Figure 10 Two-beam bright-field transmission electron micrograph showing homogeneously-nucleated acicular precipitates within a (Nb,Ti) dendrite. \mathbf{B} is close to $[001]_{(Nb)}$.

Recent Advances in Nb-Silicide In-Situ Composites

B.P. Bewlay, C.L. Briant, M.R. Jackson, and P.R. Subramanian

Plansee Seminar, 2001

Recent Advances In Nb-Silicide In-Situ Composites

B.P. Bewlay⁺, C.L. Briant^{*}, M.R. Jackson⁺, and P.R. Subramanian⁺

General Electric Company, Corporate Research and Development Center,
Schenectady, New York 12301, USA⁺

Division of Engineering, Brown University, Providence, RI 02912, USA^{*}

Summary:

In-situ composites based on Nb silicides have great potential for future high-temperature applications. These Nb-silicide composites combine a ductile Nb-based matrix with high-strength silicides. With the appropriate combination of alloying elements, such as Ti, Hf, Cr, Al, it is possible to achieve a promising balance of fracture toughness, high-temperature creep performance, and oxidation resistance. This paper will describe the effect of volume fraction of silicide on microstructure, high-temperature creep performance, and oxidation resistance. The ratio of Nb:(Hf+Ti) is critical in determining both creep rate and oxidation performance. If this ratio goes below ~1.5, the creep rate increases substantially. In more complex silicide-based systems, other intermetallics, such as Laves phases and a boron-rich T-2 phase, are added for oxidation resistance. To understand the role of each phase on the creep resistance and oxidation performance of these composites, we determined the creep and oxidation behaviors of the individual phases and composites at temperatures up to 1200°C. These data allow quantification of the load-bearing capability of the individual phases in the Nb-silicide based in-situ composites.

Keywords:

Niobium, silicide, composite high-temperature, creep, oxidation resistance, Laves phase

1. Introduction:

Nb-silicide based in-situ composites are potential candidates for very high temperature structural applications (>1150°C), including advanced turbine applications [1-6]. These composites consist of Nb₅Si₃ and Nb₃Si type silicides toughened with a Nb solid solution (abbreviated by (Nb) in the

present paper). More recent Nb-silicide based in-situ composites are highly alloyed with elements such as Cr, Ti, Hf, B and Al [2-6]. Previous work has shown that these materials exhibit a good combination of room temperature fracture toughness and high temperature strength [1-6]. However, their high-temperature creep performance has been found to be highly dependent on the alloy composition and constituent phases. With the appropriate combination of alloying elements it is possible to achieve the required balance of room temperature toughness and high-temperature creep resistance. Alloying elements such as Cr and B have beneficial effects on oxidation resistance, stabilizing Laves phases, and T2 niobium borosilicide phases, respectively.

Advances in high-temperature materials have had a major impact on the efficiency of gas turbine engines, so that currently superalloys provide a maximum surface temperature capability of $\sim 1150^{\circ}\text{C}$. A Nb-based composite system, with a melting temperature of 1800°C or more, may allow a substantial increase in surface temperature. In the past decade, the potential of new alloys strengthened with intermetallic compounds with low densities, high elastic moduli, and high melting ranges [3,6] has been explored. Intermetallic-based composite materials, such as Nb or Mo silicides, have been combined with metallic second phases in order to generate composites with a combination of attractive high-temperature properties and acceptable low-temperature properties. Nb-silicide based in-situ composites with Nb_3Si and/or Nb_5Si_3 silicides have been shown to have great potential because of their attractive balance of high- and low-temperature mechanical properties [2,4]. These materials have the potential to surpass the performance of Ni-based superalloys.

The basis for phase stability in Nb : niobium-silicide composites is the Nb-rich side of the Nb-Si phase diagram where there is a eutectic between Nb_3Si and (Nb) [7,8]. (Nb)- Nb_3Si and (Nb)- Nb_5Si_3 composites have been prepared from binary Nb-Si alloys [1,3] with compositions from 10 to 25Si (all compositions are given in atom per cent throughout the present paper). The microstructure of the composites from binary hypoeutectic alloys consists of (Nb) dendrites with an interdendritic Nb_3Si -(Nb) eutectic. In these composites extrinsic toughening is provided by the (Nb); there is no intrinsic ductility in the silicide. The Nb_5Si_3 and Nb_3Si have the tI32 and tP32 ordered tetragonal structures with 32 atoms per unit cell. The unit cells also possess large lattice parameters; the large Burgers vectors and complex dislocation cores associated with these structures would suggest that dislocation creep makes only a small contribution to creep deformation in these silicides. When Nb_5Si_3 is alloyed with Ti and Hf, the less complex hP16 structure can also be stabilized [8-10]. Nb_3Si and tetragonal Nb_5Si_3 are beneficial to creep

behavior, provided their volume fraction and distribution within the composite are controlled [10].

The present study was performed to determine the creep rates of Nb-silicide based composites, and the monolithic intermetallic phases in complex systems. This study was designed to develop both the constitutive creep laws for these phases and a predictive modeling capability for more complex two-phase and multi-phase systems [11]. The aim of the present paper is to describe high-temperature creep behavior of the monolithic intermetallic phases and the resulting Nb-silicide in-situ composites that were produced by directional solidification. Oxidation behavior is also discussed.

2. Experimental:

Nb-silicide based in-situ composites were directionally solidified from quaternary alloys with compositions of Nb-8Hf-25Ti-XSi, where X was adjusted from 12 to 22%. The starting charges were prepared from high purity elements (>99.99%). The directional solidification procedure has been described in more detail previously [1]. Monolithic intermetallic creep samples were prepared using multiple arc melting. Monolithic Nb alloys were also prepared with compositions of Nb-1Si, Nb-46Ti-1Si (denoted as Nb-3 in the present paper), and Nb-27Ti-5Hf-2Al-2Cr-0.9Si (denoted as Nb-C), in order to determine the creep performance of the Nb solid solution in the in-situ composites. The samples were examined using scanning electron microscopy and Electron Back-Scatter Diffraction in the SEM (EBSD).

Table I shows the compositions of the monolithic intermetallic phases that were investigated. The compositions of these phases were selected using electron microprobe analyses (EMPA) of the respective phases in multi-phase composites [8,9]. Monolithic intermetallics that were generated from ternary alloys were given the post-script 3, for example, the Nb₅Si₃ modified with 10% Ti was labeled silicide-3. The monolithic intermetallics that were prepared from quaternary and higher-order alloys were given the post-script C, such as silicide-C.

Compression creep tests were conducted at temperatures of 1100 and 1200°C, and at stress levels of up to 280 MPa in a vacuum of $\sim 5 \times 10^{-5}$ Torr. The cylindrical specimens that were used were 7.6 mm in diameter and up to 30 mm in length. The samples were machined by EDM to final dimensions. In each test the sample was placed between two silicon nitride platens to prevent breakage of the large graphite rams.

Nb foil was placed at the interface between the platens and the sample to prevent any contamination of the sample or reaction with the platens. Incremental loading and interruption of the creep tests at 24-hour intervals were employed to determine the creep rate at multiple stress levels.

Table I: Compositions (in atom per cent) of the monolithic phases that were investigated. The phases labeled 'silicide' are both based on the Nb_5Si_3 .

PHASE	Nb	Ti	Hf	Si	Cr	Al	B
Laves-C	21.0	11.0	5.5	8.5	53.0	1.0	
Laves-3	30.0			15.0	55.0		
Silicide-C	38.5	16.0	6.0	37.0	1.0	1.0	0.5
Silicide-3	53.0	10.0		37.0			
T2-C	41.5	13.0	3.0	12.5	4.0	0.5	25.5
T2-3	62.5			12.5			25.0
hP16-3	20	44		36.0			
hP16-C	25.5	25.5	13	36.0			
(Nb) ₃ Si-C	49.0	18.2	7.8	25.0			
(Nb)-C	63.1	27	5	0.9	2	2	
Nb-1Si	99			1			
Nb-46Ti-1Si	53	46		1			

Isothermal oxidation tests were performed at 1200 and 1315°C, in a static air MoSi₂-resistance heated furnace. Periodic removal from the furnace (at 1, 2, 4, 25, 50, and 100 hours, or until the test was terminated (due to visual observation of gross material loss), was performed to determine weight change per unit area. The samples were machined by first electro-discharge machining and then centerless grinding to final dimensions, so that the longitudinal axis was parallel to the growth direction, the sample being nominally 2.5 mm in diameter and 25 mm in length. Metallography was performed at the termination of the test to determine the approximate material loss after 100 hours of exposure.

3. Results and Discussion:

Composite Microstructures

Figure 1 shows the typical microstructure of the composites based on Nb-8Hf-25Ti-XSi alloys with Si concentrations of 20% and less. The microstructure consisted of (Nb)₃Si tP32 phase (the grey phase) with (Nb) dendrites (the light phase). The dendrites appear to have grown cooperatively to generate an interpenetrating structure. Both the (Nb)₃Si and the (Nb) possess substantial amounts of Hf and Ti in solid solution [8,9].

There was some Ti segregation in the (Nb) which led to varying back scatter electron (BSE) contrast at the interface between the (Nb) and the $(\text{Nb})_3\text{Si}$.

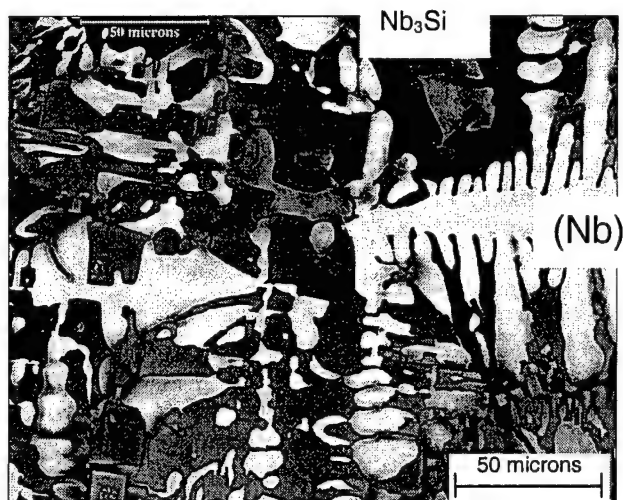


Figure 1. *Scanning electron micrograph (BSE image) of the typical microstructure of the transverse section of a DS composite generated from a quaternary Nb-25Ti-8Hf-16Si alloy. The (Nb) is the light phase and the $(\text{Nb})_3\text{Si}$ is the grey faceted phase.*

Figure 2 shows the typical microstructure of the composites with Si concentrations greater than 20% and less than 25%Si. In addition to the $(\text{Nb})_3\text{Si}$ and (Nb) phases observed in the composites from lower Si concentrations, the Nb_5Si_3 t132 phase was also observed as the primary solidification phase. The $(\text{Nb})_5\text{Si}_3$ was the large-scale, dark, faceted phase.

Creep of Composites

Figure 3 shows the creep rate as a function of Si concentration for the Nb-25Ti-8Hf-XSi composites, where X was adjusted from 12 to 22 atomic percent. Data are shown at 1200°C for stresses of 140 to 280 MPa. Quantitative microscopy indicated that as the Si concentration was increased from 12% to 18%, the volume fraction of $(\text{Nb})_3\text{Si}$ increased from 0.25 to 0.62. There is a broad range of compositions for which the creep rate is less than $3 \times 10^{-8} \text{s}^{-1}$, which is an important design goal for high-temperature applications [4].

There are two important features of these creep data. First, the creep rate possessed a minimum value between 18 and 20 %Si. The compositional width of the creep rate minimum decreased with increasing stress. Second, at higher Si concentrations (>20%) the creep rate increased. Microstructural analysis of samples after creep testing indicated that at low Si

concentrations, deformation was controlled by creep of the (Nb), but at high Si levels, creep deformation was controlled by cracking of the silicide.

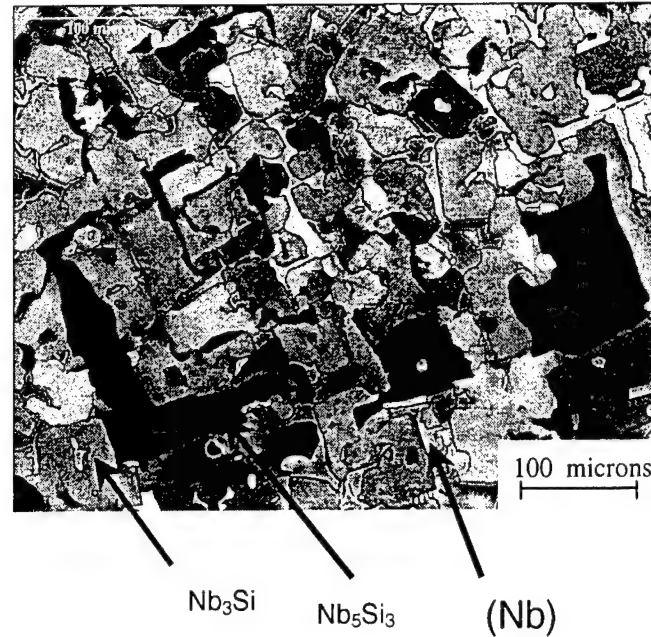


Figure 2. Scanning electron micrograph (BSE image) of the typical microstructure of a transverse section of a DS composite from a quaternary Nb-25Ti-8Hf-22Si alloy. The (Nb) is the light phase, the $(\text{Nb})_3\text{Si}$ is the grey phase, and the $(\text{Nb})_5\text{Si}_3$ the dark phase.

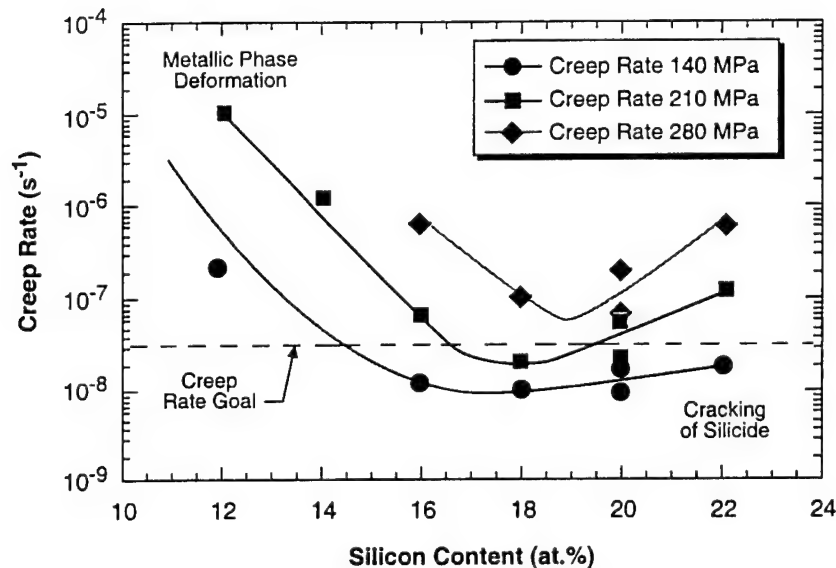


Figure 3. Effect of Si concentration (volume fraction of metal and silicide) on the secondary creep rate of Nb-Si based composites for stresses of 70-280 MPa at 1200°C. At low Si concentrations, deformation is controlled by creep of the (Nb) and at high Si concentrations, composite deformation is controlled by cracking of the silicide.

Creep Behavior of the Monolithic Phases

The creep data for the monolithic intermetallics are shown in Figure 4. Figure 4 also shows data for the binary monolithic Nb_5Si_3 , and the Nb_5Si_3 -Nb composite prepared from the binary Nb-10Si alloy [11]. The binary Nb_5Si_3 possessed the lowest creep rates and the Nb_3Si -C displayed the highest creep rates of the tetragonal phases investigated. The hP16 phases had creep rates similar to the T2-C phase at stresses up to 140 MPa. However, on increasing the stress above 140 MPa the creep rate of the hP16-C increased rapidly to a level of $3 \times 10^{-5} \text{s}^{-1}$ at 210 MPa, as shown in Figure 4. This behavior suggests a change in creep mechanism with increasing stress. The hP16 phases have the worst performance, and at high stresses these creep rates are beyond the scale of Figure 4.

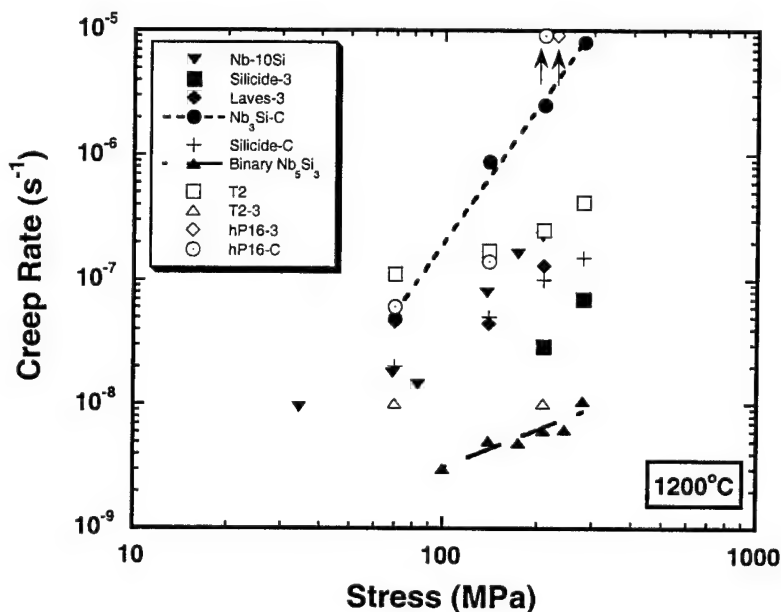


Figure 4. Secondary creep rates at 1200°C for the monolithic silicides, Laves phases, hP16 and T2 phases that were investigated.

The silicide-3 and silicide-C had creep rates that were also higher than those of the binary Nb_5Si_3 . The ternary Nb_5Si_3 with Ti had a lower creep rate than the Nb_5Si_3 -C. The T2-C creep curve was higher than those of the Nb_5Si_3 type silicides, although it is lower than that of the Nb_3Si -C. The creep rate of the T2-3 was $\sim 1 \times 10^{-8} \text{s}^{-1}$, but there was little sensitivity of the creep rate to stress. The T2-3 also had a lower creep rate than the T2-C; the addition of Ti, Hf, Cr and Al led to an increase in the creep rate of the T2. The Laves-3 possessed creep rates similar to those of the silicide-3.

The creep rates of the Nb-1Si, Nb-46Ti-1Si, and Nb-C at 1100°C and 1200°C are shown as a function of stress in Figure 5. These compositions cover the compositions of the Nb-based solid solutions in the composites that have been generated previously from ternary, quaternary, and higher-order alloys. The data at 1200°C indicate that the creep rate of the (Nb) is greater than 10^{-7}s^{-1} even at stresses as low as 70 MPa. The creep rates of these monolithic Nb alloys are similar to those of the composites from the low Si (less than 14%) quaternary alloys shown in Figure 3. These results also show that the creep rate of the Nb-Si solid solution is very sensitive to Ti additions.

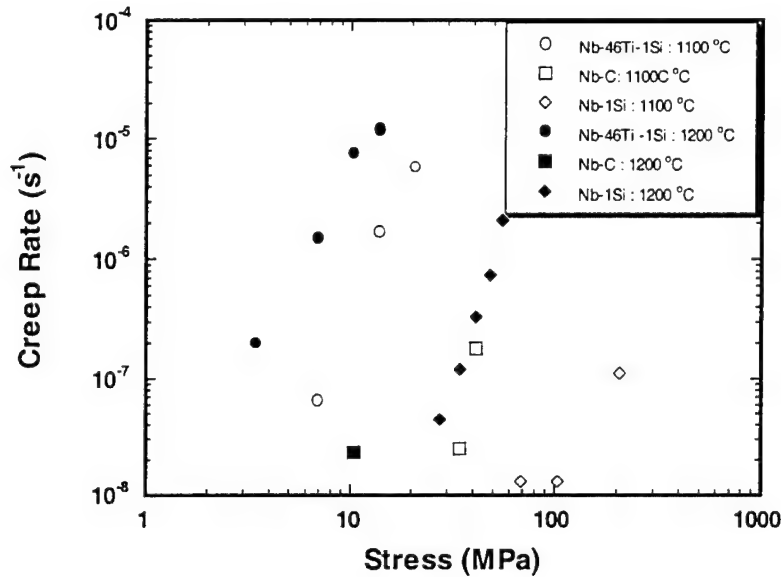


Figure 5. Secondary creep rates as a function of stress at 1100°C and 1200°C for binary Nb-Si, ternary Nb-Ti-Si, and complex Nb-based monolithic solid solutions. Note the stress range is 10 times lower than in Figures 3 and 4. The effect of alloying additions on creep rate is shown.

The stress sensitivity of the creep rate was determined by relating the creep rate ($\dot{\epsilon}$) and stress (σ) using a power law equation of the form, $\dot{\epsilon} = B \sigma^n$; where n is the stress exponent and B is a constant at any specific temperature. The grain size of all the monolithic phases was large and of approximately the same order of magnitude ($\sim 100 \mu\text{m}$). In the present study no attempt was made to incorporate any dependence of the creep rate on grain size.

The stress exponents are shown in Table II. In the case of the Nb_5Si_3 the stress exponent was almost one and the mechanism for creep deformation was reported to be Nabarro-Herring creep, the creep deformation being limited by Nb diffusion [12]. In the cast and heat treated conditions, the dislocation densities in the monolithic intermetallic phases investigated were

very low, and Harper-Dorn creep probably did not make a significant contribution to creep. Therefore, the potential creep mechanisms are Nabarro-Herring, grain boundary sliding, or power law creep for the cases where the exponents are close to unity. Examination of the creep exponents in Table II indicates that the creep deformation of the monolithic phases is controlled by a range of mechanisms. For example, the T2-C, Laves-3, and silicide-C constitute the first group that have exponents close to unity, as is the case for binary Nb_5Si_3 . Creep deformation of these phases is probably also controlled by Nabarro-Herring type creep, but the diffusing species that control deformation are still being investigated. The Nb_3Si -C and (Nb) alloys represent a second group that have higher stress exponents (>3). The monolithic (Nb) alloys have exponents of ~ 3 , and in these systems deformation is probably controlled by dislocation creep. These exponents are similar to those reported previously for Nb-1.25Si [11]. This high stress exponent suggests that creep deformation is controlled by dislocation glide, as is the case for pure metals, despite the fact that the dislocation structures in Nb_3Si -C are complicated.

Table II: Stress, temperature, and power law constants describing secondary creep of the monolithic phases that were investigated.

Phase	Stress Range (MPa)	Temperature (°C)	Constant, B	Exponent n
Nb_5Si_3	100-280	1200	6.16×10^{-11}	1.0
Nb-10Si	70-140	1200	6.57×10^{-12}	1.9
Silicide-C	70-140	1200	3.84×10^{-11}	1.5
Nb_3Si -C	70-140	1200	1.07×10^{-14}	3.6
Laves-3	70-140	1200	1.11×10^{-9}	1
T2-C	70-140	1200	2.15×10^{-9}	0.9
(Nb)-3	3-80	1100	1.9×10^{-10}	3.3
(Nb)	3-80	1100	4.7×10^{-14}	2.9
(Nb)-3	3-20	1200	4.5×10^{-9}	3.1
(Nb)	3-30	1200	5.4×10^{-16}	5.5

Composite Creep Modeling

In order to develop an improved understanding of the response of the composite to increasing silicide volume fraction and increasing stress, the creep of the composite was simulated using the equation shown below [11],

where σ_A is the applied stress, n is the stress exponent for the silicide (1.0), and m is the stress exponent for the Nb (2.9). V_s and V_w are the volume fractions of the silicide and Nb, respectively. B_s and B_w are the pre-exponents in the power law creep expressions for the silicide and Nb, respectively.

$$\sigma_A = V_s \left[\frac{1}{B_s^{1/n}} \right] \dot{\epsilon}^{1/n} + V_w \left[\frac{1}{B_w^{1/m}} \right] \dot{\epsilon}^{1/m}$$

The constitutive creep equations for the monolithic solid solutions were employed; using the data for the (Nb) and silicide solid solutions shown in Table II. The above equation can predict the increase in the creep rate with increasing stress for a given Si concentration in the hypoeutectic regime. However, the model does not incorporate any damage mechanisms in either the (Nb) or the silicide.

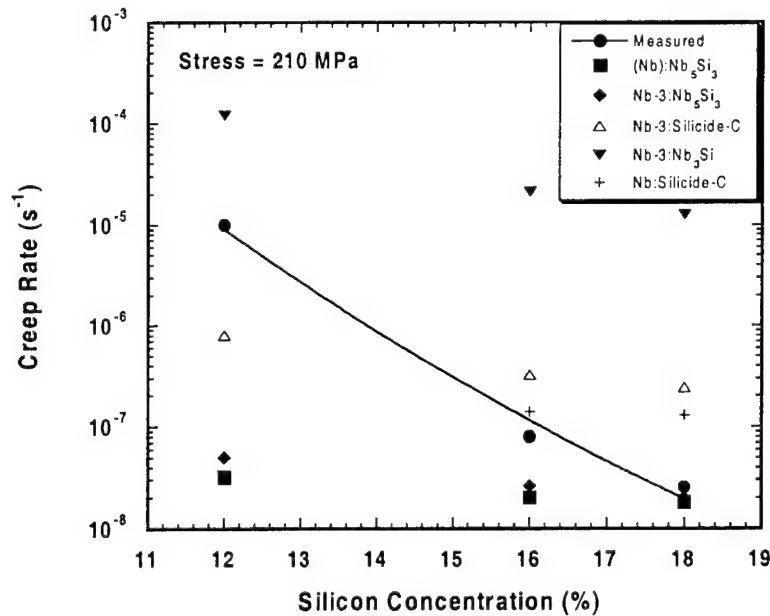


Figure 6. Comparison of the measured and the calculated composite creep rates for the range of (Nb) and silicide solid solutions investigated.

Figure 6 shows the effect of the both type of silicide and type of (Nb) on the predicted creep rates. The results show that increasing the alloying content of the (Nb) (Nb-3 vs. Nb-1Si) causes an increase in the predicted creep rate. Of the three silicides considered, the binary Nb₅Si₃ produces the composite with the lowest creep rate and the Nb₃Si produces the composite with the highest creep rate. In general the predicted creep rates are higher than those measured experimentally.

Figure 6 also shows the effect of silicide volume fraction on creep rate at a stress of 210 MPa. In Figure 6 the measured creep rates are given along with predicted creep rates for various combinations of (Nb) and silicide solid solutions. The measured creep rates decrease between 12 and 18%Si (~0.25 to ~0.7 silicide volume fraction). The calculated creep rates also decrease with increasing Si concentration from 12 to 18 %Si, but the rate at which the predicted creep rates decrease is slower than the rate at which the measured creep rates decrease. There are several possible reasons for this difference. First, in addition to the increase in the volume fraction of silicide, there is probably a change in the continuous matrix phase from (Nb) to silicide at some point between 12 and 18%Si. Second, interface diffusion may play a bigger role in the composites, whereas in the monolithic solid solutions creep was limited by bulk diffusion.

Oxidation Behavior

The composites from binary Nb-Si alloys have very poor oxidation resistance, as shown in Figure 7. However, the oxidation resistance at 1200 and 1300°C of silicide based composites is substantially improved by additions such as Ti, Al, and Cr [2,4,6,13], as shown in Figure 7. External and internal oxidation are the two principal concerns with Nb-silicide based in-situ composites. With regard to internal oxidation, additions of Hf can reduce oxygen solubility and diffusivity and thereby slow embrittlement at elevated temperatures [5,6,13].

The DS MASC shows oxidation rates intermediate between the high rates of an older Ni-based superalloy, for example IN 738, and the lower oxidation rates of third-generation single crystal superalloys. The dashed lines in Figure 6 indicate the oxidation rate goals, for a temperature of 1316°C. This goal is derived from the current superalloy capability at lower temperatures. The oxidation data for the MASC at 1200°C show a substantial improvement over the oxidation behavior of binary (Nb)-Nb₅Si₃ composites.

The addition of Cr-rich Laves phases can further improve the oxidation resistance. The oxidation resistance at 1204°C and 1316°C of a Nb-18Ti-7Hf-20Cr-2Al-18Si alloy is compared to that of MASC in Figure 8. There is a substantial improvement in oxidation resistance for the Cr-rich alloy, with ~33% Laves phase (by volume), ~25% (Nb), and ~42% M₅Si₃ silicides.

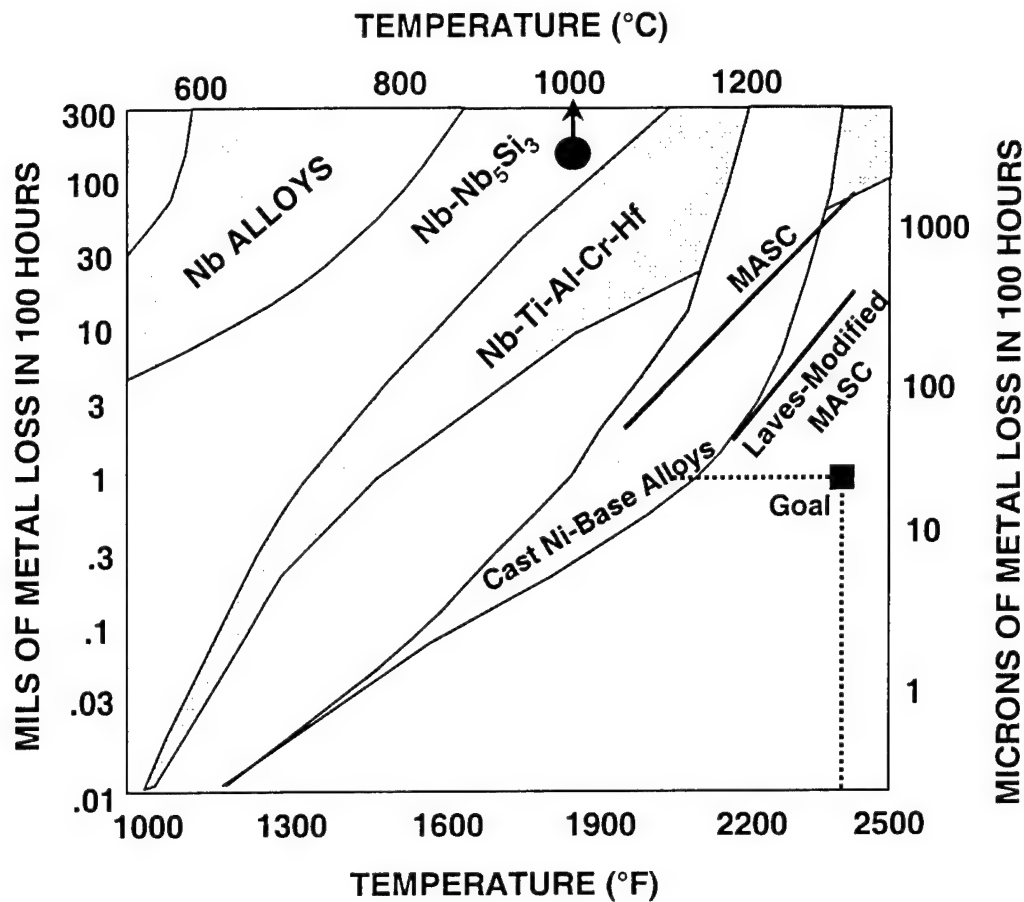


Figure 7. Comparison of the oxidation rates of silicide-based composites with those of Ni-based superalloys and monolithic Nb alloys. The metal and silicide composite (labeled MASC) shows improved oxidation behavior at temperatures greater than 1200°C.

The relationship between alloy composition and oxidation resistance of Nb-silicide based composites has been reported previously [13]. The results were characterized by regression analyses for major element effects (Nb, Ti, Hf, Cr, Si, and Al), and by direct comparison for other addition elements (B, Ge, Ta, Zr, Mo, W, and V). The oxidation rate at 1204°C (2200°F) and 1315°C (2400°F), as measured by weight loss per unit area, was related to major element concentrations by the following equations:

$$\Delta \text{wt/area} = C_{1204} - A_{1204} (1.0\text{Si} + 0.7\text{Cr} + 0.5\text{Ti} + 0.3\text{Al} + 0.01\text{Hf}), \text{ at } 1204^{\circ}\text{C}$$

$$\Delta \text{wt/area} = C_{1316} - A_{1316} (1.0\text{Si} + 0.7\text{Cr} + 0.4\text{Ti} + 0.8\text{Al} - 0.5\text{Hf}), \text{ at } 1316^{\circ}\text{C}$$

Where C and A are temperature dependent constants. At 1204°C, C was 473 and A was 11.5. At 1317°C, C was 1741 and A was 39.1. These equations show Si to be most beneficial in reducing the oxidation rate. Alloying additions of Cr and Ti are also beneficial. Al plays an increasingly important role at higher oxidation test temperatures.

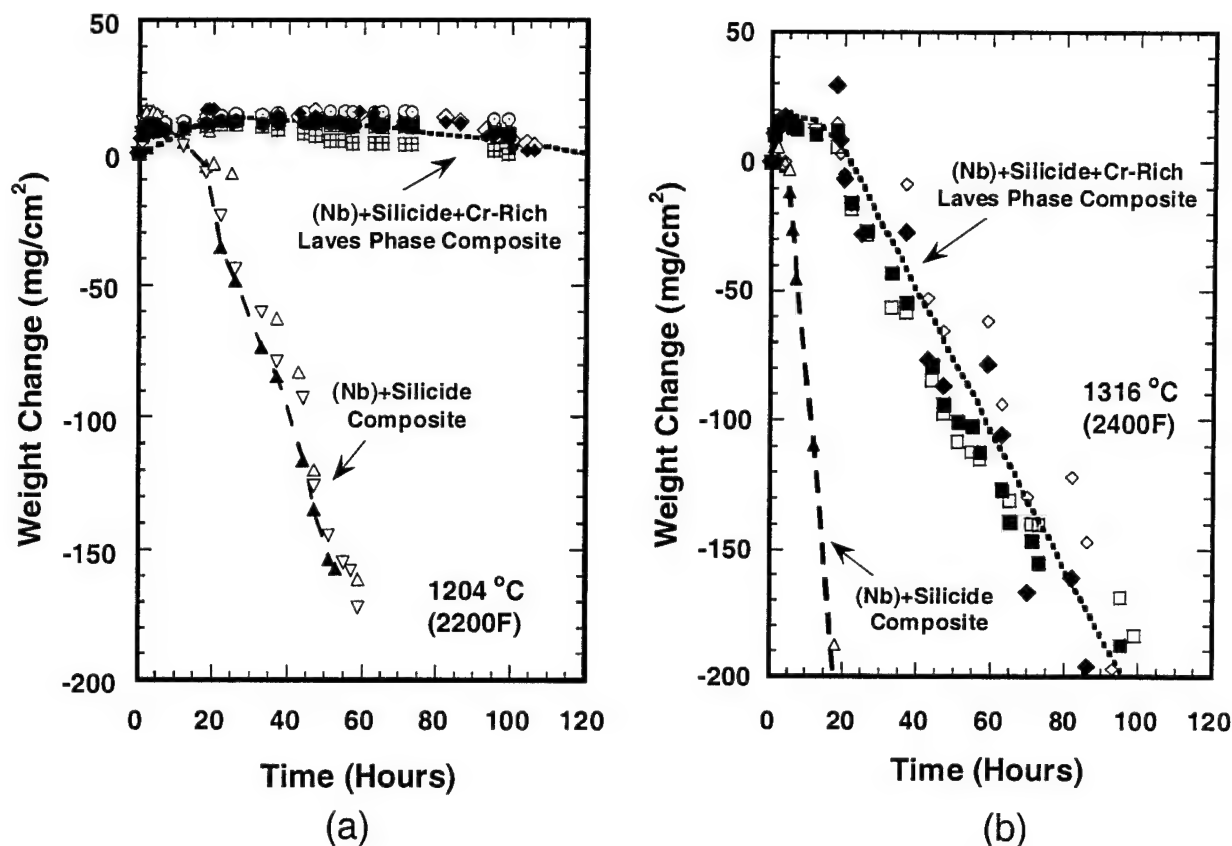


Figure 8. Comparison of oxidation behavior of Nb-18Ti-7Hf-20Cr-2Al-18Si with that of the MASC at 1204°C and 1316°C. Data are shown for 4 samples of MASC and 9 of the modified alloy of (Nb-18Ti-7Hf-20Cr-2Al-18Si) at 1204°C. Data are shown for 2 samples of baseline composition and 4 of the Laves phase modified alloy at 1316°C, (b). The higher Cr concentration in the alloy leads to stabilization of a Laves phase and improved oxidation resistance.

Studies of the effects of other alloying additions indicated that B offers a benefit to the oxidation performance of the composite when alloyed at levels greater than 3%; Ta and Zr are elements that can improve strength with the least damage to oxidation (up to concentrations of 6%). V, Mo and W can improve strength, but they severely degrade oxidation behavior. In some alloys, partial replacement of Si with Ge has been shown by to improve the oxidation resistance [6].

4. Conclusions:

This paper has described the creep behavior and oxidation performance of Nb-silicide based in-situ composites. The creep behavior of composites from model quaternary alloys and monolithic phases has been described. The creep rates of the composites from the quaternary Nb-Hf-Ti-Si alloys decreased with increasing Si concentration from 12 to 18%, and increasing

silicide volume fraction from 0.25 to 0.62. At higher Si concentrations, the creep rate increased as a result of crack linking and damage accumulation in the silicides. The quaternary alloy composite creep rate increased with increasing stress, but at each stress level there was a minimum in the creep rate at ~18Si.

Of the intermetallics investigated, the Nb₅Si₃ type silicides had the lowest creep rates. The hP16 silicide phases have higher secondary creep rates than any of the tetragonal silicides, or the T2 phases, at stresses greater than 140 MPa. Analysis of the creep exponents suggests that deformation of the complex Nb₅Si₃ type silicide is probably controlled by Nabarro-Herring type creep, as is the binary Nb₅Si₃ silicide. In contrast, creep of the Nb₃Si silicide appears to be controlled by a dislocation controlled mechanism. The (Nb) solid solutions have creep rates that are more than an order of magnitude higher than either the intermetallics or the composites that were investigated.

Modeling results and experimental data from the monolithic silicides and Nb solid solutions indicate that at low Si concentrations the creep deformation is dominated by the (Nb), but as the Si concentration is increased, and the silicide volume fraction is increased, the composite creep performance is controlled by the silicide. However, the model underestimates the effect of increasing volume fraction of the silicide on the creep rate.

5. Acknowledgments

The authors would like to thank D.J. Dalpe, E.T. Sylven, A.W. Davis, S. Sitzman, and E.H. Hearn for their contributions to the experimental work. This research was partially sponsored by AFOSR under contracts #F49620-00-C-0014 and #F33615-98-C-5215 with Dr. C.S. Hartley and Dr. P.L. Martin as Program Managers.

6. References:

1. Bewlay, B.P., Lipsitt, H.A., Jackson, M.R., Reeder, W.J., and Sutliff, J.A. (1995). *Mater. Sci. Eng.*, **A192/193**, pp. 534-543.
2. Bewlay, B.P., Jackson, M.R., and Lipsitt, H.A. (1996). *Metall. and Mater. Trans.*, **27A**, pp. 3801-3808.
3. Dimiduk, D.M., Mendiratta, M.G., and Subramanian, P.R. (1993). In *Structural Intermetallics*, Eds. R. Darolia, J.J. Lewandowski, C.T. Liu, P.L. Martin, D.B. Miracle, and M.V. Nathal, TMS Publications, Warrendale, Pa., pp. 619-630.

4. Bewlay, B.P., Lewandowski, J.J. and Jackson, M.R. (1997). *J. of Metals*, **49** (8), pp. 46-48.
5. Subramanian, P.R., Mendiratta, M.G., and Dimiduk, D.M. (1996). *Journal of Metals*, **48** (1), pp. 33-38.
6. Subramanian, P.R., Mendiratta, M.G., Dimiduk, D.M., and Stucke, M.A. (1997). *Mater. Sci. Eng.*, **A239-240**, pp. 1-13.
7. Mendiratta, M.G., and Dimiduk, D.M. (1993). *Metall. Trans. A* **24A**, pp. 501-504.
8. Bewlay, B.P., Bishop, R.R., and Jackson, M.R. (1998). *Journal of Phase Equilibria*, **19** (6), pp. 577-586.
9. Bewlay, B.P., Bishop, R.R., and Jackson, M.R. (1999). *Z. Metallkunde*, **90** (60), pp. 413-422.
10. Bewlay, B.P., Whiting, P., and Briant, C.L. (1999). *MRS Proceedings on High Temperature Ordered Intermetallic Alloys VIII*, pp. KK6.11.1-KK6.11.5.
11. Henshall, G.A., Strum, M.J., Subramanian, P.R., and Mendiratta, M.G. (1995). *Mat. Res. Soc. Symp. Proc.* **364**, pp. 937-942.
12. Subramanian, P.R., Parthasarathy, T.A., Mendiratta, M.G., and Dimiduk, D.M. (1995). *Scripta Met.* **32** (8), pp. 1227-1232.
13. Jackson, M.R., and Bewlay, B.P. (1998). USAF Delivery order report, AFML, Sept 1998.

Analyses of the Eutectoid Phase Transformation in Complex DS Nb-Silicide In-Situ Composites

S.D. Sitzman and B.P. Bewlay

Microscopy and Microanalysis, 2001

ANALYSES OF THE EUTECTOID PHASE TRANSFORMATION IN COMPLEX DS Nb-SILICIDE IN-SITU COMPOSITES

S.D. Sitzman¹ and B.P. Bewlay²

¹TiTech International, Inc., Pomona, CA 91768

²General Electric Corporate Research and Development, Schenectady, New York 12301

In-situ composites based on (Nb) and Nb silicides, such as Nb₅Si₃ (tI32 crystal structure) and Nb₃Si (tP32 crystal structure), are being investigated for revolutionary high-temperature structural applications [1, 2]. The use of Hf and Ti alloying additions to these silicides has also been examined; in these systems Nb₅Si₃ has also been observed with the hP16 structure. The present paper describes EBSD analyses of a directionally solidified (DS) Nb-silicide based composite that experienced a eutectoid transformation. The composites were directionally solidified using the Czochralski method as described previously [1]. The composites were creep tested at 1200°C for 24 hours. Microstructure and microtexture characterization were performed using scanning electron microscopy, and electron backscatter diffraction pattern analysis (EBSD).

The microstructure of a composite directionally solidified from a Nb-12.5Hf-33Ti-16Si alloy is shown in Figure 1. In the as-DS condition the microstructure consisted of primary (Nb)₃Si dendrites and coarse (Nb)₃Si-(Nb) two-phase cells. There was also a fine-scale intercellular (Nb)₅Si₃-(Nb) eutectic. After creep testing partial eutectoid decomposition of the eutectic (Nb)₃Si to (Nb)₅Si₃ + (Nb) has occurred, as shown in Figure 1(b). This is analogous to the eutectoid phase transformation that occurs in the binary Nb-Si system, where Nb₃Si is metastable and decomposes to Nb and (Nb)₅Si₃ below 1750°C. A typical micrograph showing partial eutectoid phase transformation of Nb-19Si is shown in Figure 2.

EBSD analyses indicate that the complex (Nb)₃Si has decomposed by an analogous eutectoid reaction, where the products of the reaction are (Nb) and hP16 (Nb)₅Si₃. This is an unexpected result, because the binary and ternary phase diagrams would lead one to expect tI32 (Nb)₅Si₃. It is also surprising that the eutectoid has occurred at what are relatively low temperatures for these composites. It appears that in the complex alloy where the Ti and Hf concentrations are high, stabilization of the hP16 occurs in preference to the tI32 structure. The hP16 (Nb)₅Si₃ may offer a lower nucleation energy for the eutectoid hP16 Nb)₅Si₃ than for the tI32.

The following phase orientation relationships were observed: The faceted primary (Nb)₃Si dendrites at cell cores have the same [001] orientation as eutectic (Nb)₃Si. The (Nb)₅Si₃ in the fine-scale eutectic exhibits a range of orientations in intercellular regions. The [0001] in the hP16 (Nb)₅Si₃ and the [001] (Nb)₃Si are parallel in several areas. The eutectoid hP16 (Nb)₅Si₃ grows epitaxially with the fine-scale eutectic (Nb)₅Si₃.

References

1. B.P. Bewlay, M.R. Jackson, and P.R. Subramanian, JOM, (1999) Vol 51(4) (1999), pp. 32-36.
2. M.G. Mendiratta and D.M. Dimiduk, Metall. Trans. A 24A (1993), pp. 501-504.

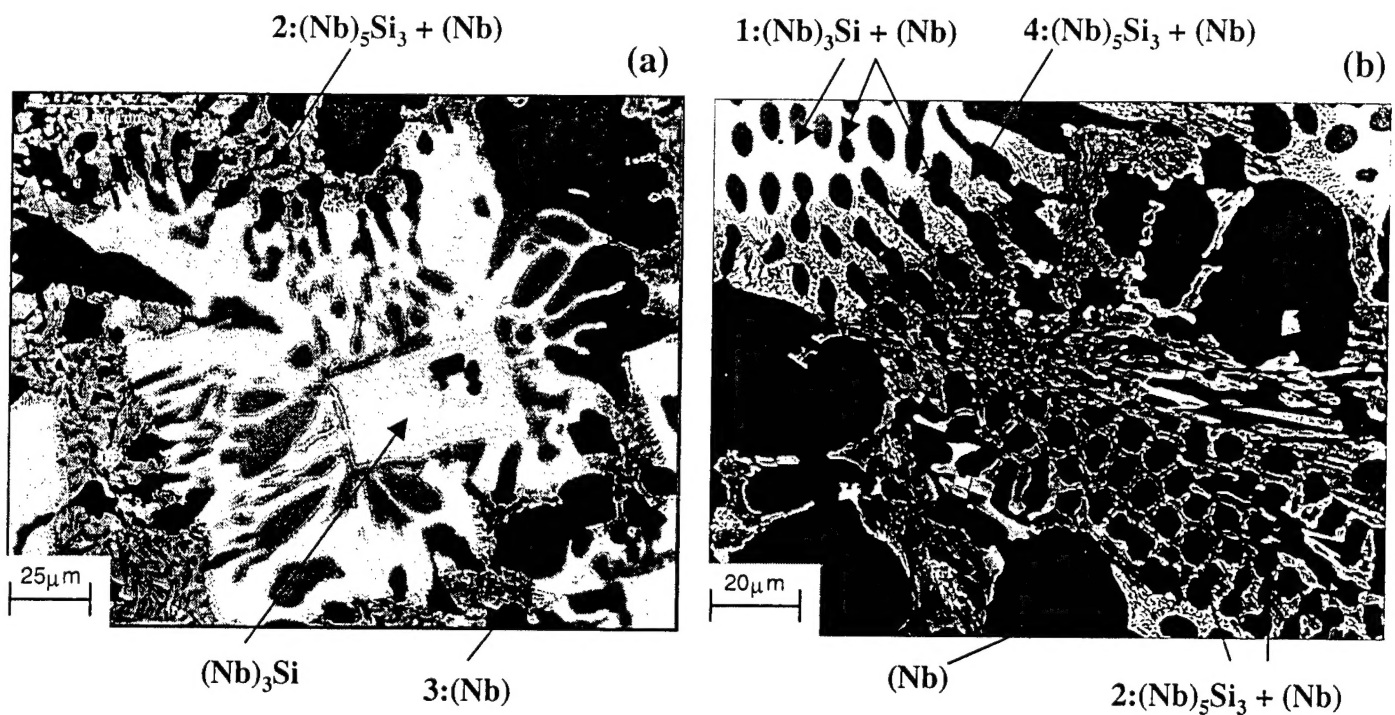


FIG. 1: Backscatter electron images (BEI) at (a) low and (b) high magnifications. The figure shows the transverse section of the DS Nb-12.5Hf-33Ti-16Si, showing the primary (Nb) dendrites (1), the primary $(\text{Nb})_3\text{Si}$ dendrites, and the fine-scale $(\text{Nb})_5\text{Si}_3$ -(Nb) interdendritic eutectic (2); the as-DS eutectic $(\text{Nb})_5\text{Si}_3$ has the hP16 structure. The $(\text{Nb})_3\text{Si}$ -(Nb) coarse eutectic can be seen at the upper left corner (1). A eutectoid reaction, $(\text{Nb})_3\text{Si} \leftrightarrow (\text{Nb})_5\text{Si}_3 + (\text{Nb})$, 4, has occurred by nucleation on the interface between the eutectics along the silicide arms; the transformation has proceeded into the $(\text{Nb})_3\text{Si}$.

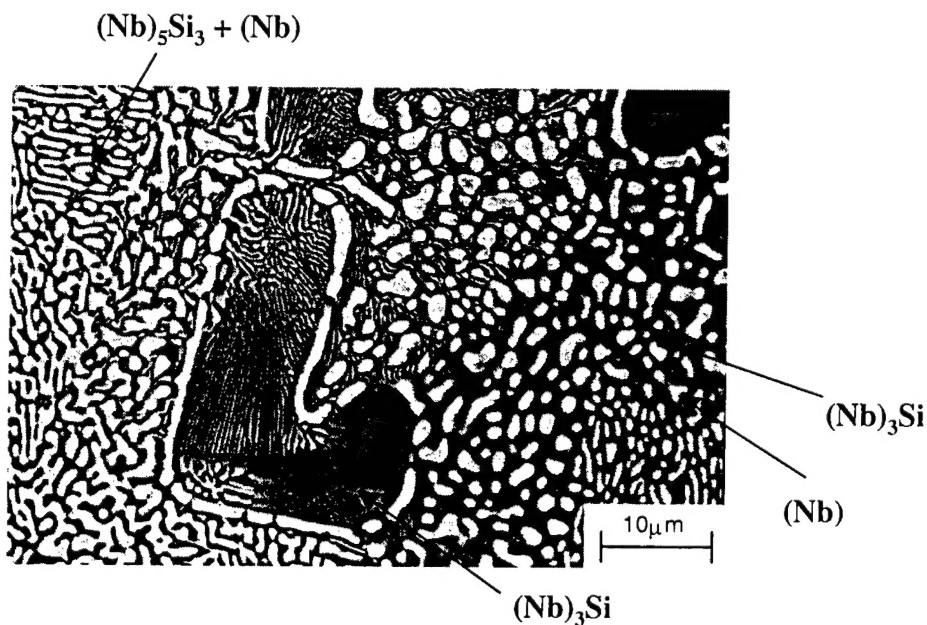


FIG. 2: Partial eutectoid phase transformation in binary Nb-19Si.